



**HAL**  
open science

# Copper-based p-type semiconducting oxides : from materials to devices

Joao Avelas Resende

► **To cite this version:**

Joao Avelas Resende. Copper-based p-type semiconducting oxides : from materials to devices. Materials. Université Grenoble Alpes; Université de Liège, 2017. English. NNT : 2017GREAI072 . tel-01793013

**HAL Id: tel-01793013**

**<https://theses.hal.science/tel-01793013>**

Submitted on 16 May 2018

**HAL** is a multi-disciplinary open access archive for the deposit and dissemination of scientific research documents, whether they are published or not. The documents may come from teaching and research institutions in France or abroad, or from public or private research centers.

L'archive ouverte pluridisciplinaire **HAL**, est destinée au dépôt et à la diffusion de documents scientifiques de niveau recherche, publiés ou non, émanant des établissements d'enseignement et de recherche français ou étrangers, des laboratoires publics ou privés.



## Doctoral Thesis

To obtain the academic doctoral double-degree joint by  
**Communauté Université Grenoble Alpes**  
and  
**Université De Liège**

Under the framework of the International Doctoral School in Functional  
Materials (IDS-FunMat)  
Arrêté ministériel : le 6 janvier 2005 - 7 août 2006

Prepared by  
**João AVELÃS RESENDE**

Supervised by **Jean-Luc DESCHANVRES** et **Ngoc Duy NGUYEN**  
And Co-supervised by **Maria del Carmen JIMENEZ AREVALO**

in **Laboratoire des Materiaux et du genie Physique (LMGP)** and  
**Solid State Physics, Interfaces and Nanostructures (SPIN)**

# Copper-based p-type semiconducting oxides: From materials to devices

Public oral defense on **October 27, 2017**

with the jury members :

**Prof. Francis MAURY**  
Research director in CNRS CIRIMAT Toulouse (President)

**Prof. Antoine BARNABE**  
Professor of Université Toulouse Paul Sabatier (Reporter)

**Dr. Stéphane JOBIC**  
Research Director in CNRS IMN Nantes HDR (Reporter)

**Dr. Catherine HENRIST**  
Assistant Professor in Université de Liège (Examiner)

**Prof. Ngoc Duy NGUYEN**  
Professor of Université de Liège (Supervisor)

**Dr. Jean-Luc DESCHANVRES**  
Researcher in CNRS (Supervisor)

**Dr. Maria del Carmen JIMENEZ AREVALO**  
Researcher engineer in CNRS (Co-Supervisor)





# Acknowledgments

Firstly, I would like to express my honest gratitude to my two supervisors Dr. Jean-Luc Deschavres and Prof. Ngoc Duy Nguyen for their patience, motivation and immense knowledge. Their guidance was unquestionably fundamental to overcome all the difficulties and doubtful moments during all the time of research and the writing of this thesis. Besides my direct two supervisors, I would like to specially thank to Dr. Carmen Jimenez as co-supervisor, for the support during these last 3 years, the insightful comments and encouragement, but also for the hard questions which incited me to widen my research and life from various perspectives.

In LMGP, I thank Michele San Martin, Josiane Viboud, Virginie Charrière, Matthieu Jouvert, Mikhail Anikin and Serge Quessada for the administrative and technical help. I would like to acknowledge Odette Chaix, Hervé Roussel, Laetitia Rapenne and Etienne Pernot for support with the characterization techniques and consequent scientific consultations. Additionally, I would thank the scientific support and endless discussions with Stephane Brochen, David Rojas-Munoz, Daniel Bellet and Vincent Consonni in the laboratory. I particular acknowledgement to the PhD students Thomas Coussuet, Viet Nguyen and Sara Aghazadehchors and the Master student Aissatou Ndong for the collaborative work we developed together. Without you, this thesis would have not been complete. In the Université de Liège, I would like to thank Bruno Baert, Emille Fourneau and Jonathan Avila Osses, as well as Yoann Malier for all the help and discussions in the SPIN lab.

The constant move between two different cities was an immense challenge that was only possible with the help of my friends (KjM, RRL, ES, MbC, AHSL, CM, ML, HL, DP, ESP, LM, RJ, AV, JF, IDS-FunMaters, MF and BE). The PhD life between Grenoble and Liege was an enrichment experience that enable be to discover two beautiful and interesting countries, both with special facts and perks that divided my heart in two parts.

Furthermore, I am grateful for the economic support provided by the International Doctoral School in Functional Materials under the project ERASMUS MUNDUS II 2009–2013.

Last but not the least, I would like to thank my family: my parents, my sister and the little Tomás, for supporting me spiritually throughout writing this thesis and my life in general.

# Abstract

The lack of a successful p-type semiconductor oxides delays the future implementation of transparent electronics and oxide-based photovoltaic devices. In the group semiconducting compounds, copper-based oxides present promising electrical, optical and manufacturing features that establish this family of materials suitable for p-type semiconductor applications. In this work, we focused on the growth of cation doped Cu<sub>2</sub>O and intrinsic CuCrO<sub>2</sub> thin films, aiming for enhancements of their optical and electrical response. Furthermore, we implemented these oxide films into pn junction devices, such as solar cells and UV photodetectors.

In the work on Cu<sub>2</sub>O, we achieved the incorporation of magnesium up to 17% in thin films by aerosol-assisted chemical vapor deposition, resulting in morphology changes. Electrical resistivity was reduced down to values as low as 6.6 ohm.cm, due to the increase of charge-carrier density up to 10<sup>18</sup> cm<sup>-3</sup>. The incorporation of magnesium had additionally an impact on the stability of the Cu<sub>2</sub>O phase. The transformation of Cu<sub>2</sub>O into CuO under oxidizing conditions is significantly postponed by the presence of Mg in the films, due to the inhibition of copper split vacancies formation. The integration into pn junctions was successfully achieved using only chemical vapor deposition routes, in combination with n-type ZnO. Nevertheless, the application of Mg-doped Cu<sub>2</sub>O in solar cells present a meager photovoltaic performance, far from the state-of-the-art reports.

In the work on CuCrO<sub>2</sub>, we demonstrate the first fabrication of ZnO/CuCrO<sub>2</sub> core-shell nanowire heterostructures using low-cost, surface scalable, easily implemented chemical deposition techniques at moderate temperatures, and their integration into self-powered UV photodetectors. A conformal CuCrO<sub>2</sub> shell with the delafossite phase and with high uniformity is formed by aerosol-assisted chemical vapor deposition over an array of vertically aligned ZnO nanowires grown by chemical bath deposition. The ZnO/CuCrO<sub>2</sub> core-shell nanowire heterostructures present a significant rectifying behavior, with a maximum rectification ratio of 5500 at ±1V, which is much better than similar 2D devices, as well as a high absorption above 85% in the UV region. When applied as self-powered UV photodetectors, the optimized heterojunctions exhibit a maximum responsivity of 187 μA/W under zero bias at 374 nm as well as a high selectivity with a UV-to-visible (374-550 nm) rejection ratio of 68 under an irradiance of 100 mW/cm<sup>2</sup>.

# Résumé

L'absence d'oxydes semi-conducteurs de type p de haute performance retarde le développement de l'électronique transparente et du photovoltaïque à base d'oxydes. Dans le groupe des composés semi-conducteurs, les oxydes à base de cuivre présentent des caractéristiques électriques, optiques et de fabrication prometteuses qui établissent cette famille de matériaux comme bien adaptés aux applications semi-conductrices de type p. Dans ce travail, nous nous concentrons sur la croissance de films minces d'une part de  $\text{Cu}_2\text{O}$  dopée par des cations et d'autre part de  $\text{CuCrO}_2$ , visant à améliorer leurs propriétés optiques et électriques. De plus, nous avons mis en œuvre ces films d'oxyde dans des dispositifs de jonction *pn* tels que des cellules solaires et des photodétecteurs UV.

Dans le travail sur  $\text{Cu}_2\text{O}$ , nous avons réalisé l'incorporation de magnésium jusqu'à 17% dans des films minces par dépôt chimique en phase vapeur assisté par aérosol, entraînant des changements de morphologie. La résistivité électrique a été réduite jusqu'à des valeurs de 6,6 ohm.cm, en raison de l'augmentation de la densité de porteur de-charges jusqu'à  $10^{18} \text{ cm}^{-3}$ . L'incorporation du magnésium a en outre eu un impact sur la stabilité de la phase  $\text{Cu}_2\text{O}$ . En effet la transformation du  $\text{Cu}_2\text{O}$  en  $\text{CuO}$  en conditions oxydantes est considérablement retardée par la présence de Mg dans les films, en raison de l'inhibition de la formation d'un type particulier de lacune de cuivre (*split vacancy*). L'intégration dans les jonctions *pn* a été réalisée avec succès en utilisant uniquement des voies de dépôt chimique en phase vapeur, en combinaison avec le  $\text{ZnO}$  de type n. Néanmoins, l'application de  $\text{Cu}_2\text{O}$  dopé au Mg dans les cellules solaires présente un effet photovoltaïc très faible, loin des meilleures valeurs de l'état de l'art.

Dans le travail sur  $\text{CuCrO}_2$ , nous démontrons la première fabrication d'hétérostructures de nanofils en configuration cœur/coquille  $\text{ZnO}/\text{CuCrO}_2$  utilisant des techniques de dépôt chimique adaptées pour des grandes surface, à faible coût, facilement implémentées à des températures modérées et leur intégration dans des photodétecteurs UV auto-alimentés. Une coquille conforme de  $\text{CuCrO}_2$  avec la phase de delafossite et avec une uniformité élevée a été élaborée par un dépôt chimique en phase vapeur assisté par aérosol sur un réseau de nanofils  $\text{ZnO}$  alignés verticalement, obtenu par dépôt par bain chimique. Les hétérostructures  $\text{ZnO}/\text{CuCrO}_2$  coeur-coquille présentent un comportement rectificateur significatif, avec un ratio de rectification maximal de 5500 à  $\pm 1\text{V}$ , ce qui est bien meilleur que les dispositifs 2D similaires

rapportés dans la littérature, ainsi qu'une absorption élevée supérieure à 85% dans la région UV. Lorsqu'ils sont appliqués en tant que photodétecteurs UV auto-alimentés, les hétérojonctions optimisées présentent une réponse maximale de  $187 \mu\text{A} / \text{W}$  sous une polarisation nulle et à 374 nm ainsi qu'une sélectivité élevée avec un ratio de rejet entre l'UV-et le visible (374-550 nm) de 68 sous irradiance de  $100 \text{ mW}/\text{cm}^2$ .

# Table of Contents

Preface.....	1
Chapter I: Introduction.....	3
1.1 Cuprous oxide (Cu <sub>2</sub> O).....	4
1.1.1 Conductivity in Cu <sub>2</sub> O.....	6
1.1.2 Cu <sub>2</sub> O deposition .....	9
1.1.3 Dopants.....	11
1.1.4 CuCrO <sub>2</sub> - Delafossite.....	13
1.2 Devices based on oxide semiconductors .....	16
1.2.1 Transparent electronics .....	16
1.2.2 Photovoltaics .....	21
1.3 Conclusion.....	32
1.4 References .....	33
Chapter II: Experimental procedure and characterization techniques .....	47
2.1 Aerosol-assisted Metal-organic Chemical Vapour Deposition.....	48
2.1.1 Metal-organic Precursors .....	52
2.1.2 Description of an AA-MOCVD experiment .....	54
2.1.3 Modification of the reactor configuration .....	61
2.1.4 Annealing treatment .....	61
2.1.5 Metals Thermal evaporation.....	62
2.2 Techniques of characterization.....	64
2.2.1 Morphological, chemical and structural characterization .....	64
2.2.2 Spectroscopic and spectrometry techniques.....	70
2.2.3 Electrical and functional properties of materials and devices.....	76
2.3 Simulation .....	80
2.3.1 Basic equations.....	80

2.3.2	Model's algorithm .....	82
2.4	References .....	84
Chapter III: Cation-doped Cuprous Oxide thin films .....		87
3.1	Intrinsic Cu <sub>2</sub> O thin films .....	87
3.2	Cation doped Cu <sub>2</sub> O thin films: screening different elements.....	92
3.3	Tin doped Cu <sub>2</sub> O thin films .....	96
3.4	References .....	99
Chapter IV: Magnesium-doped cuprous oxide thin films.....		101
4.1	Magnesium-doped cuprous oxide (Cu <sub>2</sub> O:Mg) thin films.....	103
4.1.1	Introduction .....	103
4.1.2	Deposition of Cu <sub>2</sub> O:Mg thin layers by AA-MOCVD.....	104
1.4.1	Structural characterization.....	104
1.4.2	Optic and electric characterization.....	112
4.1.3	Summary .....	116
4.2	Stability of Magnesium-doped cuprous oxide (Cu <sub>2</sub> O:Mg) thin films under thermal treatments.....	118
4.2.1	Introduction .....	118
4.2.2	Experimental .....	119
1.4.3	Structural characterization.....	119
4.2.3	<b>Electric</b> characterization under temperature.....	131
1.4.4	Discussion .....	137
4.3	Cu <sub>2</sub> O:Mg/ZnO heterojunctions .....	139
4.3.1	Introduction .....	139
4.3.2	Simulation of a pn junction formed by Cu <sub>2</sub> O/ZnO .....	140
4.3.3	Deposition of pn junction formed by Cu <sub>2</sub> O/ZnO.....	144
4.3.4	Summary .....	157
4.4	Conclusions .....	157

4.5	References .....	158
5	Chapter V: CuCrO <sub>2</sub> delafossite thin films .....	163
5.1	Deposition and characterization of CuCrO <sub>2</sub> films .....	164
5.1.1	Introduction .....	164
5.1.2	Experimental .....	164
5.1.3	Characterization of CuCrO <sub>2</sub> films .....	165
5.1.4	Conclusion on CuCrO <sub>2</sub> thin films .....	171
5.2	ZnO/CuCrO <sub>2</sub> Core-Shell Nanowire Heterostructure for Self-Powered UV Photodetectors .....	172
5.2.1	Introduction .....	172
5.2.2	Experimental .....	172
5.2.3	Structural characterization of core-shell structures .....	173
5.2.4	Electrical characterization of core-shell heterostructures .....	180
5.2.5	Conclusions on the core-shell heterostructures .....	185
5.3	Conclusions .....	186
5.4	References .....	186
6	Chapter VI - Conclusions and future perspectives .....	191
7	Appendix .....	195
7.1	A- EXAFS Data Fittings .....	196
7.2	B – PDF X-Ray Files .....	198
7.3	C – Raman spectrum of Cu <sub>2</sub> O powder .....	201
8	List of communications .....	202

# List of Abbreviations

AA-MOCVD: aerosol assisted metal organic chemical vapor deposition

AFM: atomic force microscopy

ALD: Atomic Layer Deposition

AZO: aluminum doped zinc oxide

CB: conduction band

CBM: conduction band minimum

CIGS: copper indium gallium diselenide

CuCrO<sub>2</sub>: Copper-Chromium Oxide

Cu<sub>2</sub>O: Copper(I) Oxide or Cuprous Oxide

Cu<sub>2</sub>O:Mg: Magnesium doped Cuprous Oxide

CVD: chemical vapor deposition

DOS: density of states

DSSC: dye-sensitized solar cells

EQE: external quantum efficiency

EXAFS: Extended X-ray absorption fine structure

FEG: field emission gun ii

FoM: figure of merit ( $\Omega^{-1}$ )

IR: infrared

ITO: tin doped indium oxide

PCE: Power Conversion Efficiency

PDF: powder diffraction file

PV: photovoltaics

RF: Radio-frequency

RT: room temperature

SALD: Spatial Atomic Layer Deposition

SEM: scanning electron microscopy

TCM: transparent conductive materials

TCO: transparent conductive oxides

TFT: thin film transistors

TEM: transmission electron microscopy

UV: ultraviolet

VB: valence band

VBM: valence band maximum

XRD: X-ray diffraction

XPS: X-ray photoelectron spectroscopy

ZnO: Zinc Oxide

# Symbols and Physical Quantities

$V_{Cu}$ : Copper simple vacancy

$V_{Cu}^{split}$ : Copper split vacancy

$\epsilon_s$ : permittivity.

$A$ : vector potential vector

$B$ : full width at half maximum (FWHM) of the intensity peak

$B$ : magnetic field vector

Cr(acac)<sub>2</sub>: Chromium acetylacetonate

Cu(acac)<sub>2</sub>: Copper acetylacetonate

$D$ : displacement vector

$E$ : electric field vector

$E$ : electric field

$e$ : electron and elementary charge of electrons

$e$ : thickness of the film (nm)

$E_c$ : Energy of the conduction band

$E_{Fi}$ : Fermi level

$E_{Fn}$ : Fermi level closer to the conduction band

$E_{Fp}$ : Fermi level closer to the valence band

$E_v$ : Energy of the valence band

$F$ : constant defined for sheet resistance 1.442

$f$ : excitation frequency of the transducer ( $s^{-1}$ )

$FF$ : fill factor of a solar cell

$F_n$ : quasi-Fermi energies of electrons

FoM: Figure of merit

$F_p$ : quasi-Fermi energies of holes

$F_t$ : quasi-Fermi energies of traps

$g_t$ : degeneracy factor of the trap states.

$h$ : Holes

$I$ : current (A)

$I_{sc}$ : short-circuit current (A)

$J$ : current density ( $A.cm^{-2}$ )

**J**: current density vector  
*J<sub>sc</sub>*: short-circuit current density ( $\text{A.cm}^{-2}$ )  
*k*: semi-empirical constant for droplets diameter  
*K*: Scherrer constant  
*L*: mean crystallite size  
*m\**: equivalent mass  
*Mg(acac)<sub>2</sub>*: Magnesium acetylacetonate  
*n*: electron concentration ( $\text{cm}^{-3}$ )  
*N<sub>A</sub>*: Density of acceptor defects  
*N<sub>D</sub>*: Density of donor defects  
*p*: holes concentration ( $\text{cm}^{-3}$ )  
*P<sub>inc</sub>*: power from the incident light on the cell  
*P<sub>prod</sub>*: power produced by the cell  
*R<sub>S</sub>*: sheet resistance ( $\Omega/\text{sq}$ )  
*R<sub>sh</sub>*: shunt resistance ( $\Omega/\text{sq}$ )  
*T*: Temperature  
*v*: velocity of the charge.  
*V*: voltage (V)  
*V<sub>H</sub>*: Hall potential  
*V<sub>oc</sub>*: open-circuit voltage (V)  
*x*: distance from the junction,  
*γ*: surface tension ( $\text{N.m}^{-1}$ )  
*η*: efficiency of a solar cell  
*ρ*: resistivity ( $\Omega.\text{cm}$ )  
*ρ<sub>l</sub>*: density of the liquid ( $\text{Kg.m}^{-3}$ )  
*σ*: Conductivity ( $\Omega^{-1}.\text{cm}^{-1}$  or  $\text{S.cm}^{-1}$ )  
*Ψ*: potential  
*ε*: dielectric constant  
*d*: distance between crystallographic planes  
*n*: non-ideality factor or order of diffraction  
*θ*: diffraction angle of the light  
*λ*: light wavelength (nm)  
*ρ*: charge density



# Preface

This doctoral thesis is under the framework of International Doctoral School in Functional Materials (IDS-FunMat: <https://www.idsfunmat.u-bordeaux1.fr/>). It is co-supervised by Dr. Jean-Luc Deschanvres from LMGP (CNRS, France) and Professor Dr. Duy Ngoc Nguyen from Université de Liège (ULg, Belgium); as well co-supervised by Dr. Carmen Jimenez (CNRS, France). The main work in this thesis has been conducted in two laboratories: LMGP (Laboratoire des Matériaux et du Génie Physique, <http://www.lmgp.grenoble-inp.fr/>) which is expert in deposition and characterization of functional thin film materials, and as well in the research group for Solid State Physics, Interfaces and Nanostructures (SPIN) (<http://www.spin.ulg.ac.be/>) in the department of Physics of Université de Liège which is expert in the electrical and optical properties of semiconducting materials and systems, with a particular interest in crystalline ultra-thin films and engineered nanostructures.

This PhD thesis focuses on the application of copper-based oxides combined with different cations to create *pn* junction devices, such as solar cells or Ultra-Violet (UV) photodetectors. As the title describes, *from material to devices*, all of the document here presented will follow this duality between the material fabrication and its application to functional devices.

Chapter I deals with the introduction to the materials, especially on Cu<sub>2</sub>O p-type semiconductor, explaining in detail the physical and chemical properties of the material, reporting on the doped systems already studied and other copper-based materials as delafossites, in particularly CuCrO<sub>2</sub>. In the devices part, we focus on describing transparent devices based on oxides materials as thin film transistors (TFT), which was an enabling technology for the development of oxide semiconductors. Then, we focus on the advances on *pn* junction and its possible application on solar cells or UV photodetectors. In both cases we present a historical background, explain the working mechanism, and report the state-of-the-art devices based on Cu<sub>2</sub>O, ending with the actual needs of these technologies.

A next chapter (II) works as a breaking point in the document, since here we introduce the deposition method, the different analysis techniques and the numerical model to create a *pn* junction.

## Preface

The main body of the thesis, composed by the following three chapters, explores the materials description and their application into functional devices. We start with chapter III where we present the preliminary tests on the Cu<sub>2</sub>O thin films doped with different cations, with a particular interest to Sn-doped Cu<sub>2</sub>O.

Chapter IV is based on Mg-doped Cu<sub>2</sub>O study with an extensive analysis on the crystallographic structure, microstructural topography, and optical and electrical response to understand the dopant effect. In depth study on the thermal stability is also reported. The chapter ends with a study on *pn* junction between Mg-doped Cu<sub>2</sub>O and ZnO, first with a numerical simulation and then by experimental deposition of these structures, and finally a solar cells performance results.

Chapter V starts with an optimization of CuCrO<sub>2</sub> delafossite phase deposition by aerosol-assisted MOCVD, which is latter applied to a nanostructured UV photodetector based on ZnO and CuCrO<sub>2</sub>.

The last chapter serves as a conclusion of the work developed. It contains the main highlights in terms of results, the new scientific ideas suggested, the problems or open questions and finally, we suggest the future work to be developed.

The thesis' appendix presents the fitting of EXAFS data from Cu<sub>2</sub>O and Cu<sub>2</sub>O:Mg thin films. As supplemental materials, XRD PDF files and Raman reference files of the different oxides are also present in the appendix

# Chapter I: Introduction

1.1	Cuprous oxide ( $\text{Cu}_2\text{O}$ ).....	4
1.1.1	Conductivity in $\text{Cu}_2\text{O}$ .....	6
1.1.2	$\text{Cu}_2\text{O}$ deposition .....	9
1.1.3	Dopants.....	11
1.1.4	$\text{CuCrO}_2$ - Delafossite.....	13
1.2	Devices based on oxide semiconductors.....	16
1.2.1	Transparent electronics .....	16
1.2.2	Photovoltaics .....	21
1.3	Conclusion.....	32
1.4	References .....	33

## 1.1 Cuprous oxide (Cu<sub>2</sub>O)

The exploration of novel oxide semiconductors has been intensified in the last two decades, mostly driven by transparent electronics or solar cells applications. In the p-type semiconducting compounds group, cuprous oxide, Cu<sub>2</sub>O, presents promising electrical and manufacturing features that identify it as a suitable candidate for the electronics and energy devices <sup>1</sup>.

In the family of the oxide materials, the cuprous oxide has a crystalline cubic structure with a lattice parameter of 4.2696 Å. The crystal structure corresponds to the space group  $Pn\bar{3}m$ , which incorporate a full octahedral symmetry. In the case of considering the oxygen atoms as the origin of the body centred cubic (bcc) primitive cell, the 4 copper atoms are located in the diagonals in the positions:  $(\frac{1}{4}, \frac{1}{4}, \frac{1}{4})$ ,  $(\frac{3}{4}, \frac{3}{4}, \frac{1}{4})$ ,  $(\frac{1}{4}, \frac{3}{4}, \frac{3}{4})$ ,  $(\frac{3}{4}, \frac{1}{4}, \frac{3}{4})$ , as represented in the Figure I-1 a).

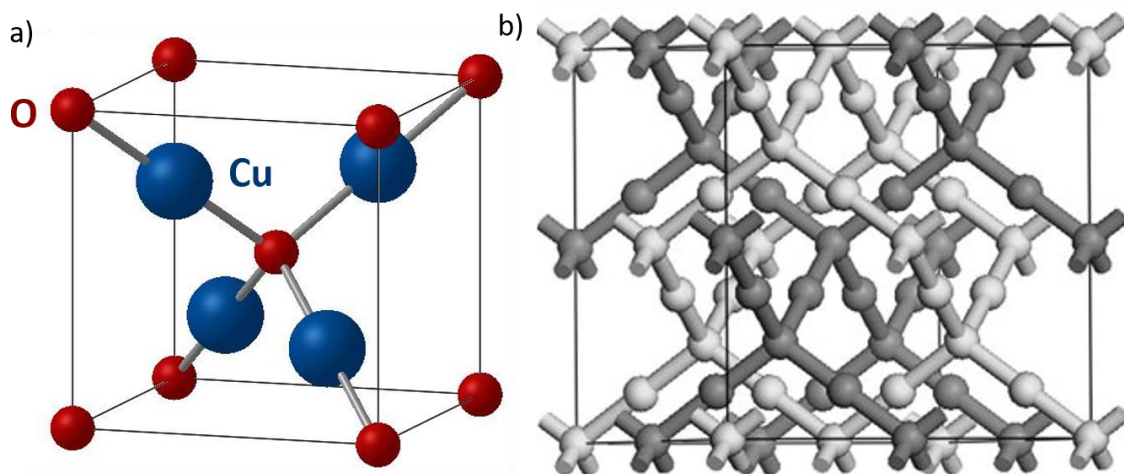


Figure I-1 Crystallographic structure of Cu<sub>2</sub>O with oxygen atoms as the origin of the bcc cell. Oxygen represented in red and Copper in blue. (b) Cu<sub>2</sub>O atomic structure of 2x2x2 cells. The two interpenetrating Cu–O–Cu networks (one light coloured and the other dark coloured). Adapted from Nolan<sup>2</sup>

The oxygen atoms are tetrahedrally coordinated by the copper, while the copper ones are linearly coordinated by the oxygen ones. The distance between Cu-O neighbouring atoms is 1.85 Å, O-O is 3.68 Å and Cu-Cu is 3.02 Å. This structure creates an oxide with a density of 6.10 g.cm<sup>-3</sup>, and a molar mass of 143.09 g.mol<sup>-1</sup>. In stoichiometry conditions, the concentration of copper is twice the concentration of oxygen, 5.05x10<sup>22</sup> cm<sup>-3</sup> and 2.52 x 10<sup>22</sup> cm<sup>-3</sup>, respectively.

The Cu<sub>2</sub>O structure has another relevant characteristic, its dichotomy. There are two identical and interpenetrating networks of Cu and O atoms inside the crystal, which do not have direct chemical bond between them. Both network have an anti-SiO<sub>2</sub> structure that are stable due to Van-der-Waals forces<sup>3</sup>. This is visible in the Figure I-1 b) by the two different tones of grey in each network.

The band gap of the cuprous oxide is 2.17 eV at 4 K, according to experimental results<sup>4</sup>. This is a direct gap at the centred of the Brillion zone and it is formed by the copper 3d<sup>10</sup> and 4s<sup>0</sup> orbitals which correspond to the valence and conduction band, respectively, both with the same parity<sup>5</sup>. The following Figure I-2 represents the bands structured of Cu<sub>2</sub>O, where  $\Gamma_6^+$  and  $\Gamma_7^+$  are the conduction and valence band, respectively.

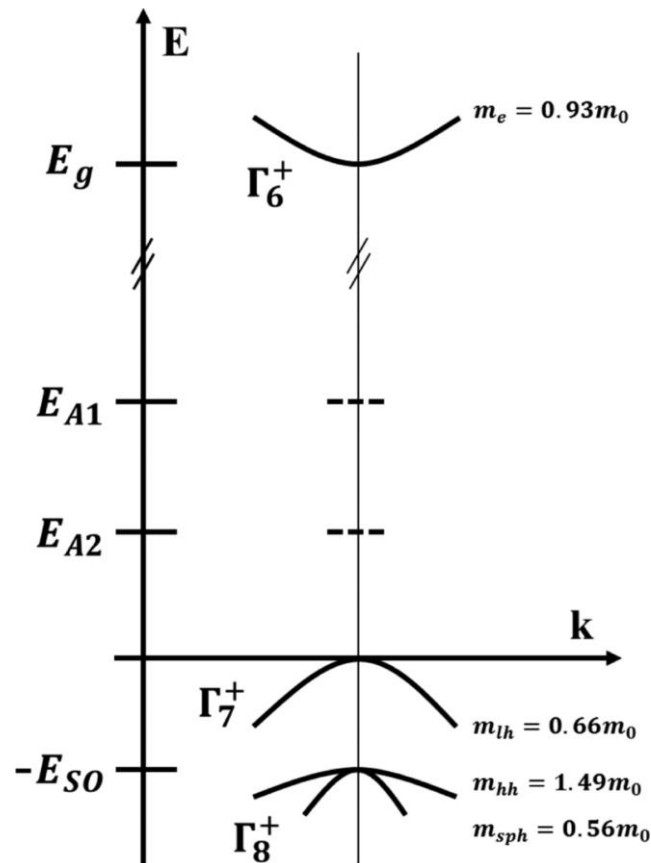


Figure I-2 Band structure of Cu<sub>2</sub>O. Adapted from Brochen et al<sup>6</sup>

At room temperature, the predicted band gap is 2.096 eV<sup>5</sup>. On the effective mass on both bands, the curvature of the bands predicts a higher effective mass for electrons in the conduction band than for the holes in the valence band. Experimental values confirm this fact, presenting 0.99 of effective mass for electrons and 0.58 for holes<sup>7</sup>.

### 1.1.1 Conductivity in $\text{Cu}_2\text{O}$

The p-type behaviour of cuprous oxide arises from the special configuration of the valence band, when compared to other oxides. In p-type transparent conductive oxides (TCO), the large electronegativity of oxygen creates a strong localized valence band edge formed by the 2p levels. Consequently, the hole effective mass is relatively high and the mobility of holes is weak. However, in  $\text{Cu}_2\text{O}$  the top of the valence band is formed by  $3d^{10}$  levels of the  $\text{Cu}^+$  cation, as visible in the Figure I-3. The existence of this different level contributes to a less localization of the holes, which improves the mobility of these charges. Due to this fact, in  $\text{Cu}_2\text{O}$  mobility values can reach up to  $100 \text{ cm}^2 \cdot \text{V}^{-1} \cdot \text{s}^{-1}$  in single-crystals<sup>8</sup>, making this material one of the few oxides with high p-type mobility.

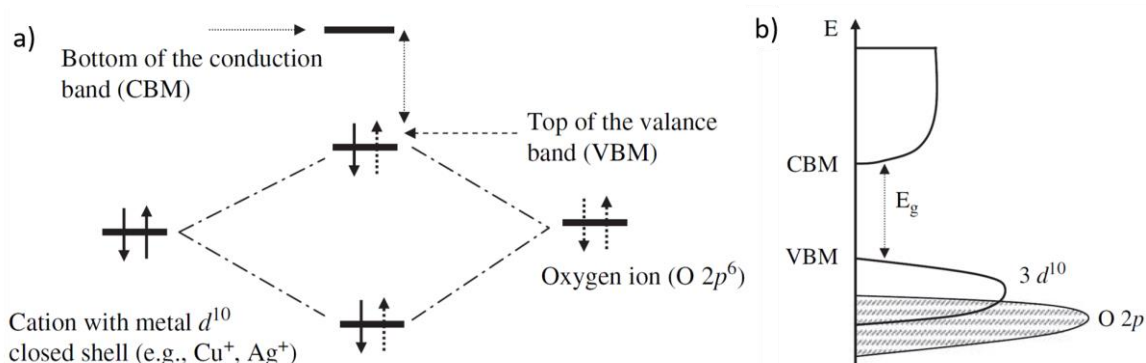


Figure I-3 Band schematic of Cu or Ag based oxides. a) chemical bond between an oxide ion and a cation with closed metal  $d$  shell and b) Schematic of where the energy levels of  $M d^{10}$  and  $O 2p^6$  are assumed to be equivalent. Reproduced from H. Kawazoe et al<sup>9</sup>

The conductivity in cuprous oxide appears by polaronic hopping, contrarily to classical semiconductors. In this mechanism and considering the p-type behaviour of  $\text{Cu}_2\text{O}$ , the conduction of holes through the material distorts the crystal lattice, causing a hole-phonon coupling. Due to the interaction of electronic charges and phonons, traps appear that localize the hole. Then, the hole migrates to another site by thermal motion, via hopping mechanism<sup>10</sup>.

As an oxide with a band gap of 2.17 eV,  $\text{Cu}_2\text{O}$  is an insulator in a stoichiometric composition. Nevertheless, the origin of the  $\text{Cu}_2\text{O}$  p-type conductivity surfaces from intrinsic defects present in the material<sup>1</sup>. As confirmed by experimental reports, the defects can vary in origin, from cation deficiency, interstitial or vacant oxygen, Schottky barrier or simply electron-hole defects<sup>11,5</sup>. Other types of defects as interstitial copper, Frenkel and anti-Frenkel defects seem to be highly unlikely to occur, based on theoretical predictions<sup>3</sup>.

## Chapter I: Introduction

Here below, in Table I-1, we present the most common types of intrinsic defects that can be present in Cu<sub>2</sub>O<sup>12</sup>.

Table I-1 Intrinsic point defects on Cu<sub>2</sub>O with respective reaction equation, charge and formation enthalpy energy

Defect point	Reaction equation	Defect Charge	Formation Enthalpy (eV/defect)
$V'_{Cu}$	$\frac{1}{2}O_2 \rightarrow O_O^X + 2V'_{Cu} + 2h$	-1	0.41-1.66 <sup>13,14</sup>
$O''_i$	$\frac{1}{2}O_2 \rightarrow O''_i + 2h$	-2	1.94/1.87 <sup>14</sup>
$V\ddot{o}$	$null \rightarrow V\ddot{o} + 2e' + \frac{1}{2}O_2$	+2	9.9 <sup>15</sup>
$2V'_{Cu} + V\ddot{o}$	$null \rightarrow 2V'_{Cu} + V\ddot{o}$	0	4.58 <sup>5</sup>

For the generation of holes, the copper vacancies,  $V'_{Cu}$ , are considered the most favourable defect, when compared to interstitial oxygen defects,  $O''_i$ . These copper vacancies can be formed by oxidation of the Cu<sub>2</sub>O, which leads to the removal of a copper atom, leaving a negatively charged vacancy. As consequence, a hole is introduced in a valence band, creating a acceptor level between 0.3 – 0.6 eV above this band<sup>14,16</sup>. The intrinsic p-type semiconductor behaviour appears from these stable copper vacancies, which can be high as 10<sup>20</sup> cm<sup>-3</sup> in concentration, considering 1 to 3% of all copper atoms removed<sup>13</sup>. However, since the ionization of these particular defects is incomplete, the free holes concentration only reaches 10<sup>18</sup> cm<sup>-3</sup> at room temperature<sup>5</sup>.

Still, the nature of these level is yet to be completely understand. Indeed, two possible copper vacancies can appear in Cu<sub>2</sub>O: the simple copper vacancy  $V'_{Cu}$  related to the removal of one copper atom, leaving two oxygen atoms with three copper neighbours, or the split copper vacancy  $V_{Cu}^{split}$  in which the copper disappearance is followed by a neighbouring copper atom movement towards the vacancy. In the latter case, the copper atom moves into a tetrahedral site with four neighbouring oxygen atoms. This is coordination is similar to one in CuO phase. The split vacancy also promotes the change of the oxidation state of the dislocated copper from 1<sup>+</sup> to 2<sup>+</sup><sup>13</sup>. A representation of both defects in visible in the Figure I-4.

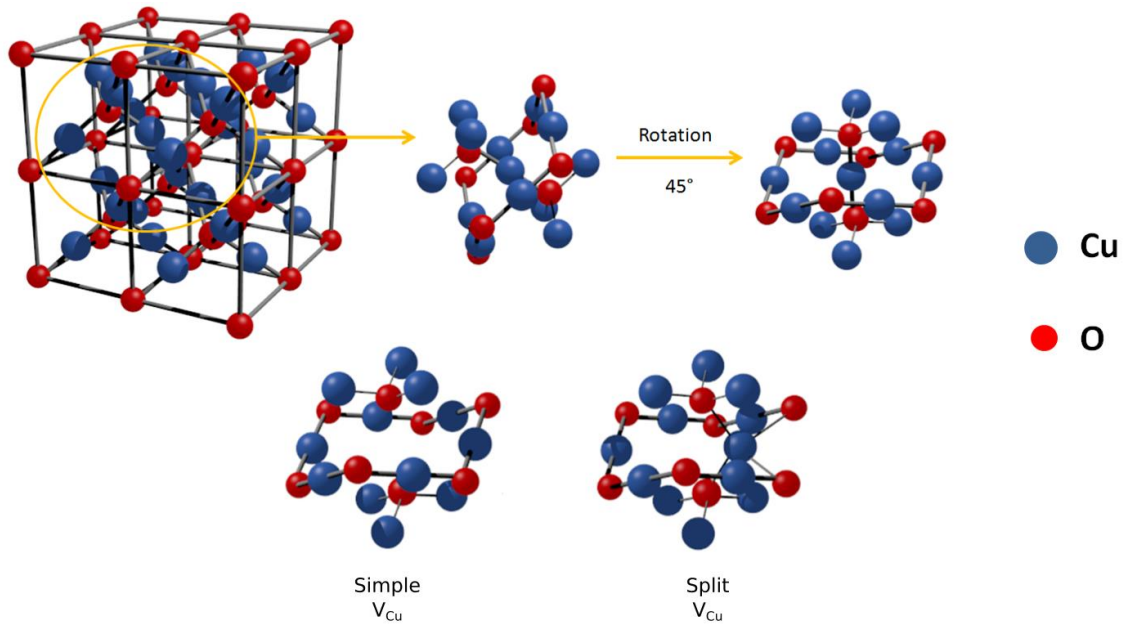


Figure I-4 Structure of a single Cu vacancy in  $\text{Cu}_2\text{O}$ . Complete structure, simple vacancy and split vacancy. Copper atoms pictured as blue circles and oxygen as red ones.

The formation energies of both copper vacancies are a controversy topic in the literature with different theoretical studies presenting distinct values. In the majority of the cases, simple vacancies are more stable than split vacancies, as reported by Raebiger et al.<sup>17</sup>, Scanlon et al.<sup>14</sup>, Nolan et al.<sup>13</sup>, Soon et al.<sup>18</sup>, and Isseroff and Carter<sup>16</sup>. Nevertheless the formation energies are quite distinct: in Nolan's study, both vacancies energy formation are around 0.4eV, while in Scanlon case  $V_{\text{Cu}}$  is around 0.41eV and  $V_{\text{Cu}}^{\text{split}}$  is 1.24eV. Soon et al. present 0.47 eV and 0.78 eV for  $V_{\text{Cu}}$  and  $V_{\text{Cu}}^{\text{split}}$ , respectively. Isseroff and Carter<sup>16</sup> present different exchange-correlation functional methods used with a consistent difference between the two vacancies of  $0.21 \pm 0.03$  eV, where the simple copper vacancy is more stable. In the position of these acceptors levels regarding the valance band, Nolan et al reports 0.47 eV for  $V_{\text{Cu}}^{\text{split}}$  and 0.23eV for  $V_{\text{Cu}}$ <sup>13</sup>.

Different studies report an increase of copper vacancies by post-deposition annealing treatments under oxidizing conditions<sup>19, 20, 21</sup>. At temperatures below 300°C, the  $\text{Cu}_2\text{O}$  thin films show a decrease of the resistivity due to the generation of holes<sup>19</sup>, as well as an increase of holes mobility<sup>20</sup>. Moreover, the transmittance can be further increased in these thermal treatments by a partial removal of defect band tail which enlarger the optical band gap<sup>20</sup>. At temperatures higher than 300 °C,  $\text{CuO}$  parasitic phase starts to be formed, degrading the  $\text{Cu}_2\text{O}$  optoelectronic properties<sup>21</sup>. Cuprous oxide thin films can also be annealed at higher temperatures, up to 700 °C, in reducing atmospheres as vacuum<sup>22</sup>. In

this case, even if the resistivity decreases due to a lower carrier density, the mobility of the thin films is improved to values higher than  $10 \text{ cm}^2 \cdot \text{V}^{-1} \cdot \text{s}^{-1}$ .

### 1.1.2 $\text{Cu}_2\text{O}$ deposition

The interest in  $\text{Cu}_2\text{O}$  has generated a large number of studies to grow thin films using a large variety of techniques, from chemical to physical, under vacuum or at atmospheric pressure. In the Figure I-5, the number of publications on  $\text{Cu}_2\text{O}$  obtained from Scopus are plotted regarding the year, from 2000 to 2017. An increase of “ $\text{Cu}_2\text{O}$ ” and “doped  $\text{Cu}_2\text{O}$ ” reports are clear in the last 17 years. The expression “copper oxide” shows a larger number of publications since it is a general term, including also  $\text{CuO}$  and  $\text{Cu}_4\text{O}_3$ .

A list of different studies developed in the last decade on intrinsic  $\text{Cu}_2\text{O}$  are presented in Table I-2, with some important parameters highlights.

Table I-2 -  $\text{Cu}_2\text{O}$  literature review with deposition technique temperature, transparency, band gap, conductivity and mobility

Technique	Temperature (°C)	Band-gap (eV)	Resistivity ( $\Omega \cdot \text{cm}$ )	Mobility ( $\text{cm}^2 \cdot \text{V}^{-1} \cdot \text{s}^{-1}$ )	Year Ref
Electrodeposited	RT	2.0	-	-	2011 <sup>23</sup>
ALD	225	2.52	125	5	2012 <sup>24</sup>
Spray pyrolysis	350	2.2	104	0.2	2014 <sup>25</sup>
Electrodeposited	RT	2.32	-	-	2014 <sup>26</sup>
DC magnetron sputtering in	RT Annealing @ 280 in air	2.51	7.3	2.7	2014 <sup>20</sup>
DC magnetron sputtering	RT - Annealing @ 475 in vacuum	2.4	149	51	2015 <sup>27</sup>
RF magnetron sputtering	RT	-	65	-	2016 <sup>28</sup>
RF sputtering	RT - Annealing @700 in vacuum	2.43	104	28	2016 <sup>22</sup>

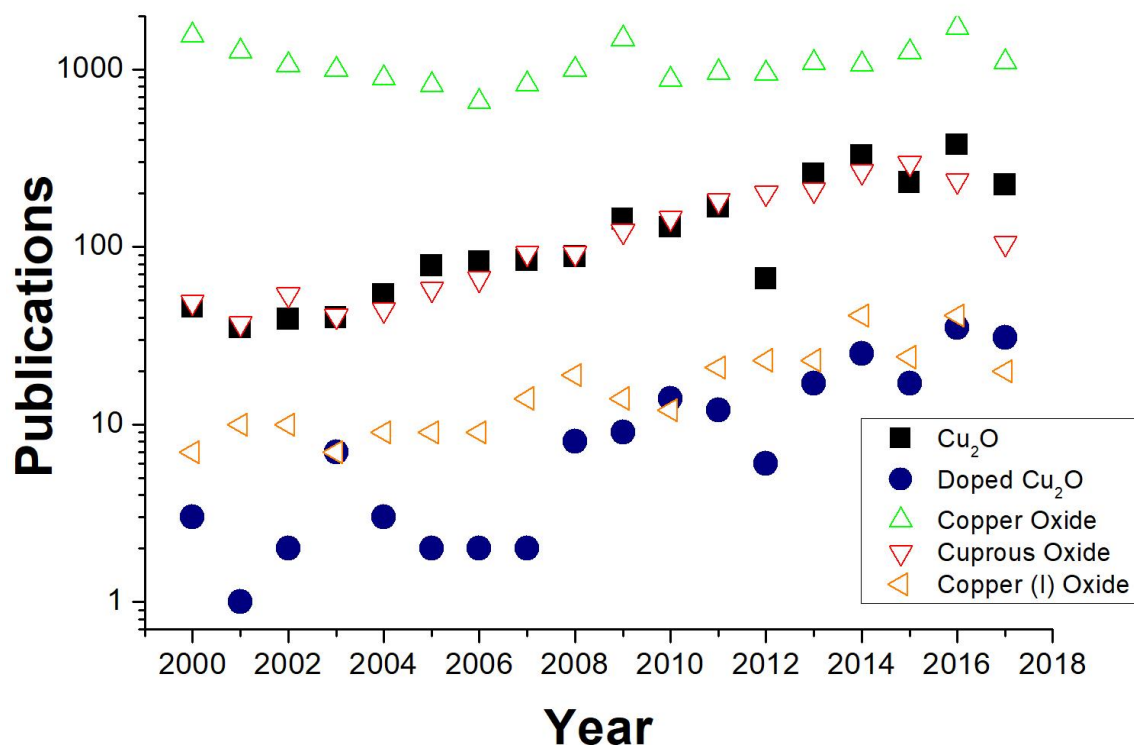


Figure I-5 Number of publications on “Cu<sub>2</sub>O”, “doped Cu<sub>2</sub>O”, “copper oxide”, “cuprous oxide” and “copper (I) oxide” are plotted from 2000 to 2017, as obtained from Scopus.

These different studies show the versatility of Cu<sub>2</sub>O to be deposited from RT to 350 °C using physical and chemical techniques. In terms of electrical properties, the resistivity values are in most of the cases close to 100 Ω.cm, with a decrease to 7.3 Ω.cm with air annealing, which leads to the formation of CuO at high temperatures<sup>20</sup>. The presence of oxygen seems to be one of main issues in the preparation of these films due to the formation of CuO parasitic phase. In the Figure I-6, the phase diagram of Cu-O for single crystals is represented. As one can observe, the Cu<sub>2</sub>O is unstable at room temperature under atmospheric pressure, 736 Torr. Thus, when one deposits thin films of Cu<sub>2</sub>O, the complete prevention of CuO phase is nearly impossible. This main issue can have large impacts on electric and optical properties of the films, since both materials present different band-gap and point defects.

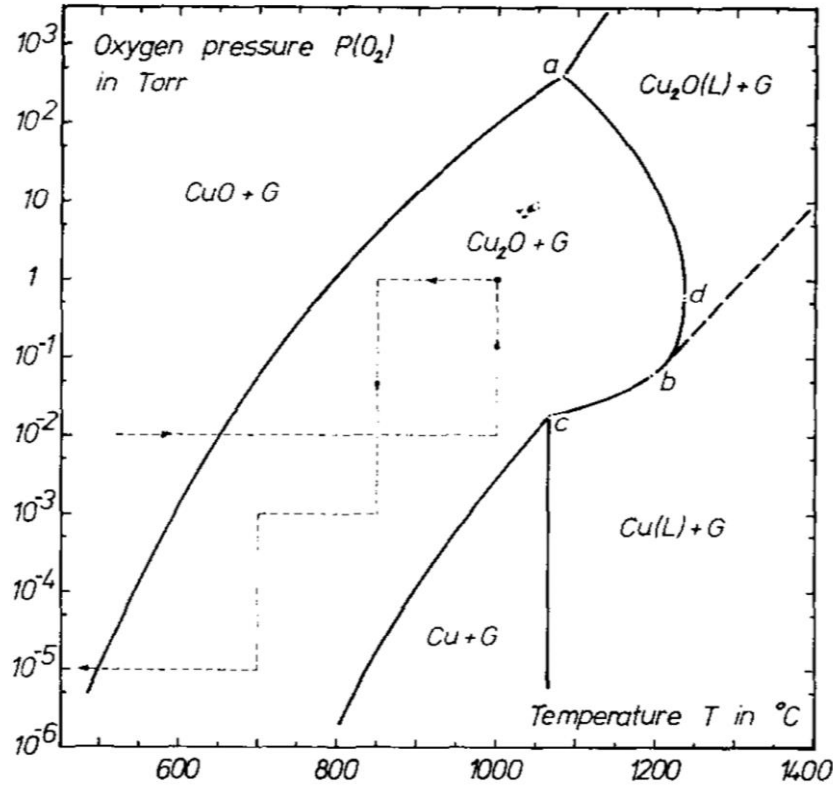


Figure I-6 Temperature pressure diagram from bulk Cu-Cu<sub>2</sub>O-CuO crystals. Adapted from Schmidt-Whitley<sup>29</sup>

The appearance of an intermediate phase between CuO and Cu<sub>2</sub>O is also reported in the literature<sup>30</sup>, paramelaconite, Cu<sub>4</sub>O<sub>3</sub>, formed by stacks of two-fold coordinated copper atoms and four-fold coordinated copper atoms. Nevertheless, studies on the experimental deposition of Cu<sub>4</sub>O<sub>3</sub> thin films are still lacking, as depositions by magnetron sputtering show a narrow oxygen flow rate process window<sup>31,32,33</sup>. Additionally, further optical and electrical properties measurements are required to access the possible applications of this material.

### 1.1.3 Dopants

The use of extrinsic elements on Cu<sub>2</sub>O has been widely tested by the literature in order to improve electric, optical and magnetic properties. In one first group of elements formed by non-metals, Cl<sup>-</sup> and N<sup>-3</sup> are atoms that created a significant impact on the properties of Cu<sub>2</sub>O thin films. Those two elements can substitute the oxygen site and act as a donor for the Cl<sup>-</sup>, and as an acceptor for the N<sup>-3</sup>. In the Cl<sup>-</sup> case, it was possible to obtain a n-type Cu<sub>2</sub>O, confirmed by photocurrent-potential measurements and presenting a low resistivity of 7 Ωcm<sup>34</sup>. Concerning acceptors, N doping seems to have also an effect on

electrical properties with a reduction of resistivity down to 15  $\Omega\cdot\text{cm}$ , and significantly high values of mobility,  $20\text{cm}^2\cdot\text{V}^{-1}\cdot\text{s}^{-1}$  <sup>35</sup>.

Additionally, metals have also been tested as dopants for  $\text{Cu}_2\text{O}$ , experimentally and in models. In the group of transition metals, there are different tested elements as: Cd <sup>36</sup>, Co <sup>37</sup>, Mn <sup>38</sup>, Ni <sup>39</sup> Ag <sup>40</sup>, Fe <sup>40</sup>, Cr <sup>40</sup>, Al <sup>37</sup>, Zn <sup>37,41</sup> and V <sup>37</sup> for different applications as ferromagnetic oxide, conductivity improvements or photocatalytic properties.

Na doping of  $\text{Cu}_2\text{O}$  has been the most successful of doping cases with large enhancements in conductivity. In a study by Tadatsugu Minami *et al.* <sup>42</sup> resistivity values were decrease to  $3.95 \cdot 10^{-2} \Omega\cdot\text{cm}$  in  $\text{Cu}_2\text{O}$  films obtained by thermal oxidation of Cu sheets. Mobility and charge carrier's values were also improved up to  $100 \text{cm}^2\cdot\text{V}^{-1}\cdot\text{s}^{-1}$  and  $10^{19} \text{cm}^{-3}$ , respectively. In the same study, this doped system was implemented for photovoltaic applications as p-type absorber layer.

In 2008, based on first-principle calculations, Nolan *et al.* <sup>2</sup> suggested the doping of cuprous oxide with larger cations than  $\text{Cu}^+$  in order to increase the band gap, while maintaining the cubic structure. These cations, such as  $\text{Mg}^{2+}$ ,  $\text{Sn}^{2+}$ ,  $\text{Sr}^{2+}$  or  $\text{Ca}^{2+}$  would distort the crystallographic lattice and consequently diminish three-dimensional Cu-Cu interactions, leading ultimately to a band gap increase. The p-type conductivity would appear consequently to the creation of a double copper vacancy. Since the dopants are divalent cations, one primary copper vacancy would compensate the dopant presence, while a secondary copper vacancy supplies an extra hole <sup>2</sup>. Additionally, the use of “electronically inert” dopants would avoid the hybridization of the valence band and conduction band edge states or the introduction of in-gap state <sup>2</sup>.

In a previous work, the incorporation of Sr had already been achieved, showing improvements in the conductivity of the films, however, without any change in the optical properties of the material <sup>43</sup>. Thin films of  $\text{Cu}_2\text{O}:\text{Sr}$  with different strontium concentrations were deposited by MOCVD. As main results, Sr can be incorporated up to 14.9% with the presence of a parasitic  $\text{SrCO}_3$  phase for films with more than 5% of Sr. The major impacts were on the film morphology and resistivity, both represented in Figure I-7. The film surface changed from smooth to granular with the increase of Sr concentration. On the electrical properties,  $\text{Cu}_2\text{O}$  thin films containing 5-6 %at of Sr showed resistivity values of about 10  $\Omega\cdot\text{cm}$ , visible in Figure I-7I, which were then decrease to 1  $\Omega\cdot\text{cm}$  with thermal annealing treatments at 200 °C in air. This films show hall carrier density and mobility values of  $2.8 \times 10^{17} \text{cm}^{-3}$  and  $15 \text{cm}^2\cdot\text{V}^{-1}\cdot\text{s}^{-1}$ , respectively, as reported in a follow-up study

by Brochen et al.<sup>6</sup>. Nevertheless, no significant effect on the band gap or optical properties was visible, as shown in Figure I-7II.

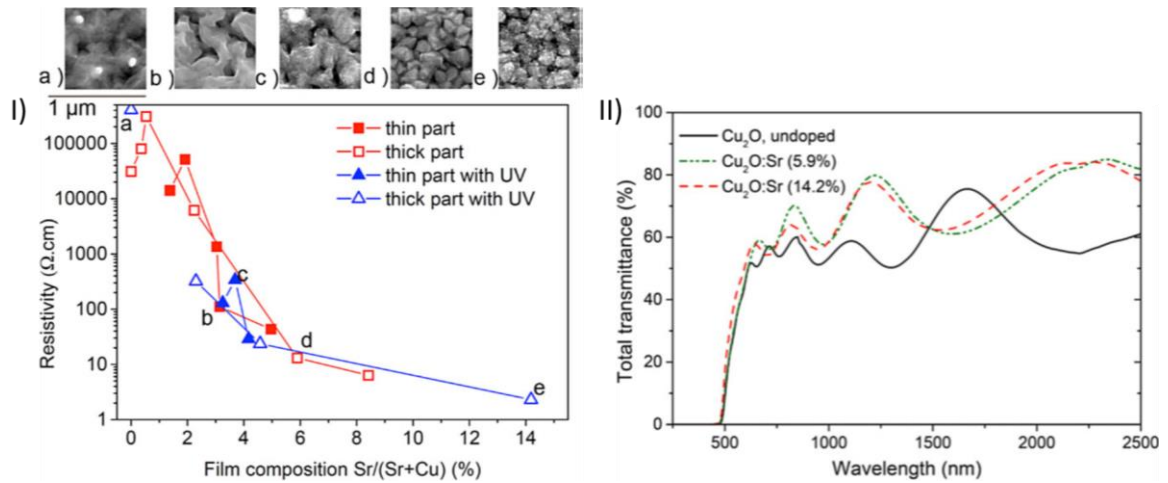


Figure I-7 I) Morphology, resistivity and II) Transmittance of Cu<sub>2</sub>O:Sr thin films from Bergerot et al.<sup>43</sup>

### 1.1.4 CuCrO<sub>2</sub> - Delafossite

The Cu<sub>2</sub>O band gap of 2.17 eV is small for transparent electronics applications, since the transmittance of Cu<sub>2</sub>O films is low in the visible part of the light spectrum<sup>1</sup>. Suggested by Kawazoe<sup>44</sup>, changing the crystallographic structure by introducing other cations in Cu<sub>2</sub>O would increase of the band gap and improve both transparency and electrical properties.

Consequently, a new family of TCO materials emerged, with a delafossite crystal structure, such as CuAlO<sub>2</sub><sup>44</sup>, CuGaO<sub>2</sub><sup>45</sup>, CuFeO<sub>2</sub><sup>46</sup>, CuCrO<sub>2</sub><sup>47</sup>, CuYO<sub>2</sub><sup>48</sup>, or CuScO<sub>2</sub><sup>49</sup>. Additionally, other non-delafossite phases also appeared as possible materials for p-type TCO, such as Cu<sub>2</sub>SrO<sub>2</sub><sup>50</sup> or (LaO)CuS<sup>51</sup>. However, none of these materials combined high conductivity, high transparency and low synthesis temperatures, as already achieved by n-type TCOs<sup>52</sup>. Among these two families of materials, CuAlO<sub>2</sub> compound shows visible transparency around 70% for a 230 nm thick film, with a direct band gap of 3.5eV, yet with relatively high resistivity values up to 3 Ω.cm<sup>53</sup>. In this cases, the temperatures of deposition were higher than 600 °C, which is impractical for the majority of transparent substrates.

Other particular case is CuCrO<sub>2</sub> that has received increasing interest as a promising p-type transparent semiconductor<sup>54</sup>, owing to its wide direct band gap energy of 2.8 eV combined with its high conductivity, which is typically larger than 200 S.cm<sup>-1</sup> when doping

with Mg<sup>54-56</sup>. The crystallographic structure of the CuCrO<sub>2</sub> delafossite phase is represented in Figure I-8a), while the number of publications of CuCrO<sub>2</sub> in Scopus since 2000 to 2017 is plotted in Figure I-8b).

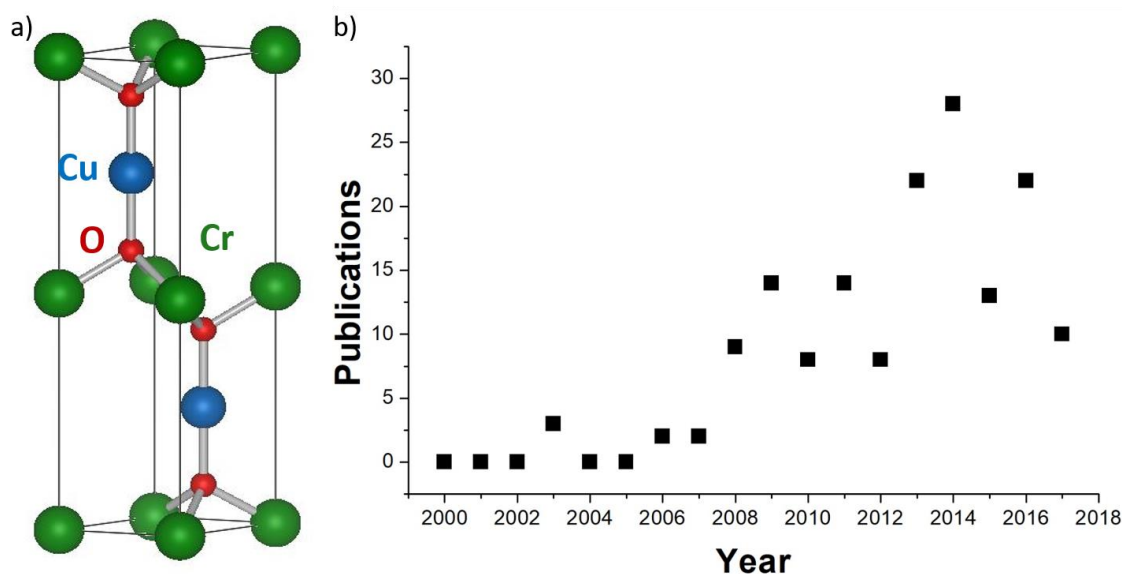


Figure I-8 a) CuCrO<sub>2</sub> crystalline structure. and b) number of publications of CuCrO<sub>2</sub> in Scopus since 2000 to 2017

In comparison with other Cu-based delafossite phases, CuCrO<sub>2</sub> is more conductive mainly due to the higher delocalization of holes produced by Cu vacancies. This is caused by a mixing of Cr *d* states with O *2p* states in the valence band, which creates shallow energy transition levels for the holes<sup>57,58</sup>. In the last twenty years, CuCrO<sub>2</sub> thin films have been deposited by a wide variety of physical and chemical deposition techniques, such as radio-frequency (RF) sputtering<sup>54,59,60</sup>, pulsed-injection metal-organic chemical vapour deposition (MOCVD)<sup>61</sup>, aerosol-assisted CVD<sup>62</sup>, spray pyrolysis<sup>63</sup>, sol-gel process<sup>64</sup>, and atmospheric pressure plasma torch<sup>65</sup>. In particular, Farrell *et al.*<sup>63</sup> reported the growth of undoped CuCrO<sub>2</sub> thin films by spray pyrolysis with a high conductivity of 12 S.cm<sup>-1</sup> combined with an optical transmittance higher than 55%. Interestingly, metal organic precursors that are compatible with aerosol-assisted CVD were used and the nano-crystallization process of the delafossite phase typically proceeds at temperatures below 400 °C, without any post-annealing treatments. Similar results were also reported by Sánchez-Alarcón *et al.*<sup>62</sup> In another recent study on magnesium-doped CuCrO<sub>2</sub><sup>66</sup>, conductivity values achieved a record high of 217 S.cm<sup>-1</sup>, with transmittance values of 70%, using a low deposition temperature of 250 °C by Atomic Layer Deposition (ALD). On physical techniques, the work from Barnabé *et al.*<sup>67</sup> using RF sputtering enable the

## Chapter I: Introduction

increase of visible transparency, with a direct optical bandgap of 3.3 eV after annealing at 600°C. This finding in combination with an effective carrier concentration of about  $10^{21}$   $\text{cm}^{-3}$ , lead to an high figure of merit of  $\text{CuCrO}_2$  thin films, up to  $1.5 \times 10^{-7} \Omega^{-1}$ .

Additionally,  $\text{CuCrO}_2$  nanoparticles have been prepared by hydrothermal synthesis<sup>68</sup>. In terms of applications,  $\text{CuCrO}_2$  thin films have until now been integrated into amorphous thin film transistors (TFT) in electronics<sup>69</sup>, ozone sensors<sup>70</sup>, photocatalytic  $\text{H}_2$  production devices<sup>71</sup> and biological devices as antibacterial agent against *E coli* bacteria<sup>72</sup>.

## 1.2 Devices based on oxide semiconductors

### 1.2.1 Transparent electronics

The development of transparent electronics has increased drastically in the last years, being considered one of the trending research topics for new advanced materials<sup>73</sup>. The possibility of creating transparent devices enables a new range of applications that starts in transparent displays for current everyday devices, such as phones, tablets and computers, but furthermore it can possibly reach smart surfaces as windows, tables or street furniture based on glass or other transparent substrates<sup>73</sup>.

The relevance of this research area justified the appearance of large and multidisciplinary ongoing European projects as Towards Oxide-Based Electronics (TO-BE) action from the European cooperation in Science and Technology initiative (COST), or the Oxide Materials Towards a Matured Post-silicon Electronics Era (ORAMA) project under the European Community's Seventh Framework Programme where the appearance of a next-generation nanoelectronics, microelectromechanical and macroelectronics can impact greatly different areas from IT technologies, energy systems to microsensing and microactuation<sup>74,75</sup>.

Even though the first documented study on transparent conductive oxides (TCO) was reported in 1907 with the production of CdO thin film<sup>76</sup>, just on the transition to the 21<sup>th</sup> century the transparent electronic research gained a relevant importance. The success of n-type semiconductor oxides, as Sn-doped In<sub>2</sub>O<sub>3</sub> (indium tin oxide, ITO), Al-doped ZnO, and Sb-doped SnO<sub>2</sub>, enable the implementation of these materials as transparent conductive oxides<sup>77</sup>. The high transparency combined with a metallic-like conductivity lead to the application in devices as organic light-emitting diodes (OLEDs), liquid crystal displays (LCDs), or 3<sup>rd</sup> generation solar cells<sup>77</sup>. Furthermore, the semiconductor behaviour of these n-type materials allowed the production of transparent thin film transistors (TFTs), due to controllable electrical conductivity. Since 2003, when the first transparent TFT based on ZnO was discovered<sup>78</sup>, the developments lead to the integration in active matrix for organic light emitting diodes (AMOLED) technology<sup>73</sup>. Consequently, ultra-thin screens appeared in the last decade, allowing a semi-transparent device that consume 90% less of energy when compared to LCD and can ultimately use ambient light to increase its energy efficiency.

As the n-type oxide semiconductor materials are already a well-established technology, the interest in p-type oxides is increasing significantly, in order to produce

complementary metal oxide semiconductors (CMOS), enabling the application of extremely compact circuits with smaller power consumption needs, and even other type of electronic devices based on p-n junctions <sup>1</sup>. A p-type oxide material with a semiconductor high performance would improve as well the anode part of an organic light emitting device (OLED), because the drain current in the saturation mode would not be influenced by the TFT hole current supplies.

Nevertheless, the performance of these type oxides is fairly poor when compared with the n-type materials. The main reason of this difference lies in the low mobility of the charge carriers, holes, as a result of the lower mobility of the derived carries in the valence band when compared with the derived carriers of the conduction band <sup>1</sup>.

### **1.2.1.1 Thin Film Transistor**

A fundamental component of the transparent electronics is the thin film transistor (TFT), a type of field-effect transistors (FET), composed of stacked layers of different materials thin films <sup>79</sup>. As it is a FET type, the TFT is composed of three different terminals: source, drain and gate, which are related to a junction transistor as emitter, collector and base, respectively. This type of transistor differs from a MOSFET in the stacking organization of the n-type or p-type component as visible in the Figure I-9. In the bottom gate approach here explained, the metal gate is deposited on top of the substrate, forming the first layer of the device. Then, a dielectric material covers the metal gate, working as isolating layer. The semiconductor material is deposited on top of this isolating layer, being referred as body. The source and gate composed of metal material are then deposited on two opposed edges of the semiconductor body. This configuration, visible in Figure I-9, represents a bottom gate field-effect transistor. Other configurations are also possible as top-gate with staggered or coplanar semiconductor bodies.

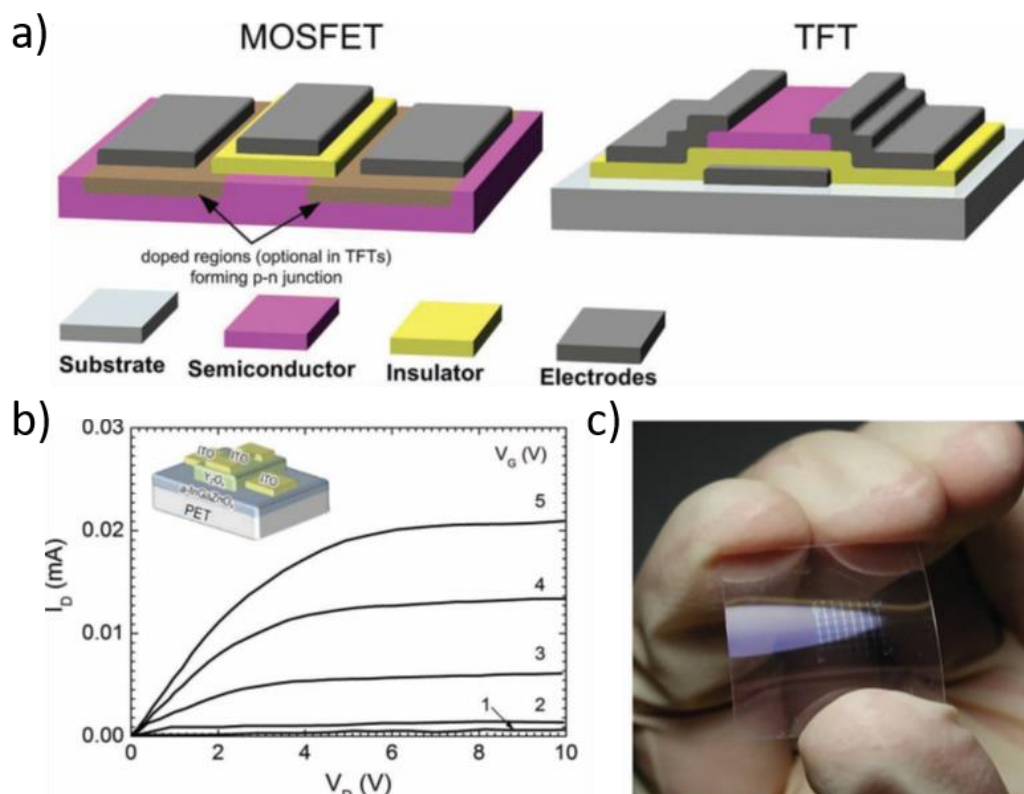


Figure I-9 a) Field-effect transistor FET scheme; b) Characteristic curve of a TFT with current at the drain in function of voltage applied between source and drain; c) Image of transparent TFT. Adapted from E. Fortunato <sup>73</sup>

The working principle of the device is based on the controlled current flow between the source and drain, by the application of a bias voltage at the gate. In the off state of the TFT, the passage of current through the semiconductor body is difficult due to the low conductivity of this layer. When a positive bias is applied on the gate, the electric field created allows the flux of electrons from the source to the drain, due to the appearance of a negatively charge region close to the isolate layer. This field-effect is the mechanism responsible for the current flow, corresponding to the on-state of the transistor.

### 1.2.1.2 $\text{Cu}_2\text{O}$ based TFT

As copper oxide is one of the few oxides with high p-type mobility values, TFTs were tested using  $\text{Cu}_2\text{O}$  as a channel semiconductor. The first publication reporting the production of a TFT based on  $\text{Cu}_2\text{O}$  was achieved in 2008 by Hosono *et al.* <sup>8</sup>, where a single crystal of  $\text{Cu}_2\text{O}$  was epitaxially grown on MgO at 700 °C. The hole mobility presented a high value for  $\text{Cu}_2\text{O}$ ,  $90 \text{ cm}^2\text{V}^{-1}\text{s}^{-1}$ . However, even if the TFT shown a p-channel operation although, the on-off ratio and the effective mobility were only 6 and  $0.26 \text{ cm}^2\text{V}^{-1}\text{s}^{-1}$  respectively <sup>8</sup>. The transfer characteristics of the TFT is visible in Figure I-10a). In other

follow-up research from 2010<sup>80</sup>, the results were substantially improved for Cu<sub>2</sub>O deposited by pulsed laser deposition in pure O<sub>2</sub> with a P(O<sub>2</sub>) = 0.6 Pa. The TFTs present a low threshold voltage of -0.8 V, an on-off current ratio of 3x10<sup>6</sup>, a saturation mobility of 4.3 cm<sup>2</sup>/V s, and a sub threshold swing of 0.18 V/decade, for films deposited at 500 °C. The temperature increase during the deposition increase the concentration of Cu<sup>2+</sup> cations, which consequently result in the formation of the CuO phase. All the electric properties and transistor functions were diminished with the CuO phase increase, as visible in the Figure I-10b).

Other study focuses on the annealing of Cu<sub>2</sub>O, at lower temperatures from 150 °C to 500°C for 7 minutes under a base pressure of 2x10<sup>-6</sup> Torr<sup>81</sup>. Holes mobility values were 47.5 cm<sup>2</sup>V<sup>-1</sup>.s<sup>-1</sup> with a low concentration of charge carriers, 2.95x10<sup>14</sup> cm<sup>-3</sup> and good transmittance of 55%, in the visible region. The morphology of the films is visible in the Figure I-10c, where the grains show a homogeneous distribution with a grain size around 100 nm. The integration of the films in a TFT transistor, with Ni contacts, show the possibility of creation a transistor with an on/off current's ration of 1.1× 10<sup>4</sup> and a V threshold of -7.5V (Figure I-10d)<sup>81</sup>.

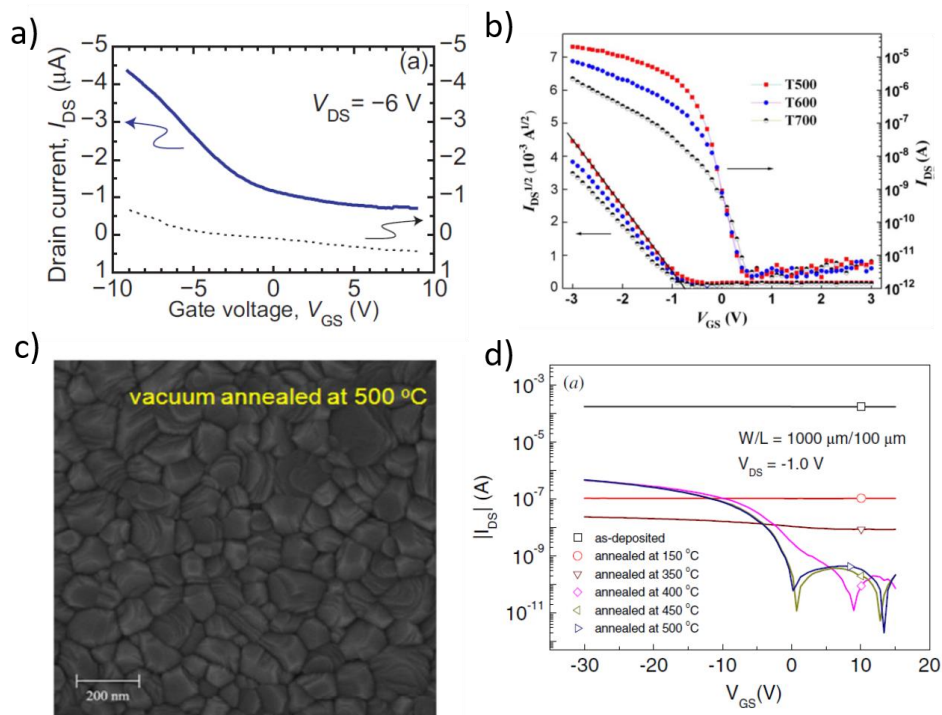


Figure I-10 Transfer curves of different TFT based on Cu<sub>2</sub>O produced by different groups a) Matsuzaki et al.<sup>8</sup> b) Xiao Zou et al.<sup>80</sup> c) and d) Joonsung Sohn et al.<sup>81</sup> where c) SEM micrograph of a Cu<sub>2</sub>O film annealed at 500 °C

## Chapter I: Introduction

Thermal oxidation of Cu metallic films were used to prepare a p-type channel TFTs<sup>82</sup>. The treatment to obtain the Cu<sub>2</sub>O phase was performed at 200 °C in an oxygen rich atmosphere. The final device show a mobility value of 2.2 cm<sup>2</sup>V<sup>-1</sup>s<sup>-1</sup> for a thickness of 112 nm, and an on-off ratio of 60. In this study, the oxidation at higher temperature, 250 °C, origins the appearance of CuO phase. The same group, Fortunato et al<sup>83</sup>, also studied Cu<sub>2</sub>O thin films by reactive RF magnetron sputtering deposited at room temperature. The TFT show a field-effect mobility of 3.9 cm<sup>2</sup>V<sup>-1</sup>s<sup>-1</sup> and an on/off ratio of 200. In Figure I-11 a) the transfer curve is plotted.

The first solution-based p-type transistor was achieved in 2013 by sol-gel using spin coating, followed by two annealing stages<sup>84</sup>. During the first annealing in N<sub>2</sub>, a thin film of metallic Cu was formed, and then oxidized to Cu<sub>2</sub>O by the second annealing in O<sub>2</sub>. In this device, a CuO layer functioned as an insulator, resulting in a limited on-off ratio of 100, while the mobility presented to be 2.2 cm<sup>2</sup>V<sup>-1</sup>s<sup>-1</sup>, for films annealed at P(O<sub>2</sub>)= 0.04Torr.

Other possible configurations is a bilayer TFT, composed of two films, enabling the production of tuneable devices at low processing temperatures (170 °C)<sup>85</sup>. Each layer had a different effect on the TFT, since the Cu<sub>2</sub>O film worked as a capping layer, while the SnO on the bottom controlled the upper layer stoichiometry. The final 25 nm bilayered structure presented in Figure I-11b), showed a p-type channel performance with a final on-to off current ratio of 1.5x10<sup>2</sup> and a threshold voltage of -5.2V.

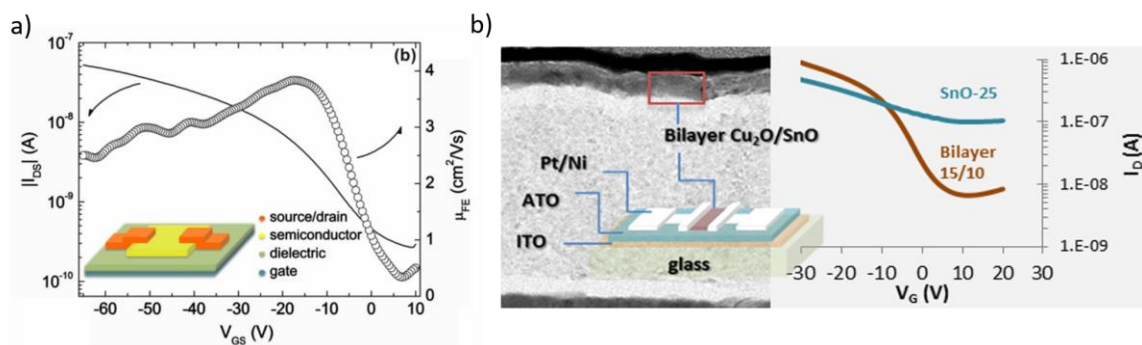


Figure I-11 Transfer curves of different TFT based on Cu<sub>2</sub>O produced by Fortunato et al.<sup>83</sup> and b) Bilayer FTF of Cu<sub>2</sub>O and SnO produced by Hala A. Al-Jawhari et al.<sup>85</sup>

### 1.2.2 Photovoltaics

This following chapter's part is based on a previously written chapter for the book "*Materials for Photovoltaic Solar Cells: Materials for Sustainable Energy Applications: Conversion, Storage, Transmission, and Consumption*", (2017). It was written in collaboration between: Munoz-Rojas, D., Liu, H., Resende, J., Bellet, D., Deschanvres, J. L., Consonni, V. and Zhang, S.

Recently, the scientific society has been concerned about the need for more energy sources. The energy dependence problem has stimulated the search for solutions and this has resulted in a significant boost to solar energy due to its future possibilities. So far, the silicon-based method has been the most common way of producing solar panels. Nevertheless, new other materials have been tested to enhance the photovoltaic capacity to produce energy.

The interest on photovoltaics lead to new scientific projects supported by the Horizon 2020 initiative on low-cost and highly efficient solar cells. Two of these projects are specific for advanced technologies using new materials as: Cheops, for the development of the recent perovskites solar cells <sup>86</sup>, or CPVMatch for the research on multi-junction solar cell architectures aiming for practical performance of high concentrating photovoltaics <sup>87</sup>.

#### 1.2.2.1 Solar Cells

A solar cell is a device capable of transforming light into electricity. Absorption of a photon causes the excitation of an electron within the absorbing material. In order to work, i.e. to collect the electrons to flow out of the cell generating a current and voltage, an asymmetry must be present in the device. This asymmetry is for instance created by having a pn junction, formed by two semiconductors with opposite electrical behaviour. As it is known, in p-type semiconductor material, the majority carriers are holes, while in n-type are electrons. In the case of inorganic semiconductors (silicon for example), when n-type and p-type are in contact so that an interface is created, the excess electrons in the n-type material will diffuse into p-type material, and the other way around for holes from the p-type into the n-type. The consequence of this spontaneous flow is the spontaneous generation of an electrical field near the interface, which opposes to a further diffusion of electrons into p-type, and holes into n-type material, until thermal equilibrium is reached <sup>88</sup>. This balancing space is called depletion region, which has a width  $W_0$ , as presented in

Figure I-12. As illustrated below,  $W_0$  depends on the carrier concentration of the semiconductors and thus the n and p-type materials can contribute differently to the depletion region. In Figure I-12 for instance, the p-type semiconductor contributes more to  $W_0$  since it has a lower carrier concentration than the n-type semiconductor.

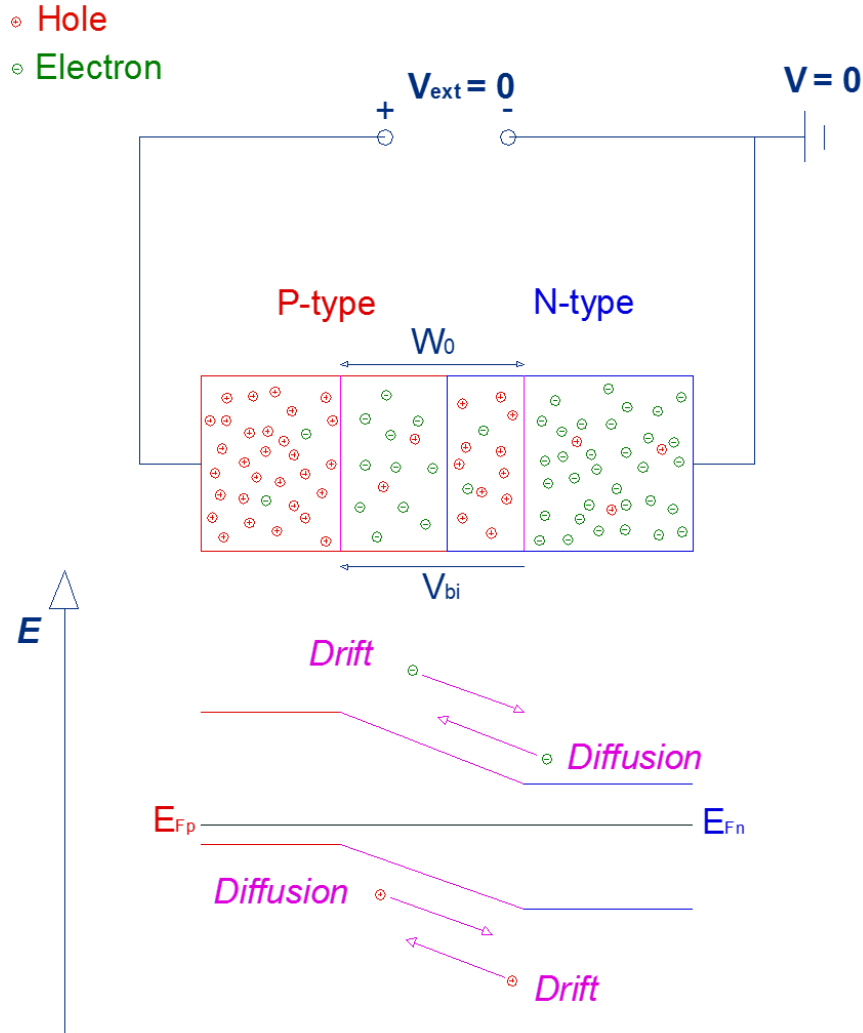


Figure I-12 Band structure of an inorganic pn junction with zero bias.

The depletion layer thickness can be affected by an imposed external bias, as shown in Figure I-13. When the applied external electrical field opposes the built-in potential, then it is called a forward bias, facilitating electron flow across the junction, as shown in Figure I-13a). When the external field is applied in the same direction of the built-in potential, it is reverse bias<sup>88</sup>, as presented in Figure I-13 b).

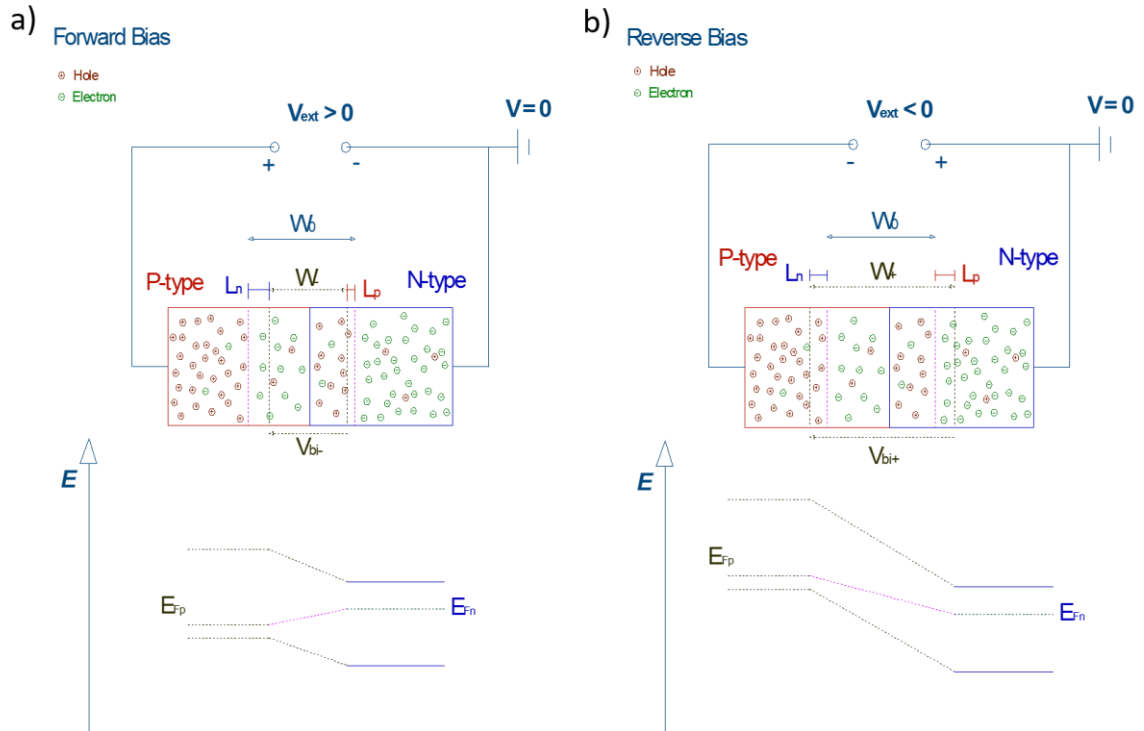


Figure I-13 a) Forward bias decreases depletion zone and built-in potential; b) Reverse bias increases depletion zone and built-in potential.

Control over the width and built-in potential can be achieved by several methods. By combining different semiconductor materials, the depletion zone and built-in potential can vary. For a specific material, in the absence of an external electrical bias, the depletion width is mainly dependent on carrier concentration and thus doping can modify the depletion region width. The built-in potential is associated with the bending of the band structure, which is a consequence of the both materials having the same Fermi level once connected, as shown in Figure I-12. In p-type material, its Fermi level  $E_{Fp}$  is closer to the valence band, while for n-type,  $E_{Fn}$  it is closer to the conduction band.

Introducing a controlled amount of impurities in very pure semiconductors (doping) allows to tune the electrical properties of semiconductor. Simple calculations show that in an intrinsic semiconductor material, the Fermi level  $E_{Fi}$  is located in the middle of the band gap. By introducing doping elements, donors in n-type, the Fermi level shifts towards the conduction band. Contrarily, introducing acceptors leads to shifting of the Fermi level towards the valence band, thus obtaining a p-type. As mentioned above, the built-in potential is due to the bending of the band structure.

To mathematically describe the depletion zone, charge neutrality and Poisson equation are used<sup>89</sup>. For simplicity, the discussion is limited to a 1D model. Thus, equations are given as follow:

$$-\frac{d^2\psi}{dx^2} = \frac{dE}{dx} = \frac{\rho(x)}{\epsilon_s} \quad W_{Dp}N_A = W_{Dn}N_D \quad (I.1)$$

$\psi$  is the potential,  $E$  is the electric field,  $\rho$  is the charge density,  $x$  is the distance from the junction and  $\epsilon_s$  is the dielectric constant. To simplify the model further, we assume an abrupt junction where  $N_D, N_A$  are both constant. A boundary condition assumes as well that at each end of the depletion zone there is no electrical field. Thus, the electrical profile can be solved by equations (I.1), (I.2) and (I.3) and being obtained.

$$E_p(x) = -\frac{qN_A(x + W_{Dp})}{\epsilon_p}, \text{ for } -W_{Dp} \leq x \leq 0 \quad (I.2)$$

$$E_n(x) = -\frac{qN_D(W_{Dn} - x)}{\epsilon_n}, \text{ for } 0 \leq x \leq W_{Dn} \quad (I.3)$$

By integration of equations (I.2) and (I.3), plus a boundary condition, the potential for p and n region can be given, as shown in equations (I.4) and (I.5).

$$\psi_p(x) = \frac{qN_A(x + W_{Dp})^2}{2\epsilon_p} \text{ for } -W_{Dp} \leq x \leq 0 \quad (I.4)$$

$$\psi_n(x) = \psi_p(0x) + \frac{qN_D(W_{Dn} - x/2)x}{\epsilon_n} \text{ for } 0 \leq x \leq W_{Dn} \quad (I.5)$$

Thus, the total potential across the device, also called built in potential  $\psi_{bi}$ , would be the sum of  $\psi_p$  and  $\psi_n$ .  $qV_{bi} = \psi_{bi} = \psi_p + \psi_n$ . With the charge neutrality equation, the depletion width on each side can be determined.

In solar cells, when one or the two semiconductors of the p-junction has a gap suitable for visible light absorption, the illumination of the  $pn$  junction creates electron-hole pairs in the depletion zone, a phenomenon called photovoltaic effect. Due to the built-in electrical field in this region, the holes will move to the p-type semiconductor, while the electrons move to the n-type material. If the circuit is open, the positive charges will accumulate in the p-type material and the negative ones in the n-type material, reducing the electric field in the depletion zone. However, if we introduce an external load in the system (i.e. the circuit is closed), the charges can move outside of the junction, generating an electrical current and increasing once again the electrical field in the depletion zone. Consequently, the energy produced in the solar cell is dependent on the rate of electron-

## Chapter I: Introduction

hole generation, bias voltage and all the conduction processes inside and at the borders of the cell <sup>90</sup>. In Figure I-14, the open and close circuit schemes of the  $pn$  junction are represented.

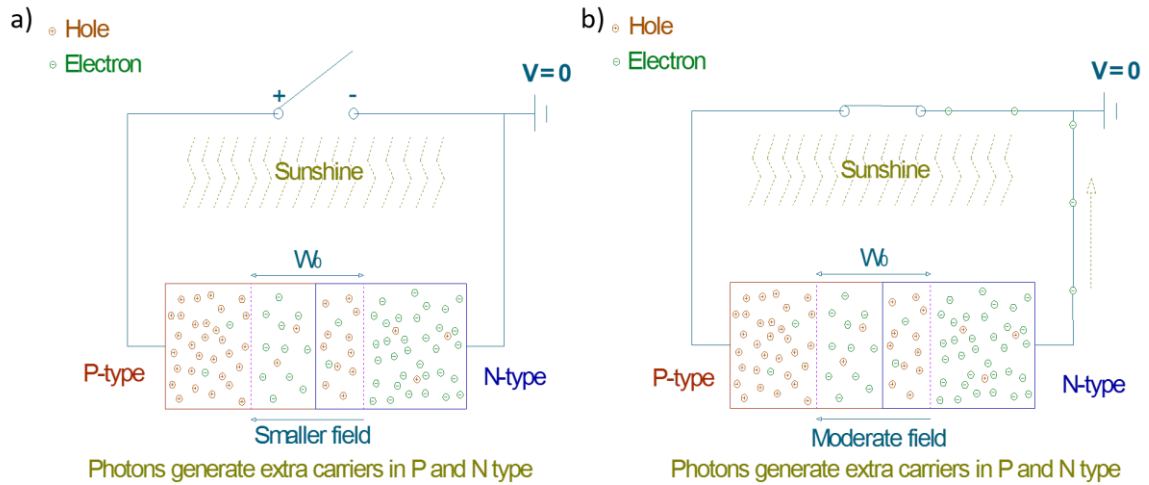


Figure I-14 a) Carrier movement in  $pn$  junction under illumination with no load; b) Carrier movement in  $p-n$  junction with load.

The performance of a photovoltaic solar cell can be evaluated using a variety of parameters<sup>91</sup>. One of the first and most important types of analysis is the Power Conversion Efficiency (PCE), defined as the ratio of the power produced by the cell ( $P_{prod}$ ) with regards to the power from the incident light on the cell ( $P_{inc}$ ). It is given by:

$$\eta = \frac{P_{prod}}{P_{inc}} \quad (I.6)$$

The values for the incident light power are usually standardized for light sources with an AM 1.5G spectrum and a light flux of  $100 \text{ mW.cm}^{-2}$ . This solar spectrum is a standard value taking into account for example the absorption by  $\text{H}_2\text{O}$  or  $\text{CO}_2$  molecules in the atmosphere.

The produced power is the result of multiplying the obtained current for a particular applied voltage. For the calculation of the PCE, the maximum power is considered, as indicated in equation (I.7).

$$P_{prod} = I_i V_i \quad (I.7)$$

where  $I_i$  and  $V_i$  are the electric current and potential values that give maximum power. Thus, IV curves are measured to estimate the maximum power as well as other parameters. The IV curves are obtained by measuring the electrical current dependence on the bias voltage applied to the terminals of the cell, under illumination. When the applied voltage is zero,

the current measured,  $I_{sc}$ , corresponds to the short circuit current. This current is described as the electric flow produced by the illumination of the cell (photocurrent) with no external loads, which strongly depends on the number of photons absorbed and the efficiency with which carriers are collected.

When the bias voltage increases, the electrical current drops, due to the increase of the recombination current, opposite to the electric current generated in the cell. When the current is annulled, the recombination and photocurrent are equal, and the voltage applied is called the open circuit voltage  $V_{oc}$ . This voltage depends on the p- and n-type properties of the materials and the contacts between the electrodes and the semiconductors on the cell. Figure I-15a) represents the variation of the produced power with the bias voltage, while the Figure I-15b) shows a typical IV curve.

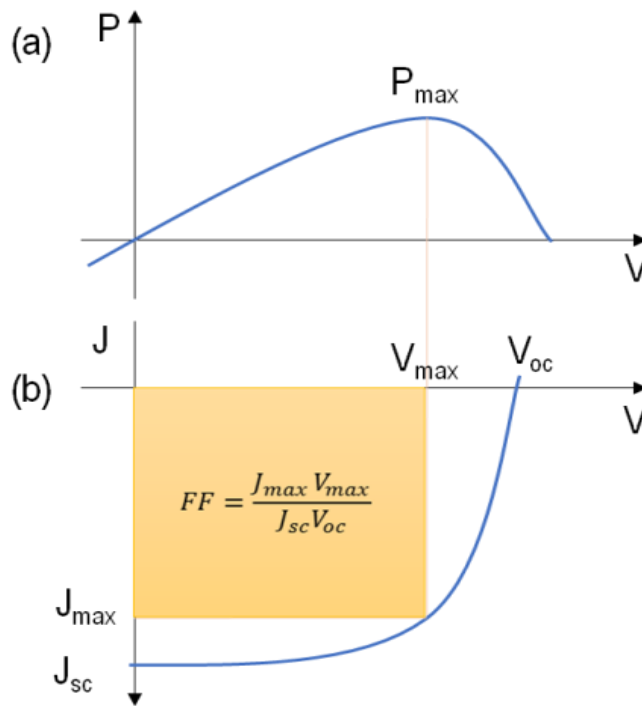


Figure I-15 - a) Power variation with bias voltage b) IV curve of a solar cell

Considering the two concepts,  $V_{oc}$  and  $I_{sc}$ , we can define the PCE based on these two parameters:

$$\eta = \frac{V_{oc} I_{sc} FF}{P_{inc}} \quad (I.8)$$

where  $FF$  is defined as fill factor.

$$FF = \frac{P_{max}}{I_{sc} V_{oc}} \quad (I.9)$$

In Figure I-15b) the power produced by the solar cell is directly related to the area of the square whose edges are equal to  $V_{max}$  and  $I_{max}$ . Therefore, the fill factor can then be graphically interpreted as the ratio between the maximum power obtained from the cell and the product of the short circuit current and open circuit voltage (power that would be obtained from an ideal  $pn$  junction, i.e. diode).

The shape of the IV curve, which can be depicted in the FF value, is strongly dependent on the different resistances of the solar cell. The shunt resistance,  $R_{sh}$ , is mainly responsible for the leakage current throughout the cell. In this case, the resistance should be maximized to prevent recombination of electron-holes in the  $pn$  junction, reducing the leakage current on the cell. In the IV curve, this maximization is expressed by a smoother slope at lower bias voltages. While the series resistance,  $R_s$ , is the component of resistance regarding to the electrodes contacts, bulk resistance or other interfacial barriers (i.e. series resistance). The reduction of this type of resistance leads to an increase of electrical current, which increases the slope of the IV curve at bias voltages near  $V_{OC}$ , thus a more squared shape of the curve (i.e. closer to the ideal diode). The control of both resistances is fundamental to increase the final PCE of the cell.

In general, the equation that expresses the dependence of current and voltage can be defined as:

$$I = I_{SC} - I_0 \left( e^{\frac{q(V-IR_s)}{nkT}} - 1 \right) + \frac{V - IR_s}{R_{sh}} \quad (1.10)$$

where  $n$  is the non-ideality factor. In practice, because measurements are made illuminating a particular cell area, short-circuit current density ( $J_{sc}$ , i.e.  $I_{sc}$ /illuminated area) is commonly quoted when evaluating IV curves. While the evaluation of IV curves under illumination is a basic evaluation of cell performance, dark IV curves (i.e. without any illumination) are also routinely performed. This measurement allows to evaluate the non-ideality factor of the  $pn$  junction in the absence of any light induced bias. The comparison of  $R_s$  and  $R_{sh}$  for light and dark measurements also provides useful information

### 1.2.2.2 Copper oxide based Solar cells

In order to have solar cells with a higher efficiency/cost ratio, the used materials should ideally be abundant and manufactured using low-cost and scalable techniques. In this context, there has been a recent drive towards the use of stable inorganic

semiconductors based on earth abundant elements, mainly Si, Fe, Cu, O, S, and their theoretical capacity of producing enough energy to cover the demand<sup>93</sup>. In Figure I-16 the annual electricity potential of each material is shown, regarding the materials extraction costs. The graphs shows that  $\text{Cu}_2\text{O}$  has higher potential and lower extraction costs than silicon, therefore being proposed as an interesting energy material.

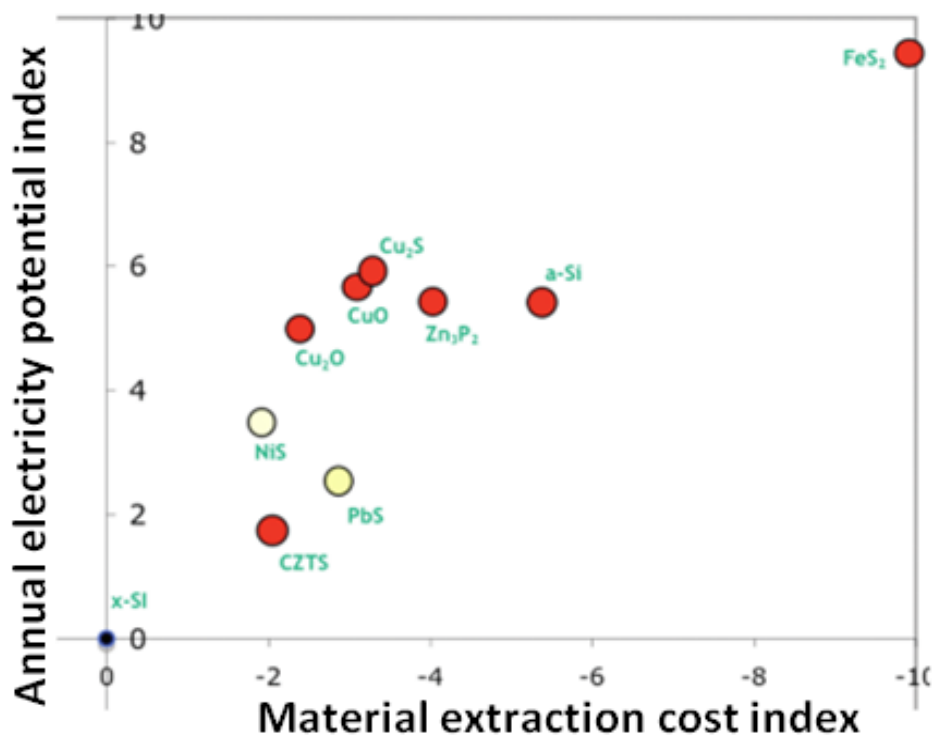


Figure I-16 Annual electricity potential vs. materials extraction cost for several semiconductors. Those with better ratio than the currently used crystalline Si are located in the first quadrant<sup>93</sup>

For application into solar cells,  $\text{Cu}_2\text{O}$  is being heavily investigated since Cu is abundant, non-toxic and theoretical maximum obtainable efficiencies for  $\text{Cu}_2\text{O}$ -based single junction cells are high, around 20%<sup>94</sup>. However, the low energy band-gap of  $\text{Cu}_2\text{O}$ , 2.17eV, limits the absorption of the blue and green part of the solar spectrum, significantly limiting the potential of a single  $\text{Cu}_2\text{O}$ -based solar cell. As a solution, copper oxide can be used as a PV material by combining several cells of different band gap stacked on top of each other, called a tandem cell. Each cell absorbs a different portion of the solar spectrum, with band gap decreasing in the direction of light incidence. Therefore each cell absorbs photons closer to its band gap, which also results in a lower thermalisation of the electron-hole pairs generated. Tandem cells allow a theoretical efficiency limit of 42.5% for a two-cell stack and 47.5% for a three-cell stack tandem cell, as opposed to the Shockley-

Queisser limit of 31% for a single band gap cell <sup>95</sup>. For this purpose, a high efficiency Cu<sub>2</sub>O-based solar cell would be intended for tandem cell implementation.

The difficulty in obtaining n-type Cu<sub>2</sub>O is the main factor limiting the maximum efficiencies that can be obtained, since it has not been possible to make an efficient homojunction of the type n-Cu<sub>2</sub>O/p-Cu<sub>2</sub>O. Although there are some reports on n-type Cu<sub>2</sub>O fabricated <sup>96-98</sup>, the origin of the n-type character is not well established and the homojunction cells prepared with such materials presented very low efficiencies <sup>99,100</sup>.

This fact can be overcome by the use of a different n-type semiconductor that presents a band structure compatible with Cu<sub>2</sub>O to form a heterojunction. ZnO as an n-type semiconductor oxide can be combined with Cu<sub>2</sub>O which will function as p-type absorber material. The combination of these two oxide semiconductors has been widely investigated for an oxide based solar cell <sup>101, 102, 103</sup>. For this junction, a built-in bias of approximately 0.6 to 0.7 V is expected, which should approximate the achievable open-circuit voltage ( $V_{oc}$ ) <sup>104</sup>. In a Cu<sub>2</sub>O/ZnO solar cell, light is absorbed by Cu<sub>2</sub>O and the generated electrons are injected into the ZnO conduction band and extracted, thanks to the high electron mobility of ZnO, through the contact towards the external circuit, holes being transported through the Cu<sub>2</sub>O layer to the external circuits as majority carriers, and electrons towards the junction as minority carriers.

The maximum value achieved by functional devices is only 4.12% <sup>105</sup> for an intrinsic ZnO/Cu<sub>2</sub>O junction, which was recently increased to 8.1% in a MgF<sub>2</sub>/ZnO:Al/Zn<sub>0.38</sub>Ge<sub>0.62</sub>O/Cu<sub>2</sub>O:Na heterojunction <sup>106</sup>. Also, this record of efficiency was achieved by thermal oxidized Cu<sub>2</sub>O, which produce large grains, in the tens of microns range, reducing the fraction of grain boundaries and increasing the mobility. However, this technique is not suitable for industrialization, since it requires very high temperatures, 1000 °C <sup>107</sup>. Thus, the values are still far from predicted efficiency, and using energy intensive methods not suitable for large scale production <sup>108</sup>.

There has been an intensive study on ZnO/Cu<sub>2</sub>O cells fabricated by electrodeposition. Although, the initial reports suffered from rather low  $V_{oc}$  values, engineering of the ZnO/Cu<sub>2</sub>O and of the Cu<sub>2</sub>O/contact interface has had a huge impact on efficiency, clearly showing that in addition to the bulk properties of the different semiconductors used, the interfaces (surface chemistry and morphology) play a key role on device efficiency <sup>109,110</sup>. By engineering the interfaces, maximum efficiencies of 2.61 % and 5% have been achieved for cells prepared by low temperature and high temperature approaches, respectively <sup>108,110</sup>.

In other study, atmospheric pressure spatial atomic layer deposition (AP-SALD) was used to deposit  $\text{Cu}_2\text{O}$  and applied to  $\text{ZnO}/\text{Cu}_2\text{O}$  solar cells<sup>103</sup>. The low hole concentration of electrodeposited  $\text{Cu}_2\text{O}$  imposes the use of thick  $\text{Cu}_2\text{O}$  films in order to have a full depletion layer. The depletion width in a semiconductor depends mainly on the carrier concentration and, therefore, synthesizing  $\text{Cu}_2\text{O}$  with a higher hole concentration would result in higher  $V_{OC}$  values for a same cell thickness and higher electric field within the  $\text{Cu}_2\text{O}$  layer<sup>103</sup>. The  $\text{Cu}_2\text{O}$  films obtained using AP-SALD presented mobility values from 1.5 to 5.5  $\text{cm}^2\text{V}^{-1}\text{s}^{-1}$ , for deposition temperatures from 125 to 225 °C. In terms of carrier concentration the films reach up to  $10^{16} \text{ cm}^{-3}$ , which is three orders of magnitude higher than for electrodeposited films<sup>24</sup>.

Taking advantage of the high carrier concentration of the AP-SALD  $\text{Cu}_2\text{O}$  films, a Back Surface Field (BSF) cell with the following structure  $\text{Cu}_2\text{OSALD}/\text{Cu}_2\text{OED}/\text{ZnOED}$ , where ED stands for electrodeposited, was implemented<sup>103</sup>. In a BSF cell, the top layer, with a high carrier concentration, dopes the layer underneath thus contributing to decrease the depletion width in the cell, and increasing the electric field within the electrodeposited  $\text{Cu}_2\text{O}$  layer. In this way, record current densities were obtained for a  $\text{ZnO}/\text{Cu}_2\text{O}$  cell deposited by low temperature, atmospheric methods, while using a  $\text{Cu}_2\text{O}$  layer of around 1  $\mu\text{m}$ , as opposed to the standard 3  $\mu\text{m}$  for fully electrodeposited devices. Apart from enhanced electric field, the use of a thinner  $\text{Cu}_2\text{O}$  layer and the nanoparticulated AP-SALD  $\text{Cu}_2\text{O}$  layer also contributed to a more effective collection of charges generated by photons of wavelengths above 450 nm. The obtained  $V_{OC}$  was lower than expected, due to the nanometric nature of the AP-SALD  $\text{Cu}_2\text{O}$  films, from 50 nm to ~250 nm, in Figure I-17, which is believed to cause charge recombination.

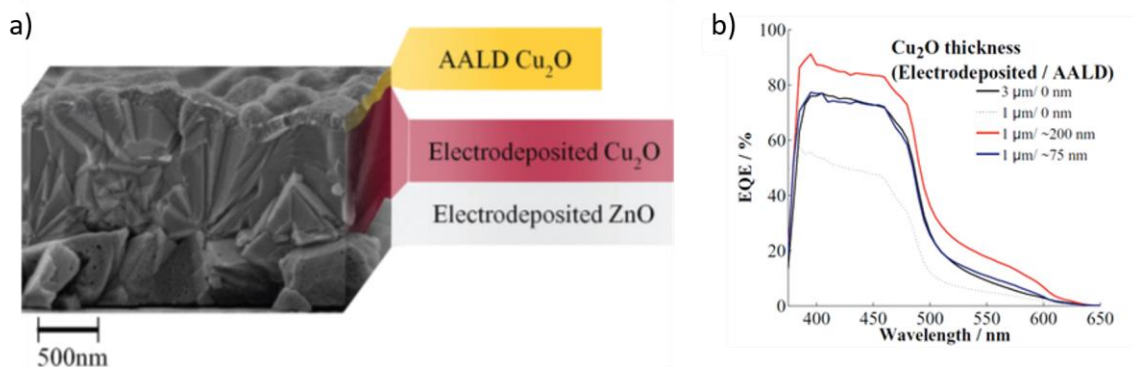


Figure I-17 a) Cross section SEM images of an SALD-enhanced cell; b) EQE spectra of a thin (~75 nm) and thick (~200 nm) SALD enhanced cell ( $\text{ZnO}/\text{Cu}_2\text{OED}/\text{Cu}_2\text{OSALD}$ ) compared to a 1  $\mu\text{m}$ - $\text{Cu}_2\text{O}$  and 3  $\mu\text{m}$ - $\text{Cu}_2\text{O}$  fully-ED ( $\text{ZnO}/\text{Cu}_2\text{O}$ ) cell<sup>103</sup>

### 1.2.2.3 UV Photodetector based on oxides

Considering the same principles as a solar cells, UV photodetectors can be created using high band-gap semiconductors, larger than 3 eV. Over the past years, increasing efforts have been dedicated to the development of self-powered nano-sensors thanks to the increasing demand of autonomous, wireless, nanoscale engineering devices with various functionalities, and to their extensive range of applications <sup>111</sup>. A promising path for the fabrication of self-powered UV photodetectors is to use the internal built-in potential difference of a pn heterojunction at zero bias to prevent the recombination of photo-generated electron-hole pairs and to generate the photocurrent <sup>112</sup>. Other strategies include photo-electrochemical cells <sup>113,114</sup> and Schottky metal semiconductor heterojunctions <sup>112,115,116</sup>.

Owing to its wide direct band gap energy of 3.37 eV and large exciton binding energy of 60 meV at room temperature as well as to its high electron mobility around 200 cm<sup>2</sup>V<sup>-1</sup>s<sup>-1</sup>, ZnO has been considered as a key n-type semiconductor for modern electronics and optoelectronics <sup>55,117,118</sup>. The combination of p-type CuCrO<sub>2</sub> or Mg-doped CuCrO<sub>2</sub> thin films in transparent *pn* diodes has previously been achieved with n-type ZnO thin films deposited by pulsed laser deposition <sup>119,120</sup> and magnetron sputtering <sup>121</sup>. However, the resulting transparent p-n diodes presented low rectifying behavior, with the highest reported rectification ratio of 75 between the forward current to the reverse current at ±1.5 V <sup>119</sup>. The poor characteristics for such pn heterojunctions were attributed to the large lattice mismatch between both oxides and to structural imperfections at grain boundaries in the delafossite phase <sup>119,121</sup>.

A promising path for improving the device performances is to introduce nanostructured architectures, such as one-dimensional nanowires (NWs), in order to benefit from their remarkable chemical and physical properties related to their large surface-to-volume ratio <sup>122</sup>. The possibility to form ZnO nanowires (ZnO NW) using various deposition techniques <sup>123–127</sup>, including the low-cost, low-temperature chemical bath deposition <sup>123</sup>, and to take advantage of their unique properties <sup>122,128</sup> has thus raised even more interest. Within the core-shell NW heterostructure configuration, and following the type-II band alignment, ZnO NW-based heterojunction devices offer efficient light trapping processes through optically guided and radiated modes <sup>129–131</sup>, efficient charge carrier separation over the small radius of the NW and efficient charge carrier collection owing to the high mobility electron pathways provided by the NWs <sup>129,132</sup>.

ZnO NW based core-shell heterostructures have successfully been integrated into gas sensors<sup>133</sup>, UV-photodetectors<sup>134</sup>, dye-sensitized<sup>135</sup>, and extremely thin absorber solar cells<sup>136</sup>. Among them, the conventional ZnO NW based-UV photodetectors rely on the photo-generation of electron-hole pairs upon UV illumination, and on the hole trapping at the NW surface through oxygen adsorption-desorption processes while unpaired electrons are collected using an applied bias voltage<sup>137</sup>. High photoconductive gains and responsivity were achieved following that approach, but the long relaxation time and the dependence on an external power source both limit their mobility and adaptability. Self-powered UV photodetectors made of ZnO NW core-shell heterostructures in combination with wide band gap p-type inorganic semiconductors such as GaN<sup>138</sup>, CuSCN<sup>139,140</sup>, and NiO<sup>141</sup> have already been reported. These heterostructures operate at zero bias and typically show high absorption in the UV part of the electromagnetic spectrum, responsivities as large as 20 mA/W<sup>140</sup> and UV-to-visible rejection ratios of the order of 100. Fast rise and decay times below 1  $\mu$ s and 10  $\mu$ s, respectively, have been achieved<sup>139</sup>.

Very recently, self-powered UV photodetectors based on ZnO / Cu<sub>2</sub>O core-shell NW heterostructures have been shown to exhibit high responsivity in the UV and visible parts of the electromagnetic spectrum owing to the 2.2 eV band gap energy of Cu<sub>2</sub>O<sup>142,143</sup>. I.Y.Y. Bu used the sol-gel process to fabricate ZnO/CuAlO<sub>2</sub> core-shell NW heterostructures with a rectification ratio of 4.7 at  $\pm 1$  V, an open-circuit voltage ( $V_{oc}$ ) of 250 mV, and a short-circuit current ( $I_{sc}$ ) of 6.6  $\mu$ A<sup>144</sup>, however, no responsivity measurements were presented. Despite the high p-type conductivity of CuCrO<sub>2</sub>, its wide direct band gap energy and proper type-II band alignment with ZnO, no nanostructured heterojunctions including core-shell NW heterostructures have been reported so far.

### 1.3 Conclusion

The state-of-the-art analysis of copper oxides-based thin films and devices lead us to foresee two scientific gaps in the literature. Firstly, the possible enhancements of Cu<sub>2</sub>O via cation doping is still unexplored with only a few studies dedicated to the topic, while the application of CuCrO<sub>2</sub> into active devices, as UV photo-detectors, is at this moment in a preliminary stage.

## 1.4 References

- (1) Nandy, S.; Banerjee, A.; Fortunato, E.; Martins, R. A Review on Cu<sub>2</sub>O and Cu-Based P-Type Semiconducting Transparent Oxide Materials: Promising Candidates for New Generation Oxide Based Electronics. *Rev. Adv. Sci. Eng.* **2013**, 2 (4), 273–304.
- (2) Nolan, M.; Elliott, S. D. Tuning the Transparency of Cu<sub>2</sub>O with Substitutional Cation Doping. *Chem. Mater.* **2008**, 20 (17), 5522–5531.
- (3) Korzhavyi, P. A.; Johansson, B. Literature Review on the Properties of Cuprous Oxide Cu<sub>2</sub>O and the Process of Copper Oxidation. *Swedish Nucl. Fuel Waste Manag. Co* **2011**, *Technical* (October).
- (4) Al-Jawhari, H. A. A Review of Recent Advances in Transparent P-Type Cu<sub>2</sub>O-Based Thin Film Transistors. *Materials Science in Semiconductor Processing*. 2015, pp 241–252.
- (5) Biccari, F.; Malerba, C.; Mittiga, A. Defects and Doping in Cu<sub>2</sub>O: General Properties and Applications. **2009**, No. 688774, 1–28.
- (6) Brochen, S.; Bergerot, L.; Favre, W.; Resende, J.; Jiménez, C.; Deschanvres, J.-L.; Consonni, V. Effect of Strontium Incorporation on the P-Type Conductivity of Cu<sub>2</sub>O Thin Films Deposited by Metal–Organic Chemical Vapor Deposition. *J. Phys. Chem. C* **2016**, 120 (31), 17261–17267.
- (7) Hodby, J. W.; Jenkins, T. E.; Schwab, C.; Tamura, H.; Trivich, D. Cyclotron Resonance of Electrons and of Holes in Cuprous Oxide, Cu<sub>2</sub>O. *J. Phys. C Solid State Phys.* **1976**, 9 (8), 1429–1439.
- (8) Matsuzaki, K.; Nomura, K.; Yanagi, H.; Kamiya, T.; Hirano, M.; Hosono, H. Epitaxial Growth of High Mobility Cu<sub>2</sub>O Thin Films and Application to P-Channel Thin Film Transistor. *Appl. Phys. Lett.* **2008**, 93 (20), 202107.
- (9) Hiroshi Kawazoe, H. Y.; Kazushige Ueda, and H. H. Transparent Conductive CuCrO<sub>2</sub> Thin Films Deposited by Pulsed Injection Metal Organic Chemical Vapor Deposition: Up-Scalable Process Technology for an Improved Transparency/conductivity Trade-Off. *J. Mater. Chem.* **2016**, 31–37.
- (10) Deskins, N. A.; Dupuis, M. Electron Transport via Polaron Hopping in Bulk TiO<sub>2</sub>: A Density Functional Theory Characterization. *Phys. Rev. B - Condens. Matter Mater. Phys.* **2007**, 75 (19), 1–10.

- (11) Park, J. H.; Natesan, K. Oxidation of Copper and Electronic Transport in Copper Oxides. *Oxid. Met.* **1993**, *39* (5–6), 411–435.
- (12) Yanagi, H.; Inoue, S.; Ueda, K.; Kawazoe, H.; Hosono, H.; Hamada, N. Electronic Structure and Optoelectronic Properties of Transparent P-Type Conducting CuAlO<sub>2</sub>. *J. Appl. Phys.* **2000**, *88* (7), 4159.
- (13) Nolan, M.; Elliott, S. D. The P-Type Conduction Mechanism in Cu<sub>2</sub>O: A First Principles Study. *Phys. Chem. Chem. Phys.* **2006**, *8* (45), 5350–5358.
- (14) Scanlon, D. O.; Morgan, B. J.; Watson, G. W.; Walsh, A. Acceptor Levels in P-Type Cu<sub>2</sub>O: Rationalizing Theory and Experiment. *Phys. Rev. Lett.* **2009**, *103* (9), 1–4.
- (15) Nolan, M. Defects in Cu<sub>2</sub>O, CuAlO<sub>2</sub> and SrCu<sub>2</sub>O<sub>2</sub> Transparent Conducting Oxides. *Thin Solid Films* **2008**, *516* (22), 8130–8135.
- (16) Isseroff, L. Y.; Carter, E. A. Electronic Structure of Pure and Doped Cuprous Oxide with Copper Vacancies: Suppression of Trap States. *Chem. Mater.* **2013**, *25* (3), 253–265.
- (17) Raebiger, H.; Lany, S.; Zunger, A. Origins of the P-Type Nature and Cation Deficiency in Cu<sub>2</sub>O and Related Materials. *Phys. Rev. B - Condens. Matter Mater. Phys.* **2007**, *76* (4), 1–5.
- (18) Soon, A.; Cui, X. Y.; Delley, B.; Wei, S. H.; Stampfl, C. Native Defect-Induced Multifarious Magnetism in Nonstoichiometric Cuprous Oxide: First-Principles Study of Bulk and Surface Properties of Cu<sub>2-δ</sub>O. *Phys. Rev. B - Condens. Matter Mater. Phys.* **2009**, *79* (3), 1–15.
- (19) Figueiredo, V.; Elangovan, E.; Gonçalves, G.; Barquinha, P.; Pereira, L.; Franco, N.; Alves, E.; Martins, R.; Fortunato, E. Effect of Post-Annealing on the Properties of Copper Oxide Thin Films Obtained from the Oxidation of Evaporated Metallic Copper. *Appl. Surf. Sci.* **2008**, *254* (13), 3949–3954.
- (20) Wang, Y.; Miska, P.; Pilloud, D.; Horwat, D.; Mücklich, F.; Pierson, J. F. Transmittance Enhancement and Optical Band Gap Widening of Cu<sub>2</sub>O Thin Films after Air Annealing. *J. Appl. Phys.* **2014**, *115* (7), 2–7.
- (21) Johan, M. R.; Suan, M. S. M.; Hawari, N. L.; Ching, H. A. Annealing Effects on the Properties of Copper Oxide Thin Films Prepared by Chemical Deposition. *Int. J. Electrochem. Sci.* **2011**, *6* (12), 6094–6104.

- (22) Han, S.; Niang, K. M.; Rughoobur, G.; Flewitt, A. J. Effects of Post-Deposition Vacuum Annealing on Film Characteristics of P-Type Cu<sub>2</sub>O and Its Impact on Thin Film Transistor Characteristics. *Appl. Phys. Lett.* **2016**, *109* (17), 2–7.
- (23) Mohamad Fariza, B.; Sasano, J.; Shinagawa, T.; Nakano, H.; Watase, S.; Izaki, M. Electrochemical Growth of (0001)-N-ZnO Film on (111)-P-Cu<sub>2</sub>O Film and the Characterization of the Heterojunction Diode. *J. Electrochem. Soc.* **2011**, *158* (10), D621.
- (24) Muñoz-Rojas, D.; Jordan, M.; Yeoh, C.; Marin, A. T.; Kursumovic, A.; Dunlop, L.; Iza, D. C.; Chen, A.; Wang, H.; MacManus-driscoll, J. L. Growth of 5 cm<sup>2</sup>V<sup>-1</sup>s<sup>-1</sup> Mobility, P-Type Copper (I) Oxide (Cu<sub>2</sub>O) Films by Fast Atmospheric Atomic Layer Deposition (AALD) at 225 °C and below. *AIP Adv.* **2012**, *2* (4), 42179.
- (25) Ikenoue, T.; Sakamoto, S.; Inui, Y. Fabrication and Characteristics of P-Type Cu<sub>2</sub>O Thin Films by Ultrasonic Spray-Assisted Mist CVD Method. *Jpn. J. Appl. Phys.* **2014**, *53*, 4–7.
- (26) Brandt, I. S.; Martins, C. A.; Zoldan, V. C.; Viegas, A. D. C.; Dias Da Silva, J. H.; Pasa, A. A. Structural and Optical Properties of Cu<sub>2</sub>O Crystalline Electrodeposited Films. *Thin Solid Films* **2014**, *562*, 144–151.
- (27) Murali, D. S.; Kumar, S.; Choudhary, R. J.; Wadikar, A. D.; Jain, M. K.; Subrahmanyam, A. Synthesis of Cu<sub>2</sub>O from CuO Thin Films: Optical and Electrical Properties. *AIP Adv.* **2015**, *5* (4), 47143.
- (28) Deuermeier, J.; Wardenga, H. F.; Morasch, J.; Siol, S.; Nandy, S.; Calmeiro, T.; Martins, R.; Klein, A.; Fortunato, E. Highly Conductive Grain Boundaries in Copper Oxide Thin Films. *J. Appl. Phys.* **2016**, *119* (23).
- (29) Schmidt-Whitley, R. D.; Martinez-Clemente, M.; Revcolevschi, A. Growth and Microstructural Control of Single Crystal Cuprous Oxide Cu<sub>2</sub>O. *J. Cryst. Growth* **1974**, *23* (2), 113–120.
- (30) Meyer, B. K.; Polity, A.; Reppin, D.; Becker, M.; Hering, P.; Klar, P. J.; Sander, T.; Reindl, C.; Benz, J.; Eickhoff, M.; Heiliger, C.; Heinemann, M.; Bläsing, J.; Krost, A.; Shokovets, S.; Muller, C.; Ronning, C. Binary Copper Oxide Semiconductors: From Materials towards Devices. *Phys. Status Solidi* **2012**, *249* (8), 1487–1509.
- (31) Pierson, J. F.; Thobor-Keck, A.; Billard, A. Cuprite, Paramelaconite and Tenorite Films Deposited by Reactive Magnetron Sputtering. *Appl. Surf. Sci.* **2003**, *210* (3–4), 359–367.
- (32) Thobor, A.; Pierson, J. F. Properties and Air Annealing of Paramelaconite Thin Films. *Mater. Lett.* **2003**, *57* (22–23), 3676–3680.

- (33) Wang, Y.; Ghanbaja, J.; Soldera, F.; Migot, S.; Boulet, P.; Horwat, D.; Mücklich, F.; Pierson, J. F. Tuning the Structure and Preferred Orientation in Reactively Sputtered Copper Oxide Thin Films. *Appl. Surf. Sci.* **2015**, *335*, 85–91.
- (34) Han, X.; Han, K.; Tao, M. Characterization of Cl-Doped N-Type Cu<sub>2</sub>O Prepared by Electrodeposition. *Thin Solid Films* **2010**, *518* (19), 5363–5367.
- (35) Ishizuka, S.; Kato, S.; Maruyama, T.; Akimoto, K. Nitrogen Doping into Cu<sub>2</sub>O Thin Films Deposited by Reactive Radio-Frequency Magnetron Sputtering. *Japanese J. Appl. Physics, Part 1 Regul. Pap. Short Notes Rev. Pap.* **2001**, *40* (4 B), 2765–2768.
- (36) Papadimitriou, L. Acceptor States Distributed in Energy in Cd-Doped Cu<sub>2</sub>O. *Solid State Commun.* **1989**, *71* (3), 181–185.
- (37) Kale, S. N.; Ogale, S. B.; Shinde, S. R.; Sahasrabudde, M.; Kulkarni, V. N.; Greens, R. L.; Venkatesan, T. Magnetism in Cobalt-Doped Cu<sub>2</sub>O Thin Films without and with Al, V, or Zn Codopants. *Appl. Phys. Lett.* **2003**, *82* (13), 2100–2102.
- (38) Ivill, M.; Overberg, M. E.; Abernathy, C. R.; Norton, D. P.; Hebard, A. F.; Theodoropoulou, N.; Budai, J. D. Properties of Mn-Doped Cu<sub>2</sub>O Semiconducting Thin Films Grown by Pulsed-Laser Deposition. *Solid. State. Electron.* **2003**, *47* (12), 2215–2220.
- (39) Kikuchi, N.; Tonooka, K. Electrical and Structural Properties of Ni-Doped Cu<sub>2</sub>O Films Prepared by Pulsed Laser Deposition. *Thin Solid Films* **2005**, *486* (1–2), 33–37.
- (40) Biccari, F.; Malerba, C.; Mittiga, A. Impurity Effects in Cu<sub>2</sub>O. **2013**.
- (41) Zhang, L.; Jing, D.; Guo, L.; Yao, X. In Situ Photochemical Synthesis of Zn-Doped Cu<sub>2</sub>O Hollow Microcubes for High Efficient Photocatalytic H<sub>2</sub> Production. *ACS Sustain. Chem. Eng.* **2014**, *2* (6), 1446–1452.
- (42) Minami, T.; Nishi, Y.; Miyata, T. Impact of Incorporating Sodium into Polycrystalline P-Type Cu<sub>2</sub>O for Heterojunction Solar Cell Applications. *Appl. Phys. Lett.* **2014**, *105* (21), 1–6.
- (43) Bergerot, L.; Jiménez, C.; Chaix-Pluchery, O.; Rapenne, L.; Deschanvres, J.-L. Growth and Characterization of Sr-Doped Cu<sub>2</sub>O Thin Films Deposited by Metalorganic Chemical Vapor Deposition. *Phys. Status Solidi* **2015**, *212* (8), 1735–1741.
- (44) Kawazoe, H.; Yasukawa, M.; Hyodo, H.; Kurita, M.; Yanagi, H.; Hosono, H. P-Type Electrical Conduction in Transparent Thin Films of CuAlO<sub>2</sub>. *Nature* **1997**, *389* (6654), 939–942.

## Chapter I: Introduction

- (45) Ueda, K.; Hase, T.; Yanagi, H.; Kawazoe, H.; Hosono, H.; Ohta, H.; Orita, M.; Hirano, M. Epitaxial Growth of Transparent P-Type Conducting CuGaO<sub>2</sub> Thin Films on Sapphire (001) Substrates by Pulsed Laser Deposition. *J. Appl. Phys.* **2001**, *89* (3), 1790–1793.
- (46) Zhao, T.; Hasegawa, M.; Takei, H. Crystal Growth and Characterization of Cuprous Ferrite (CuFeO<sub>2</sub>). *J. Cryst. Growth* **1996**, *166* (1–4), 408–413.
- (47) Mahapatra, S.; Shivashankar, S. a. Low-Pressure Metal-Organic CVD of Transparent and P-Type Conducting CuCrO<sub>2</sub> Thin Films with High Conductivity. *Chem. Vap. Depos.* **2003**, *9* (5), 238–240.
- (48) Jayaraj, M. K.; Draeseke, A. D.; Tate, J.; Sleight, A. W. P-Type Transparent Thin Films of CuY<sub>1-x</sub>Ca<sub>x</sub>O<sub>2</sub>. *Thin Solid Films* **2001**, *397* (1), 244–248.
- (49) Duan, N.; Sleight, A. W.; Jayaraj, M. K.; Tate, J. Transparent P-Type Conducting CuScO<sub>2+x</sub> Films. *Appl. Phys. Lett.* **2000**, *77* (9), 2–4.
- (50) Khan, a.; Jimenez, C.; Chaix-Pluchery, O.; Roussel, H.; Deschanvres, J. L.; Jiménez, C.; Chaix-Pluchery, O.; Roussel, H.; Deschanvres, J. L. In-Situ Raman Spectroscopy and X-Ray Diffraction Studies of the Structural Transformations Leading to the SrCu<sub>2</sub>O<sub>2</sub> Phase from Strontium-Copper Oxide Thin Films Deposited by Metalorganic Chemical Vapor Deposition. *Thin Solid Films* **2013**, *541*, 136–141.
- (51) Hiramatsu, H.; Ueda, K.; Ohta, H.; Orita, M.; Hirano, M.; Hosono, H. Heteroepitaxial Growth of a Wide-Gap P-Type Semiconductor, LaCuOS. *Appl. Phys. Lett.* **2002**, *81* (4), 598–600.
- (52) Nagarajan, R.; Duan, N.; Jayaraj, M. K.; Li, J.; Vanaja, K. A.; Yokochi, A.; Draeseke, A.; Tate, J.; Sleight, A. W. P-Type Conductivity in the Delafossite Structure. *International Journal of Inorganic Materials*. 2001, pp 265–270.
- (53) Yanagi, H.; Inoue, S.; Ueda, K.; Kawazoe, H.; Hosono, H.; Hamada, N. Electronic Structure and Optoelectronic Properties of Transparent P-Type Conducting CuAlO<sub>2</sub>. *J. Appl. Phys.* **2000**, *88* (7), 4159–4163.
- (54) Nagarajan, R.; Draeseke, A. D.; Sleight, A. W.; Tate, J. P -Type Conductivity in CuCr<sub>1-x</sub>Mg<sub>x</sub>O<sub>2</sub> Films and Powders. *J. Appl. Phys.* **2001**, *89* (12), 8022–8025.
- (55) Robertson, J.; Clark, S. J. Limits to Doping in Oxides. *Phys. Rev. B - Condens. Matter Mater. Phys.* **2011**, *83* (7), 1–7.

- (56) Tripathi, T. S.; Niemelä, J.-P.; Karppinen, M. Atomic Layer Deposition of Transparent Semiconducting Oxide CuCrO<sub>2</sub> Thin Films. *J. Mater. Chem. C* **2015**, 8364–8371.
- (57) Scanlon, D. O.; Walsh, A.; Watson, G. W. Understanding the P-Type Conduction Properties of the Transparent Conducting Oxide CuBO<sub>2</sub>: A Density Functional Theory analysis. *Chem. Mater.* **2009**, 21 (19), 4568–4576.
- (58) Scanlon, D. O.; Watson, G. W. Understanding the P-Type Defect Chemistry of CuCrO<sub>2</sub>. *J. Mater. Chem.* **2011**, 21 (11), 3655.
- (59) Nagarajan, R.; Duan, N.; Jayaraj, M. K.; Li, J.; Vanaja, K. A.; Yokochi, A.; Draeseke, A.; Tate, J.; Sleight, A. W. P-Type Conductivity in the Delafossite Structure. *Int. J. Inorg. Mater.* **2001**, 3 (3), 265–270.
- (60) Yu, R. S.; Wu, C. M. Applied Surface Science Characteristics of P-Type Transparent Conductive CuCrO<sub>2</sub> Thin Films. **2013**, 282, 92–97.
- (61) Crépellière, J.; Popa, P. L.; Bahlawane, N.; Leturcq, R.; Werner, F.; Siebentritt, S.; Lenoble, D. Transparent Conductive CuCrO<sub>2</sub> Thin Films Deposited by Pulsed Injection Metal Organic Chemical Vapor Deposition: Up-Scalable Process Technology for an Improved Transparency/conductivity Trade-Off. *J. Mater. Chem. C* **2016**, 4 (19), 4278–4287.
- (62) Sánchez-Alarcón, R. I.; Oropeza-Rosario, G.; Gutierrez-Villalobos, A.; Muro-López, M. A.; Martínez-Martínez, R.; Zaleta-Alejandre, E.; Falcony, C.; Alarcón-Flores, G.; Fragoso, R.; Hernández-Silva, O.; Perez-Cappe, E.; Laffita, Y. M.; Aguilar-Frutos, M. Ultrasonic Spray-Pyrolyzed CuCrO<sub>2</sub> Thin Films. *J. Phys. D: Appl. Phys.* **2016**, 49 (17), 175102.
- (63) Farrell, L.; Norton, E.; Smith, C. M.; Caffrey, D.; Shvets, I. V.; Fleischer, K. Synthesis of Nanocrystalline Cu Deficient CuCrO<sub>2</sub> a High Figure of Merit P-Type Transparent Semiconductor. *J. Mater. Chem. C* **2016**, 4 (1), 126–134.
- (64) Götzendörfer, S.; Bywalez, R.; Löbmann, P. Preparation of P-Type Conducting Transparent CuCrO<sub>2</sub> and CuAl<sub>0.5</sub>Cr<sub>0.5</sub>O<sub>2</sub> Thin Films by Sol–gel Processing. *J. Sol-Gel Sci. Technol.* **2009**, 52 (1), 113–119.
- (65) Chen, H.-Y.; Yang, W.-J.; Chang, K.-P. Characterization of Delafossite-CuCrO<sub>2</sub> Thin Films Prepared by Post-Annealing Using an Atmospheric Pressure Plasma Torch. *Appl. Surf. Sci.* **2012**, 258 (22), 8775–8779.

- (66) Tripathi, T. S.; Karppinen, M. Enhanced P-Type Transparent Semiconducting Characteristics for ALD-Grown Mg-Substituted CuCrO<sub>2</sub> Thin Films. *Adv. Electron. Mater.* **2016**, 1600341.
- (67) Barnabe, A.; Thimont, Y.; Lalanne, M.; Presmanes, L.; Tailhades, P. P-Type Conducting Transparent Characteristics of Delafossite Mg-Doped CuCrO<sub>2</sub> Thin Films Prepared by RF-Sputtering. *Journal of Materials Chemistry C*. 2015, pp 6012–6024.
- (68) Xiong, D.; Xu, Z.; Zeng, X.; Zhang, W.; Chen, W.; Xu, X.; Wang, M.; Cheng, Y.-B. Hydrothermal Synthesis of Ultrasmall CuCrO<sub>2</sub> Nanocrystal Alternatives to NiO Nanoparticles in Efficient P-Type Dye-Sensitized Solar Cells. *J. Mater. Chem.* **2012**, 22, 24760–24768.
- (69) Sanal, K. C.; Jayaraj, M. K. Room Temperature Deposited P-Channel Amorphous Cu<sub>1-x</sub>Cr<sub>x</sub>O<sub>2-δ</sub> Thin Film Transistors. *Appl. Surf. Sci.* **2014**, 315 (1), 274–278.
- (70) Deng, Z.; Fang, X.; Li, D.; Zhou, S.; Tao, R.; Dong, W.; Wang, T.; Meng, G.; Zhu, X. Room Temperature Ozone Sensing Properties of P-Type Transparent Oxide CuCrO<sub>2</sub>. *J. Alloys Compd.* **2009**, 484 (1–2), 619–621.
- (71) Ma, Y.; Zhou, X.; Ma, Q.; Litke, A.; Liu, P.; Zhang, Y.; Li, C.; Hensen, E. J. M. Photoelectrochemical Properties of CuCrO<sub>2</sub>: Characterization of Light Absorption and Photocatalytic H<sub>2</sub> Production Performance. *Catal. Letters* **2014**, 144 (9), 1487–1493.
- (72) Chiu, T.-W.; Yang, Y.-C.; Yeh, A.-C.; Wang, Y.-P.; Feng, Y.-W. Antibacterial Property of CuCrO<sub>2</sub> Thin Films Prepared by RF Magnetron Sputtering Deposition. *Vacuum* **2013**, 87, 174–177.
- (73) Fortunato, E.; Barquinha, P.; Martins, R. Oxide Semiconductor Thin-Film Transistors: A Review of Recent Advances. *Adv. Mater.* **2012**, 24 (22), 2945–2986.
- (74) European Commission. COST Action MP1308 - Towards Oxide-Based Electronics (TO-BE) <http://to-be.spin.cnr.it/> (accessed Jul 14, 2017).
- (75) European Commission. Project ORAMA - Oxide Materials for the Post-Silicon Electronics Era <http://orama-fp7.eu/en/project/> (accessed Jul 14, 2017).
- (76) K. Bädeker. Über Die Elektrische Leitfähigkeit Und Die Thermoelektrische Kraft Einiger Schwermetallverbindungen. *Ann. Phys.* **1907**, 327 (4), 749–766.
- (77) Ohta, H.; Hosono, H. Transparent Oxide Optoelectronics. *Mater. Today* **2004**, 7 (6), 42–51.
- (78) Hoffman, R. L.; Norris, B. J.; Wager, J. F. ZnO-Based Transparent Thin-Film Transistors. *Appl. Phys. Lett.* **2003**, 82 (5), 733–735.

- (79) Aber, W. Thin Film Transistors & Flexible Displays. *Electronics* **2006**, 1–11.
- (80) Zou, X.; Fang, G.; Yuan, L.; Li, M.; Guan, W.; Zhao, X. Top-Gate Low-Threshold Voltage P-Cu<sub>2</sub>O Thin-Film Transistor Grown on SiO<sub>2</sub>/Si Substrate Using a High-κ HfON Gate Dielectric. *IEEE Electron Device Lett.* **2010**, *31* (8), 827–829.
- (81) Sohn, J.; Song, S.-H.; Nam, D.-W.; Cho, I.-T.; Cho, E.-S.; Lee, J.-H.; Kwon, H.-I. Effects of Vacuum Annealing on the Optical and Electrical Properties of P-Type Copper-Oxide Thin-Film Transistors. *Semicond. Sci. Technol.* **2013**, *28* (1), 15005.
- (82) Figueiredo, V.; Pinto, J. V.; Deuermeier, J.; Barros, R.; Alves, E.; Martins, R.; Fortunato, E. P-Type CuO Thin-Film Transistors Produced by Thermal Oxidation. *J. Disp. Technol.* **2013**, *9* (9), 735–740.
- (83) Fortunato, E.; Figueiredo, V.; Barquinha, P.; Elamurugu, E.; Barros, R.; Gonçalves, G.; Park, S.-H. K.; Hwang, C.-S.; Martins, R. Thin-Film Transistors Based on P-Type Cu<sub>2</sub>O Thin Films Produced at Room Temperature. *Appl. Phys. Lett.* **2010**, *96* (19), 192102.
- (84) Kim, S. Y.; Ahn, C. H.; Lee, J. H.; Kwon, Y. H.; Hwang, S.; Lee, J. Y.; Cho, H. K. P - Channel Oxide Thin Film Transistors Using Solution-Processed Copper Oxide. **2013**.
- (85) Al-jawhari, H. A.; Caraveo-frescas, J. A.; Hedhili, M. N.; Alshareef, H. N. P - Type Cu<sub>2</sub>O/SnO Bilayer Thin Film Transistors Processed at Low Temperatures. **2013**, 1–5.
- (86) Horizon 2020. Cheops - Cost and Highly Efficient photovoltaic Perovskite Solar cells <http://www.cheops-project.eu/> (accessed Jul 14, 2017).
- (87) Horizon 2020. Cpvmatch - high concentrating photovoltaics <https://cpvmatch.eu/> (accessed Jul 14, 2017).
- (88) Kittel, C.; McEuen, P.; McEuen, P. *Introduction to Solid State Physics*; Wiley New York, 1976; Vol. 8.
- (89) Pierret, R. F. *Semiconductor Device Fundamentals*; Addison-Wesley Reading, MA, 1996.
- (90) Möller, H. J. *Semiconductors for Solar Cells*; Artech House Publishers, 1993.
- (91) Boyle, G. Renewable Energy: Power for a Sustainable Future. *J. energy Lit.* **1996**, *2*, 106–107.

## Chapter I: Introduction

- (92) Servaites, J. D.; Ratner, M. a.; Marks, T. J. Organic Solar Cells: A New Look at Traditional Models. *Energy Environ. Sci.* **2011**, *4* (11), 4410.
- (93) Wadia, C.; Alivisatos, a P.; Kammen, D. M. Materials Availability Expands the Opportunity for Large-Scale Photovoltaics Deployment. *Environ. Sci. Technol.* **2009**, *43* (6), 2072–2077.
- (94) Olsen, L. C.; Addis, F. W.; Miller, W. Experimental and Theoretical Studies of Cu<sub>2</sub>O Solar Cells. *Sol. Cells* **1982**, *7* (3), 247–279.
- (95) Green, M. A. *Third Generation Photovoltaics*; Springer series in photonics; Springer Berlin Heidelberg, 2003.
- (96) Xiong, L.; Huang, S.; Yang, X.; Qiu, M.; Chen, Z.; Yu, Y. P-Type and N-Type Cu<sub>2</sub>O Semiconductor Thin Films: Controllable Preparation by Simple Solvothermal Method and Photoelectrochemical Properties. *Electrochim. Acta* **2011**, *56* (6), 2735–2739.
- (97) McShane, C. M.; Choi, K.-S. Photocurrent Enhancement of N-Type Cu<sub>2</sub>O Electrodes Achieved by Controlling Dendritic Branching Growth. *J. Am. Chem. Soc.* **2009**, *131* (7), 2561–2569.
- (98) Fernando, C. A. N.; de Silva, P. H. C.; Wethasinha, S. K.; Dharmadasa, I. M.; Delsol, T.; Simmonds, M. C. Investigation of N-Type Cu<sub>2</sub>O Layers Prepared by a Low Cost Chemical Method for Use in Photo-Voltaic Thin Film Solar Cells. *Renew. Energy* **2002**, *26* (4), 521–529.
- (99) Jiang, T.; Xie, T.; Yang, W.; Chen, L.; Fan, H.; Wang, D. Photoelectrochemical and Photovoltaic Properties of P–n Cu<sub>2</sub>O Homojunction Films and Their Photocatalytic Performance. *J. Phys. Chem. C* **2013**, *117* (9), 4619–4624.
- (100) McShane, C. M.; Choi, K.-S. Junction Studies on Electrochemically Fabricated P-N Cu<sub>2</sub>O Homojunction Solar Cells for Efficiency Enhancement. *Phys. Chem. Chem. Phys.* **2012**, *14* (17), 6112–6118.
- (101) Katayama, J.; Ito, K.; Matsuoka, M.; Tamaki, J. Performance of Cu<sub>2</sub>O/ZnO Solar Cell Prepared by Two-Step Electrodeposition. *J. Appl. Electrochem.* **2004**, *34* (7), 687–692.
- (102) Mittiga, A.; Salza, E.; Sarto, F.; Tucci, M.; Vasanthi, R. Heterojunction Solar Cell with 2% Efficiency Based on a Cu<sub>2</sub>O Substrate. *Appl. Phys. Lett.* **2006**, *88* (16), 163502.
- (103) Marin, A. T.; Muñoz-Rojas, D.; Iza, D. C.; Gershon, T.; Musselman, K. P.; MacManus-Driscoll, J. L. Novel Atmospheric Growth Technique to Improve Both Light

Absorption and Charge Collection in ZnO/Cu<sub>2</sub>O Thin Film Solar Cells. *Adv. Funct. Mater.* **2013**, *23*, 3413–3419.

(104) Musselman, K. P.; Wisnet, A.; Iza, D. C.; Hesse, H. C.; Scheu, C.; Macmanus-driscoll, J. L.; Schmidt-mende, L. Strong Efficiency Improvements in Ultra-Low-Cost Inorganic Nanowire Solar Cells. *Adv. Mater.* **2010**, *22*, E254–E258.

(105) Nishi, Y.; Miyata, T.; Minami, T. The Impact of Heterojunction Formation Temperature on Obtainable Conversion Efficiency in N-ZnO/p-Cu<sub>2</sub>O Solar Cells. *Thin Solid Films* **2013**, *528*, 72–76.

(106) Tadatsugu, M.; Yuki, N.; Toshihiro, M. Efficiency Enhancement Using a Zn<sub>1-x</sub>Ge<sub>x</sub>O Thin Film as an N-Type Window Layer in Cu<sub>2</sub>O-Based Heterojunction Solar Cells. *Appl. Phys. Express* **2016**, *9* (5), 52301.

(107) Minami, T.; Nishi, Y.; Miyata, T. High-Efficiency Cu<sub>2</sub>O-Based Heterojunction Solar Cells Fabricated Using a Ga<sub>2</sub>O<sub>3</sub> Thin Film as N-Type Layer. *Appl. Phys. Express* **2013**, *6* (4), 44101.

(108) Minami, T.; Nishi, Y.; Miyata, T. High-Efficiency Cu<sub>2</sub>O-Based Heterojunction Solar Cells Fabricated Using a Ga<sub>2</sub>O<sub>3</sub> Thin Film as N-Type Layer. *Appl. Phys. Express* **2013**, *6* (4), 44101.

(109) Gershon, T. S.; Sigdel, A. K.; Marin, A. T.; Hest, M. F. A. M. van; Ginley, D. S.; Friend, R. H.; MacManus-Driscoll, J. L.; Berry, J. J. Improved fill factors in solution-processed ZnO/Cu<sub>2</sub>O photovoltaics.

(110) Lee, Y. S.; Heo, J.; Siah, S. C.; Mailoa, J. P.; Brandt, R. E.; Kim, S. B.; Gordon, R. G.; Buonassisi, T. Ultrathin Amorphous Zinc-Tin-Oxide Buffer Layer for Enhancing Heterojunction Interface Quality in Metal-Oxide Solar Cells. *Energy Environ. Sci.* **2013**, *6* (7), 2112–2118.

(111) Wang, Z. L. Self-Powered Nanosensors and Nanosystems. *Adv. Mater.* **2012**, *24* (2), 280–285.

(112) Peng, L.; Hu, L.; Fang, X. Energy Harvesting for Nanostructured Self-Powered Photodetectors. *Adv. Funct. Mater.* **2014**, *24* (18), 2591–2610.

(113) Li, Q.; Wei, L.; Xie, Y.; Zhang, K.; Liu, L.; Zhu, D.; Jiao, J.; Chen, Y.; Yan, S.; Liu, G.; Mei, L. ZnO nanoneedle/H<sub>2</sub>O Solid-Liquid Heterojunction-Based Self-Powered Ultraviolet Detector. *Nanoscale Res. Lett.* **2013**, *8* (1), 415.

(114) Bai, Z.; Fu, M.; Zhang, Y. Vertically Aligned and Ordered ZnO/CdS Nanowire Arrays for Self-Powered UV–visible Photosensing. *J. Mater. Sci.* **2017**, *52* (3), 1308–1317.

## Chapter I: Introduction

(115) Bai, Z.; Yan, X.; Chen, X.; Liu, H.; Shen, Y.; Zhang, Y. ZnO Nanowire Array Ultraviolet Photodetectors with Self-Powered Properties. *Curr. Appl. Phys.* **2013**, *13* (1), 165–169.

(116) Lu, S.; Qi, J.; Liu, S.; Zhang, Z.; Wang, Z.; Lin, P.; Liao, Q.; Liang, Q.; Zhang, Y. Piezotronic Interface Engineering on ZnO/Au-Based Schottky Junction for Enhanced Photoresponse of a Flexible Self-Powered UV Detector. *ACS Appl. Mater. Interfaces* **2014**, *6* (16), 14116–14122.

(117) Look, D. C. Recent Advances in ZnO Materials and Devices. *Mater. Sci. Eng. B* **2001**, *80* (1–3), 383–387.

(118) Janotti, A.; Van de Walle, C. G. Fundamentals of Zinc Oxide as a Semiconductor. *Rep Prog Phy* **2009**, *72* (12), 126501.

(119) Tonooka, K.; Kikuchi, N. Preparation of Transparent CuCrO<sub>2</sub>:Mg/ZnO P-N Junctions by Pulsed Laser Deposition. *Thin Solid Films* **2006**, *515* (4), 2415–2418.

(120) Chiu, T. W.; Tonooka, K.; Kikuchi, N. Fabrication of Transparent CuCrO<sub>2</sub>:Mg/ZnO P-N Junctions Prepared by Pulsed Laser Deposition on Glass Substrate. *Vacuum* **2008**, *83* (3), 614–617.

(121) Chen, L. F.; Wang, Y. P.; Chiu, T. W.; Shih, W. C.; Wu, M. S. Fabrication of Transparent CuCrO<sub>2</sub> : Mg / ZnO P – N Junctions Prepared by Magnetron Sputtering on an Indium Tin Oxide Glass Substrate. **2013**, *52*, 05EC02.

(122) Lieber, C. M.; Wang, Z. L. Functional Nanowires. *MRS Bull.* **2007**, *32* (2), 99–108.

(123) Vayssieres, L.; Keis, K.; Lindquist, S.-E.; Hagfeldt, A. Purpose-Built Anisotropic Metal Oxide Material: 3D Highly Oriented Microrod Array of ZnO. *J. Phys. Chem. B* **2001**, *105* (17), 3350–3352.

(124) Kong, Y. C.; Yu, D. P.; Zhang, B.; Fang, W.; Feng, S. Q. Ultraviolet-Emitting ZnO Nanowires Synthesized by a Physical Vapor Deposition Approach. *Appl. Phys. Lett.* **2001**, *78* (4), 407–409.

(125) Park, W. I.; Yi, G.-C.; Kim, M.; Pennycook, S. J. ZnO Nanoneedles Grown Vertically on Si Substrates by Non-Catalytic Vapor-Phase Epitaxy. *Adv. Mater.* **2002**, *14* (24), 1841–1843.

(126) Sun, Y.; Fuge, G. M.; Ashfold, M. N. R. Growth of Aligned ZnO Nanorod Arrays by Catalyst-Free Pulsed Laser Deposition Methods. *Chem. Phys. Lett.* **2004**, *396* (1–3), 21–26.

(127) Xu, L.; Guo, Y.; Liao, Q.; Zhang, J.; Xu, D. Morphological Control of ZnO Nanostructures by Electrodeposition. *J. Phys. Chem. B* **2005**, *109* (28), 13519–13522.

(128) Zhang, P.; Shi, Y.; Chi, M.; Park, J.-N.; Stucky, G. D.; McFarland, E. W.; Gao, L. Mesoporous Delafossite  $\text{CuCrO}_2$  and Spinel  $\text{CuCr}_2\text{O}_4$ : Synthesis and Catalysis. *Nanotechnology* **2013**, *24* (34), 345704.

(129) Garnett, E. C.; Brongersma, M. L.; Cui, Y.; McGehee, M. D. Nanowire Solar Cells. *Annu. Rev. Mater. Res.* **2011**, *41* (1), 269–295.

(130) Michallon, J.; Bucci, D.; Morand, A.; Zanucoli, M.; Consonni, V.; Kaminski-Cachopo, A. Light Trapping in ZnO Nanowire Arrays Covered with an Absorbing Shell for Solar Cells. *Opt. Express* **2014**, *22* (S4), A1174.

(131) Michallon, J.; Bucci, D.; Morand, A.; Zanucoli, M.; Consonni, V.; Kaminski-Cachopo, A. Light Absorption Processes and Optimization of ZnO/CdTe Core-shell Nanowire Arrays for Nanostructured Solar Cells. *Nanotechnology* **2015**, *26* (7), 75401.

(132) Zhang, Y.; Wang; Mascarenhas, A. “Quantum Coaxial Cables” for Solar Energy Harvesting. *Nano Lett.* **2007**, *7* (5), 1264–1269.

(133) Hwang, I.-S.; Kim, S.-J.; Choi, J.-K.; Choi, J.; Ji, H.; Kim, G.-T.; Cao, G.; Lee, J.-H. Synthesis and Gas Sensing Characteristics of Highly Crystalline ZnO–SnO<sub>2</sub> Core-shell Nanowires. *Sensors Actuators B Chem.* **2010**, *148* (2), 595–600.

(134) Rai, S. C.; Wang, K.; Ding, Y.; Marmon, J. K.; Bhatt, M.; Zhang, Y.; Zhou, W.; Wang, Z. L. Piezo-Phototronic Effect Enhanced UV/Visible Photodetector Based on Fully Wide Band Gap Type-II ZnO/ZnS Core/Shell Nanowire Array. *ACS Nano* **2015**, *9* (6), 6419–6427.

(135) Yodyingyong, S.; Zhang, Q.; Park, K.; Dandeneau, C. S.; Zhou, X.; Triampo, D.; Cao, G. ZnO Nanoparticles and Nanowire Array Hybrid Photoanodes for Dye-Sensitized Solar Cells. *Appl. Phys. Lett.* **2010**, *96* (7), 73115.

(136) Xu, J.; Yang, X.; Wang, H.; Chen, X.; Luan, C.; Xu, Z.; Lu, Z.; Roy, V. A. L.; Zhang, W.; Lee, C. Arrays of ZnO/Zn<sub>x</sub>Cd<sub>1-x</sub>Se Nanocables: Band Gap Engineering and Photovoltaic Applications. *Nano Lett.* **2011**, *11* (10), 4138–4143.

(137) Soci, C.; Zhang, A.; Xiang, B.; Dayeh, S. A.; Aplin, D. P. R.; Park, J.; Bao, X. Y.; Lo, Y. H.; Wang, D. ZnO Nanowire UV Photodetectors with High Internal Gain. *Nano Lett.* **2007**, *7* (4), 1003–1009.

(138) Bie, Y. Q.; Liao, Z. M.; Zhang, H. Z.; Li, G. R.; Ye, Y.; Zhou, Y. B.; Xu, J.; Qin, Z. X.; Dai, L.; Yu, D. P. Self-Powered, Ultrafast, Visible-Blind UV Detection and

Optical Logical Operation Based on ZnO/GaN Nanoscale P-N Junctions. *Adv. Mater.* **2011**, 23 (5), 649–653.

(139) Hatch, S. M.; Briscoe, J.; Dunn, S. A Self-Powered ZnO-Nanorod/CuSCN UV Photodetector Exhibiting Rapid Response. *Adv. Mater.* **2013**, 25 (6), 867–871.

(140) Garnier, J.; Parize, R.; Appert, E.; Chaix-Pluchery, O.; Kaminski-Cachopo, A.; Consonni, V. Physical Properties of Annealed ZnO Nanowire/CuSCN Heterojunctions for Self-Powered UV Photodetectors. *ACS Appl. Mater. Interfaces* **2015**, 7 (10), 5820–5829.

(141) Ni, P.-N.; Shan, C.-X.; Wang, S.-P.; Liu, X.-Y.; Shen, D.-Z. Self-Powered Spectrum-Selective Photodetectors Fabricated from N-ZnO/p-NiO Core-shell Nanowire Arrays. *J. Mater. Chem. C* **2013**, 1 (29), 4445.

(142) Elfadill, N. G.; Hashim, M. R.; Saron, K. M. A.; Chahrour, K. M.; Qaeed, M. A.; Bououdina, M. Ultraviolet-Visible Photo-Response of P-Cu<sub>2</sub>O/n-ZnO Heterojunction Prepared on Flexible (PET) Substrate. *Mater. Chem. Phys.* **2015**, 156, 54–60.

(143) Wang, C.; Xu, J.; Shi, S.; Zhang, Y.; Gao, Y.; Liu, Z.; Zhang, X.; Li, L. Optimizing Performance of Cu<sub>2</sub>O/ZnO Nanorods Heterojunction Based Self-Powered Photodetector with ZnO Seed Layer. *J. Phys. Chem. Solids* **2017**, 103 (November 2016), 218–223.

(144) Bu, I. Y. Y. Optoelectronic Properties of Novel Amorphous CuAlO<sub>2</sub>/ZnO NWs Based Heterojunction. *Superlattices Microstruct.* **2013**, 60, 160–168.



# Chapter II: Experimental procedure and characterization techniques

2.1	Aerosol-assisted Metal-organic Chemical Vapour Deposition	48
2.1.1	Metal-organic Precursors .....	52
2.1.2	Description of an AA-MOCVD experiment .....	54
2.1.3	Modification of the reactor configuration .....	61
2.1.4	Annealing treatment .....	61
2.1.5	Metals Thermal evaporation.....	62
2.2	Techniques of characterization	64
2.2.1	Morphological, chemical and structural characterization .....	64
2.2.2	Spectroscopic and spectrometry techniques.....	70
2.2.3	Electrical and functional properties of materials and devices.....	76
2.3	Simulation	80
2.3.1	Basic equations.....	80
2.3.2	Model's algorithm.....	82
2.4	References	84

In this second chapter, we expose the details of the methodology used in the preparation of copper-based oxide thin films, as well as a description of the characterization techniques and the numerical simulations adopted throughout this work. The chapter is divided in three main parts, with a first section dedicated to material synthesis, annealing conditions and devices fabrication. Then, in a second part the characterization techniques for morphological, structural and functional properties are developed. The chapter ends with the development of the numerical simulations of a *pn* junction, focusing on the physics of the model and the algorithm used for the implementation.

## 2.1 Aerosol-assisted Metal-organic Chemical Vapour Deposition

In the *Laboratoire des Matériaux et du Génie Physique* (LMGP) in Grenoble, the expertise on different types of chemical vapour deposition (CVD) processes has started since the early stages of the laboratory. The chemical vapour deposition process is defined as a chemical reaction between reacting species, provided as vapours, in the neighbourhood of a heated substrate, which results into the deposition of solid by-products on the surface<sup>1</sup>. The possibility of producing different structures as films, powders or fibres, with a large variety of materials types as metals, oxides, carbides, silicon or nitrides established CVD as a powerful and flexible technique for materials production<sup>1</sup>.

A specific variant of the technique, the Metal-organic chemical vapour deposition (MOCVD), is based on the deposition of materials starting from metal-organic compounds as precursors. These precursor compounds are characterized by organic molecules with metallic elements presenting metal-carbon, metal-oxygen-carbon bonds that are decomposed by a reactive gas in a thermally-energetic environment, resulting in the formation of a solid material. In this case, the possible applications already harnessed in the industry are diverse, ranging from optoelectronics (lasers and diodes), telecommunications, solar cells or microelectronics (transistors), with a growth use in the last years due to its versatility<sup>2</sup>. The broad use of the MOCVD is motivated by the various advantages in materials processing, from high purity and molecular homogeneity of the films; particle size in sub-micron range with high reactivity and surface area of the structures produced. There are also economic advantages since it enables lower decomposition temperatures of the precursors, larger processed areas and relatively simple apparatus, when compared to MBE or other techniques. Nevertheless, some drawbacks do exist and mainly concern the risk associated to the use of chemicals, since the environmental impact of the toxicity of reactants and by-products as well as the safety lab operators are still an important issue to be addressed<sup>2</sup>.

From the different types of MOCVD techniques available we focused our research on Aerosol-assisted Metal-organic Chemical Vapour Deposition (AA-MOCVD)<sup>3</sup>. This type of CVD process uses an aerosol medium to transport the precursor into the deposition chamber. It was developed first and patented at Grenoble by the CEA with the commercial name Pyrosol (Pyrolysis of aerosol)<sup>4,5</sup>. AA-MOCVD enables the growth of high-quality

and homogeneous thin films from fundamental studies to low-cost and large-area-deposition for industrial applications <sup>6</sup>. The use of aerosol-assisted generation places this procedure within the liquid source delivery CVD processes and offers the possibility to produce films without any vacuum system, at conditions close to atmospheric pressure and even in open air <sup>7</sup>.

The process uses a solution-based precursor that is sprayed into micro-size droplets, forming the aerosol mist. This solution can be obtained from a pure liquid precursor, or by dissolving solid or liquid precursors in a solvent <sup>3</sup>. The formation of an aerosol from a liquid solution avoids the use of highly volatile precursors since the first requirement is their solubility in the solvent. Moreover, for the deposition of multicomponent materials, different precursors can also be mixed, as long as solubility and stability in liquid phase is guaranteed. Compared to other types of CVD processes, this precursor's versatility enables the use of more thermally stable and lower price precursors, reducing the final cost of materials production. Specifically, in the case used for this work, the aerosol mist is generated by an ultrasonic vibration of a piezoelectric transducer at a specific resonance frequency (close to 800 kHz) that maximizes the mist quantity. The size of the created droplets  $d$  can be estimated by the following expression:

$$d = k \left( \frac{2\pi\gamma}{\rho_l f^2} \right)^{\frac{1}{3}} \quad (II.1)$$

Where  $f$  is the excitation frequency of the transducer,  $k$  is semi-empirical constant,  $\rho_l$  is the density of the liquid and  $\gamma$  the correspondent surface tension <sup>3</sup>. The equation (II.1) shows that by changing the solvent or the concentration of the solution, the size of the droplets can be varied through the value of the viscosity, even if the resonance frequency is kept constant. An image of the mist generated by mechanical vibration is shown in Figure II-18.

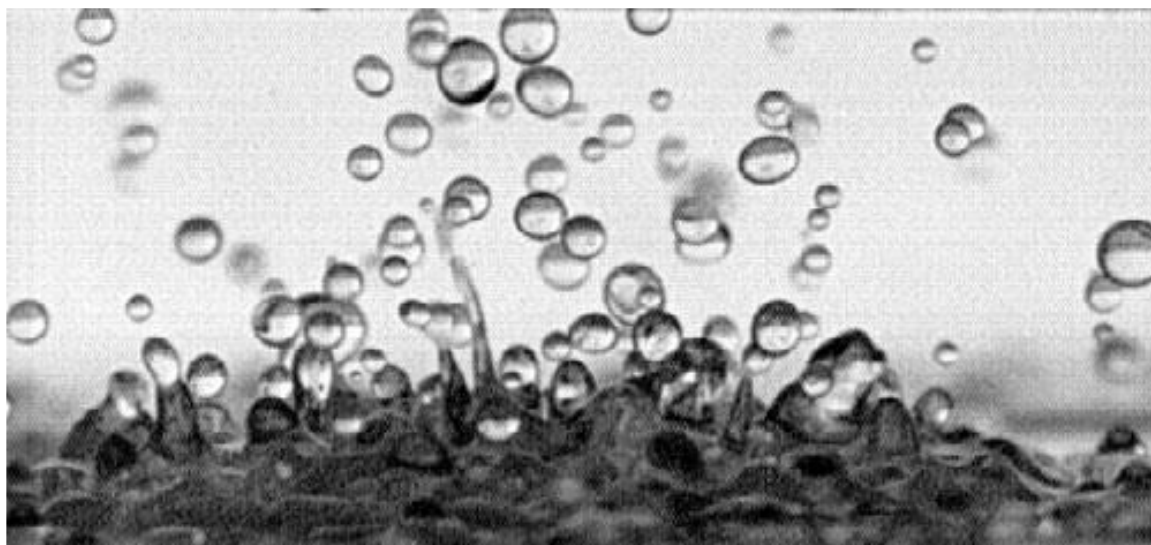


*Figure II-18 Droplets in a mist generated vibration* <sup>8</sup>

After the creation of the aerosol, the mist is mixed with a carrier inert gas that transports the aerosol to the reaction chamber. In the path from the aerosol generation and the reaction chamber, a reaction gas is added to the aerosol and heating of the mist can be induced by external elements. When the mist arrives to the heated substrate, its temperature increases and the solvent is evaporated. Then, the precursor in its gaseous state reaches the heated substrate, evaporates, decomposes and deposition occurs <sup>4,6</sup>. In the Figure II-19, a scheme shows the different steps in a AA-MOCVD process <sup>3</sup>, where all the different steps in the process of a film deposition from the atomization of the aerosol droplets, the transport and heating, evaporation of solvent and precursor, and absorption on the substrate. Other possible phenomena are also represented, as powder production or direct spray-pyrolysis deposition.

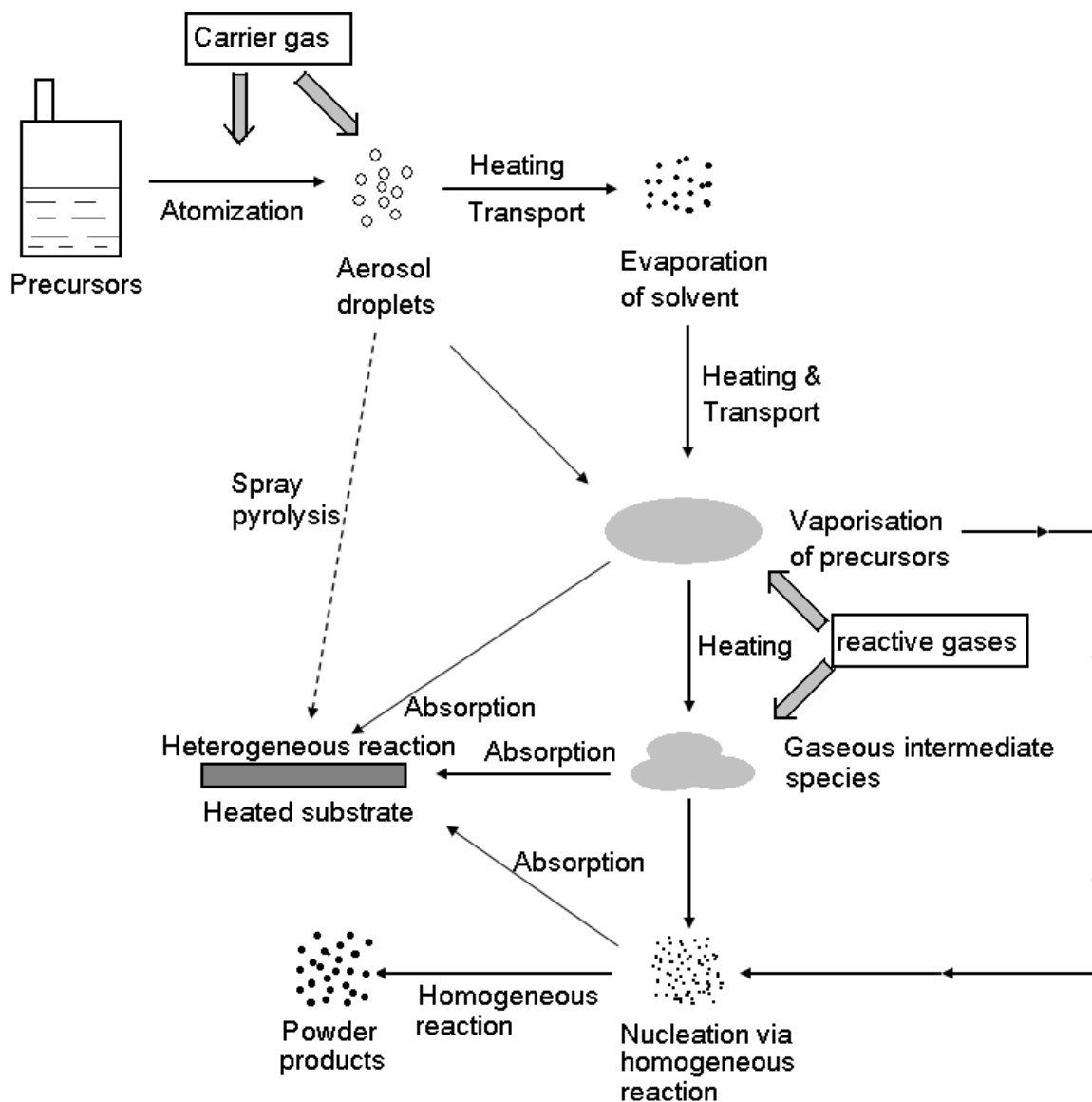


Figure II-19 Schematic diagram of the AACVD process for the deposition of films and powders from Hou and Choy <sup>3</sup>.

The nucleation and growth of the film occurs by thermally-activated surface reaction of the precursor with the reactive gas. During the adsorption on the heated substrate, the bond between the metal and organic components of the precursor is broken, leading to the subsequent interaction between the metal and the reaction gas, which is oxygen in the case of this study. This leads to the formation of small nuclei on the substrate, while the organic species are released and eliminated from the surface. Consequently, the number and size of the adsorbed nuclei increase, which induces the formation of the film due to a continuous arrival of metal precursor and reactive gas. Figure II-20 shows the process of nucleation and growth of the film.

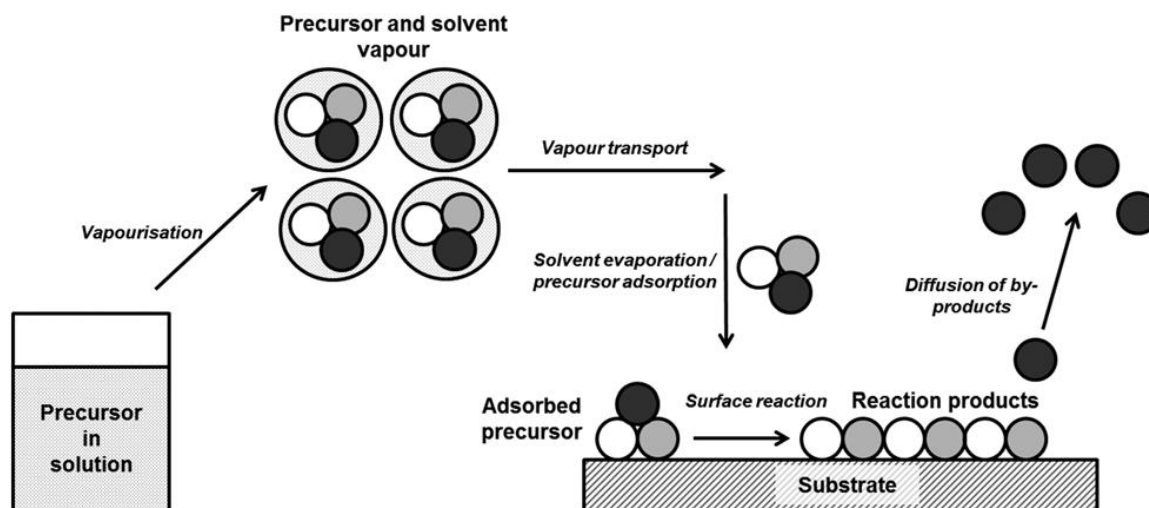


Figure II-20 Aerosol process at the substrate representing the nucleation and growth of the film. From Carmalt *et al.*<sup>6</sup>

The density and the growth rate of each nucleus is the main factor to control the size of the grains and stoichiometry of the phase. During all of the process, a group of parameters have to be controlled with the aim of enhancing the deposition growth rate and the film physical and chemical properties. Regarding the film composition, the nature of the precursor solution, the substrate temperature and the oxygen pressure have important roles, while the aerosol parameters such as piezoelectric frequency and power, density of flux, speed, total pressure and nature of the gases have a more direct effect on the growth rate and thickness of the films.

According to Hou and Choy<sup>3</sup>, there are five main advantages to the use of aerosol assisted MOCVD, namely (i) larger number of available precursors at a lower price, (ii) simplicity of the technique for transport and vaporization of the precursors, (iii) high volume transport of the precursor which can increase the deposition rate, (iv) flexibility in terms of atmosphere, since it can work from low pressure to open atmosphere and (v) the accurate stoichiometric control of multicomponent materials. Nevertheless, the stabilization of the aerosol flux and the geometric conditions of its delivery in the chamber are large issues for the efficiency of this procedure<sup>7</sup>.

### 2.1.1 Metal-organic Precursors

The precursors used in the development of this work were all metal-organic species, where a metal atom is combined with an organic group, which stabilizes it. Since the organic part is unstable under high temperatures, these precursors have to be decomposed

using a heated source. In our case, it is the heating plate below the substrate which fulfils this requirement. Different types of precursors were tested, from acetates to 2,2,6,6-tetramethyl-3,5-heptanedione (TMHD) precursors, all of them  $\beta$ -diketonates. The main changes are in the number of organic bonds present in the precursor and the type of organic compound, as well as, the type of bonding, monodentate or bidentate. For all the results shown in this work, we will focus on acetylacetonate precursors which derive from the acetylacetonate anion ( $\text{CH}_3\text{COCHCOCH}_3^-$ ) which act as a bidentate ligand, sharing 2 chemical bonding for one shared electronic charge. Normally it is abbreviated as *acac*, with the copper case being commonly referred to as  $\text{Cu}(\text{acac})_2$ . As visible in Figure II-21, the copper atom is connected to four oxygen atoms, which form 2 six-membered chelate rings.

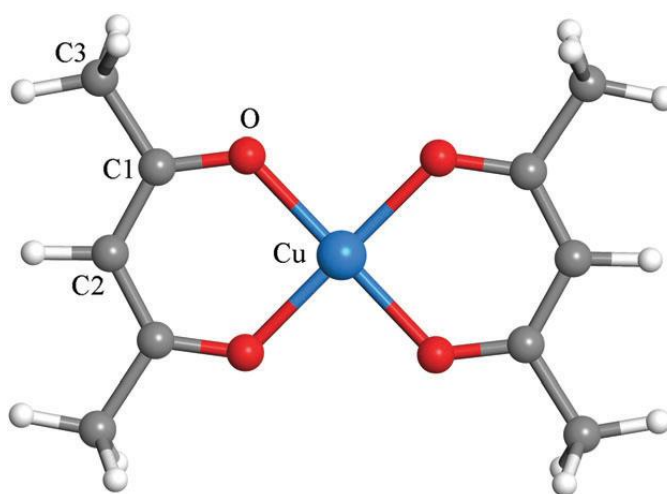


Figure II-21 Schematic representation of  $\text{Cu}(\text{acac})_2$  with copper atom represented in blue, oxygen in red, carbon in grey and hydrogen in white <sup>9</sup>.

There were various reasons motivating the choice of this type of metal-organic precursor, starting from their solubility in different solvents, water, butanol or ethanol, with or without using additives. In the case of  $\text{Cu}(\text{acac})_2$ , the decomposition temperature of 284 °C is slightly lower than the formation of copper oxide phases and lower than the melting point of glass, which allows the deposition process to occur in a range between 300 and 500 °C. This precursor presents a complete decomposition into a Cu atom and *acac*-ligands <sup>9</sup>, which enables the formation of metallic copper,  $\text{Cu}_2\text{O}$  or  $\text{CuO}$  depending on the oxygen partial pressure. Additionally, the precursor has a low moisture sensitivity <sup>10</sup>, it is generally used in the literature, which simplifies the determination of ideal conditions and finally, it has a reduced cost (2.96€/g in Sigma-Aldrich) allowing the use of large amounts of precursor for dense solutions and long times of deposition.

### 2.1.2 Description of an AA-MOCVD experiment

The preliminary step in the deposition process is the preparation of the solution. Usually based on solvents as butanol or ethanol, the solution is produced by simply mixing the precursor and the solvent, followed by a constant stirring. As the precursors used were acetylacetonate, ethylenediamine was added to increase the solubility, at a double concentration in relation with the total molar concentration of precursors<sup>11</sup>. In case of a doped material, the ratio of precursors indicated is always the fraction between the dopant molar concentration and the total molar concentration of all precursors, being presented as  $X/Cu+X$ . The stirring lasted 15 hours until a homogeneously solution was obtained. The temperature of the solution is also increased to 50 °C to promote the precursor dissolution. Figure II-22 a) and b) shows the appearance of the precursors used,  $Cu(acac)_2$  and  $Mg(acac)_2$  for the doped case.  $Cr(acac)_2$  was a similar appearance to  $Cu(acac)_2$  with a dark blue colour, however with larger sized particles. In Figure II-22 c) is shown the solution with ethanol as solvent and before the addition of ethylenediamine, while Figure II-22 d) depicts the stirring step, already with ethylenediamine as additive.



Figure II-22 Precursor used in the solution a)  $\text{Cu}(\text{acac})_2$  and b)  $\text{Mg}(\text{acac})_2$ ; solution after the addition of the solvent; d) stirring step in the magnetic plate.

The next step is the preparation of the substrates. In the majority of the cases, alkaline earth boroaluminosilicate glass (Corning 1737) and p-type silicon wafer were used as substrates, in order to study the different chemical, microstructural, optical and electrical properties. Nevertheless, other materials were also tested as glass micro-slides, Au-covered silicon wafer, covered glass with different transparent conductive materials as ITO, FTO or even Ag nanowires networks. The substrates are cut to fit the dimensions of the holder, 2.5cm to 7.5cm, visible in Figure II-23.



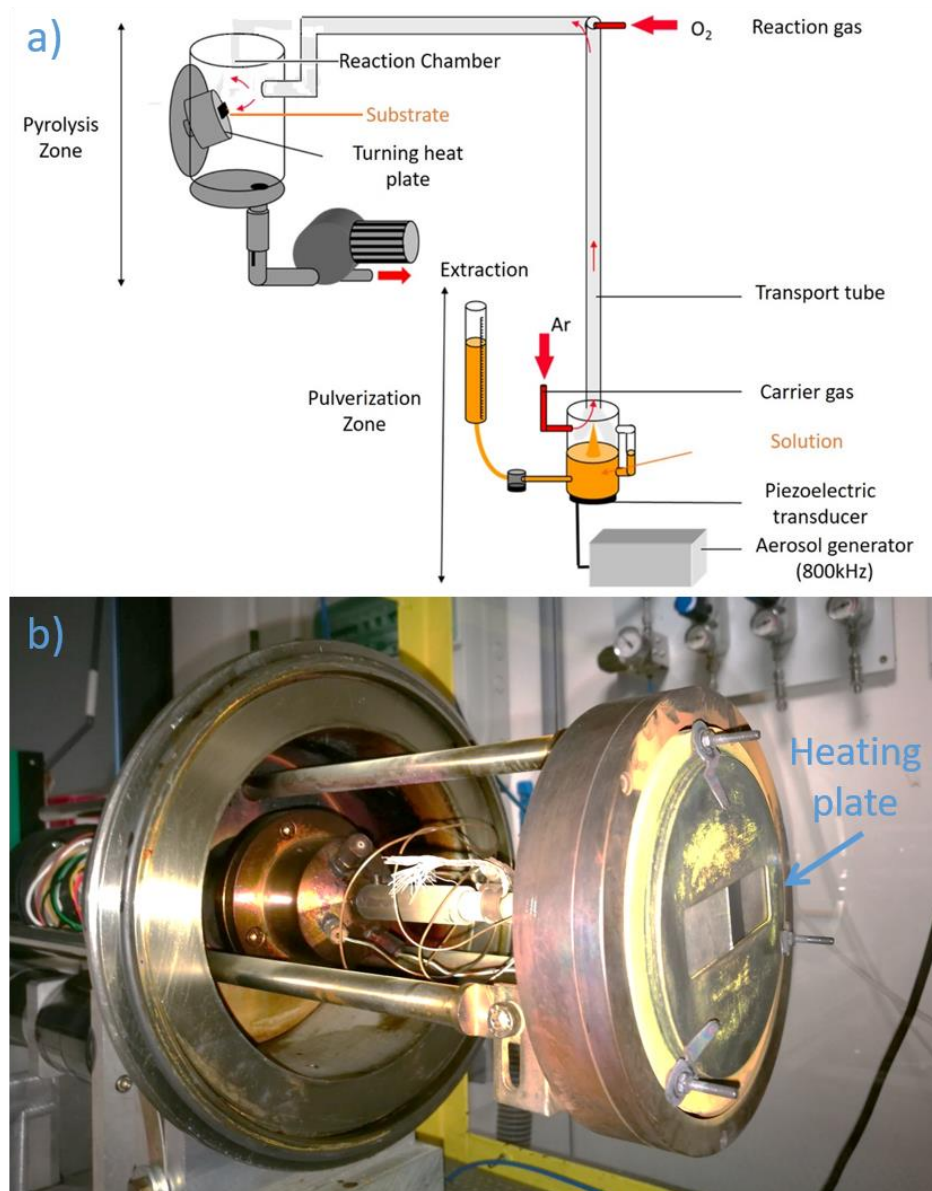


Figure II-24 a) Scheme of deposition set-up and b) heating plate with substrates supported by a metallic holder

The heating step has nominally a duration of 30 minutes, followed by a stabilizing period for 5 minutes, while the plate is rotating. Before the deposition starts, the solution is transferred to a vessel and connected to the piezoelectric transducer by a valve. The height of the vessel allows the control of the solution quantity on top of the piezoelectric transducer, visible in the Figure II-25 a). A piezoelectric transducer, visible in Figure II-25 b), generates the aerosol mist in a separate vessel, with a frequency of 800 kHz, with a controllable power depending on the desirable solution's consumption. In Figure II-25 b), the mist is visible on top of the solution and below the connecting glass tube for the mist transport.



Figure II-25 a) solution vessel with the level of solution visible; b) piezoelectric transducer and created mist.

Argon is used as carrier gas injected on the top of the solution vessel, while  $O_2$  is used as reaction gas, which enters in the system at a higher position, visible in Figure II-26 a). The mixture consisting of the mist and the gases is transported to a home-made reactor, beginning the deposition on the substrates, placed in a vertical position, Figure II-26 c). In the configuration presented here, the mist enters preferably into the chamber from the side, which leads to a horizontal flow, however, a vertical flow is also possible. The pressure inside the chamber and consequent exhaustion of the mist is controlled by an external pump connected to a liquid nitrogen trap to collect the residual solution. The barometer that controls the exhaustion is visible in Figure II-26b).

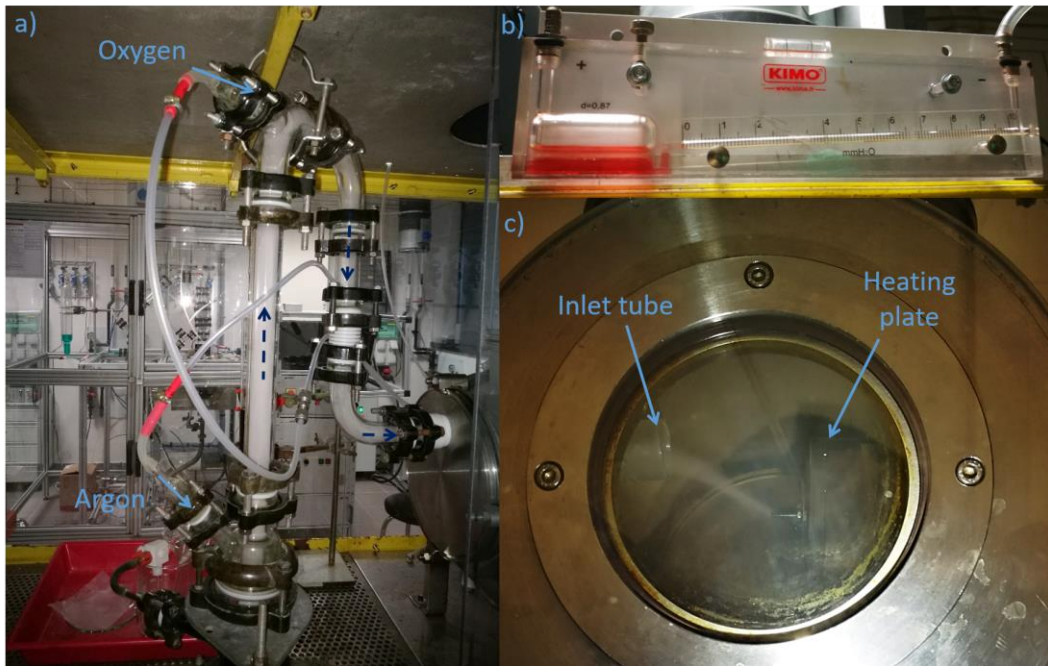


Figure II-26 a) Transport of mist, with the inlet of Argon and Oxygen highlighted; b) barometer for control of exhaustion; c) window of chamber with visible inlet tube, mist and heating plate.

At the end of the deposition, the mist generation is stopped, the gas flux is decreased and the heating of the plate is switched off. After 1 hour, the films can be removed, and the different parts of the equipment are cleaned.

All the different steps previously described have a direct impact on the film properties, in terms of phase, stoichiometry, thickness, homogeneity, grain size, microstructural morphology, dopant absorption and carbon residual content. In Table II-3 we present a summary of the different deposition parameters and the consequent impact on the properties of the deposited materials.

## Chapter II: Experimental procedure and characterization techniques

Table II-3 Deposition parameters and impact of the thin films deposition

<b>Parameter</b>	<b>Impact on</b>	<b>Result in maximal conditions</b>	<b>Variation or range</b>
<b>Solvent</b>	Dissolution of precursor Evaporation during deposition	Precursor residue in case of low dissolution Residue of carbon species detected in film	Butanol or Ethanol
<b>Solution Concentration</b>	Dissolution of precursor Amount of precursor in the vapour	Faster film growth with smaller grains. Precursor residues in glass pieces	From 0.01 mol.l <sup>-1</sup> to 0.03 mol.l <sup>-1</sup>
<b>Frequency of vibration</b>	Size of the droplets	Smaller size of droplets	Around 800 kHz for resonance
<b>Piezoelectric Power</b>	Amount of aerosol generated	Denser vapour, faster deposition, smaller grains, lower O <sub>2</sub> content in the film	35% to 50% of the generator power
<b>Gas Flux</b>	Velocity and concentration of vapour	Possible turbulent flow, faster deposition, smaller grains	5 l.min <sup>-1</sup> to 10 l.min <sup>-1</sup>
<b>O<sub>2</sub> ratio</b>	Amount of oxygen in the film	High O <sub>2</sub> content in the film or presence CuO phase	20% to 33%
<b>Temperature</b>	Evaporation of vapour, decomposition of precursor and grain growth	Higher film thickness and grain growth, reduction of organic species, possible formation of CuO phase	300°C to 400°C
<b>Extraction pressure</b>	Velocity and concentration of vapour	Laminar flow, higher deposition speed	Pressure of 4~5 mmH <sub>2</sub> O
<b>Time</b>	Thickness and saturation	Up to 600nm films	1h to 6h

### 2.1.3 Modification of the reactor configuration

In the middle of the development of this thesis, an incident occurred that led to significant changes in the deposition system. As a consequence, two types of reaction configurations were tested.

The initial configuration, named “vertical configuration”, visible in Figure II-27, had a vertical inlet on the aerosol flux, combined with a tilted substrate holder. In this configuration, mainly butanol was used as solvent. The problems of this configuration were mainly associated to the risk for a macroscopic drop of solvent or a large non-dissolved precursor particle to hit the heated substrate and to create an explosion. Additionally, the use of butanol in a heated oxygen rich atmosphere could cause auto inflammation, since the auto-inflammation point is 343 °C and the low flammability limit (LFL) is 1.7%.

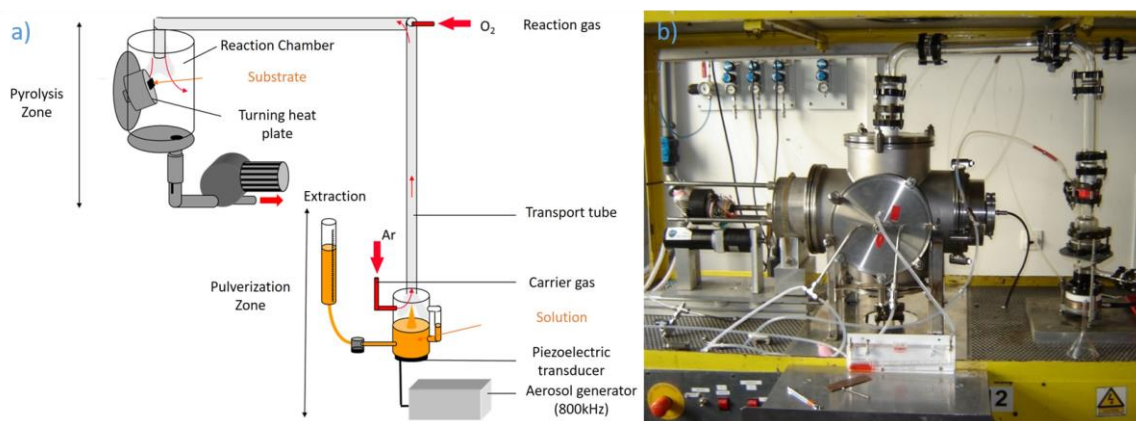


Figure II-27 Vertical configuration of the reaction; a) scheme with all the components and b) photograph

Therefore, a second configuration, named “horizontal configuration” was tested, presented before in the deposition description, where the flux enters in the chamber horizontally and the heated substrate holder is kept in a vertical configuration. Moreover, the solvent was also changed to ethanol with an auto inflammation point at 363 °C and a LFL at 3.3%. However, this configuration can impact the laminar flow of the aerosol and increase the presence of organic contamination in the films.

### 2.1.4 Annealing treatment

The improvements in optical and electric performance of oxide-based materials can, in general, be achieved by post deposition annealing treatments<sup>12</sup>. In our case, different annealing studies were conducted in a traditional box furnace under air. Two main

parameters were varied: temperature variation from 200°C to 450 °C and anneal duration from short plateaus of 5 minutes up to 5 hours. Previous tests were conducted under O<sub>2</sub> atmosphere, however, they show similar results as the ones under air. Therefore, the annealing treatments here presented were developed under air conditions. Additionally, annealing treatments were conducted in a 2-probe stage that allowed the measurement of resistance while heating, once again under air. Figure II-28 show both setups used.

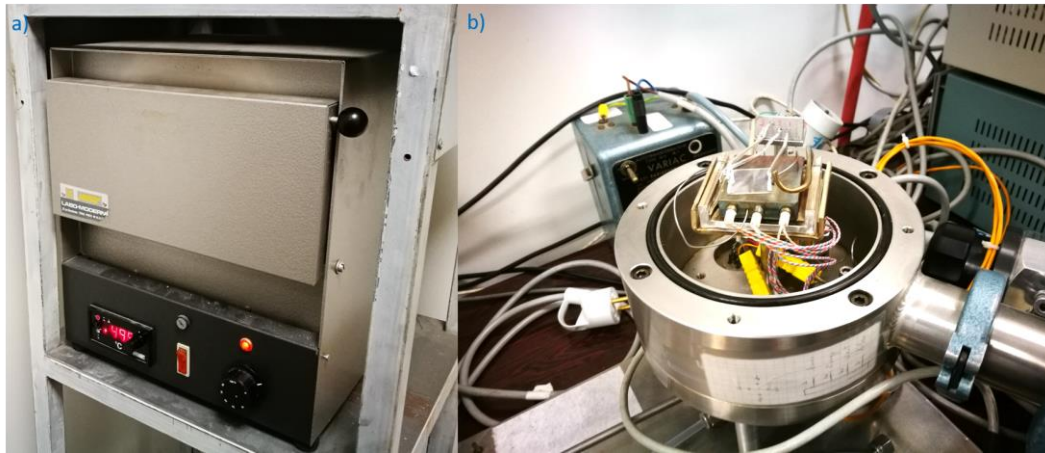


*Figure II-28 a) Box furnace used for air annealing treatments; b) 2-probe stage used for annealing treatments with in situ resistance measurements*

### *2.1.5 Metals Thermal evaporation*

The finalization of some devices as well as the electric analysis of thin films required metallization of contacts in order to improve and simplify the measurements. Usually, gold or silver contacts were thermally evaporated by Joule effect heating of the source in a vacuum chamber using highly pure wires of both metals. The process is based on the increase of temperature of these metals by applying an electric current to a molybdenum crucible. The metal passes from a solid to liquid and then vapour state that travels to the surface of the sample, previously covered by a designed mask. The thermal evaporator and the crucible are visible in Figure II-29.

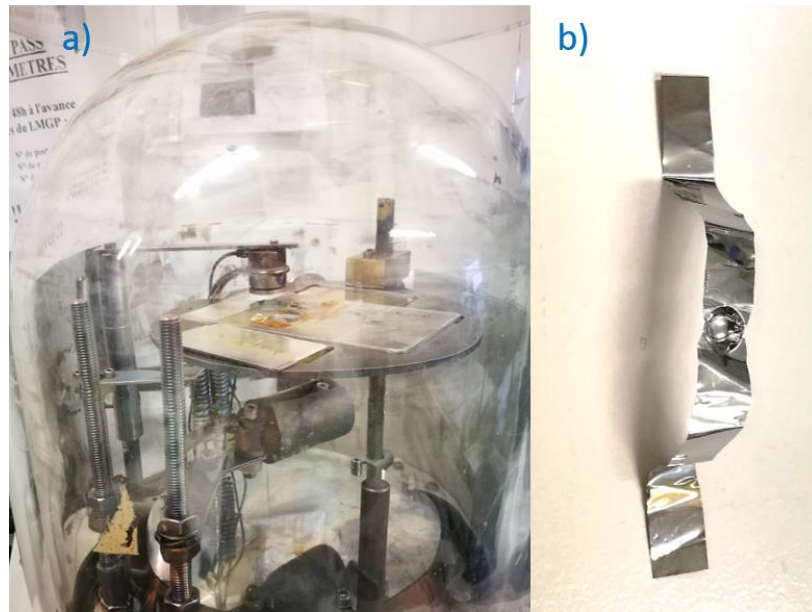


*Figure II-29 Thermal-evaporator for metals evaporation with b) molybdenum crucible*

## 2.2 Techniques of characterization

In the course of the thesis, a detailed characterization of the synthesized materials was conducted using a wide range of standard analysis techniques. Separated in two different axes, the first group of techniques relied on thin films characterization, focusing on crystallographic, microstructural, optical and electrical properties. In parallel, the analysis techniques of the second group were centred on device performance both in electrical and optical characteristics.

### 2.2.1 Morphological, chemical and structural characterization

#### 2.2.1.1 Visual aspect and Optical Microscope (OM)

The first elemental analysis of the films was conducted by visual inspection of the grown specimen. After the removal of the film from the chamber, different characteristics can be detected by the naked eye: thickness of the film and respective gradient, presence of oxide powders, dust or other centres of inhomogeneity. Specially, the estimation of thickness is accurate from the fringes of refraction in the silicon substrate, covered by native  $\text{SiO}_2$ . As a colour chart of  $\text{Cu}_2\text{O}$  on  $\text{SiO}_2$  could not be found in the literature and the refractive light is dependent on the refractive index of the material, a colour chart of  $\text{Si}_3\text{N}_4$  was used to estimate the thickness, visible in Figure II-30a). This material has a refractive index of 1.98 at  $1000\text{nm}$ <sup>13</sup>, while  $\text{Cu}_2\text{O}$  presents a value of 2.4<sup>14</sup> at the same wavelength.

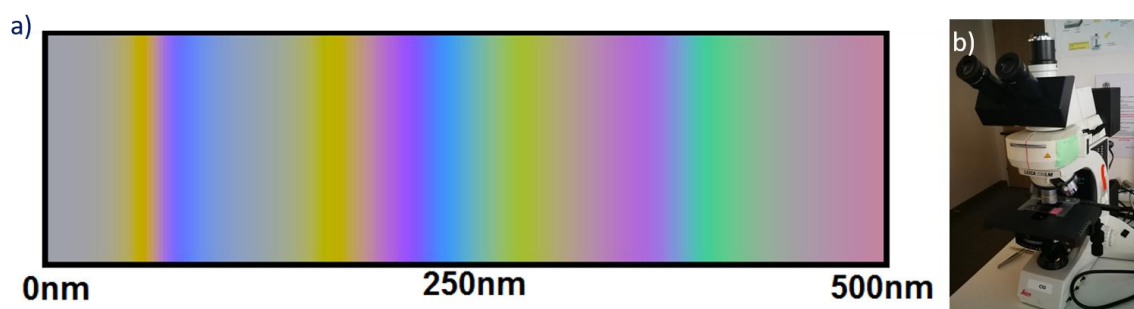


Figure II-30 a) Colour chart for refracted light on  $\text{Si}_3\text{N}_4$ , comparable to  $\text{Cu}_2\text{O}$  thin films using Brigham Young University Silicon Nitride colour simulator<sup>15</sup>; b) Optical microscope setup – Leica DM/LM

The optical microscope (OM) was occasionally used in this work to have a general view of the specimen surface. This technique is based on the magnification of an image using optical lenses that creates an amplified micrograph of the sample. The OM allows a preliminary view in terms of surface roughness and heterogeneity of the sample, providing

an easy way to compare qualitatively different samples. The control of contrast, colors and brightness is fundamental to highlight the information provided by the image. The equipment used for this analysis was a Leica microscope, visible in Figure II-30 b). It is a DM/LM system equipped with a CCD camera and magnifying lenses up to 500 times, that can use different polarization of light and interference mode.

### **2.2.1.2 Scanning Electron Microscope (SEM), Energy dispersive spectroscopy (EDS) and Wavelength dispersive X-ray spectroscopy (WDS)**

The imaging of the microstructure of the samples and the determination of their physical thickness were obtained using a scanning electron microscope (SEM). This technique has a large domain of application especially important in physics, chemistry and materials engineering but also in biology or medical science. SEM allows to obtain images with high resolution and magnification, showing the topography of the sample, through the interaction of electrons emitted by an electron gun with the surface of the material <sup>16</sup>. The incident electron beam is focused on the surface of the sample by a system of electronic lenses, as visible in Figure II-31 a). The interaction between the beam and the surface is mainly dependent on the energy of the beam and the atomic number of the atoms in the samples, resulting in different types of electrons emission or photons radiation by the probed sample. The emitted entities can be X-rays, Auger electrons, primary backscattered electrons or secondary electrons, as represented in Figure II-31 b). The detection of secondary scattered electrons allows the creation of a scanned image with different brightness levels, reflecting the roughness differences of the specimen, determined by the amount of electrons detected. In direct comparison with optical microscope, SEM enables spatial resolution of the order of nanometres, while the visible-light based microscopy only allows resolution higher than 500nm, limited by the diffraction barrier.

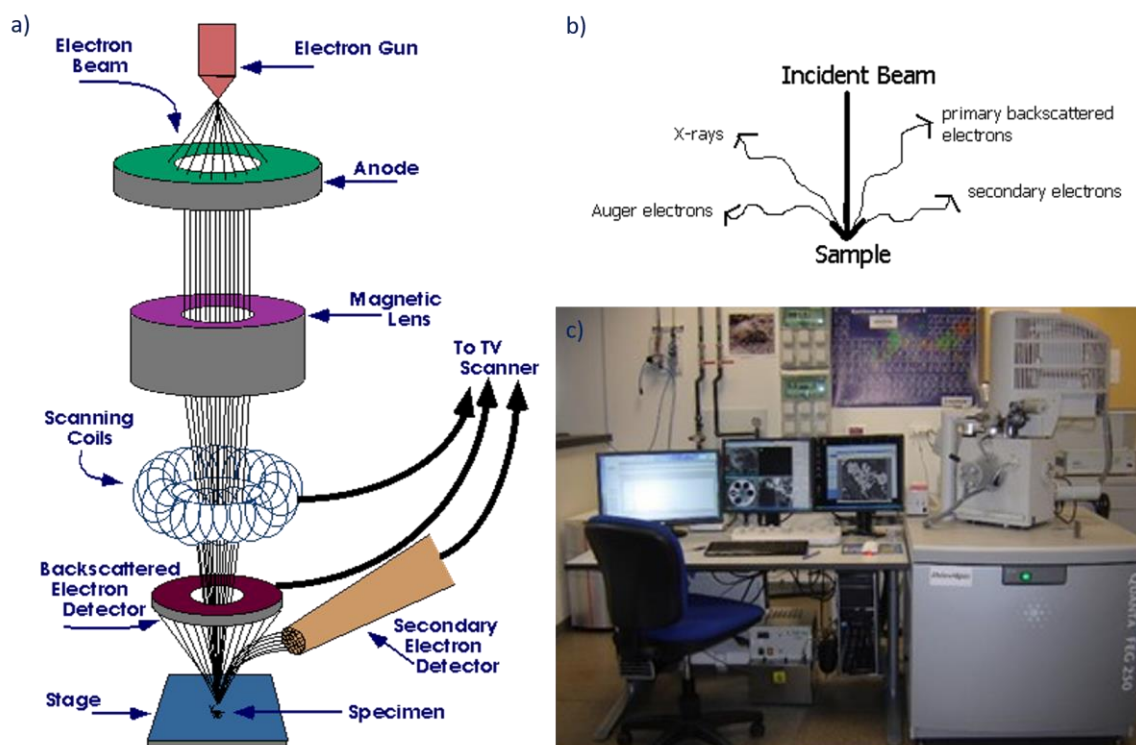


Figure II-31 a) Scheme of SEM function mode; b) Emitted particles from electron beam interaction (from *Radiological and Environmental Management of Purdue University*<sup>17</sup>); c) FEI Quanta 250 equipment present in LMGP

The energy dispersive spectroscopy (EDS) was additionally performed to analyse the chemical composition of the sample at the microscopic scale. In this case, the energy of the incident electron beam excites electrons located on the atom inner shells, causing their injection. Due to the displacement from a higher energy shell electron and consequent relaxation of the excited charge, the energy difference is released by an X-ray photon. These energies depend on the shell of the electron in each element and can be used to detect different elements on the specimen. In general, an energy beam of 5 keV was used to quantify the different elements in the film without a significant signal from the substrate. The Cu  $L\alpha$  line is at 0.930 keV, while in the case of Mg  $K\alpha$  line is at 1.253 keV. Additionally, elemental maps can be created to observe segregation of elements. The SEM and EDS were conducted in a FEI Quanta 250 MEB FEG ESEM tool visible in the Figure II-31c).

Complementary to EDS, Wavelength dispersive X-ray spectroscopy (WDS) was also performed in a selected number of samples. This technique, based on the same principle as EDS, provides additional information about the elements present in the film in a volume of  $1\mu\text{m}^3$ . By performing analysis at different acceleration voltages (12, 16,

22KeV) it is possible, via software, to determine the composition and the surface mass of the film by using software the Stratagem. The equipment used was a CAMECA SX50.

### 2.2.1.3 Transmission electron microscope (TEM)

The transmission electron microscope (TEM) operates on the same basic principles as the transmission optical microscope but uses electrons as in the SEM case. However in this case, the information is obtained through the electrons that cross the sample. Moreover, this technique allows to observe the fine structure of the specimen (observation mode), as well as the crystallographic characterization (diffraction mode)<sup>18</sup>. In the observation mode, the electrons are captured after passing through the sample and we can obtain an image in a sensor located at the focal point. The created images depend mainly on the composition density and thickness of the sample. In the diffraction mode, the electrons that pass through the sample are diffracted in case the material is crystallized, forming a pattern. The comparison of this created pattern with diffraction files already known can be used to analyse the crystallographic phase detected as well as other parameters of the network. A scheme of the TEM components is visible in Figure II-32 a).

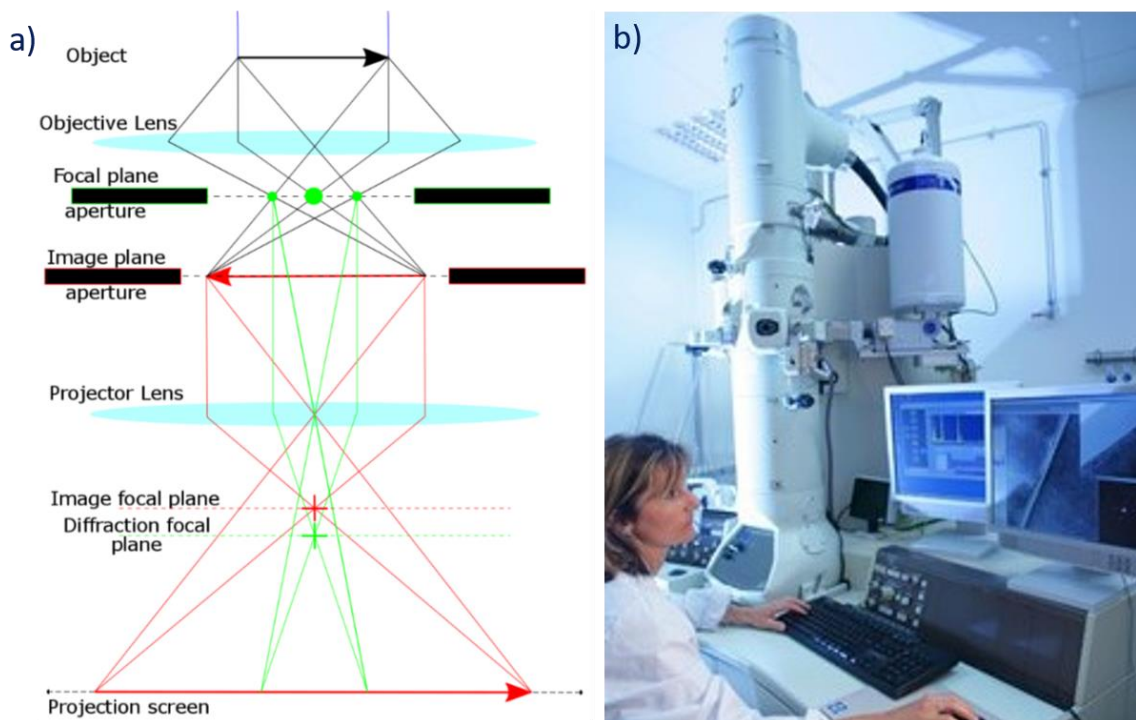


Figure II-32 a) Scheme of components of a TEM Drawing by Graham Colm, courtesy of Wikimedia Commons; b) JEOL JEM 2010 microscope in LMGP

The equipment used for TEM imaging was a JEOL JEM 2010 microscope, visible in Figure II-32 b) operating at 200 kV (0.19 nm resolution), provided with an EDS system, INCA Energy TEM 100 X-Max 65T. Cross-section samples were prepared from films deposited on silicon and glued to a copper grid by tripod polishing resulting in a sample thickness of about 10  $\mu\text{m}$ . Argon ion beam milling was used until perforation of the interface. Automated crystal phase and orientation mapping (ACOM) with precession (ASTAR) system implemented in the JEOL 2100F FEG microscope was also used to obtain the crystal phase and orientation maps. This method is based on the precession of the primary electron beam around the microscope's optical axis at an angle of  $1.16^\circ$  while collecting the electron diffraction patterns at a rate of 100 frames per second with a step size of 1 nm.

### 2.2.1.4 Atomic force microscope (AFM)

In the group of microscopy analysis, another technique used in this work was atomic force microscopy to measure the roughness of the sample. This technique uses mechanic interaction of a small tip with the atoms at the surface of the specimen. Located at the end of a cantilever, the tip is deflected by peaks and valleys on the film, due to forces of attraction or repulsion at the nano-newton scale<sup>19</sup>. Two modes were used to scan the thin films. In the contact mode, the tip is pressed on the surface of the film and it moves through the sample to scan it. The deflection movements of the tip are detected due to a reflection of a laser beam illuminating the end of the cantilever, as represented in Figure II-33 a). The variation of laser intensity detected by photodiode sensor allows creating a topographic map of the sample surface. The second mode, traditionally called tapping-mode, avoids possible problems caused by the contact with the sample in the first mode described. In this case the tip oscillates over the sample with a specific frequency, causing brief intermittent contacts. The changes in amplitude of oscillation permit to reconstruct an image of the roughness of the surface. The difference between both modes is represented in Figure II-33 b).

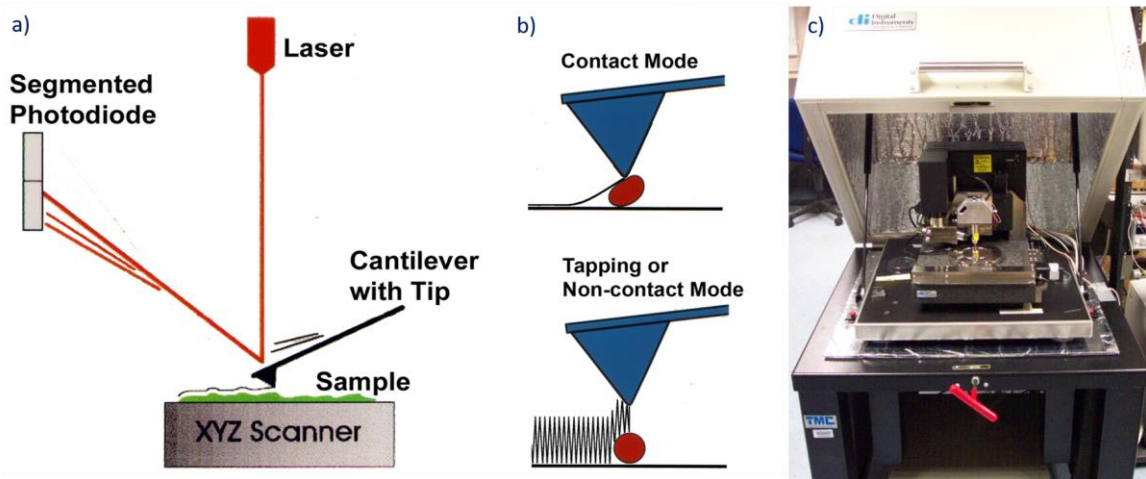


Figure II-33 a) and b) Description of AFM modes of operation( from University of California Santa Barbara <sup>20</sup>) c) Veeco D3100 AFM in LMGP

The analysis was performed in Veeco D3100 AFM with  $5\mu\text{m} \times 5\mu\text{m}$  images, shown in Figure II-33 c), in order to observe grains and the roughness of the films.

### 2.2.1.5 X-Ray diffraction (XRD)

The analysis of the crystallographic structure of the thin film was performed by X-ray diffraction (XRD). The interaction of X-rays with the atoms of a crystal allows a suitable probing of the atomic positions and consequentially their arrangement in the crystal structure. The interference of reflected X-rays is possible due to the small wavelength of these electromagnetic waves, which are comparable to the lengths between crystallographic planes, producing diffraction patterns that can be subsequently detected. The variation of the incident beam in the sample will satisfy different diffraction conditions determined by Bragg's equation (II.2):

$$2d\sin(\theta) = n\lambda \quad (II.2)$$

where  $d$  corresponds to the distance between crystallographic planes,  $\theta$  is the diffraction angle of the light,  $n$  is the order of diffraction and  $\lambda$  is the wavelength used, in this case the Cu K-edge (0,1519 nm). A scheme of the interplanes distances and X-Ray diffraction is visible in Figure II-34 a). The detection of the XRD peaks can then be related to the lattice parameter and structure of the crystalline material <sup>21</sup>, enabling the detection of different phases in the sample and differences in lattice size.

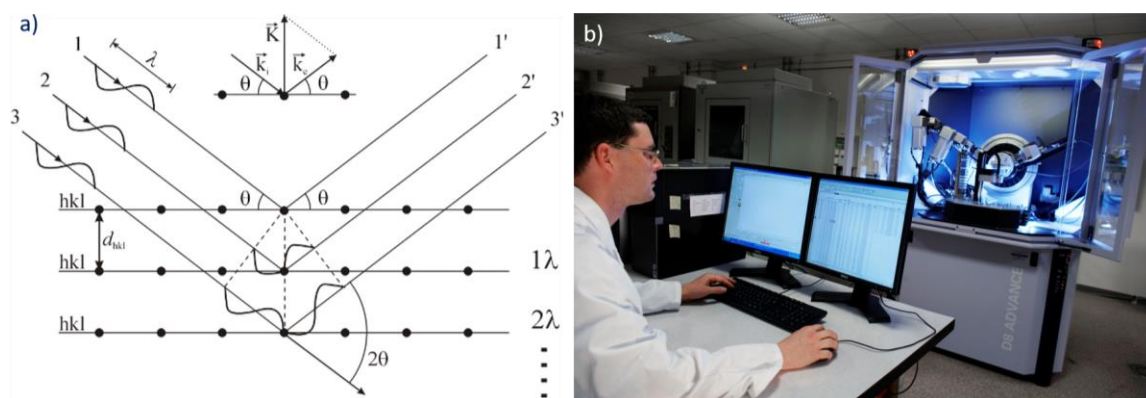


Figure II-34 a) X-Ray diffraction on a crystal, where the crystallographic planes and X-Ray wave-vectors are represented <sup>22</sup>; b) Bruker D8 Advance in LMGP

The analysis was performed at room temperature using a Bruker D8 Advance diffractometer in the Bragg-Brentano ( $\theta$ - $2\theta$ ) configuration with Cu  $K\alpha$ 1 radiation (0.15406 nm). The range of the spectrum obtained varied from  $20^\circ$  to  $80^\circ$  in the diffraction angle ( $2\theta$ ) with a scanning rate of 3 degrees per minute. In order to evaluate the grain growth of the  $\text{Cu}_2\text{O}$  films, the crystallite sizes in the films was estimated using Scherrer's equation <sup>23</sup>:

$$L = \frac{K\lambda}{B \cos(\theta)} \quad (\text{II. 3})$$

where  $L$  is the mean crystallite size,  $B$  is the full width at half maximum (FWHM) of the intensity peak,  $K$  is the Scherrer constant,  $\lambda$  is X-ray wavelength and  $\theta$  is the Bragg angle.

## 2.2.2 Spectroscopic and spectrometry techniques

### 2.2.2.1 Raman spectroscopy and Photoluminescence

Concerning the chemical analysis of the films, Raman spectroscopy is a powerful tool to access vibrational, rotational, and other low-frequency modes in a material. This type of spectroscopy technique relies on the Raman scattering (inelastic) occurring within the samples upon illumination with a monochromatic light source. When a high intensity monochromatic light, in this case a laser, impinges a material, most photons are scattered with the same energy as the incident light. This elastically scattering process is called Rayleigh scattering. However, some of the scattered photons, around 1 in 10 millions, have a shift of energy in comparison with the original energy. In case of a lower or higher energy scattering, this inelastic process is called Raman scattering, with a scheme visible in Figure II-35 a). The intensity of photos regarding each energy difference are directly linked to

chemical bonds, therefore, a spectrum of Raman light can be obtained<sup>24</sup>. In this technique, it is usual to use wavenumber,  $\text{cm}^{-1}$ , instead of wavelength, since we always present the shift from the original light source. In the context of  $\text{Cu}_2\text{O}$  thin films, this technique was key to for the detection of the  $\text{CuO}$  phase.

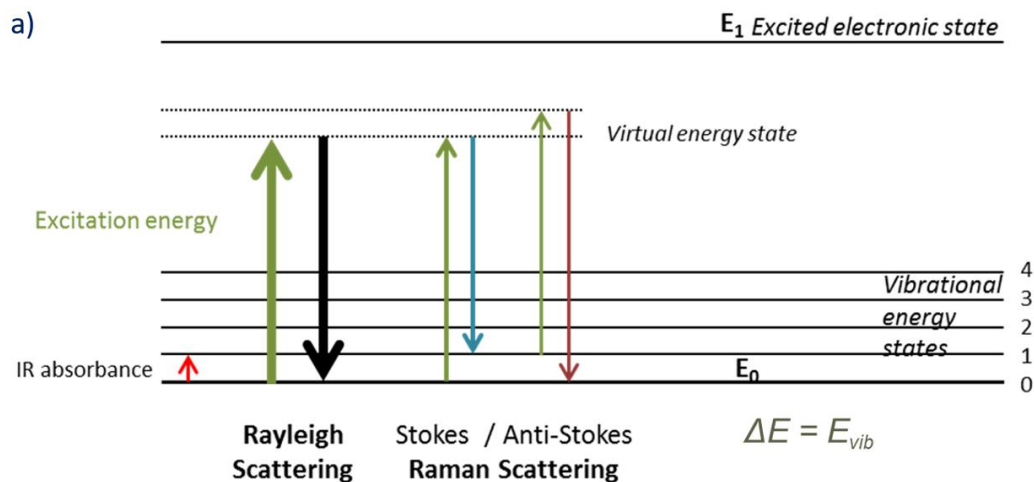


Figure II-35 a) Scheme with Rayleigh and Raman scattering representation<sup>25</sup>; b) Jobin Yvon/Horiba LabRam spectrometer in LMGP

Raman spectroscopy was carried out with a Jobin Yvon/Horiba LabRam spectrometer, shown in Figure II-35 b), covering the range from 50 to 2000  $\text{cm}^{-1}$ , with the use of different monochromatic lights. In the majority of the analysis, the 488 nm blue line of an  $\text{Ar}^+$  laser with a power of 0.4 mW on the substrate surface was used. The laser was focused to a spot size close to 1  $\mu\text{m}^2$  by using a 50x long working distance objective. Moreover, photoluminescence measurements were also performed in the same equipment. However, in this case, the emission of light from the sample after the excitation occurs due to different phenomena, mostly excitons and defects in the material<sup>26</sup>. The interest of PL measurements for  $\text{Cu}_2\text{O}$  thin films is mainly connected to the detection of vacancies of copper or oxygen.

### 2.2.2.2 Fourier transform infrared spectroscopy (FTIR)

Complementary to Raman spectroscopy, Fourier transform infrared spectroscopy (FTIR) is a technique that enables the detection of chemical compounds in the films due to the absorption of infrared light, which are represented in Figure II-35 a). In this case, an infrared beam composed of different wavelengths passes through the film, interacting with the different chemical species. If one specific chemical bond has the same energy of the infrared light, it will be absorbed. However, the collection of the absorption spectrum is in this case based on interferometry. The light beam is separated into two different beams, using a Michelson Interferometer, which then will pass through the sample and create an interferogram (interference pattern) in the detector. The Fourier transform of the created pattern will provide an infrared spectrum, used for the detection of chemical bonds. The scheme of this technique is visible in Figure II-36 a). In the analysis of  $\text{Cu}_2\text{O}$  films, this technique proves to be interesting for the detection of organic species in the material. In case of incomplete degradation of the precursors, residual organic substances can indeed be present in the film, which can lead to meagre physical properties. Additionally, metal-oxygen bonds can be detected, confirming the presence of dopants in the films.

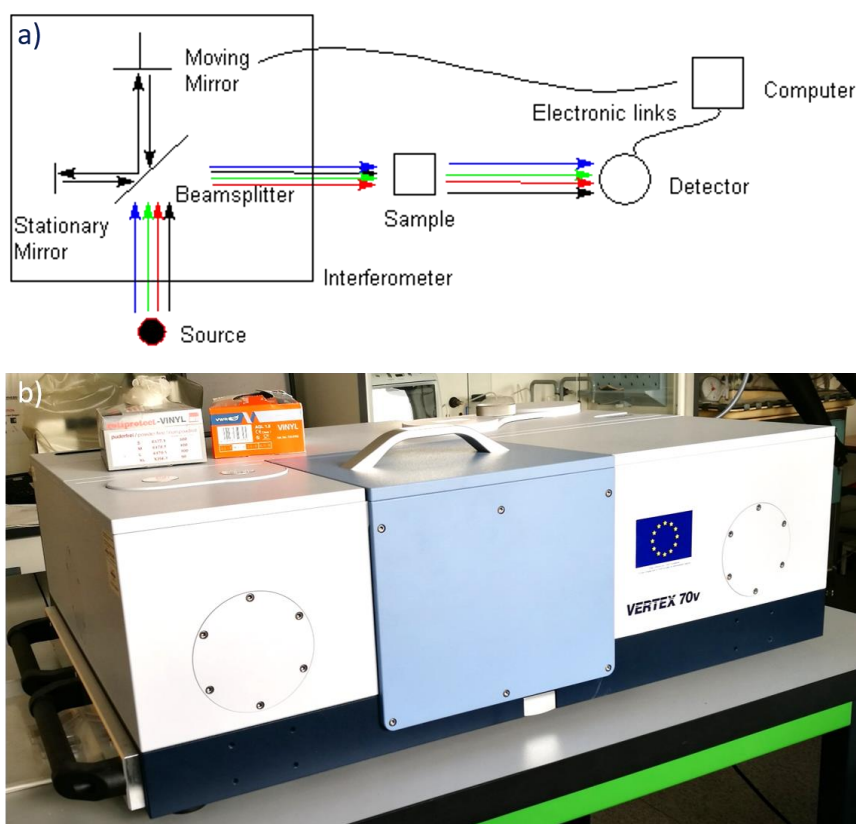


Figure II-36 - a) Scheme of FTIR function mode <sup>27</sup>; b) Bruker Vertex 70V spectrometer present in LMGP

Fourier-transform infrared (FTIR) measurements were performed in a Bruker Vertex 70V spectrometer, visible in Figure II-36 b), equipped with a CsI beamsplitter and working under vacuum. Spectra were recorded with a resolution of  $4\text{ cm}^{-1}$  by accumulating 64 scans in transmission mode using silicon substrates, transparent to infrared light.

### 2.2.2.3 X-ray photoelectron spectroscopy (XPS)

X-ray photoelectron spectroscopy is a surface technique that analyse the energy of bonds between atoms. A monochromatic beam of X-Ray bombards the sample, causing the ionization of the atoms. Each ejected electron will be emitted from the atom and by measuring its kinetic energy,  $E_k$ , and with previously known energy of the X-ray beam,  $h\nu$ , the bond energy,  $E_b$ , required for the ionization can be determined:

$$E_b = h\nu - E_k \quad (II. 4)$$

The binding energy distribution provides quantitative information about the atomic composition of the film. Moreover, spectra obtained with the highest resolution can additionally probe the nature of the chemical bonds and oxidation state of the atoms <sup>28</sup>.

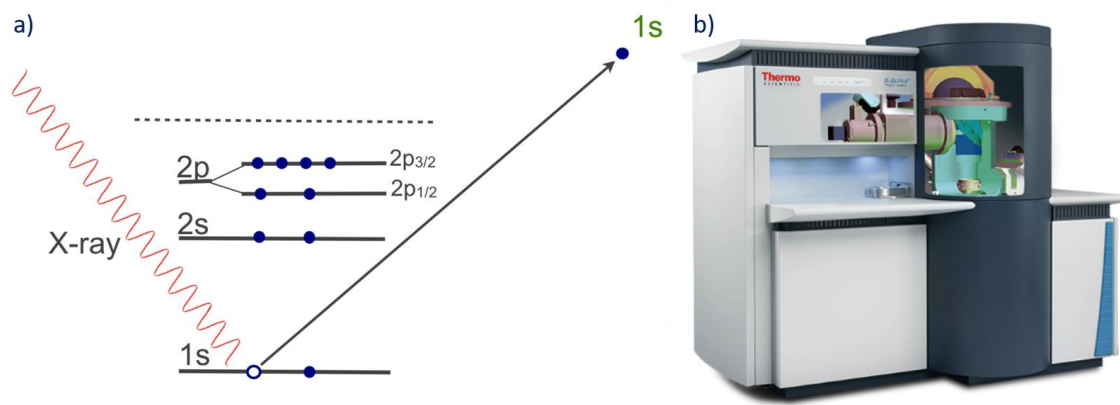


Figure II-37 X-Ray interaction with atoms during XPS analysis b) K-alpha spectrometer at SIAM – Synthesis, Irradiation and Analysis of Materials in the Université de Namur

Integrating the electrons at different energy bonds produces a spectrum where the peaks correspond to characteristic orbitals of each element. In the context of this study, XPS was fundamental to observe differences in copper oxidation state, in order to detect the presence of CuO in the films. This technique is very sensible to the surface (several Angströms).

The analysis was conducted in SIAM – Synthesis, Irradiation and Analysis of Materials in the Université de Namur, using a K-alpha spectrometer, from Thermo Scientific, with a X-ray source Al K $\alpha$ 1,2 (1486.6 eV), represented in Figure II-37 b).

### **2.2.2.4 Extended X-Ray Absorption Fine Structure (EXAFS)**

In order to probe the chemical environment of a single element and obtain the interatomic distances, Extended X-Ray Absorption Fine Structure (EXAFS) was performed with synchrotron at a large scale instrumental facilities. In a simple approximation, EXAFS measures the energy dependence of X-rays absorption by an atom near a defined core level. These spectra show oscillations near the band edge that can be correlated to different near-neighbour coordination shells and respective distance to these neighbours<sup>29</sup>. In this case, the analysis was performed at ESRF, in Grenoble, in the BM31 line, where the Cu K edge line was studied in detail. The use of EXAFS was fundamental to observe the neighbouring environment of the Cu<sup>+</sup> cation by measuring distances to neighbour atoms.

### **2.2.2.5 UV-VIS-IR transmittance**

The optical characterization of the films was in a large part based on optical spectroscopy analysis, where the transmittance was the main analysed property. The transmitted part of the light is then collected in an integrated sphere and the detector compares the intensity obtained with a previously measured baseline. A representation of this technique is shown in Figure II-38 a). Additionally, in the system used, we can discriminate between total and direct transmittance.

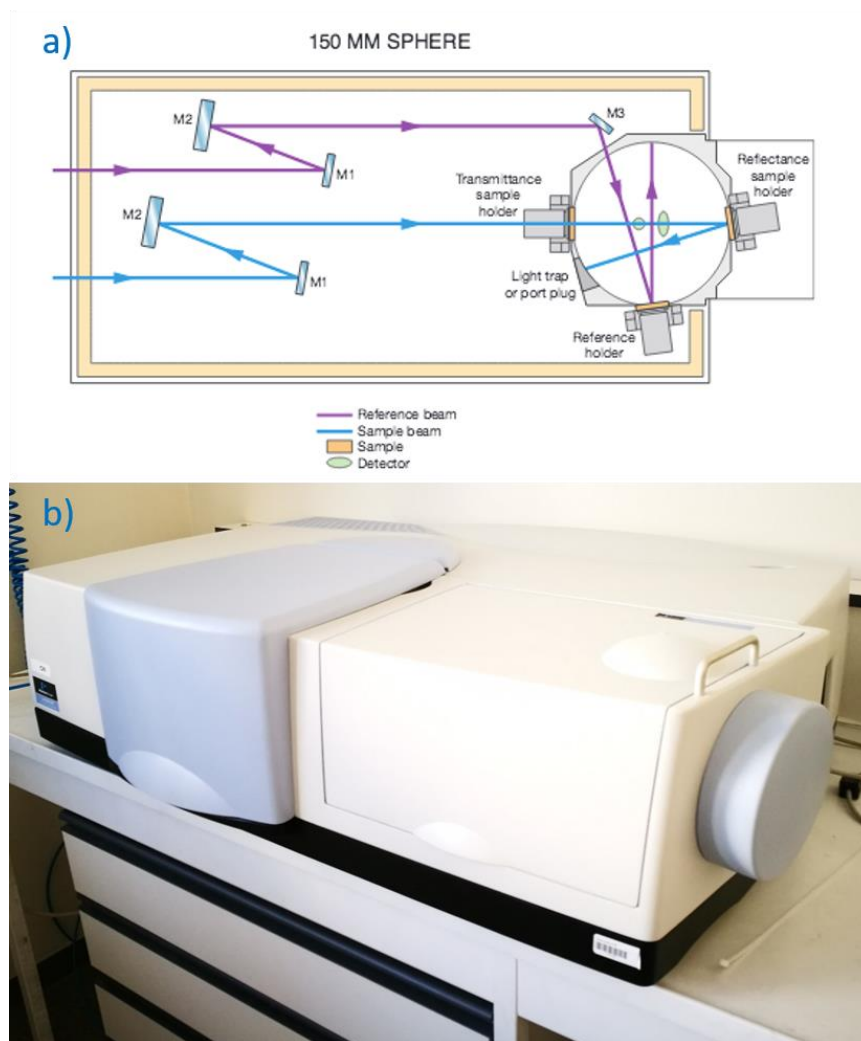


Figure II-38 a) Scheme of light pass in the UV VIS NIR spectrometer; b) Lambda 950 spectrophotometer from Perkin Elmer present in LMGP

The measurements from Ultraviolet to near-infrared were conducted in a Lambda 950 spectrophotometer from Perkin Elmer, visible in Figure II-38 b), in the range of 250 nm to 2500 nm, presenting a wavelength step of 5nm. The reported average transmittance in the visible is defined as the ratio between the integrated transmittance between 390nm and 700nm and the wavelength interval. The spectra were used to calculate the band gap by tracing the Tauc plot using the PARAV-V2.0 software, with a given uncertainty of 0.1eV.

### 2.2.3 *Electrical and functional properties of materials and devices*

#### 2.2.3.1 **4-Probe**

Combined with optical inspection, the determination of the sheet resistance by 4-probe measurement is one of the first analyses to be performed in the sample. In this approach, the applied current flows between the outer probes while the voltage is measured in the inner probes, providing a resistance value based on Ohm's law. The combination of two different conditions allow the conversion of the measured total resistance to sheet resistance and finally to resistivity. The first requirement relies on the film thickness to be less than half of the constant spacing between the probes; while the second important requirement imposes the measuring point to be away from the edges of the film, at least 4 times the spacing between probes. Under those conditions, the sheet resistance can be given by:

$$R_S = F \frac{V}{I} \quad (II. 5)$$

where  $R_S$  is the sheet resistance,  $V$  the voltage measures,  $I$  the current applied and  $F$  a constant defined as:

$$F = \frac{\pi}{\ln(2)} = 1.442 \quad (II. 6)$$

Finally, the resistivity is determined by following equation:

$$\rho = R_S e \quad (II. 7)$$

where  $\rho$  is the resistivity and  $e$  the thickness of the film. At LMGP, the measurements were performed using a Por-4 probe provided by Lucas Lab, Figure II-39 b), with a distance between tips of 1.066 mm and connected to a Keithley multimeter, Figure II-39 a).

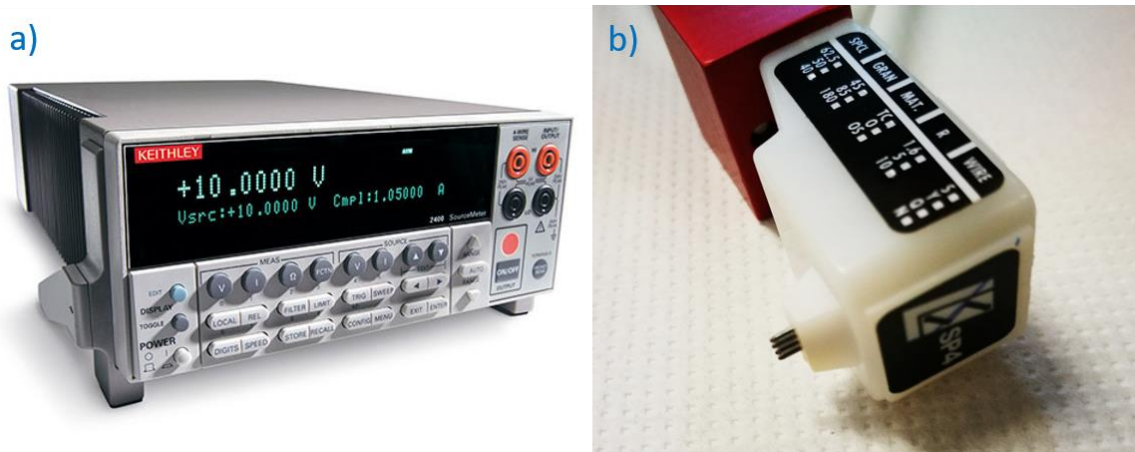


Figure II-39 a) Keithley multimeter and b) 4 probe tips

### 2.2.3.2 Van der Pauw

In this case, similarly to 4-probe, the resistivity of the film is analysed by applying current to the film and measuring voltage. However, this technique allows a more precise determination of resistivity than the previous one described. Instead of a linearly-aligned probes, the van der Pauw requires four small ohmic contacts placed on the corners of a square on the top of the thin film<sup>30</sup>. The extraction of the sheet resistance  $R_S$  is based on the measurement of two different characteristic resistances  $R_A$  and  $R_B$  as represented in Figure II-40.

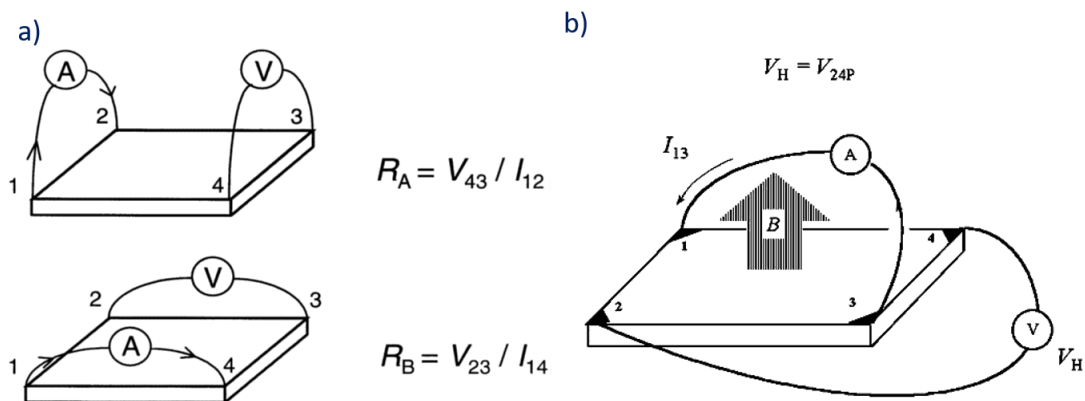


Figure II-40 a) Representation of van der Pauw measurements<sup>30</sup> b) Hall Effect potential measuring set-up<sup>31</sup>.

While applying the current between two contacts in one direction, the voltage is measured in parallel contacts. It is demonstrated that the two measured resistances are related to  $R_S$  by the following expression:

$$e^{-\frac{\pi R_A}{R_S}} + e^{-\frac{\pi R_B}{R_S}} = 1 \quad (II. 8)$$

The numerical resolution of this equation can provide the sheet resistance and converted into resistivity, by the expression previously described.

### 2.2.3.3 Hall Effect measurements

Complementary to van der Pauw measurements, Hall-effect measurements were used to determine the density and the mobility of free charge carriers of the film. The Hall Effect is based on the charge build-up in a medium due to magnetic forces. A magnetic field,  $B$  perpendicular to the film surface, produces a force on moving charges, in an electric current  $I$ , those charges are deflected in a direction perpendicular to the original movement and the magnetic field. The caused force is called Lorentz force,  $F_L$ . The magnetic part of this force can be expressed as:

$$F_L = e v \times B \quad (II. 9)$$

where  $e$  ( $1.602 \times 10^{-19}$  C) is the elementary charge,  $v$  the velocity of the charge. The perpendicular movement of the charges creates a transversal potential to the electric field sense, which can be represented as:

$$V_H = \frac{I B}{e p t} \quad (II. 10)$$

where  $V_H$  is the Hall potential,  $I$  is the current,  $p$  the carriers density and  $t$  is the sample thickness. The measured Hall potential can then be used to determine the nature and concentration of charge carrier, as well as their mobility  $\mu$ , as follows:

$$p = \frac{I B}{d e |V_H|} \quad (II. 11)$$

$$\mu = \frac{|V_H|}{R_s} I B = \frac{1}{e p t R_s} \quad (II. 12)$$

In Figure II-40b), a scheme of  $V_H$  measurement is represented. The electronic transport properties were obtained at room temperature using a Van der Pauw configuration and a RH2035 Hall effect measurement setup from Phys Tech equipped with a magnetic field of 0,43T.

### 2.2.3.4 IV and PV measurements

The characterization of the fabricated devices first involved current-voltage (I-V) measurements, which are fundamental to evaluate the quality of the  $pn$  junctions. By applying a bias voltage between 2 electrodes and sweeping different voltage values, the resistance between the two contact points is measured simultaneously, resulting in an

electric current calculation. Additionally, if this analysis is performed under a light source, we can access to the efficiency of a solar cell, a key performance indicator for such a device. The solar simulator is represented in Figure II-41 a).

The photovoltaic performance of the solar cells was conducted by using a home-designed holder, represented in Figure II-41 b) and c). This holder is composed of 11 gold pogo pins. Each pin contacts a different electrode on the sample, which is upside down. The light enters from the top mask that has circular holes with the same area as the metallic contacts.

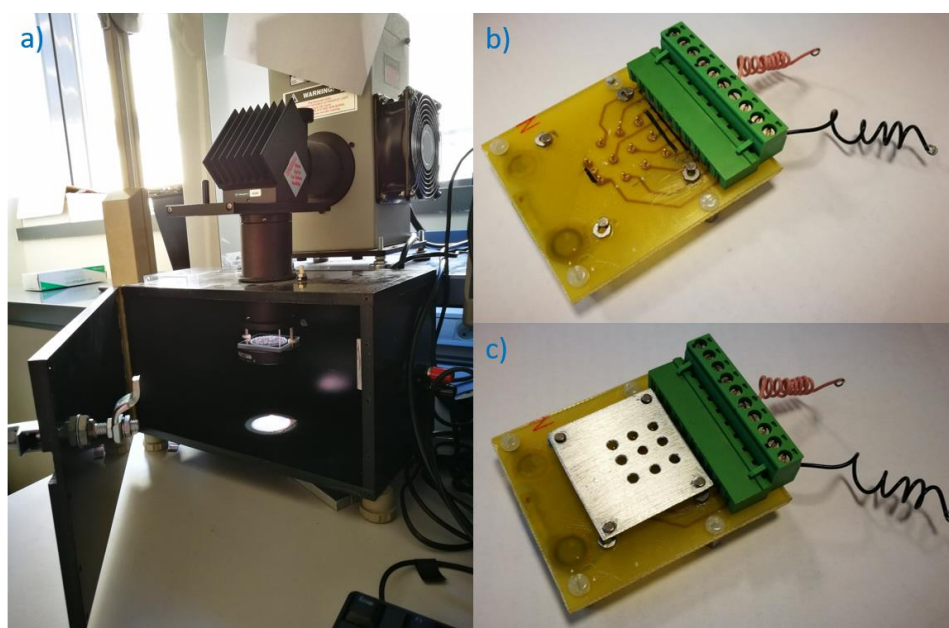


Figure II-41 a) Solar simulator; PV sample holder b) without mask, c) with mask

### 2.2.3.5 Responsivity

The responsivity analysis was used to evaluate the UV selectivity of the photodetector. The technique measures the amount of electrical output from the device due to an optical environmental input. In this specific case, we measure the current generated in the detector per incident radiant power of a specific wavelength. Therefore, the responsivity is expressed in Amperes per Watt. The analysis was performed at room temperature in the range of 300 to 800 nm using a xenon arc lamp. The short-circuit current ( $I_{sc}$ ) from the sample was recorded every 10 nm across the spectrum and compared to the  $I_{sc}$  from a calibrated Si-photodiode with a known responsivity.

## 2.3 Simulation

Device modelling was performed to simulate the electrical characteristics of  $pn$  junctions formed with  $\text{Cu}_2\text{O}$  and  $\text{ZnO}$ . Numerical analysis is a powerful tool to analyse a large quantity of different phenomena, providing valued information to improve the experimentally grown materials and consequently the applied devices. This study was used for a direct comparison with the experimentally fabricated junctions, in order to access carrier's concentrations distributions, size of depletion region and ideal diode behaviour. This part of the study was developed at the Université de Liège, using a Fortran program originally created within the SPIN laboratory. In this section we explain the basic semiconductor equations used in the model, as well as some technical details on the procedure leading to the computer program.

### 2.3.1 Basic equations

In a first approach, Maxwell's equations are rewritten to obtain the distribution of charges and the electrical potential. In the differential form, we use Gauss's law to relate the electric flux leaving a certain volume the electric charge density. In an isotropic material, the displacement vector ( $\mathbf{D}$ ) is proportional to the electric field ( $\mathbf{E}$ ) by a scalar quantity, the semiconductor permittivity  $\varepsilon_s$ . Therefore, the electric flux equation can be simplified as:

$$\varepsilon_s \nabla \cdot \mathbf{E} = \rho \quad (\text{II. 13})$$

Subsequently, we have to consider Faraday-Henry's law of electromagnetic induction and the vector potential  $\mathbf{A}$  relation to the magnetic field  $\mathbf{B}$ :

$$\nabla \times \mathbf{E} = - \frac{\partial \mathbf{B}}{\partial t} \quad (\text{II. 14})$$

$$\nabla \times \mathbf{A} = \mathbf{B} \quad (\text{II. 15})$$

$$\nabla \cdot \mathbf{A} = 0 \quad (\text{II. 16})$$

The combination of the previous equations considered leads to:

$$\nabla \times \left( \mathbf{E} + \frac{\partial \mathbf{A}}{\partial t} \right) = 0 \quad (\text{II. 17})$$

This last expression results in a creation of a gradient field,  $-\nabla\psi$ , due to the fact that the curl of a vector field is equal to zero. Therefore, the electric field is equal to:

$$\mathbf{E} = -\frac{\partial \mathbf{A}}{\partial t} - \nabla \psi \quad (II. 18)$$

As a consequence, Gauss's law can be expressed as:

$$\nabla \cdot \epsilon_s \frac{\partial \mathbf{A}}{\partial t} + \nabla \cdot \epsilon_s \nabla \psi = -\rho \quad (II. 19)$$

Considering the precious definition of  $A$ ,  $\nabla \cdot A = 0$ , we obtain a final expression for the gradient field of:

$$\epsilon_s \Delta \psi = -\rho \quad (II. 20)$$

The second side of the equation, the space charge density  $\rho$ , can also be considered in terms of the sum of all charged defects multiplied by the elementary charge  $q$ . In the group of total defects we count as contributions to the total positive charge the hole concentration  $p$  and the ionized shallow donor concentration  $N_D$ , while the negative charge incorporates the electron concentration  $n$ , the ionized shallow acceptor concentration  $N_A$ , and the occupied trap concentration  $n_t^*$ . Putting all terms together, we reach the following expression for the total charge density :

$$\rho = q(p + N_D - n - N_A + n_t^*) \quad (II. 21)$$

The next part of the model development is connected to how the space charge density varies with respect to time which leads to the continuity equations. The application of a divergence to the Ampère's circuital law leads to the relation between current density and the time derivative of the charge densities.

$$\nabla \cdot (\nabla \times \mathbf{H}) = \nabla \cdot \left( \mathbf{J} + \epsilon_s \frac{\partial \mathbf{E}}{\partial t} \right) \quad (II. 22)$$

Since the application of the divergence operator to the curl of a vector field is equal to zero, we can extract that:

$$\nabla \cdot \mathbf{J} = -\nabla \cdot \left( \epsilon_s \frac{\partial \mathbf{E}}{\partial t} \right) \quad (II. 23)$$

And with some extra manipulation of the (II. 23) equation, we obtain:

$$\nabla \cdot \mathbf{J} = -\frac{\partial \rho}{\partial t} \quad (II. 24)$$

We can separate the current density in the sum of the different components, electrons and holes and by considering the donor and acceptor dopant as time independent we obtain:

$$\nabla \cdot \mathbf{J}_n - q \frac{\partial n}{\partial t} = q R_n \quad (II. 25)$$

$$\nabla \cdot \mathbf{J}_p + q \frac{\partial p}{\partial t} = -q R_p \quad (II. 26)$$

$$-q \frac{\partial n_t^*}{\partial t} = -q (R_n - R_p) \quad (II. 27)$$

where  $R_n$  and  $R_p$  are the net recombination or generation rates for electrons and holes. The last 2 equations required for the simulations come from the definition of current density, in terms of carriers concentration, mobility and diffusivity, within a semi-classical drift/diffusion model :

$$\mathbf{J}_n = q n \mu_n \mathbf{E} + q D_n \nabla n \quad (II. 28)$$

$$\mathbf{J}_p = q p \mu_p \mathbf{E} + q D_p \nabla p \quad (II. 29)$$

where  $\mu_n$  and  $\mu_p$  are respectively the electron and hole mobilities. The diffusion constants of both charges is defined as  $D_n$  and  $D_p$ . The physical consideration for the model is completed by using Boltzmann's approximations for carrier concentrations in the nondegenerate case and Fermi-Dirac occupied level concentration. The equations for the electrons, holes and electrons in trap states are expressed as:

$$n = N_c e^{\frac{E_c - F_n}{kT}} \quad (II. 30)$$

$$p = N_v e^{-\frac{F_p - E_v}{kT}} \quad (II. 31)$$

$$n_t^* = \frac{N_t}{1 + g_t e^{-\frac{E_t - F_t}{kT}}} \quad (II. 32)$$

where  $F_n$ ,  $F_p$  and  $F_t$  are the quasi-Fermi energies of electrons, holes and trap states.  $E_c$  and  $E_v$  are the position of the conduction and valence band respectively, while  $g_t$  is the degeneracy factor of the trap states.

The numerical simulation was then based on this group of equations: the relation between the different current densities and the charge carriers and electric field, as well as the charge carriers' density distributions.

### 2.3.2 Model's algorithm

The set of equations presented here above is a system of nonlinear, coupled, partial differential equations. Therefore, linearization and discretization of the initial problem into a step-sized mesh are required. The system of equations is linearized by a Newton approach and the initial values are introduced using a guessed solution. The algorithm chosen to solve this model is based on iterative methods that involve a series of corrections to the initial

guess. These iterations continue until a defined set of convergence criteria is reached. These methods are usually quite efficient for large linear systems, converging rapidly and using memory efficiently. Though, the results are inaccurate within the round-off error and the convergence is not always obtained.

The whole problem size depends on the number  $m$  of unknown quantities per node and the total number of mesh points  $N$ , which provides a total number of unknowns that can be expressed by the product  $m \times N$ . In the case of Newton's method, which is used in this framework, the coefficient matrix contains  $(m \times N)^2$  elements and exhibits a block-diagonal shape, for which dedicated algorithms are known. The quality of the numerical solution to the equation system depends thus on an optimal trade-off between precision and size of the linear system. If we consider a large number of mesh points, the quality and precision of the solution rises, with an increase in computation time and memory capacity requirement. For more specific details, the reader can consider the works by Baert <sup>32</sup> and Nguyen <sup>33</sup> where the authors present a full description of the physical considerations and the algorithm behind the implemented model.

## 2.4 References

- (1) Park, J.-H.; Sudarshan, T. S. *Chemical Vapor Deposition*; ASM international, 2001; Vol. 2.
- (2) Zilko, J. L. *Metal Organic Chemical Vapor Deposition : Technology and Equipment*. **1968**, 155.
- (3) Hou, X.; Choy, K. L. Processing and Applications of Aerosol-Assisted Chemical Vapor Deposition. *Chem. Vap. Depos.* **2006**, *12* (10), 583–596.
- (4) Viguie, J. C.; Spitz, J. Chemical Vapor Deposition at Low Temperatures. *J. Electrochem. Soc* **1975**, *122* (4), 585–588.
- (5) Deschanvres, J. L.; Cellier, F.; Delabouglise, G.; Labeau, M.; Langlet, M.; Joubert, J. C. Thin Film of Ceramic Oxides by Modified CVD. *Le J. Phys. Colloq.* **1989**, *50* (C5), C5-695.
- (6) Marchand, P.; Hassan, I. A.; Parkin, I. P.; Carmalt, C. J. Aerosol-Assisted Delivery of Precursors for Chemical Vapour Deposition: Expanding the Scope of CVD for Materials Fabrication. *Dalton Trans.* **2013**, *42* (26), 9406–9422.
- (7) Choy, K. L. Chemical Vapour Deposition of Coatings. *Prog. Mater. Sci.* **2003**, *48* (2), 57–170.
- (8) Vukasinovic, B.; Smith, M. K.; Glezer, A. Dynamics of a Sessile Drop in Forced Vibration. *J. Fluid Mech.* **2007**, *587* (2007), 395–423.
- (9) Hu, X.; Schuster, J. R.; Schulz, S. E.; Gessner, T. Surface Chemistry of Copper Metal and Copper Oxide Atomic Layer Deposition from copper(II) Acetylacetonate: A Combined First-Principles and Reactive Molecular Dynamics Study. *Phys. Chem. Chem. Phys. Phys. Chem. Chem. Phys* **2009**, *17* (17), 26892–26902.
- (10) Willis, A. L.; Chen, Z.; He, J.; Zhu, Y.; Turro, N. J.; O'Brien, S. Metal Acetylacetonates as General Precursors for the Synthesis of Early Transition Metal Oxide Nanomaterials. *J. Nanomater.* **2007**, 2007.
- (11) Ikenoue, T.; Sakamoto, S.; Inui, Y. Fabrication and Characteristics of P-Type Cu<sub>2</sub>O Thin Films by Ultrasonic Spray-Assisted Mist CVD Method. *Jpn. J. Appl. Phys.* **2014**, *53*, 4–7.
- (12) Wang, Y.; Miska, P.; Pilloud, D.; Horwat, D.; Mücklich, F.; Pierson, J. F. Transmittance Enhancement and Optical Band Gap Widening of Cu<sub>2</sub>O Thin Films after Air Annealing. *J. Appl. Phys.* **2014**, *115* (7), 2–7.

## Chapter II: Experimental procedure and characterization techniques

- (13) Lee, H. J.; Henry, C. H.; Orłowski, K. J.; Kazarinov, R. F.; Kometani, T. Y. Refractive-Index Dispersion of Phosphosilicate Glass, Thermal Oxide, and Silicon Nitride Films on Silicon. *Appl. Opt.* **1988**, *27* (19), 4104–4109.
- (14) Sebastian, T. M. and J. S. P. C. and S. R. and P. J. Potentiostatic Deposition and Characterization of Cu<sub>2</sub>O Thin Films. *Semicond. Sci. Technol.* **2002**, *17* (6), 565.
- (15) Henrie, J.; Kellis, S.; Schultz, S.; Hawkins, A. Electronic Color Charts for Dielectric Films on Silicon. *Opt. Express* **2004**, *12* (7), 1464–1469.
- (16) Goldstein, J.; Newbury, D. E.; Echlin, P.; Joy, D. C.; Romig Jr, A. D.; Lyman, C. E.; Fiori, C.; Lifshin, E. *Scanning Electron Microscopy and X-Ray Microanalysis: A Text for Biologists, Materials Scientists, and Geologists*; Springer Science & Business Media, 2012.
- (17) Scanning Electron Microscope  
<https://www.purdue.edu/ehps/rem/rs/sem.htm> (accessed Mar 1, 2017).
- (18) Williams, D. B.; Carter, C. B. The Transmission Electron Microscope. In *Transmission electron microscopy*; Springer, 1996; pp 3–17.
- (19) Binnig, G.; Quate, C. F.; Gerber, C. Atomic Force Microscope. *Phys. Rev. Lett.* **1986**, *56* (9), 930.
- (20) Helen Greenwood Hansma, P. Research on Biological Atomic Force Microscopy <http://web.physics.ucsb.edu/~hhansma/biomolecules.htm> (accessed Mar 1, 2017).
- (21) Marra, W. C.; Eisenberger, P.; Cho, A. Y. X-Ray Total-External-Reflection-Bragg Diffraction: A Structural Study of the GaAs-Al Interface. *J. Appl. Phys.* **1979**, *50* (11), 6927–6933.
- (22) KU Leuven. X-Ray Diffraction – Bruker D8 Discover <https://fys.kuleuven.be/iks/nvsf/experimental-facilities/x-ray-diffraction-2013-bruker-d8-discover> (accessed Mar 1, 2017).
- (23) Scherrer, P. Göttinger Nachrichten Math. *Phys* **1918**, *2*, 98–100.
- (24) Le Ru, E.; Etchegoin, P. *Principles of Surface-Enhanced Raman Spectroscopy: And Related Plasmonic Effects*; Elsevier, 2008.
- (25) Surf Group, V. U. B. Raman Spectroscopy <https://www.surfgroup.be/raman> (accessed Mar 1, 2017).
- (26) Baron, a. R. Photoluminescence Spectroscopy and Its Applications. *Phys. Methods Chem. Nano Sci.* **2012**, 295–305.

## Chapter II: Experimental procedure and characterization techniques

(27) Department of Chemistry, O. S. U. FTIR Spectroscopy Oregon State University. FTIR Spectroscopy. (accessed Mar 1, 2017).

(28) Chastain, J.; King, R. C.; Moulder, J. F. *Handbook of X-Ray Photoelectron Spectroscopy: A Reference Book of Standard Spectra for Identification and Interpretation of XPS Data*; Physical Electronics Eden Prairie, MN, 1995.

(29) Newville, M. Fundamentals of XAFS. *Rev. Mineral. Geochemistry* **2014**, 78 (1), 33–74.

(30) Rietveld, G.; Koijmans, C. V.; Henderson, L. C. A.; Hall, M. J.; Harmon, S.; Warnecke, P.; Schumacher, B. DC Conductivity Measurements in the Van Der Pauw Geometry. *IEEE Trans. Instrum. Meas.* **2003**, 52 (2), 449–453.

(31) W. Robert Thurber. The Hall Effect <https://www.nist.gov/pml/engineering-physics-division/hall-effect> (accessed Mar 1, 2017).

(32) Baert, B. Impact of Electron Trap States on the Transport Properties of GeSn Semiconducting Heterostructures Assessed by Electrical Characterizations. **2016**.

(33) Nguyen, N. D. Electrical Characterization of III-Nitride Heterostructures by Thermal Admittance Spectroscopy. Université de Liège, Belgium 2004.

# Chapter III: Cation-doped Cuprous Oxide thin films

3.1	Intrinsic Cu <sub>2</sub> O thin films .....	87
3.2	Cation doped Cu <sub>2</sub> O thin films: screening different elements.....	92
3.3	Tin doped Cu <sub>2</sub> O thin films .....	96
3.4	References .....	99

In order to improve the optical and electrical properties of Cu<sub>2</sub>O films as a p-type semiconductor, possible cations as dopant candidates were screened from a large group of atoms. This general study allows to narrow down the list of potential dopants and to identify the most promising elements to be used in a more in-depth experimental work.

As it is well known, the properties of a thin film are strongly dependent of the synthesis method, therefore, we established the “background line” by performing a study on the properties of Cu<sub>2</sub>O thin films deposited by AA-MOCVD and correspondent annealing process as the starting point of the study. Then, using a mixed solution of precursors, including the dopant source, the incorporation of the doping species into the copper oxide films was investigated. Here, we present in more detail the use of several cations as dopant which had an impact on the structural properties as well as on the electric response, with a special consideration to Tin as a dopant due to resistivity improvements. The study containing the incorporation of Mg is comprehensively reported in the next chapter (IV), fully devoted to this cation doping system.

## 3.1 Intrinsic Cu<sub>2</sub>O thin films

The deposition of intrinsic Cu<sub>2</sub>O by aerosol-assisted MOCVD was preliminarily studied in order to obtain the required crystallographic phase, homogeneity, thickness, electrical and optical properties. In this first study, the aerosol-assisted apparatus and the home-made reactor were assembled as described in configuration 1 in Chapter II. An

important optimization work on the deposition of undoped Cu<sub>2</sub>O deposition by Pulsed injection MOCVD (PIMOCVD) was developed previously by L. Bergerot<sup>1</sup>. The results of that study were used in this research as supporting information for the parameters variation in the system. Although the techniques differ substantially, as PI-MOCVD operated under vacuum and aerosol-assisted MOCVD is developed at atmospheric pressure; notably, they share a few common features such as the composition of the precursors used in solution, as well as their concentration and range of temperature during deposition. This comparison also provides interesting conclusions for the understanding of the influence of the oxygen partial pressure.

The main studied parameter was the substrate temperature during deposition. The lower temperature value was 300°C, motivated by the temperature at which the Cu(acac)<sub>2</sub> precursor decomposes, namely 284 °C. All other parameters, shown in Table III-4, were kept constants as based on the previous work on Cu<sub>2</sub>O and the AA-MOCVD expertise achieved in LMGP. The general impact of each parameters was discussed in Table 1 of Chapter II. In the films here presented, the total gas flow, extraction pressure and time were fixed at, 7 l.min<sup>-1</sup>, 4.5 mmH<sub>2</sub>O and 1 hour to obtain 100 nm thick films.

*Table III-4 Parameters fixed for the deposition of Cu<sub>2</sub>O*

<b>Parameter</b>	<b>Value</b>
Solvent	Butanol
Solution Concentration	0.02 mol.l <sup>-1</sup>
Frequency of vibration	800 kHz
Gas Flux	7 l.min <sup>-1</sup>
O <sub>2</sub> ratio	25%
Extraction pressure	4.5 mmH <sub>2</sub> O
Time	1h

Deposition temperature was increased from 300 °C to 375 °C by steps of 25°C. The appearance of the films observed directly after the deposition gives basic information related to the optical and structural properties. For the lowest temperatures, 300 °C, 325 °C and 350 °C, the films showed good homogeneity with a yellow color, as visible in Figure III-42 a). The deposition at 375 °C, however, led to the formation of loose powder on top of the substrate. The powder formation is expected at high temperature in this process due to the starting reaction in homogenous phase, rather than in the heterogeneous phase at the

substrate surface. Consequently, powder is formed before the arrival of the precursor at the substrate surface. It subsequently settles on the substrate without the required adhesion. The presence of loose powder is not adapted for the type of application that we are aiming for. The SEM micrograph of top view and cross-section corresponding to the film deposited at 350 °C are visible in Figure III-42 b) and c). The film presents a homogeneous surface, with no individual grains resolved at this magnification level; however, a small roughness is observed, probably due to a nano-crystalline film. The cross-section confirms the homogeneity of the film thickness, with an average thickness in the 100 nm range.

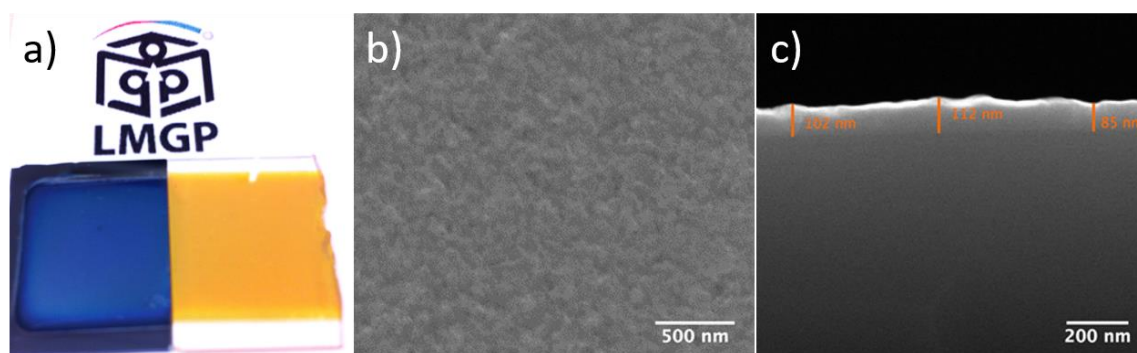


Figure III-42 Results obtained from a  $\text{Cu}_2\text{O}$  thin films deposited by AA-MOCVD using a butanol-based solution and  $\text{Cu}(\text{acac})_2$  as precursor. a) visual appearance on Si (left part) and glass (right part) substrate; b) and c) SEM image of top view and of cross-section, respectively, of film deposited at 350 °C;

The effect of deposition temperature on films properties were based mostly on XRD (Figure III-43 a)) and sheet resistance (Figure III-43 b)). From available crystallographic data (pdf number in appendix), it is established that the presence of  $\text{Cu}_2\text{O}$  is confirmed in all samples. Nevertheless, small shifts on the peak location compared to the theoretical ones are observed, which could be related to strain effect. The insert in Figure III-43 a) represents the crystallite size of the three deposited films, resulting in a size of 50 nm in the 350 °C deposition. The electric properties are significantly influenced by the temperature of deposition, both on absolute value and on homogeneity throughout the sample. With the increase of temperature from 300 °C to 350 °C, sheet resistance decreases from an average value of 60  $\text{M}\Omega/\text{sq}$  to 39  $\text{M}\Omega/\text{sq}$ , which translates to a resistivity decrease from around 600  $\Omega\cdot\text{cm}$  to 390  $\Omega\cdot\text{cm}$  for a 100 nm thick layer. The decrease of resistivity with the temperature is related to a higher crystallization, visible in the inset of Figure III-43 d). The crystallite size in these films increase up to 50nm with a temperature of deposition of 350°C. Additional improvements of resistivity can be related to the increase of oxygen content in non-stoichiometric film. Additionally, the dispersion in the measure decreases as indicated

by the standard deviation out of 5 measurements, which decreases from 15 M $\Omega$ /sq to 1 M $\Omega$ /sq, denoting a more homogeneous resistivity over the film. This result lead us to fix from here now the deposition temperature at 350 °C.

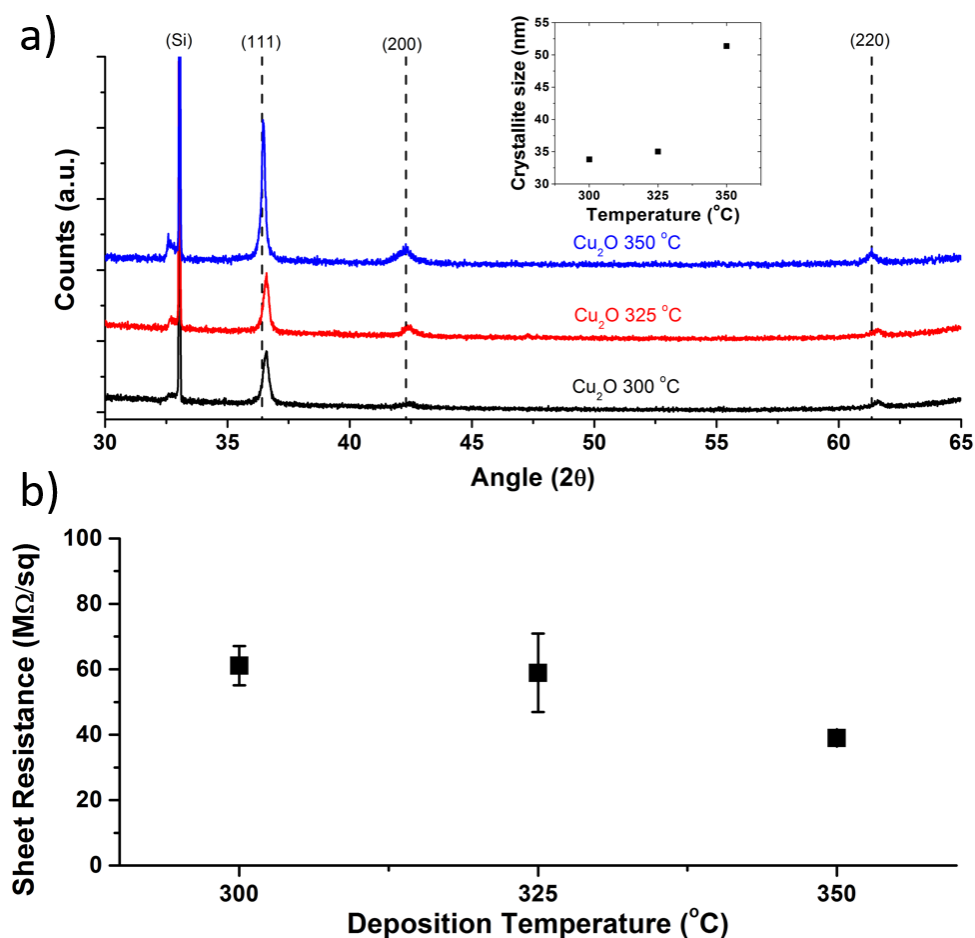


Figure III-43  $\text{Cu}_2\text{O}$  thin films deposited by AA-MOCVD: a) XRD spectra on Si substrate with the crystallite size dependence with temperature and b) sheet resistance of films with different temperatures of deposition on glass substrate. Reference spectrum of  $\text{Cu}_2\text{O}$ : JCPDS n° 04-007-9767 presented in Appendix B

The investigation will therefore aim at optimizing the  $\text{Cu}_2\text{O}$  with other parameters. It was also observed from this study that most of the effect on the optical properties is due to the variation of the film thickness.

In order to reduce furthermore the sheet resistance of intrinsic  $\text{Cu}_2\text{O}$  films, post-deposition annealing treatments under air were studied. The duration of the post-deposition anneal was 1 hour, which is in the same range of time as other previous studies <sup>2,3</sup>. The temperature varied from 225 °C to 300 °C. The use of pure oxygen instead of air was also tested. However, no significant difference was observed in the oxygen case when compared to air annealing treatments. The treatment at 225 °C and 250 °C reduced the sheet resistance

from 40 M $\Omega$ /sq up to 20 M $\Omega$ /sq (resistivity of 200  $\Omega$ .cm) without compromising the optical characteristics of the film. The corresponding transmittance is represented in Figure III-44 a) and b) and amounts to about 50% in the visible part of the spectrum, the value of band gap for these two annealed samples, as determined by was 2.2 eV, consistent with the literature work in spray-pyrolysis deposited films <sup>4</sup>.

The use of a higher temperature for the annealing treatment induces the formation of the CuO phase at 300 °C, as detected by Raman , using the 488 nm wavelength or blue laser, with the observation of the A<sub>g</sub> mode at 290 cm<sup>-1</sup> <sup>5</sup> (Figure III-44 c)). The formation of this parasitic phase leads to a reduction of the average transmittance in the visible range (390-700nm), as shown in Figure III-44 a), due to the lower band-gap of CuO of 1.2eV. Nevertheless, the sheet resistance decreased compared to the as-deposited film. Further considerations about the annealing process will be developed in Chapter IV for the case of doped materials

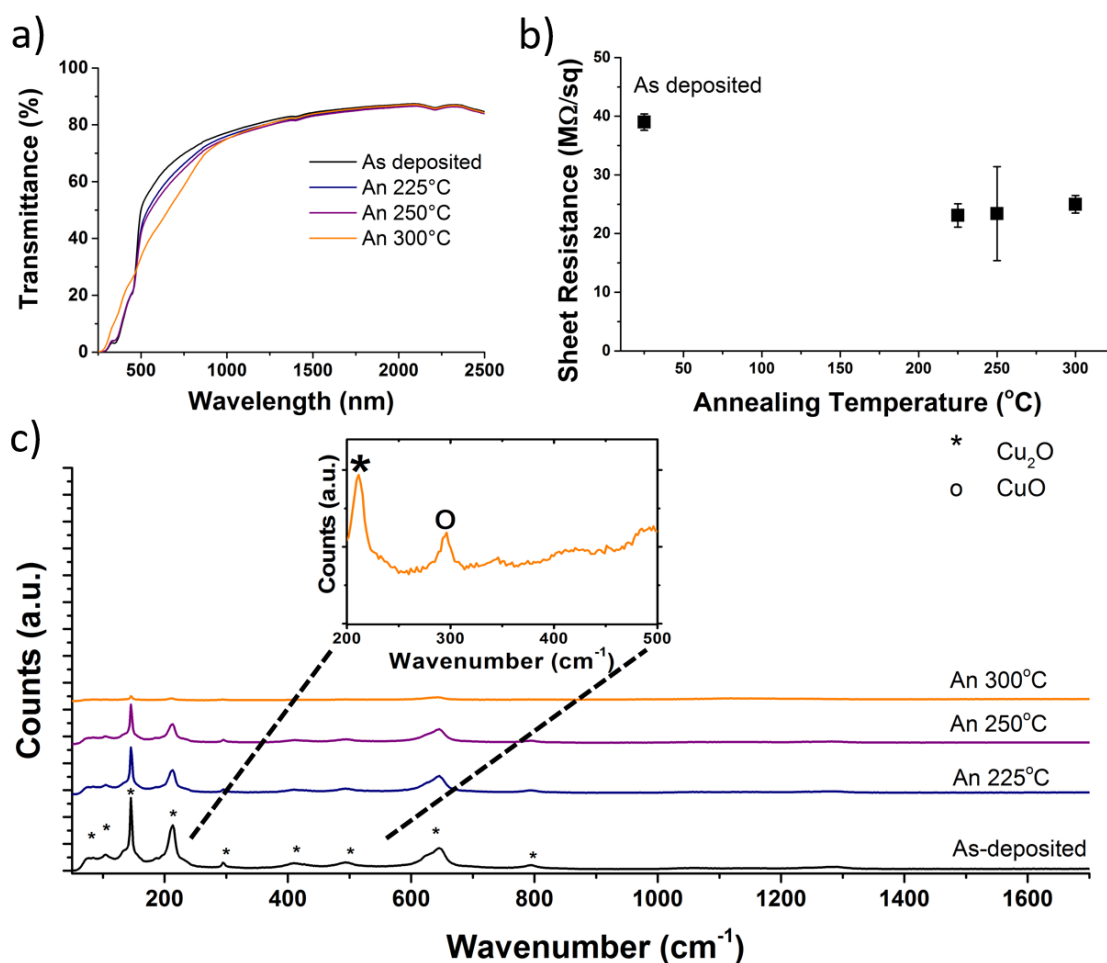


Figure III-44 Effect of annealing treatment on intrinsic Cu<sub>2</sub>O thin films a) Raman spectra for the film annealed at 300 °C, inset shows a zoom of the 200 – 500 cm<sup>-1</sup> region; b) Optical direct transmittance of films and c) Sheet resistance dependence with temperature of annealing.

From these preliminary results we can infer that for the optimized films of pure Cu<sub>2</sub>O, with a thickness of 100 nm, the lowest value of sheet resistance is around 20 MΩ/sq, corresponding to a resistivity value of 200 Ω.cm and a transparency of 50% in the visible electromagnetic spectrum.

### 3.2 Cation doped Cu<sub>2</sub>O thin films: screening different elements

In the perspective of improving the optical and electrical properties of Cu<sub>2</sub>O films, the incorporation of different cations as potential dopants was systematically studied. The elements used in these trials were chosen based on different characteristics, mainly theoretical predictions from Nolan<sup>6</sup>, atomic radius of the cation, compatibility of the required precursor with AA-MOCVD. Therefore, we present in Table III-5, the list of cations tested, with the respective atomic radius and precursor used.

*Table III-5 List of elements tested with respective radius, coordination number precursor used and its molar mass from Sigma Aldrich supplier<sup>6,7</sup>. The elements with smaller radius than Cu<sup>+</sup> 4-fold coordinated are represented in green while the ones with larger radius are represented in blue.*

Cation	Atomic Number	Radius (pm)	Precursor and molecular mass
Li <sup>+</sup>	3	73(IV)	Li(acac) M= 106.05 g.mol <sup>-1</sup>
Mg <sup>2+</sup>	12	71(IV)	Mg(acac) <sub>2</sub> M= 258.55g.mol <sup>-1</sup>
Ca <sup>2+</sup>	20	100(IV)	Ca(acac) <sub>2</sub> M= 257.15g.mol <sup>-1</sup>
Co <sup>2+</sup>	27	72(IV)	Co(acac) <sub>2</sub> M= 356.26g.mol <sup>-1</sup>
Ni <sup>2+</sup>	28	69(IV)	Ni(acac) <sub>2</sub> M= 256.91 g.mol <sup>-1</sup>
Cu <sup>+</sup>	29	60 (II) 74(IV)	Cu(acac) <sub>2</sub> M=261.76 g.mol <sup>-1</sup>
Zn <sup>2+</sup>	30	74(IV)	Zn(acac) <sub>2</sub> M= 263.61g.mol <sup>-1</sup>
Sr <sup>2+</sup>	38	132 (IV)	Sr(acac) <sub>2</sub> M= 285.84 g.mol <sup>-1</sup>
Cd <sup>2+</sup>	48	95	Cd(acac) <sub>2</sub> M= 310.63 g.mol <sup>-1</sup>
Sn <sup>2+</sup> /Sn <sup>4+</sup>	50	132(VI)/69(IV)	Dibutyltin diacetate M= 351.03 g.mol <sup>-1</sup>
Ba <sup>2+</sup>	56	149(VI)	Ba(TMHD) <sub>3</sub> M= 503.86 g.mol <sup>-1</sup>
La <sup>3+</sup>	57	177(VI)	La(TMHD) <sub>3</sub> M= 688.71g.mol <sup>-1</sup>
Er <sup>3+</sup>	68	103(VI)	Er(TMHD) <sub>3</sub> M= 717.06 g.mol <sup>-1</sup>

The deposition were conducted using a 10% of the dopants precursor molar concentration in relation to the total concentration of precursor in solution. The rest of deposition parameters were maintained constant as previously described in Table III-4,

with the deposition temperature fixed at 350°C. The films were also annealed at 250 °C for 1 hour under air.

The preliminary characterization of these films was based on EDS analysis, to detect the presence of the dopant, and on sheet resistance measurements, to confirm the functional enhancement of the film resistivity. Figure III-45 shows the plot of dopant amount in the film in relation to total cations ( $\frac{X}{X+Cu}$ ), as well as the sheet resistance values, after annealing. The thickness of the films presented similar values, all around 100nm.

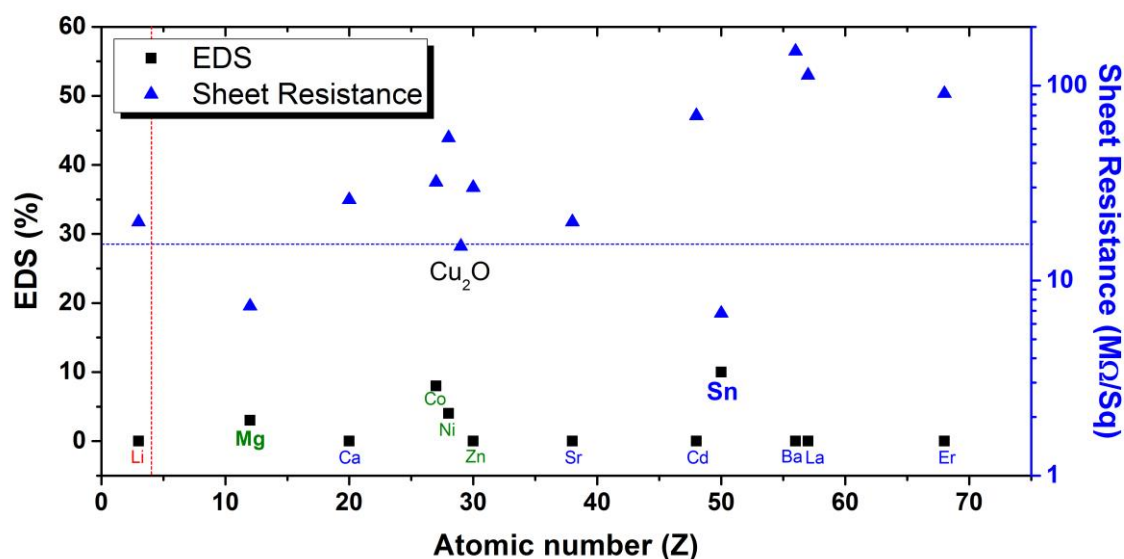


Figure III-45 Atomic concentration of dopant atoms in films (left) and sheet resistance (right) in relation to the dopant atomic number for each tested element. Dashed blue line represents the optimal sheet resistance value of intrinsic  $Cu_2O$  thin film. Dashed red line represents the limit of detection by EDS. Green and blue dopants represent smaller or bigger radius, respectively.

Among the total group of cations, only Mg, Co, Ni and Sn were detected by EDS analysis. However, it is important to state that the Li cation detection is under the limit of EDS due to the low atomic weight. Nevertheless, no significant differences in sheet resistance were observed with the use of Li.

From the point of view of electrical properties, the presence of Mg and Sn lowered the sheet resistivity to values below 10  $M\Omega/sq$ , which present significant improvements comparing to 20 $M\Omega/sq$  of intrinsic  $Cu_2O$ . In terms of optical appearance and transmittance, no significant changes were visible in the transparency with the dopants used at 10% of concentration. Therefore, we continue the study focusing on Sn and Mg-doped systems, since both of these dopants show improvements of the electric transport properties; they were detected by EDS in a relevant amount and their radius were similar to  $Cu^+$  cation.

Nonetheless, the deposition of  $\text{Cu}_2\text{O}$  with cations had an effect on the microstructure morphology even in the case of cations not detected or weakly detected by EDS. In Figure III-46, the surfaces of the films deposited in the presence of precursors doping with Li, Ca, Co, Ni, Zn, Sr and Mg, as well as intrinsic  $\text{Cu}_2\text{O}$  for comparison are represented. Here are the main observations.

- Even when no detection by EDS could be achieved, Li precursor creates a film with a granular shaped surface and visible porosity between some grains.
- The presence of  $\text{Ca}(\text{acac})_2$  during the  $\text{Cu}_2\text{O}$  deposition seems to increase the porosity of the film; however, these features have been also observed in some intrinsic  $\text{Cu}_2\text{O}$  films.
- Both Co and Ni were detected by EDS however with different effects on the microstructure. While Ni seems to create a rough surface similar to the intrinsic film, the Co presence forms flower-like structures on the top of the surface. These structures seem to be Co-rich by EDS analysis, and generally dispersed throughout the whole film.
- The presence of Zn leads to an observable granular structure, with small grains better revealed when compared to the  $\text{Cu}_2\text{O}$  films.
- At last, Sr incorporation yields a strongly rougher surface with grain clusters visible, which are similar to the previous work by PI-MOCVD<sup>1</sup> and also to the films doped with Mg, represented as well in Figure III-46. However, the presence of Sr could not be detected by EDS analysis, even if the experiment was reproduced several times with different concentrations of the precursor solution.

Further analysis of the  $\text{Cu}_2\text{O}$  growth with the presence of these elements could be relevant to understand the origin of these morphological changes. The effect on the microstructure could be attributed to different growth mechanisms, not explored in this work.

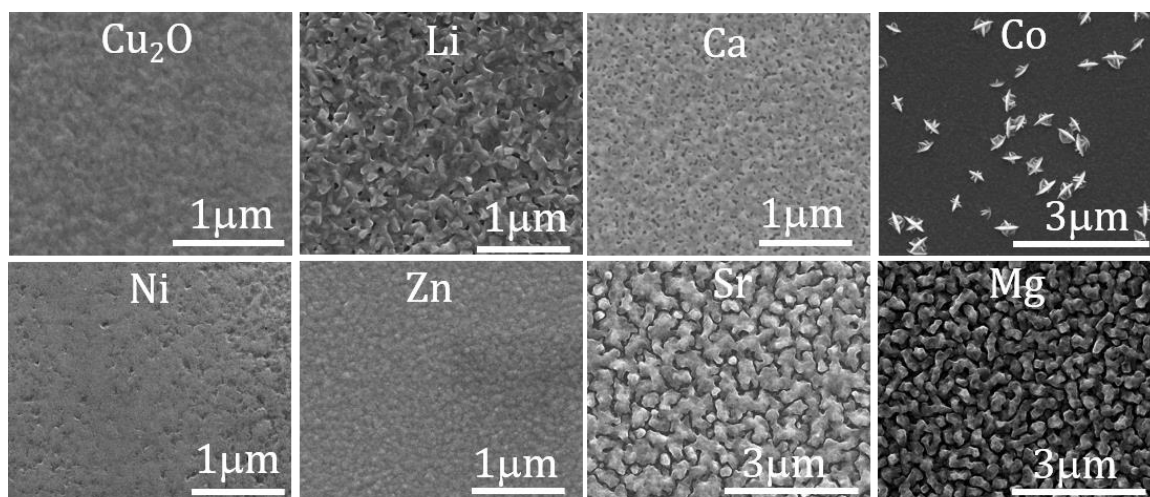


Figure III-46 SEM microstructure images of  $\text{Cu}_2\text{O}$  films: intrinsic and deposited with precursors containing Li, Ca, Co, Ni, Zn, Sr and Mg.

Only the  $\text{Cu}_2\text{O}$  phase could be detected from XRD measurements in Bragg-Brentano configuration in any case, as shown in the Figure III-47 XRD spectra of  $\text{Cu}_2\text{O}$  films: intrinsic and deposited with precursors containing Li, Ca, Co, Ni, Zn, Sr. Figure III-47. The spectra show peaks corresponding to the crystal planes (111), (200) and (220) reference pdf with small shifts in relation to the reference position.

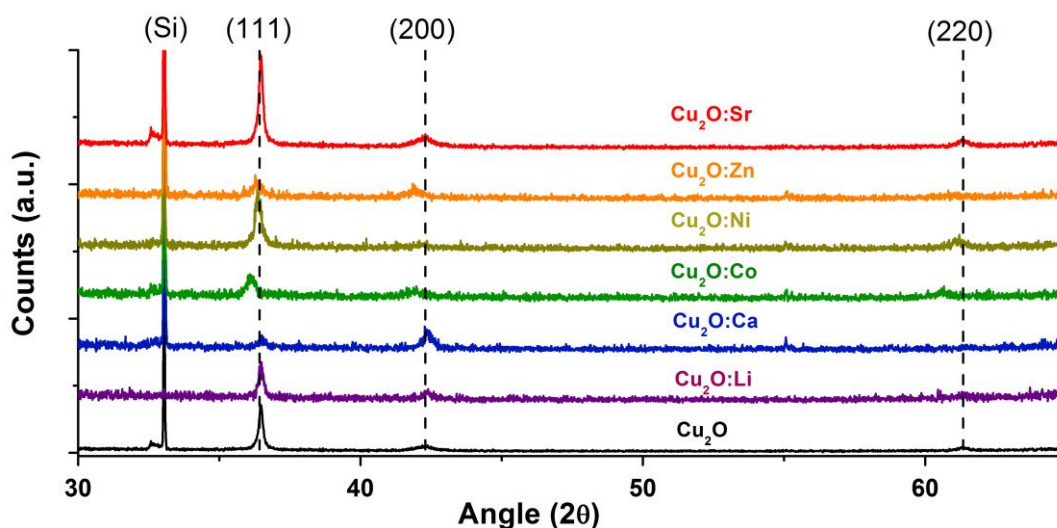


Figure III-47 XRD spectra of  $\text{Cu}_2\text{O}$  films: intrinsic and deposited with precursors containing Li, Ca, Co, Ni, Zn, Sr. Reference spectrum of  $\text{Cu}_2\text{O}$ : JCPDS n° 04-007-97679767 presented in Appendix B

From these results, tin and magnesium were selected as doping elements. In the next section we present the characterization of  $\text{Cu}_2\text{O}$  films co-deposited with tin. The

combination of Sn with Cu<sub>2</sub>O was not found in the literature, which additionally contributed for its interest. The study on magnesium doped Cu<sub>2</sub>O films is carried out in Chapter IV. A recent study from 2016, Kardarian *et al.*<sup>8</sup>, presented the incorporation of Mg into Cu<sub>2</sub>O and their application to solar cells. However, a comprehensive study of the films' properties with the dopant concentration was missing, providing a motivation for a systematic work reported in the next chapter (IV).

### 3.3 Tin doped Cu<sub>2</sub>O thin films

Tin oxide presents different oxidation states with different semiconductor behaviours: SnO<sub>2</sub>, a well-known n-type semiconductor oxide, and SnO that behaves as a p-type semiconductor, with resistivity values close to 1 Ω.cm<sup>9</sup>. The formation of each phase is dependent on the oxygen partial pressure during deposition or annealing treatments<sup>10</sup>, where the transformation from SnO to SnO<sub>2</sub> common under oxidizing atmosphere<sup>11</sup>.

The improvements in sheet resistance with the Sn incorporation lead us to yield some focus on this cation as a dopant for Cu<sub>2</sub>O. To incorporate the dopant in the films, we added Di-n-butyltin diacetate to the precursor solution in different concentrations, 0.002, 0.01 and 0.02 mol.l<sup>-1</sup>, which corresponds to a Sn/(Cu+Sn) atomic ratio in the solution of 9%, 33% and 50%, respectively. The other deposition parameters were maintained as presented in Table III-4, as in the previous depositions.

The increase in concentration from 9% to 33% of Sn precursor in solution induced a large impact in the optical appearance, as noticeable in Figure III-48a) and b), leading to a large transparency as shown in Figure III-48 c), and consequently an increase of band-gap to form 2.2 to 2.8 eV. In this case, we assume that an increase in tin content could lead to the formation of SnO or SnO<sub>2</sub>. Therefore, we have to discard the possibility of creating a mixed amorphous phase between the two oxides. However this film showed a larger sheet resistance, larger than 100 MΩ/sq, which limited the Hall Effect measurements and the determination of the semiconductor type.

In order to determine whether we could combine high transparency with lower resistivity, we increased the Sn content furthermore, until both cations had the same concentration in solution. This led to a large increase of transparency as shown in Figure III-48 c), with a band-gap of 3.0 eV and at the same time a drastic reduction of the sheet resistance to values below KΩ/sq as shown in and Figure III-49 a). In terms of cation incorporation, the Sn-doped Cu<sub>2</sub>O films presented a similar Sn atomic concentration of

cations, Sn/Sn+Cu, as the cationic ratio of the prepared solution as shown in Figure III-49b), where measurements were performed by WDS.

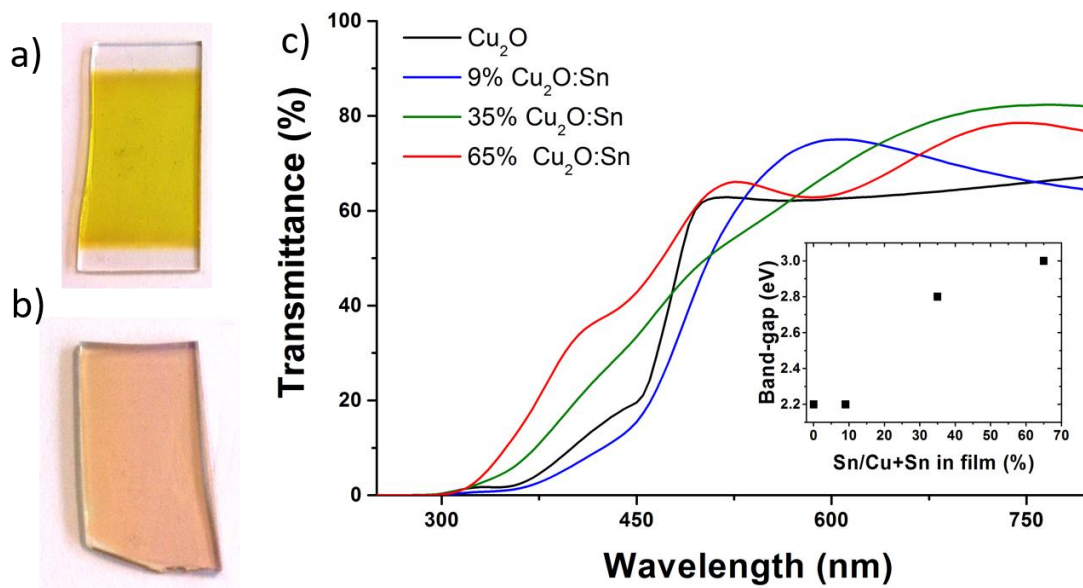


Figure III-48 Visual appearance  $\text{Cu}_2\text{O}$  thin films a) intrinsic  $\text{Cu}_2\text{O}$  and b)  $\text{Cu}_2\text{O}:\text{Sn}$ ; c) Optical Transmittance of  $\text{Cu}_2\text{O}$  thin films doped with Sn with variation of band-gap.

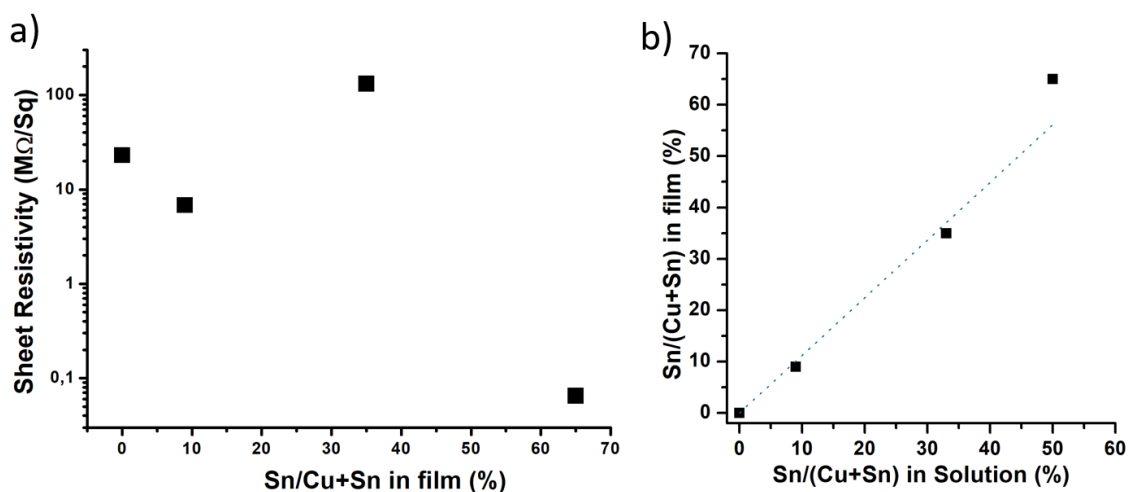


Figure III-49 a) Sheet resistance and b) EDS quantification of Sn doped  $\text{Cu}_2\text{O}$  thin films

Nevertheless, the high quantity of Sn in the 65% sample lead to the formation of  $\text{SnO}_2$  phase. This was confirmed by the detection of  $\text{SnO}_2$  peaks of in XRD, visible in Figure III-50 a) and the disappearance of all  $\text{Cu}_2\text{O}$  active modes in Raman, Figure III-50 b), where only carbon induced modes are present.

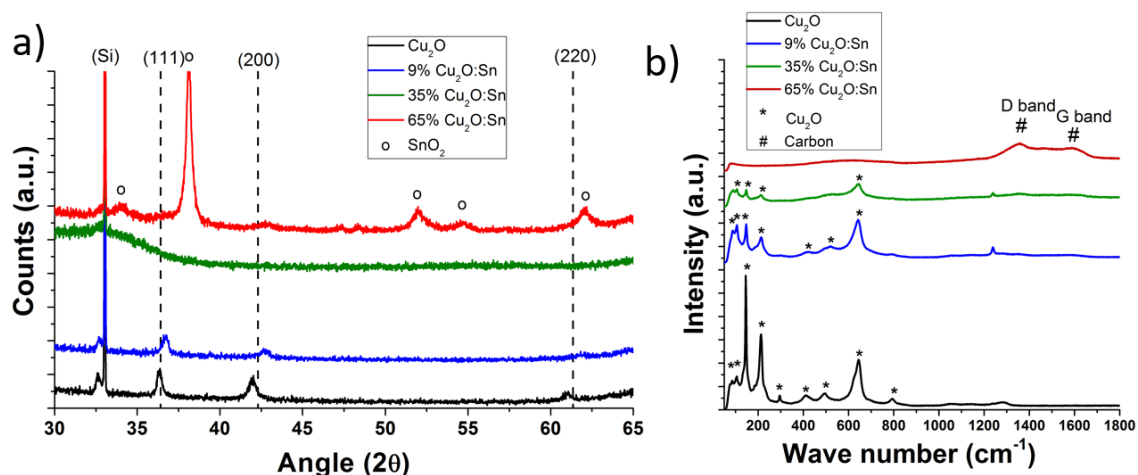


Figure III-50 a) XRD and b) Raman quantification of Sn doped  $\text{Cu}_2\text{O}$  thin films Reference spectrum of  $\text{Cu}_2\text{O}$ : JCPDS n° 04-007-9767 presented in Appendix B

In terms of microstructure view by SEM and represented in Figure III-51 c), the 50%  $\text{Cu}_2\text{O}:\text{Sn}$  shows a granular structure surrounded by a glassy matrix that can be attributed to the  $\text{SnO}_2$  phase. The thickness also increases drastically, reaching the 300 nm range, Figure III-51 d).

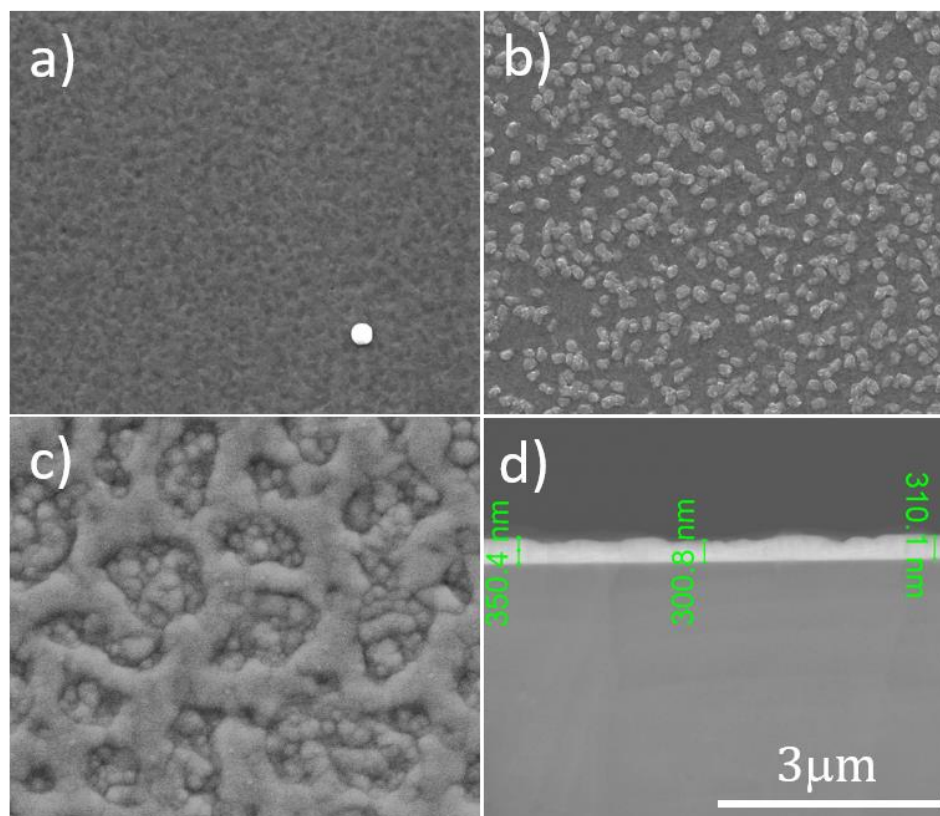


Figure III-51 SEM images of Sn doped  $\text{Cu}_2\text{O}$  thin films: a) 10%  $\text{Cu}_2\text{O}:\text{Sn}$ ; b) 33%  $\text{Cu}_2\text{O}:\text{Sn}$ ; c) and d) 50%  $\text{Cu}_2\text{O}:\text{Sn}$  top-view and cross-section respectively

The presence of SnO<sub>2</sub>, a well-known n-type semiconductor oxide<sup>12</sup>, lead to lower resistivity, however with a change of charge sign confirmed by Hall Effect. In this sample, the resistivity values were around 0.24 Ω.cm, and the respectively mobility and free-electrons density was 1.6 cm<sup>2</sup>.V<sup>-1</sup>.s<sup>-1</sup> and 1.7 x 10<sup>19</sup> cm<sup>-3</sup>.

As brief conclusions of this dopant, Tin was selected as a promising candidate to improve the optical and electrical properties of Cu<sub>2</sub>O, however, low mobility and formation of n-type SnO<sub>2</sub> phase were detrimental for the applicability as a p-type transparent semiconductor. In a future work, the analysis of this system using lower content of Sn can provide an additional route for the enhancement of Cu<sub>2</sub>O thin films.

### 3.4 References

(1) Bergerot, L. Etude de L'élaboration D'oxyde Transparent Conducteur de Type-P En Couches Minces Pour Des Applications À L'électronique Transparente Ou Au Photovoltaïque. Université Grenoble Alpes 2015.

(2) Figueiredo, V.; Elangovan, E.; Gonçalves, G.; Barquinha, P.; Pereira, L.; Franco, N.; Alves, E.; Martins, R.; Fortunato, E. Effect of Post-Annealing on the Properties of Copper Oxide Thin Films Obtained from the Oxidation of Evaporated Metallic Copper. *Appl. Surf. Sci.* **2008**, *254* (13), 3949–3954.

(3) Wang, Y.; Miska, P.; Pilloud, D.; Horwat, D.; Mücklich, F.; Pierson, J. F. Transmittance Enhancement and Optical Band Gap Widening of Cu<sub>2</sub>O Thin Films after Air Annealing. *J. Appl. Phys.* **2014**, *115* (7), 2–7.

(4) Ikenoue, T.; Sakamoto, S.; Inui, Y. Fabrication and Characteristics of P-Type Cu<sub>2</sub>O Thin Films by Ultrasonic Spray-Assisted Mist CVD Method. *Jpn. J. Appl. Phys.* **2014**, *53*, 4–7.

(5) H. F. Goldstein, Dai-sik Kim, Peter Y. Yu, and L. C. B. Raman Study of CuO Single Crystals. *Phys. Rev. B* **1990**, *41* (10).

(6) Nolan, M.; Elliott, S. D. Tuning the Transparency of Cu<sub>2</sub>O with Substitutional Cation Doping. *Chem. Mater.* **2008**, *20* (17), 5522–5531.

(7) Shannon, R. D. Revised Effective Ionic Radii and Systematic Studies of Interatomic Distances in Halides and Chalcogenides. *Acta Crystallogr. Sect. A* **1976**, *32* (5), 751–767.

(8) Kardarian, K.; Nunes, D.; Maria Sberna, P.; Ginsburg, A.; Keller, D. A.; Vaz Pinto, J.; Deuermeier, J.; Anderson, A. Y.; Zaban, A.; Martins, R.; Fortunato, E. Effect

of Mg Doping on Cu<sub>2</sub>O Thin Films and Their Behavior on the TiO<sub>2</sub>/Cu<sub>2</sub>O Heterojunction Solar Cells. *Sol. Energy Mater. Sol. Cells* **2016**, *147*, 27–36.

(9) Nguyen, N. D. Electrical Characterization of III-Nitride Heterostructures by Thermal Admittance Spectroscopy. Université de Liège, Belgium 2004.

(10) Liang, L. Y.; Liu, Z. M.; Cao, H. T.; Yu, Z.; Shi, Y. Y.; Chen, A. H.; Zhang, H. Z.; Fang, Y. Q.; Sun, X. L. Phase and Optical Characterizations of Annealed SnO Thin Films and Their P-Type TFT Application. *J. Electrochem. Soc.* **2010**, *157* (6), H598–H602.

(11) Nose, K.; Suzuki, A. Y.; Oda, N.; Kamiko, M.; Mitsuda, Y. Oxidation of SnO to SnO<sub>2</sub> Thin Films in Boiling Water at Atmospheric Pressure. *Appl. Phys. Lett.* **2014**, *104* (9), 4–8.

(12) Isono, T.; Fukuda, T.; Nakagawa, K.; Usui, R.; Satoh, R.; Morinaga, E.; Mihara, Y. Highly Conductive SnO<sub>2</sub> Thin Films for Flat-Panel Displays. *J. Soc. Inf. Disp.* **2007**, *15* (2), 161–166.

# Chapter IV: Magnesium-doped cuprous oxide thin films

4.1	Magnesium-doped cuprous oxide (Cu <sub>2</sub> O:Mg) thin films.....	103
4.1.1	Introduction .....	103
4.1.2	Deposition of Cu <sub>2</sub> O:Mg thin layers by AA-MOCVD.....	104
4.1.3	Structural characterization.....	104
4.1.4	Optic and electric characterization.....	112
4.1.5	Summary .....	116
4.2	Stability of Magnesium-doped cuprous oxide (Cu <sub>2</sub> O:Mg) thin films under thermal treatments.....	118
4.2.1	Introduction .....	118
4.2.2	Experimental .....	119
4.2.3	Structural characterization.....	119
4.2.4	Electric characterization under temperature.....	131
4.2.5	Discussion .....	137
4.3	Cu <sub>2</sub> O:Mg/ZnO heterojunctions .....	139
4.3.1	Introduction .....	139
4.3.2	Simulation of a pn junction formed by Cu <sub>2</sub> O/ZnO .....	140
4.3.3	Deposition of pn junction formed by Cu <sub>2</sub> O/ZnO.....	144
4.3.4	Summary .....	157
4.4	Conclusions .....	157
4.5	References .....	158

## Chapter IV: Magnesium-doped cuprous oxide thin films

Magnesium has been highlighted in the frame of the elements' screening as a promising dopant for Cu<sub>2</sub>O from the first electrical resistivity results in Chapter III. The following chapter is focused on an in-depth study of the deposition and characterization of magnesium-doped cuprous oxide (Cu<sub>2</sub>O:Mg) thin films. The first part of the chapter describes in detail the effect of magnesium on cuprous oxide by varying the concentration of the dopant. The main content of this study was published as a peer-review article: Resende, J., Jiménez, C., Nguyen, N. D. and Deschanvres, J.-L. (2016), "Magnesium-doped cuprous oxide (Cu<sub>2</sub>O:Mg) thin films as a transparent p-type semiconductor" Phys. Status Solidi A, 213: 2296–2302. Additionally, it is important to report on the work about strontium-doped cuprous oxide and the comparison to the magnesium case developed in this chapter, which finally led to another publication: Brochen, S., Bergerot, L., Favre, W., Resende, J., Jiménez, C., Deschanvres, J. L., & Consonni, V. (2016). "Effect of Strontium Incorporation on the p-Type Conductivity of Cu<sub>2</sub>O Thin Films Deposited by Metal–Organic Chemical Vapor Deposition". Journal of Physical Chemistry C, 120(31), 17261-17267. On the second part of the chapter, we focus on the study of the stability of the magnesium-doped cuprous oxide thin films under different oxidizing thermal treatments.

In the last third section of this chapter, we study the feasibility and the performance of an oxide-based *pn* junction integrating Mg-doped Cu<sub>2</sub>O films. For the purpose of that investigation, the selected n-type semiconductor is ZnO, which is stacked in combination with intrinsic and Mg-doped Cu<sub>2</sub>O thin films. The *pn* junction study is divided in two different parts: numerical simulations and device measurements of experimentally deposited films. The ZnO oxide thin films were obtained by chemical methods in collaboration with two other PhD students from LMGP: Thomas Cossuet for the PI-MOCVD and Viet Nguyen in the SALD case. Some results of this study led to a peer-reviewed publication: Nguyen, V. H., Resende, J., Jiménez, C., Deschanvres, J.-L., Carroy, P., Muñoz, D., Bellet, D. and Muñoz-Rojas, D. (2017) "Deposition of ZnO based thin films by atmospheric pressure spatial atomic layer deposition for application in solar cells." Journal of Renewable and Sustainable Energy 9, no. 2: 021203.

## 4.1 Magnesium-doped cuprous oxide (Cu<sub>2</sub>O:Mg) thin films

### 4.1.1 Introduction

As previously discussed in Chapter I and III, cuprous oxide (Cu<sub>2</sub>O) presents promising electrical and versatile processing features that establish it as a highly researched p-type transparent semiconductor. However, its high absorbance in the visible range reduces the application in practical devices. In 2008, based on first-principle calculations, Nolan *et al.*<sup>1</sup> suggested the doping of cuprous oxide with cations larger than Cu<sup>+</sup> in order to increase the band gap, while maintaining the cubic structure. These cations, such as Mg<sup>2+</sup>, Sn<sup>2+</sup>, Sr<sup>2+</sup> or Ca<sup>2+</sup> would distort the crystallographic lattice and diminish the three-dimensional Cu-Cu interactions. As a consequence, the Cu 3d and 4s partial electronic density of states would be changed which could ultimately led to a band gap increase, depending on the cation used. The p-type conductivity would simultaneously be enhanced, due to the creation of a double copper vacancy. Since the dopants are divalent cations, one primary copper vacancy compensates the dopant presence, while a secondary copper vacancy supplies an extra hole<sup>1</sup>. Additionally, the use of “electronically inert” dopants would avoid the hybridization of the valence band and conduction band edge states or the introduction of in-gap states<sup>1</sup>. Both optical and electrical consequences of Nolan’s hypothesis would suggest improvements on the Cu<sub>2</sub>O application into devices.

In a previous work, the incorporation of strontium (Sr) had already been achieved, showing improvements in the resistivity of the films, up to 1 Ω.cm; but without any change in the optical gap energy of the material<sup>2</sup>. The lower resistivity of Cu<sub>2</sub>O:Sr was associated to an increase of simple copper vacancies (V<sub>Cu</sub>)<sup>-</sup>, attributed to a decrease of its formation energy with strontium presence<sup>2,3</sup>. Moreover, the incorporation of strontium also leads to the emergence of a coexisting shallow acceptor level, which is tentatively assigned to large size impurity–vacancy complexes<sup>3</sup>.

In this study, we deposited magnesium-doped cuprous oxide (Cu<sub>2</sub>O:Mg) thin films by aerosol-assisted metal-organic chemical vapour deposition (AA-MOCVD). The choice of magnesium as dopant was motivated by theoretical predictions on the band gap changes<sup>1</sup>, the ionic radius and the set of deposition conditions which is comparable to that of Cu<sub>2</sub>O<sup>4</sup>. As discussed extensively in Chapter II, AA-MOCVD is a well-established deposition technique for copper-based oxides, using cheap and efficient metal organic precursors and allowing the growth at atmospheric pressure, avoiding high vacuum.

#### 4.1.2 Deposition of $\text{Cu}_2\text{O}:\text{Mg}$ thin layers by AA-MOCVD

We used a butanol-based solution for the deposition of Mg doped  $\text{Cu}_2\text{O}$  thin films by AA-MOCVD. The copper precursor was copper acetylacetonate ( $\text{Cu}(\text{acac})_2$ ), and the molar concentration was fixed at  $0.02 \text{ mol.l}^{-1}$  all along this study on magnesium doping. To incorporate magnesium in the films, we added magnesium acetylacetonate,  $\text{Mg}(\text{acac})_2$ , in different molar concentrations: 0.001, 0.002, 0.004 and  $0.013 \text{ mol.l}^{-1}$ , corresponding to  $\text{Mg}/(\text{Mg}+\text{Cu})$  atomic ratio of 0%, 5%, 9%, 17% and 40%, respectively. All the other parameters were maintained as described in the Chapter III, where  $\text{Cu}_2\text{O}$  thin deposition was optimized.

The deposition was performed at  $350^\circ\text{C}$  in a homemade cold-wall chemical vapour deposition chamber on substrates of alkaline earth boroaluminosilicate glass (Corning 1737) or p-type single crystal silicon wafer (001) oriented. Argon was used as carrier gas, with a flow of  $6 \text{ l.min}^{-1}$ , while  $\text{O}_2$  was used as reaction gas, with a flow of  $2.5 \text{ l.min}^{-1}$ . These flow-rate values allowed us to maintain a solution consumption rate of  $2 \text{ ml.min}^{-1}$ . The deposition lasted for 60 minutes, resulting in a consumption of 120 ml. After the deposition, the films were annealed at  $250^\circ\text{C}$  under air for 1 hours to improve physical properties. These conditions were previously optimized on intrinsic cuprous oxide (Chapter III), in order to obtain monophasic films with no change in colour.

##### 1.4.1 Structural characterization

As a primarily qualitative analysis of the samples, the optical appearance of an Mg-doped  $\text{Cu}_2\text{O}$  film (5% in solution) is shown in Figure IV-52. On glass, the coating presents a yellow colour, transparent and homogenous throughout the whole sample (area of  $4 \text{ cm}^2$ ), while on silicon the colour depends on the film thickness. In the case of the sample shown in Figure IV-52, the thickness was 77 nm and the surface appears mostly dark blue. In both cases, the films adhere to the substrate, resist to water and Scotch-Tape tests. Similar appearance is visible in all  $\text{Cu}_2\text{O}:\text{Mg}$  films.

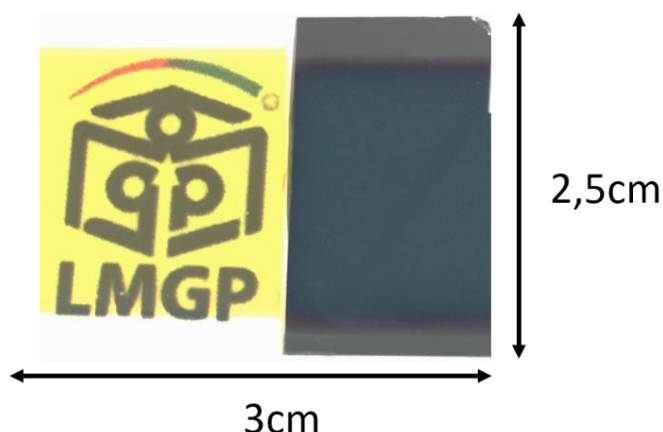


Figure IV-52 Photographs of the Mg doped  $\text{Cu}_2\text{O}$  thin film on glass (left) and silicon (right) with a thickness of 77nm using a solution prepared with 5% atom of Mg.

In order to estimate the magnesium incorporation, EDS measurements were performed on the films deposited on glass with an acceleration voltage of 5 kV; results are represented in Figure IV-53. Higher voltage were previously used to validate the purity of the samples. Al and Si detected in the spectra originate from the borosilicate substrate, together with Cu, Mg, O and C. As the magnesium content increases in solution, the magnesium peak at 1.254eV also intensifies in the EDS spectrum from the thin film

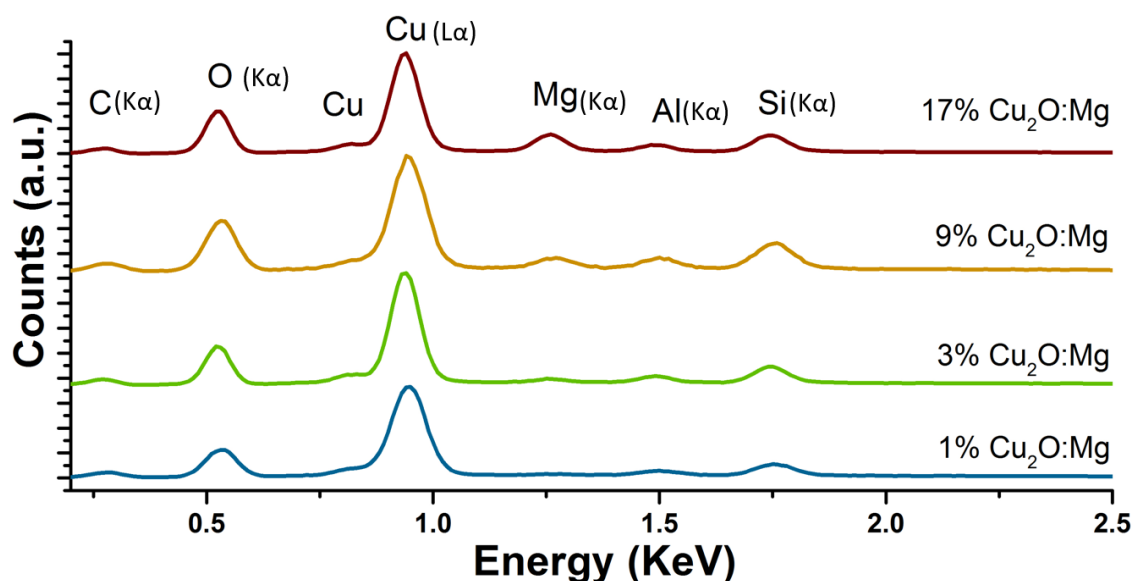


Figure IV-53 EDS spectra obtained at an acceleration voltage of 5 keV of  $\text{Cu}_2\text{O}:\text{Mg}$  thin films on glass. The Mg ratio indicated was quantified by EDS analysis (Table IV-6). The different elements X-Ray emission lines are also indicated.

The magnesium incorporation in each film was quantified from the EDS spectra, using the P/B-ZAF method provided by Bruker. The  $\text{Mg}/(\text{Mg}+\text{Cu})$  ratio is presented in Table IV-6. The magnesium content in the solid film increases linearly with the content in the solution, but the value is about 2.3 times lower than that in the solution, as shown in

Figure IV-54. This suggests a more efficient deposition of copper than magnesium under the selected deposition conditions. Higher temperature of deposition might increase the presence of magnesium as reported previously <sup>4</sup>, since MgO polycrystalline films are normally deposited at temperatures between 400°C and 500°C. Though, these high temperatures must induce the presence of CuO phase <sup>5</sup> or powder deposition on the substrates, as reported in Chapter III.

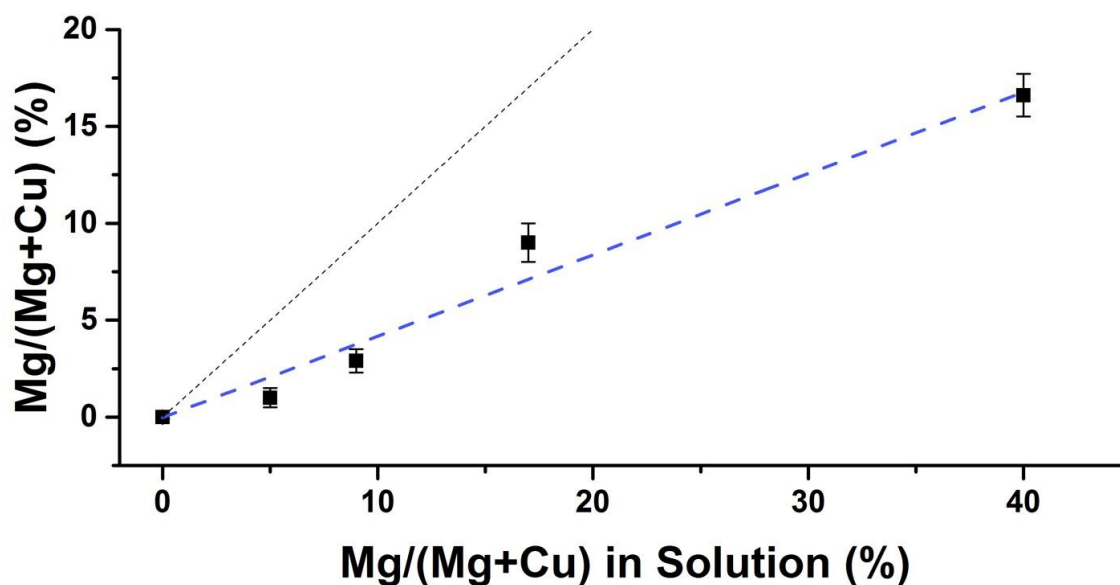


Figure IV-54 Relative atomic Mg content in the deposited  $\text{Cu}_2\text{O}:\text{Mg}$  films on glass as obtained from EDS data compared to the amount in solution. Black dotted line represents the 1:1 relation.

From this point of the work, we will use the  $\text{Mg}/(\text{Mg}+\text{Cu})$  ratio values provided by EDS as nomenclatures, i.e. 17%  $\text{Cu}_2\text{O}:\text{Mg}$ , for the different films. Inspection of the thin film surface by SEM showed the effect of magnesium incorporation on the grain morphology (Figure IV-55). In the intrinsic film case, grains are difficult to observe and roughness appears low. When the magnesium increases, the morphology becomes granular and rough, with grains higher than 100 nm for the highest magnesium-rich film (Figure IV-55 f)).

The films thicknesses were determined from SEM images of the cross section on silicon. For the sake of illustration, a  $\text{Cu}_2\text{O}$  film cross section on glass is displayed in Figure IV-55 b), with an average thickness of 86 nm. Table IV-6 contains the complete thickness measurements by SEM. The film thicknesses ranged between 77 nm and 99 nm, showing a variability, intrinsically attributed to the MOCVD system. The magnesium content seems independent of the thickness variation.

Table IV-6 Mg/(Mg+Cu) atomic ratio in solution and detected by EDS together with the thickness of each film

Mg/(Mg+Cu) solution (%)	Mg/(Mg+Cu) EDS (%)	Thickness (nm)
0	-	86 ± 3
5	1 ± 1	77 ± 2
9	3 ± 1	99 ± 9
17	9 ± 1	82 ± 4
40	17 ± 1	77 ± 5

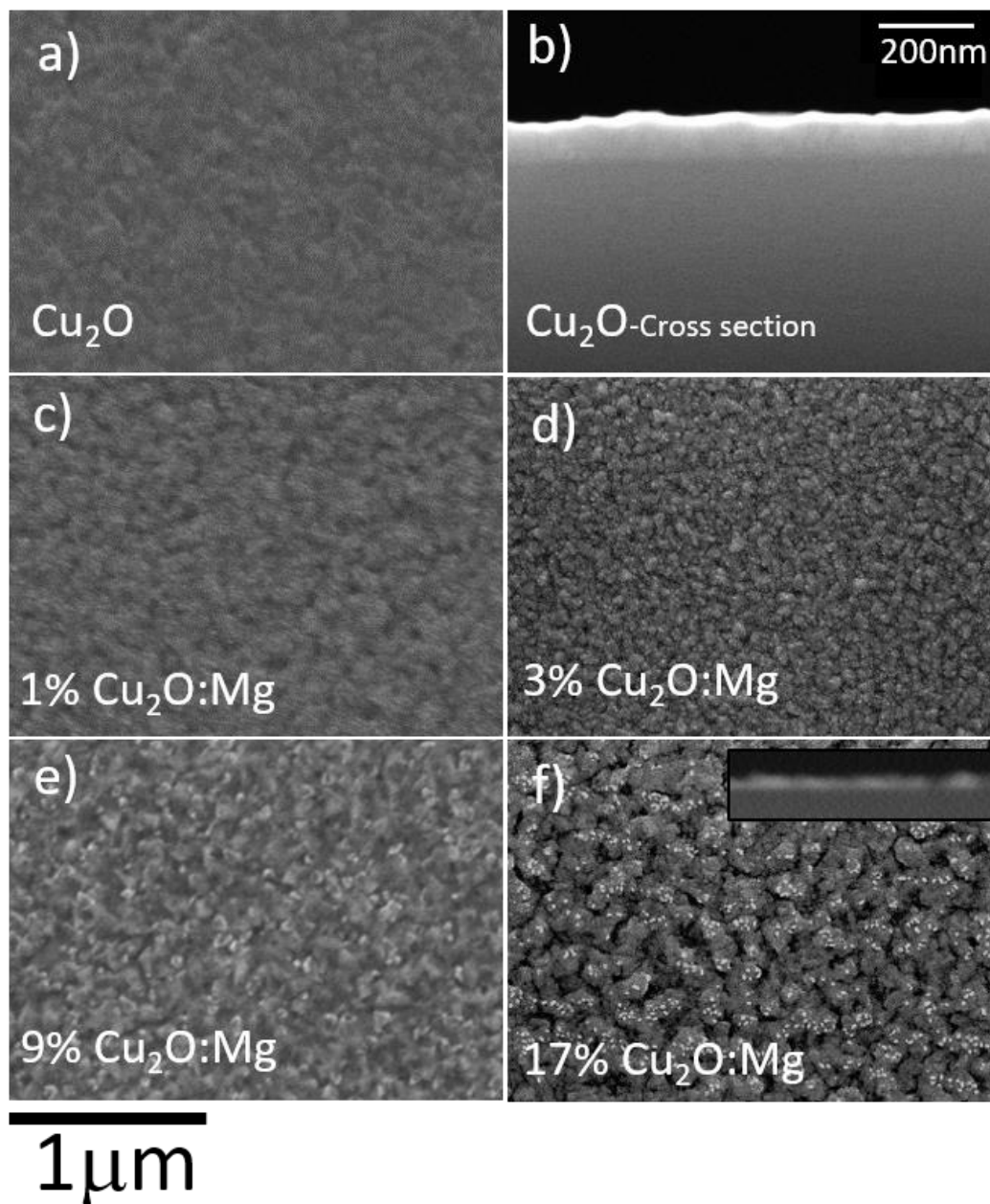


Figure IV-55 SEM images of  $\text{Cu}_2\text{O}:\text{Mg}$  thin films with different Mg content deposited on glass at  $350^\circ\text{C}$ . a)  $\text{Cu}_2\text{O}$  intrinsic, b) 1%, c) 3%, d) 9% and e) 17%  $\text{Cu}_2\text{O}:\text{Mg}$  with respective cross-section. Same magnification was used for all the top-view pictures. Top right sample corresponds to a cross-section view of intrinsic  $\text{Cu}_2\text{O}$ . Grain size enlarges with the increase of Mg content

In order to assess the location of magnesium within the  $\text{Cu}_2\text{O}$  structure, a highly doped 17%  $\text{Cu}_2\text{O}:\text{Mg}$  sample on silicon was prepared in cross section by the tripod method and by grating for TEM observation. The micrograph of Figure IV-56 a) shows randomly oriented  $\text{Cu}_2\text{O}$  grains deposited on Si substrate covered with native  $\text{SiO}_2$ . In the diffraction pattern, only the  $\text{Cu}_2\text{O}$  phase was identified, with no  $\text{MgO}$  or other complex visible. The TEM images also allowed us to clarify the crystal morphology of the grain films: the rough structures observed in top-view by SEM, defined as grains, are indeed agglomerates of smaller crystals with sizes ranging from 10 to 30 nm, as visible in Figure IV-56 c) and d), and not a unique crystallite. Spot EDS analysis in TEM confirm the presence of Mg through all film without significant segregation in the grain boundaries. Nevertheless, quantification of Mg content in relation to Cu was not possible due to the copper grid used in the sample apparatus, contaminating the copper signal.

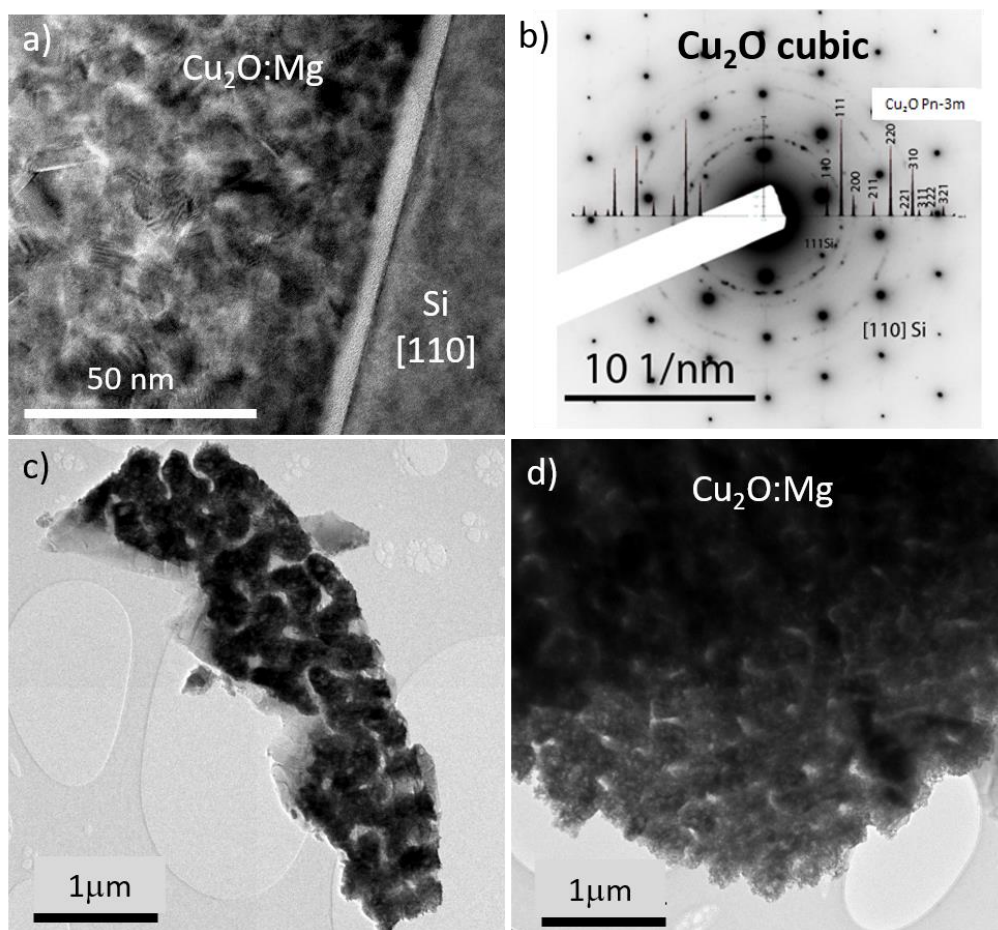


Figure IV-56 HRTEM image of the 17% Mg doped  $\text{Cu}_2\text{O}$  thin film: a) cross section view on the silicon interface region, b) corresponding diffraction pattern identified as  $\text{Cu}_2\text{O}$  structure; c) and d) detail of the film top part removed by scratching

## Chapter IV: Magnesium-doped cuprous oxide thin films

Cu<sub>2</sub>O:Mg films were also characterized by AFM, which allows to quantify the roughness through the root-mean-square ( $R_{RMS}$ ) of height deviation, visible in Table IV-7. This quantitative technique agrees with the SEM observation indicating higher roughness with the increase of Mg content, comparatively to the intrinsic Cu<sub>2</sub>O film (2.6nm). The film with 17% of Mg present the highest value of  $R_{RMS}$  of 16nm. The images of the AFM are represented in Figure IV-57.

Table IV-7 Crystallite size, roughness and thickness of the Cu<sub>2</sub>O:Mg thin films

Mg/(Mg+Cu) (%)	$R_{RMS}$ (nm)	Crystallite size (nm)	Thickness (nm)
0	2.6	30	86 ± 3
1	8.4	32	77 ± 2
3	11	30	99 ± 9
9	7.2	29	82 ± 4
17	16	41	77 ± 5

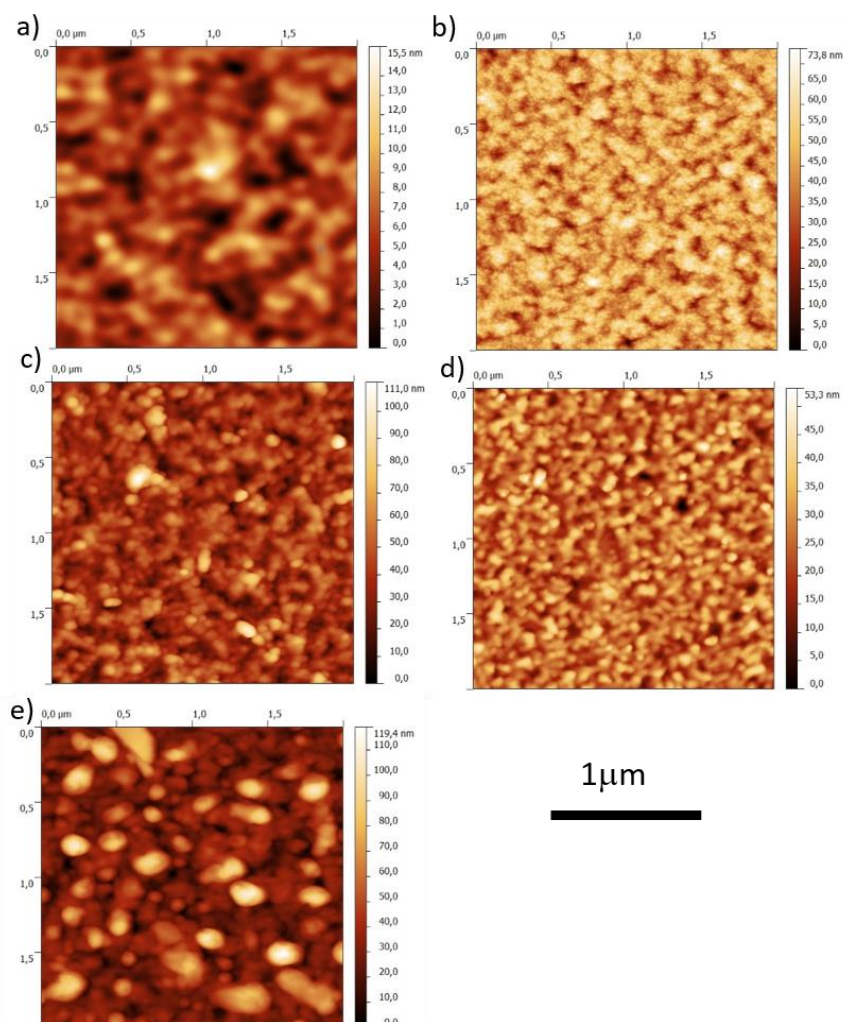


Figure IV-57 AFM images  $2\mu\text{m} \times 2\mu\text{m}$  of the Cu<sub>2</sub>O:Mg thin films – a) Cu<sub>2</sub>O intrinsic, b) 1%, c) 3%, d) 9% and e) 17% Cu<sub>2</sub>O:Mg. The Z scale is different for each sample.

As shown in Figure IV-58, the XRD spectra obtained from  $\text{Cu}_2\text{O}:\text{Mg}$  films on silicon match with those associated to a cubic  $\text{Cu}_2\text{O}$  phase. It is important to notice that there is no significant visible shift compared to intrinsic  $\text{Cu}_2\text{O}$  film. No preferential orientation could either be detected. The  $\text{MgO}$  diffraction pattern, characterized by a main peak at  $43^\circ$ , remains undetected as well as other binary oxides of magnesium and copper. Nonetheless, it is not possible to discard the presence of other amorphous phases due to the high content of Mg detected by EDS.

The crystallite size was obtained from the analysis of the XRD spectra, by using the Scherrer equation <sup>6</sup>. The results are shown in Table IV-7. The size of the crystallites varies is around 30 nm for all the Mg contents and increases to 41 nm for the highest Mg content of 17%. The effect of the magnesium content seems especially visible in the highly doped film, 17% Mg, however the crystallite size is a magnitude smaller when compared to the structures observed in SEM (Figure IV-55 f) and AFM (Figure IV-57 e)). This confirm the TEM results in Figure IV-56, where the large round structures, visible in SEM, are indeed composed of agglomerate smaller polycrystalline grains, in a similar range as the crystallite size.

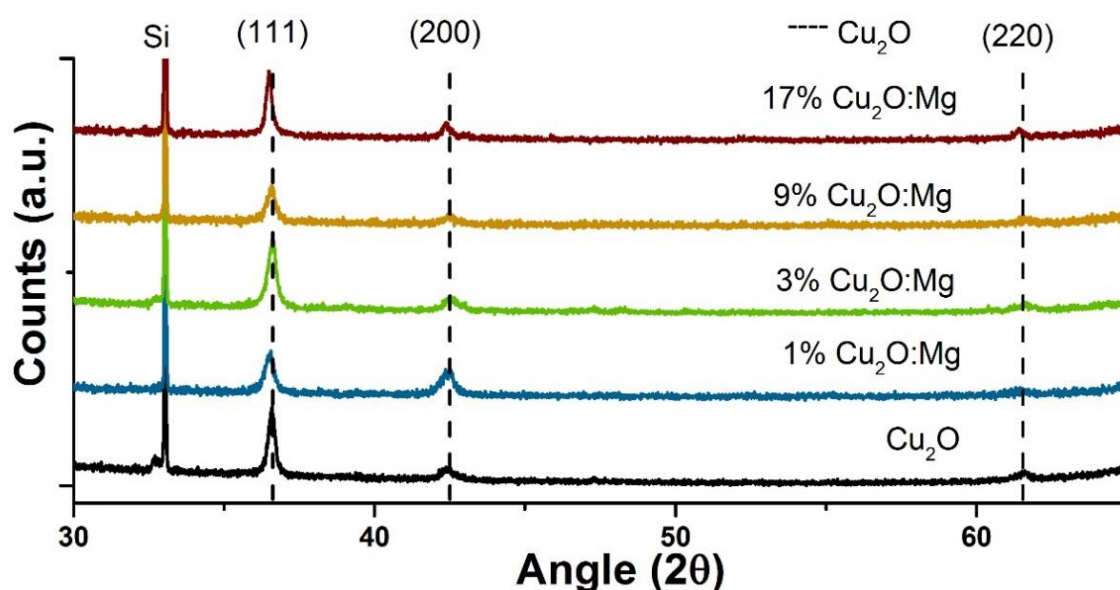


Figure IV-58 Spectra of the  $\text{Cu}_2\text{O}:\text{Mg}$  thin films on silicon obtained in a Bragg-Brentano configuration. Reference spectrum of  $\text{Cu}_2\text{O}$ : JCPDS n° 04-007-9767 presented in Appendix B

Raman spectroscopy confirmed the formation of the  $\text{Cu}_2\text{O}$  phase based on the presence of standard associated modes, which were detected in all samples, as represented in Figure IV-59 a). The magnesium presence reduced the intensity of the  $\text{Cu}_2\text{O}$  Raman peaks. Furthermore, fluorescence appeared in the samples with more magnesium, which

was evidenced via a change in the base line slope above  $800\text{ cm}^{-1}$ ; this effect might be attributed to the presence of organic impurities or electronic defects in the films <sup>7</sup>. Additionally, by analysing the peak at  $149\text{ cm}^{-1}$  in Figure IV-59 b), corresponding to the  $T_{1u}$  mode <sup>8</sup>, we can see an increase of the full width at half maximum (FWHM), once again confirming the peak broadening with the presence of magnesium.

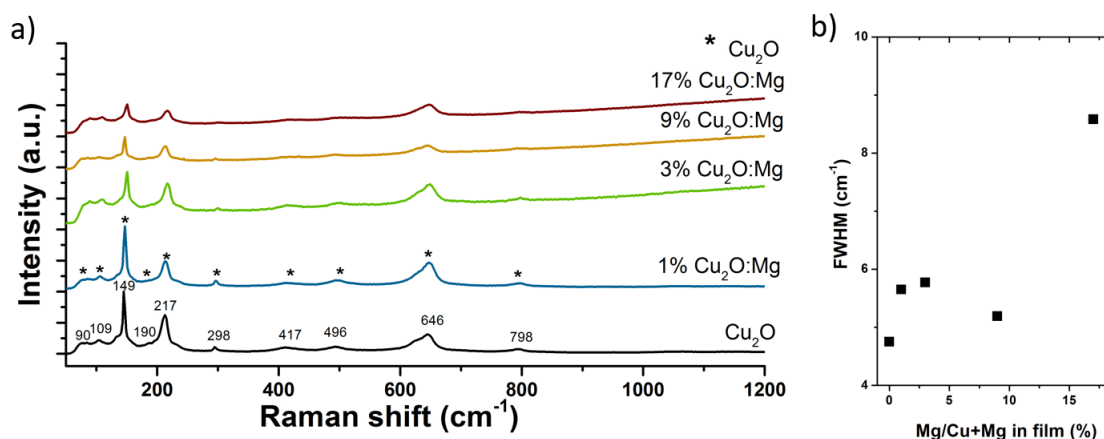


Figure IV-59 a) Raman spectra of the Cu<sub>2</sub>O:Mg thin films on glass; b) FWHM analysis of  $149\text{ cm}^{-1}$  peak with the variation of Mg content

FTIR was used as a complementary technique to Raman, and was performed specifically on films deposited on silicon substrates, shown in Figure IV-60a). The spectra exhibit a peak at  $618\text{ cm}^{-1}$  corresponding to the stretching band of Cu<sub>2</sub>O <sup>5</sup>. This peak shifts gradually to higher wave numbers and its width (FWHM) broadens with the increasing incorporation of the dopant, as shown in Figure IV-60 b). The magnesium presence leads to the appearance of a second band, at  $436\text{ cm}^{-1}$  which can be associated to the Mg–O stretching vibration <sup>9</sup>, together with a reduction of the Cu<sub>2</sub>O band intensity. The combination of this result with XRD and Raman could indicate that Mg is present inside the grain or at the grain boundaries in an amorphous form. Organic bonds from the precursor remain undetected.

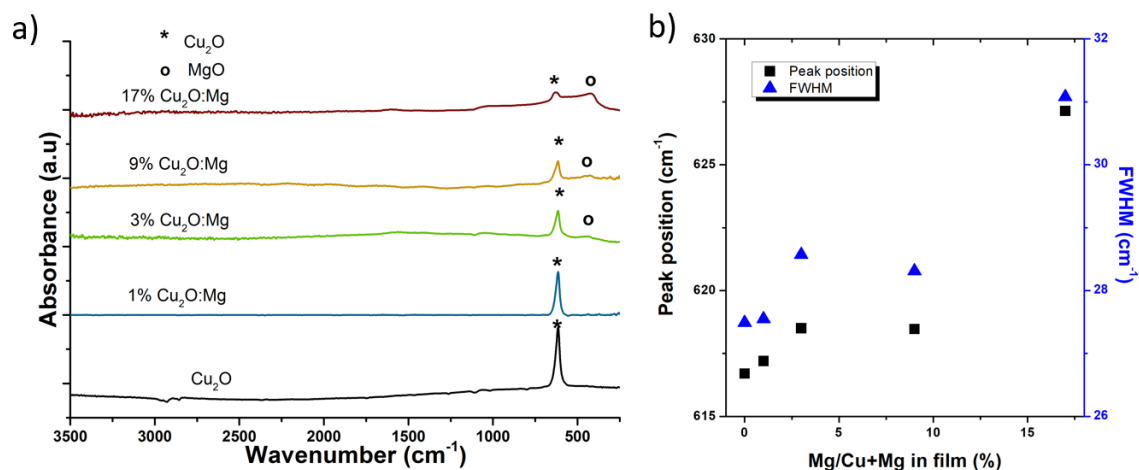


Figure IV-60 a) FTIR spectra of the  $\text{Cu}_2\text{O}:\text{Mg}$  thin films on silicon. b) FWHM and position analysis of  $436\text{cm}^{-1}$  peak with the variation of Mg content

#### 1.4.2 Optic and electric characterization

The visible direct optical transparency was assessed by transmittance measurements (Table IV-8). The corresponding data representing three of the films representative of all the samples are plotted in

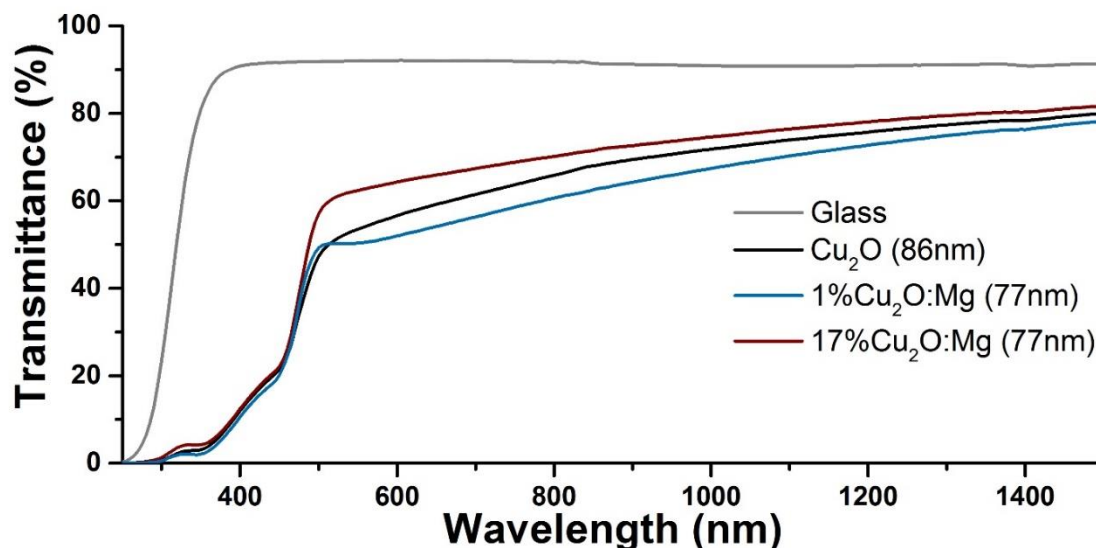


Figure IV-61. The transmittance in the visible range (390 nm – 700 nm) varies between 42% and 51%, while the most transparent sample is the  $\text{Cu}_2\text{O}:\text{Mg}$  film with 17% of magnesium. When we compare the transmittance between the undoped and the 17%  $\text{Cu}_2\text{O}:\text{Mg}$  films in the visible range, a similar wavelength dependence is recognized close to the absorption edge. Nevertheless, the increase in transparency above 500nm is more abrupt for the highly doped  $\text{Cu}_2\text{O}$  film than for the others. An improvement of 6% in

transparency is observed, even when the thicknesses are comparable, around 80 nm. Additionally, the optical band gap values as calculated from the Tauc representation, are given in Table IV-8, which also confirm a small increase of 0.2 eV from the intrinsic to the highly doped film.

Table IV-8 Average transmittance in the visible range (390 nm - 700 nm) and respective band gap of the Cu<sub>2</sub>O:Mg thin films on glass

Mg/(Mg+Cu) (%)	Transmittance Visible (%)	Bandgap (eV)
0	45	2.2±0.1
1	42	2.3±0.1
3	46	2.3±0.1
9	50	2.2±0.1
17	51	2.4±0.1

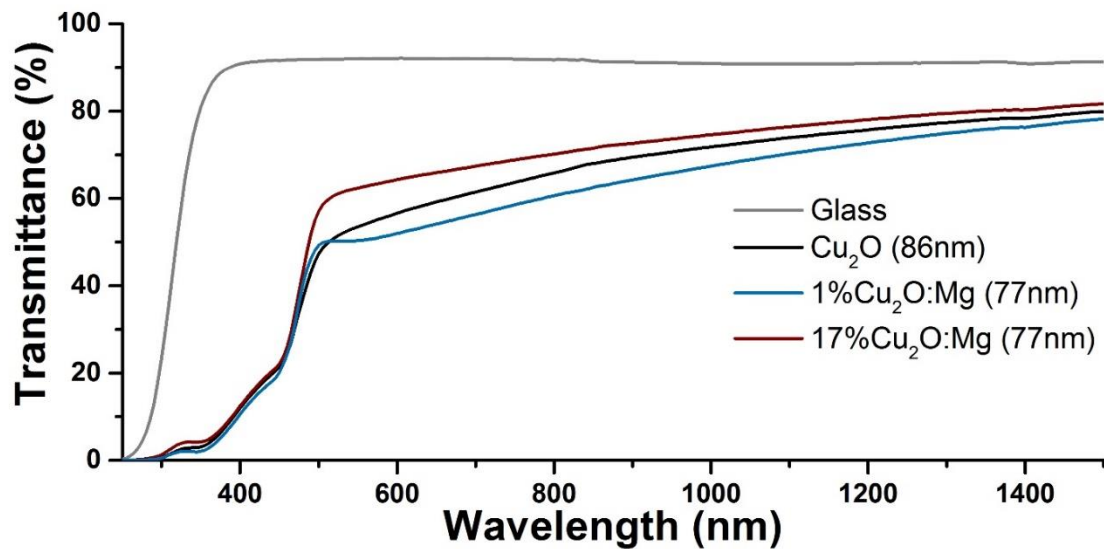


Figure IV-61 Transmittance spectra from 250 nm to 1500 nm of the Cu<sub>2</sub>O and Cu<sub>2</sub>O:Mg (1% and 17%) thin films on glass. The bare glass substrate transmittance is also represented as reference

A preliminary analysis of the sheet resistance of as-deposited samples revealed a fluctuating results with values ranging from 15 up to 70 MΩ/sq, which corresponds to an electrical resistivity in the range of 10<sup>3</sup>-10<sup>2</sup> Ω.cm, without any clear relation to the Mg content. The dependence of the resistivity with respect to the Mg content for films, which received a heat treatment at 250°C in air for 1 hour, is represented in Figure IV-62. The magnesium incorporation affects the resistivity drastically, inducing a decrease from 202 Ω.cm to 6.6 Ω.cm for the 17% Cu<sub>2</sub>O:Mg film. This result agrees with previous results obtained by doping with other divalent cations such as Sr<sup>2+</sup>, presenting values around 10 Ω.cm<sup>2</sup>. Nevertheless the minimum resistivity value is still higher than for N-doped Cu<sub>2</sub>O thin films, with a resistivity value of 2x10<sup>-1</sup> Ω.cm<sup>10</sup>.

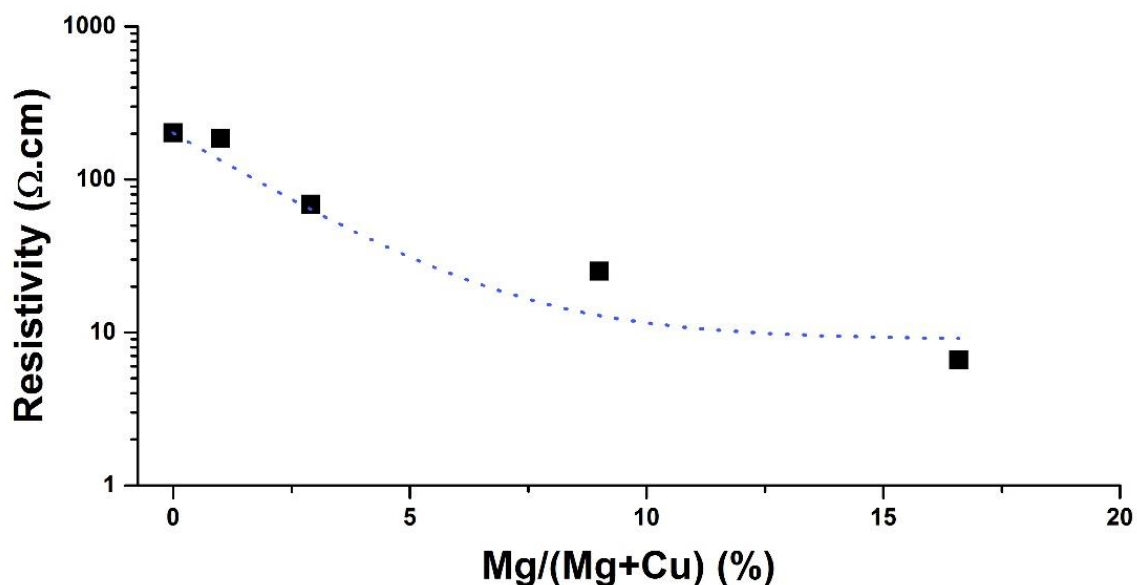


Figure IV-62 Electrical resistivity dependence on the magnesium content of  $\text{Cu}_2\text{O}:\text{Mg}$  thin films after thermal annealing. The dotted line is represented as a guide for the eye.

The origin of this lower resistivity was further investigated by Hall Effect measurements using a Van der Pauw configuration for the samples. The results for the charge carrier concentrations and the mobility values are plotted Figure IV-63. The Hall coefficient was positive for all films, which confirmed the p-type conductivity.

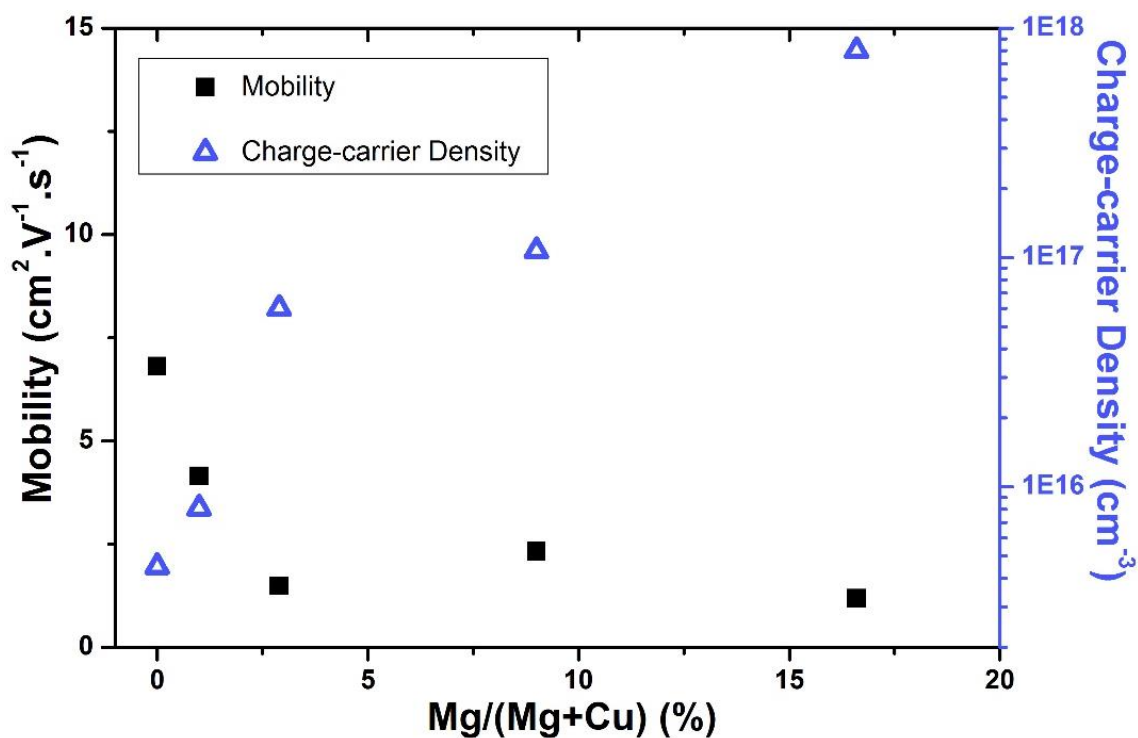


Figure IV-63 Mobility (left vertical axis) and charge-carrier density (right vertical axis) as function of the magnesium content in  $\text{Cu}_2\text{O}:\text{Mg}$  thin films

On the one hand, as shown in Figure IV-63 the carrier mobility presents a decreasing behaviour with Mg content, and varies from  $6.8 \text{ cm}^2 \cdot \text{V}^{-1} \cdot \text{s}^{-1}$  in the  $\text{Cu}_2\text{O}$  film to  $1.1 \text{ cm}^2 \cdot \text{V}^{-1} \cdot \text{s}^{-1}$  in the 17%  $\text{Cu}_2\text{O}:\text{Mg}$  film. On the other hand, the charge carrier density increases, ranging from  $4.5 \times 10^{15} \text{ cm}^{-3}$  up to  $8.1 \times 10^{17} \text{ cm}^{-3}$  for an increasing in Mg content from 0% to 17%. The two combined properties lead to a general decrease of resistivity, as visible in Figure IV-62.

The values of carrier concentration obtained in this work are higher than those found in the literature, which range from  $10^{13}$  to  $10^{16} \text{ cm}^{-3}$ . This fact can be explained by the substitution of copper by magnesium, creating copper vacancies<sup>12</sup>. Indeed, two possible copper vacancies can appear in  $\text{Cu}_2\text{O}$ : the simple copper vacancy ( $V_{\text{Cu}}$ ) related to the removal of one copper atom, leaving two oxygen atoms with three copper neighbours; or the split copper vacancy ( $V_{\text{Cu}}^{\text{split}}$ ) in which the copper disappearance is followed by a neighbouring copper atom movement towards the vacancy<sup>12</sup>. In the latter case, the copper atom moves into a tetrahedral site with four neighbouring oxygen atoms. The split vacancy is usually associated to highly localized hole, responsible for the change in oxidation of copper cation from  $1^+$  to  $2^+$ , similar to  $\text{CuO}$  phase.

Magnesium as a divalent cation would be incorporated in a tetrahedral position, similar to a split copper vacancy, as described by Isseroff and Carter<sup>13</sup>. This defect would be electrically inert, since the  $\text{Mg}^{2+}$  cation would replace a  $\text{Cu}^+$  cation and one additional  $\text{Cu}^+$  would be removed, visible in Figure IV- 64. However, this incorporation would reduce the formation of Cu based split vacancies and therefore inhibit the nucleation of the  $\text{CuO}$  phase<sup>13</sup>. Therefore, during the annealing, more simple copper vacancies are created, leading to an increase of the hole concentration without forming the extra  $\text{CuO}$ <sup>13</sup>. Further analysis on the stability of Mg-doped  $\text{Cu}_2\text{O}$  during thermal treatments would be required to confirm the occurrence of this mechanism.

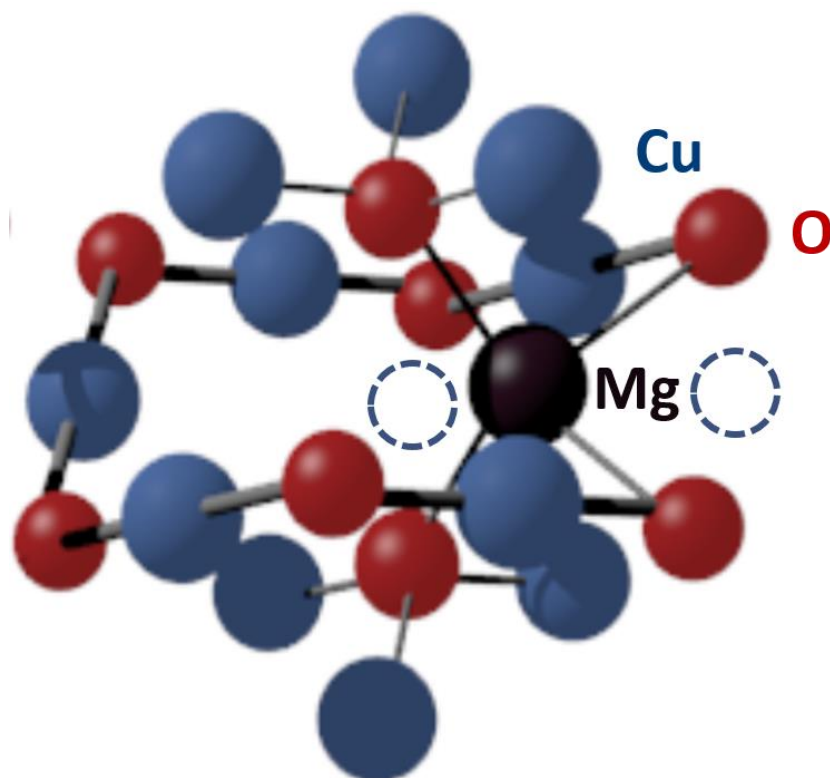


Figure IV- 64 Incorporation of Mg in a tetrahedral position of Cu<sub>2</sub>O crystalline structure. Copper atoms pictured as blue circles, oxygen as red ones and magnesium as black ones.

The presence of magnesium in the film also has an additional role, both on grain shape and consequently on the carrier mobility of Cu<sub>2</sub>O. As the amount of dopant inside the film is fairly high (17%), it is reasonable to think that a fraction of the magnesium content is present at the grain boundary. Therefore, hole scattering is more enhanced at the boundaries, reducing the material mobility. As the exact position of Mg in the films was not possible to be clarified by the techniques used until now, other analysis as EXAFS and XPS are fundamental to probe the chemical environment of the cations (Mg and Cu). These results are present in the following section of this chapter.

#### 4.1.3 Summary

The incorporation of magnesium in cuprous oxide thin films was successfully achieved by aerosol-assisted metal-organic chemical vapour deposition under atmospheric pressure condition at 350°C. The use of physicochemical analysis techniques such as FTIR and EDS confirmed the presence of magnesium up to 17% in cation concentration, while the analysis of XRD and Raman spectra led to the detection of cubic Cu<sub>2</sub>O material, without

the appearance of any magnesium-related phase. Therefore, we can conclude that the incorporation of the dopant atom is localized inside the structure or at the grain boundaries of the cuprous oxide. However, the exact location of the dopant is still unclear based on SEM and TEM micrographs. The presence of Mg affected the microstructure of the film, forming agglomerates of grains, reaching sizes in the hundreds of nanometres, which led to a higher roughness of the films surface.

The incorporation of magnesium in Cu<sub>2</sub>O films had a strong effect on the electrical properties, reducing the electrical resistivity to 6.6 Ω.cm, by mainly increasing the charge carrier density up to 8.1x10<sup>17</sup> cm<sup>-3</sup>. The doping effect can be attributed to the increase of simple copper vacancies, probably by the magnesium presence in a tetrahedral position, leading to an increase of the hole concentration, as proposed by Nolan *et al.* <sup>1</sup>. This work reports, to our knowledge, the first experimental evidence of a hole concentration increase correlated to the addition of a divalent cation in Cu<sub>2</sub>O, complementary to previous reports on lower resistivity <sup>2</sup>.

However, the assessment of the impact of the doping on the optical transparency was inconclusive since the bandgap (2.4eV) and the total transparency (51%) only improved slightly when comparable with intrinsic Cu<sub>2</sub>O.

In conclusion, transparent conductive properties of magnesium-doped cuprous oxide were improved when compared to intrinsic Cu<sub>2</sub>O thanks to a strong reduction of the resistivity. Ultimately, the control of the charge carrier density can provide a way to use Cu<sub>2</sub>O in transparent electronic devices in the future. Additionally, the observed reduction of electrical resistivity, associated with an increase of charge carrier concentration, can enhance the efficiency of Cu<sub>2</sub>O-based solar cells <sup>11</sup>.

## 4.2 Stability of Magnesium-doped cuprous oxide (Cu<sub>2</sub>O:Mg) thin films under thermal treatments

In the second section of this chapter, we will continue the study of Mg incorporation in Cu<sub>2</sub>O, focusing on the dopant impact on the properties of Cu<sub>2</sub>O under thermal treatments. As suggested before, the use of annealing treatments on both intrinsic and Mg-doped Cu<sub>2</sub>O thin films can clarify the influence of the dopant on the copper vacancy generation mechanism, both simple and split vacancies, as well as the transformation of Cu<sub>2</sub>O into CuO parasitic phase.

### 4.2.1 Introduction

The use of post-deposition annealing treatments on Cu<sub>2</sub>O have been widely studied as a method to increase the free carrier concentration<sup>14</sup>. It has been established that annealing in oxidizing environments promotes the creation of copper vacancies,  $V_{Cu}$ , which is the main mechanism for the increase of p-type conductivity in the material by the generation of holes. The concentration of charge carriers can reach up to  $10^{16} \text{ cm}^{-3}$ <sup>15</sup>, leading to resistivity values as low as  $100 \text{ } \Omega \cdot \text{cm}$  in intrinsic Cu<sub>2</sub>O<sup>16</sup>. While when annealing doped films, the values can increase up to  $10^{18} \text{ cm}^{-3}$ , which reduces de resistivity to the  $1 \text{ } \Omega \cdot \text{cm}$  range<sup>3,17</sup>.

Nevertheless, the use of higher temperature promotes the transition from Cu<sub>2</sub>O thin films into tenorite oxide, CuO, which usually starts at temperatures ranging from 250 to 300 °C in an oxidizing atmosphere<sup>18,19</sup>. Even if Cu<sub>2</sub>O is considered an unstable oxide at room temperature under air, in fact, the transformation to CuO takes place but it is extremely slow, that the system can be considered as thermodynamically stable for the main applications<sup>20</sup>. At higher temperatures, the conversion of Cu<sub>2</sub>O into CuO is attributed to the diffusion of copper to the surface, which consequently generates copper vacancies. As explained in the previous section, simple copper vacancy ( $V_{Cu}$ ) and split copper vacancy ( $V_{Cu}^{split}$ ) can be formed during thermal treatments in Cu<sub>2</sub>O. In the split vacancy, the shifted copper becomes 4-fold coordinated, combined with a highly localized hole, which is associated to a nucleation centre for CuO phase. Additionally, the diffusion of copper to the surface of the film in an oxidizing atmosphere can also lead to the formation of CuO due to the direct oxidation of the cation, from Cu<sup>+</sup> to Cu<sup>2+</sup>. In the case of bulk Cu<sub>2</sub>O, the

complete transformation occurs at higher temperature, above 600 °C<sup>21</sup>, due to the low rate speed of this phase transformation. Additionally, there is the report of the inverse phase transition from CuO to Cu<sub>2</sub>O by annealing treatments at 425 °C under vacuum<sup>22</sup>.

In this study, we annealed both intrinsic and doped Cu<sub>2</sub>O thin film at different temperatures, from 250 °C to 500 °C in air and we analysed the effect of Mg incorporation on the stability of the Cu<sub>2</sub>O phase. We studied the changes on structural, morphological and electrical properties. Such a deeper investigation provide a comprehensive insight into the phase transformation and the electronic impact of the Mg incorporation.

### 4.2.2 *Experimental*

For the study on the stability of the Cu<sub>2</sub>O films under thermal annealing, two samples, with and without magnesium, were deposited. Once again, a butanol-based solution was used for the deposition by AA-MOCVD. The total concentration of the solution was fixed at 0.03 mol.l<sup>-1</sup>. The first solution was composed of pure Cu(acac)<sub>2</sub>, while in the second one the Mg/Mg+Cu ratio in the solution was fixed at 33%, as it was considered the lowest resistivity sample in the previous Mg variation study (17% Mg in the films). In order to have a thicker film, the time of deposition was increased to 3 hours and the solution consumption rate decreased to 1.5 ml.min<sup>-1</sup>. The lower solution consumption enabled a slow deposition rate, beneficial electrically for thicker films. The other deposition parameters were kept constant: 350 °C for the temperature of the substrates (Corning 1737 and p-type silicon wafer); Argon flow of 6 l.min<sup>-1</sup>; O<sub>2</sub> flow of 2.5 l.min<sup>-1</sup>. The study of the stability films under thermal annealing was performed in a heating plate under air, coupled with in-situ resistance measurements preformed using a 2-probe system. Three stages of temperature were chosen, 250 °C, 350 °C and 450 °C, all for 30 minutes, while the heating rate was kept constant at 10°C/min. One additional annealing treatment was performed at 500 °C for 30 minutes, only analysed by EXAFS. The temperature bounds were defined as follows: the lower limit is set by the preliminary annealing study in Chapter III for undoped Cu<sub>2</sub>O while the upper limit is determined by the major transformation to CuO phase.

### 1.4.3 *Structural characterization*

The as-deposited films were routinely characterized in order to obtain the Mg content in the film, thickness and sheet resistance. The preliminary results are visible in

Table IV-9, and follow similar trends as observed before for this system. The films were then annealed and characterized from different points of view.

Table IV-9 General properties of deposited  $\text{Cu}_2\text{O}$  and  $\text{Cu}_2\text{O}:\text{Mg}$  films for the stability study

Sample	Mg/(Mg+Cu) in solution (%)	Mg/Mg+Cu in film (%)	Thickness (nm)	Sheet Resistance ( $\text{M}\Omega/\text{sq}$ )
$\text{Cu}_2\text{O}$	0	0	244	6.3
$\text{Cu}_2\text{O}:\text{Mg}$	33	18%	164	4.7

The difference in appearance can be evaluated even by the naked eye, as the phase change from  $\text{Cu}_2\text{O}$  to  $\text{CuO}$  is accompanied by a change in colour and morphology of the films. As the  $\text{CuO}$  phase presents a darker brown colour, the visual analysis of the films is a clear evidence when the films change their phase. In the Figure IV-65, the 8 samples studied are represented.

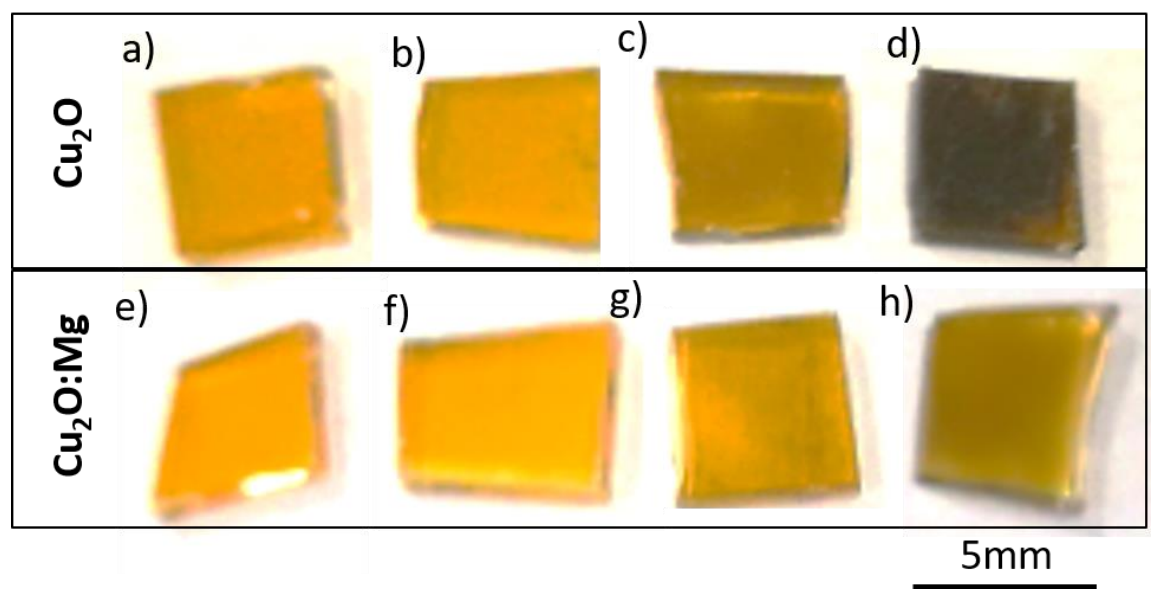


Figure IV-65 Optical appearance of the copper oxide thin films.  $\text{Cu}_2\text{O}$ : as deposited (a), 250°C (b), 350°C (c), 450°C (d);  $\text{Cu}_2\text{O}:\text{Mg}$ : as deposited (e), 250°C (f), 350°C (g), 450°C (h).

Initially both films present a yellow colour as-deposited. When the films are annealed at 250°C, no clear difference is visible. However a colour change is detected after 350°C, in both cases, especially in the undoped case. At 450°C, we can see a darker film in the intrinsic copper oxide film, while the Mg-doped one present a brown colour, however not completely dark and opaque. This fact led us to infer that the magnesium presence has an impact in the phase transformation from  $\text{Cu}_2\text{O}$  to  $\text{CuO}$  as compared to undoped  $\text{Cu}_2\text{O}$  films, since the darker phase is not yet completely visible in the Mg-doped films.

To follow the phase transformation, the structural properties of the films were evaluated by grazing incidence X-ray diffraction (GI-XRD), more sensitive to a phase

present in lower proportion. When analysing results obtained from undoped films presented in Figure IV-66, only the diffraction peaks corresponding to the  $\text{Cu}_2\text{O}$  phase are detected in the as-deposited film and on the film annealed at  $250^\circ\text{C}$ . When the annealing temperature increases to  $350^\circ\text{C}$ , diffraction peaks at  $35.5^\circ$  and  $38.7^\circ$  are detected, which can be attributed to the (11-1) and (111), reflection of the  $\text{CuO}$  phase. For the sample annealed at  $450^\circ\text{C}$ , the majority of the diffraction peaks are associated to the  $\text{CuO}$  phase, while a small residue corresponding to the  $\text{Cu}_2\text{O}$  phase is still visible, mainly diffraction peaks at  $36.4^\circ$ ,  $42.3^\circ$  and  $61.3^\circ$  angles corresponding to the (111) (200) and (220) reflections.

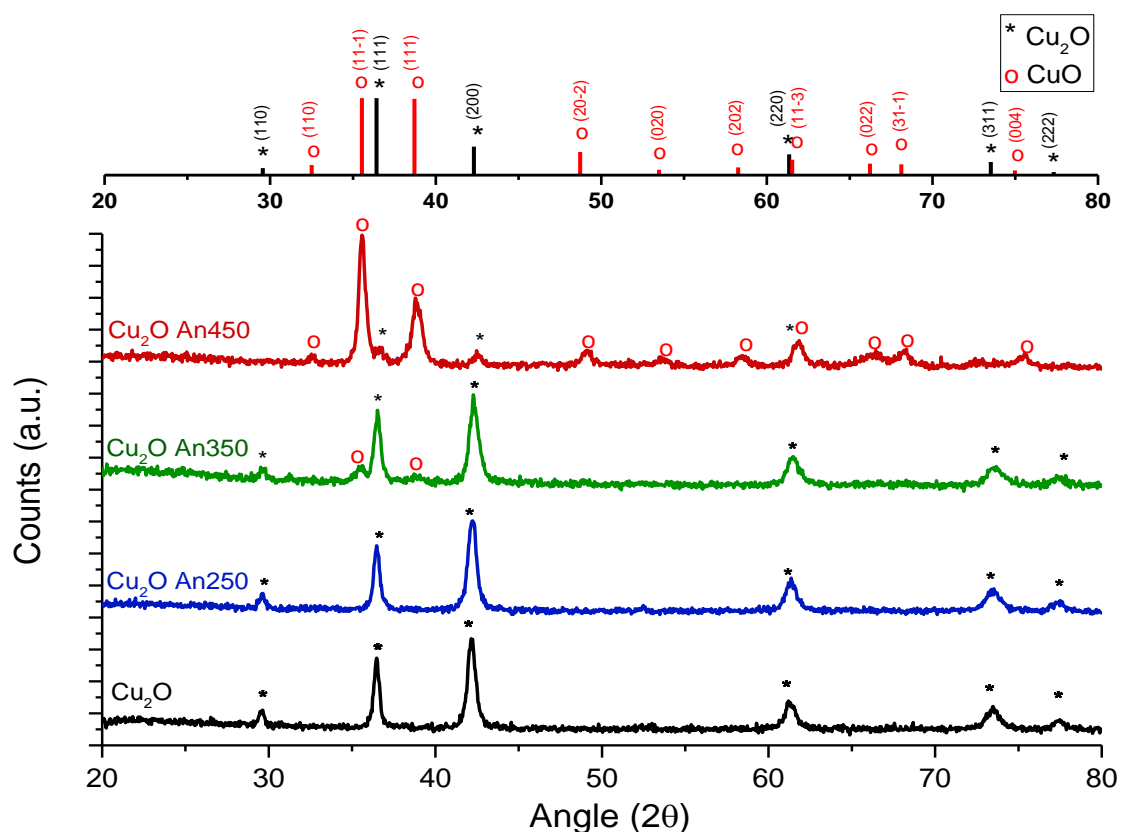


Figure IV-66 GI-XRD spectra of undoped  $\text{Cu}_2\text{O}$  thin films on glass corresponding to the as-deposited and annealed samples. Reference spectrum of  $\text{Cu}_2\text{O}$ : JCPDS n° 04-007-9767 and  $\text{CuO}$ : ICDD n° 00-048-1548 presented in Appendix B and C

The GI-XRD spectra of the second set of samples corresponding to films of  $\text{Cu}_2\text{O}$  doped with magnesium are presented in Figure IV-67. In this case and similarly to the intrinsic films, the as-deposited and annealed at  $250^\circ\text{C}$  films present only diffraction peaks corresponding to the  $\text{Cu}_2\text{O}$  phase. In the film annealed at  $350^\circ\text{C}$ , a small diffraction peak attributed to the  $\text{CuO}$  phase is detected (111) while the intensity of the  $\text{Cu}_2\text{O}$  peaks decreases. For the film annealed at the higher temperature,  $450^\circ\text{C}$ , the intensity of the  $\text{CuO}$  diffraction peaks is higher, however, the (111)  $\text{Cu}_2\text{O}$  diffraction peak at  $36.4^\circ$  is still the

most intense. It is worth noting that the  $\text{Cu}_2\text{O}$  diffraction peak also shows a shift of  $0.42^\circ$  degrees from the original position of  $36.42^\circ$  to  $36.84^\circ$ . This can be an evidence of the change in lattice parameter from  $4.270 \text{ \AA}$  to  $4.226 \text{ \AA}$ , decreasing the size of the unit cell.

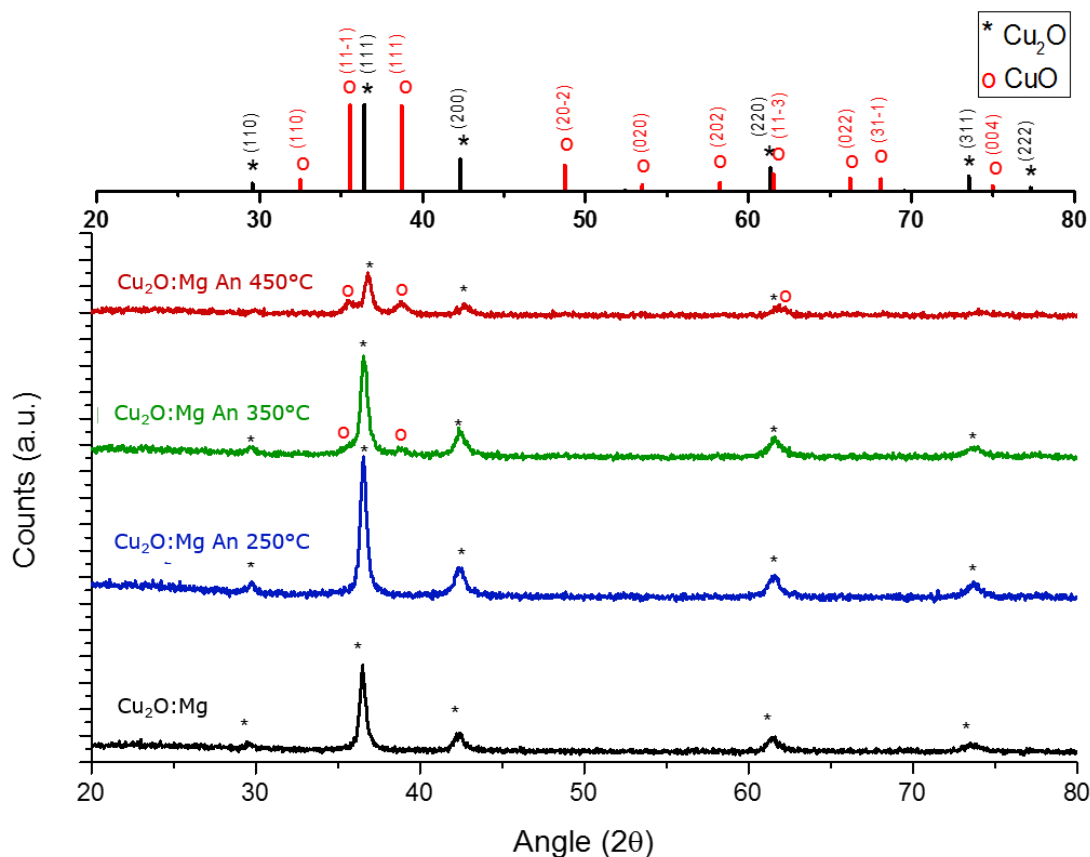


Figure IV-67 GI-XRD spectra of the Mg doped  $\text{Cu}_2\text{O}$  thin films on glass corresponding to the as-deposited and annealed samples. Reference spectrum of  $\text{Cu}_2\text{O}$ : JCPDS n° 04-007-9767 and  $\text{CuO}$ : ICDD n° 00-048-1548 presented in Appendix C and D

In order to evaluate the phase formation of  $\text{CuO}$  regarding the structural modifications, the films of intrinsic  $\text{Cu}_2\text{O}$  were observed by SEM; the morphology of films is visible in Figure IV-68. The cross-section of the as-deposited film inserted in the figure shows a homogeneous layer with an average thickness of  $244\text{nm}$ . When observed in top-view, this film shows a porous surface and grains are hardly visible, which remains after the annealing at  $250^\circ\text{C}$  (Figure IV-68 b)). The increase of temperature in the thermal treatment leads to changes in the film annealed at  $350^\circ\text{C}$ , where small grains are now visible and the porosity seems to be reduced. In the film annealed at  $450^\circ\text{C}$ , larger grains are visible, in the  $100\text{nm}$  range, forming a rougher structure when compared to previous samples.

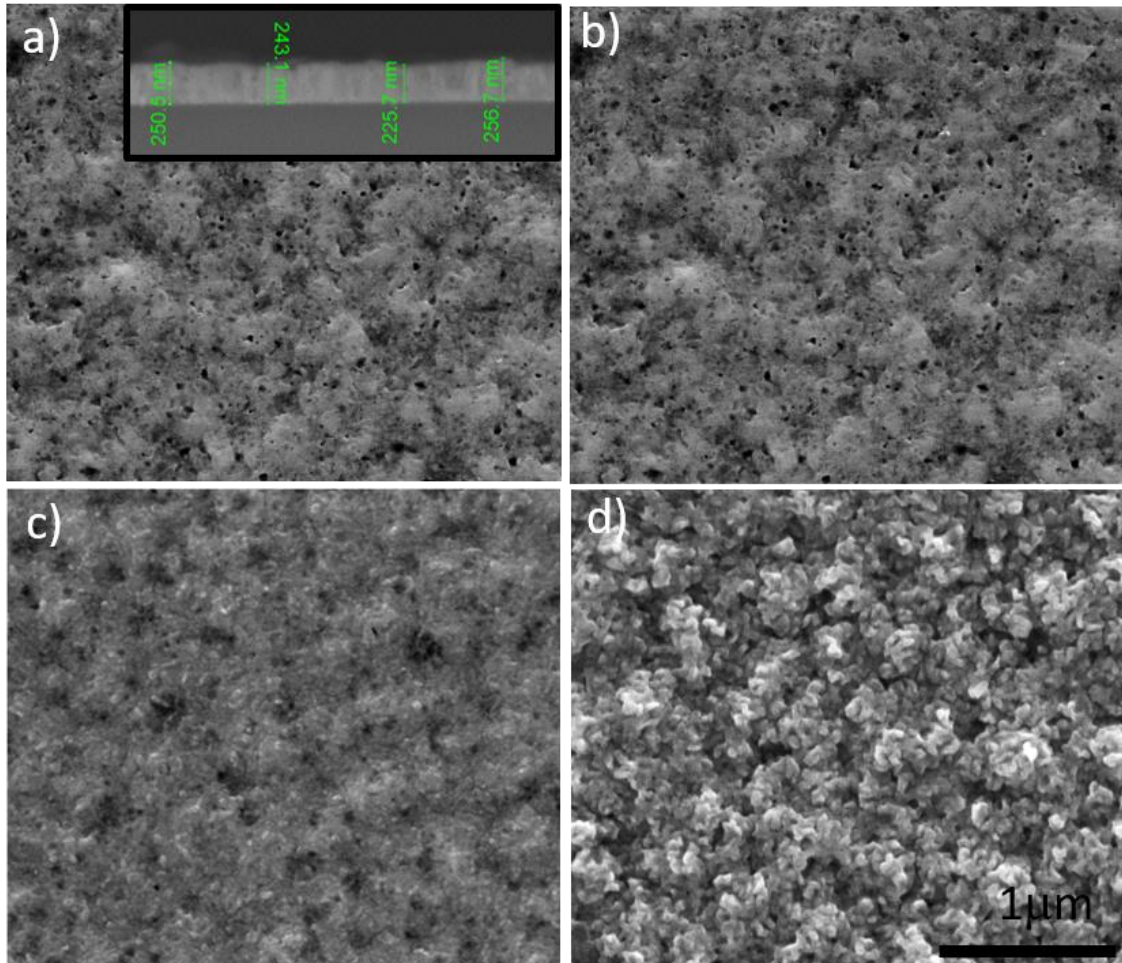


Figure IV-68 SEM micrographs of  $\text{Cu}_2\text{O}$  thin films: as deposited (a), 250°C (b), 350°C (c), 450°C (d); Cross-section image visible on image a)

The SEM micrographs Mg-doped  $\text{Cu}_2\text{O}$  films are presented in Figure IV-69, the cross-section of the as-deposited sample inserted in Figure IV-69 a) shows a rougher and more irregular layer, with an average thickness of 167nm. This irregular morphology is also detected in the top view imaging of the original Mg-doped  $\text{Cu}_2\text{O}$  film, where a rough surface with larger grains is visible (Figure IV-69 a)). As in the intrinsic films, the sample annealed at 250°C shows the same morphology as the as-deposited film. When the thermal treatment is performed at 350°C, small grains start to appear on the top of the original viewed morphology hinting at a size smaller than 100 nm and apparently only formed at the surface. At the sample annealed at 450°C, a widespread of grains occurs with approximate size below 100nm, but in a different way compared to the undoped  $\text{Cu}_2\text{O}$  films, as they cover here all the surface. The rough surface of the film is maintained even with the presence of the recently formed grains.

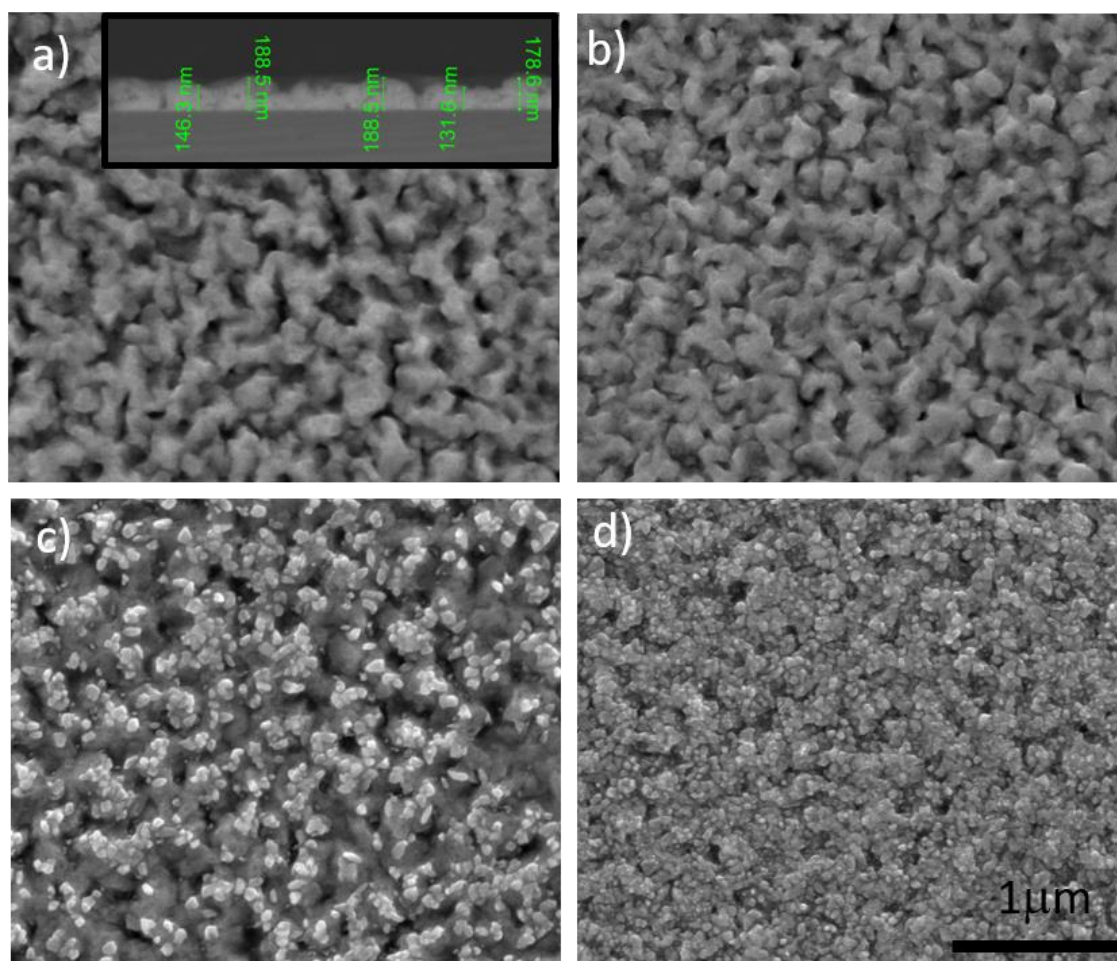


Figure IV-69 SEM micrographs of Mg doped  $\text{Cu}_2\text{O}$  thin films: as deposited (a), 250°C (b), 350°C (c), 450°C (d); Cross-section image visible on image a)

The direct comparison between the effects of the annealing on the two sets of samples establishes differences in terms of growth of the secondary phase, CuO. As already stated before in the Mg content study, the main differences in the as-deposited intrinsic and doped  $\text{Cu}_2\text{O}$  films are related to the roughness of the film, visible in top view but also in the cross-section. Combining SEM images with XRD results, the formation of CuO is associated to the formation of smaller and brighter grains at the surface. The formation of these grains occurs in a unlike way for the two samples annealed at 350°C, since in the intrinsic case the newly formed grains seem to be generalized on the surface of the film, while in the Mg doped films the grains are only formed in a fraction of the visible surface. For the  $\text{Cu}_2\text{O}:\text{Mg}$  films it is necessary to perform the thermal treatment at 450°C to obtain a look like that of the undoped annealed at 350°C, consisting in small grains covering completely the surface of the film. Moreover, the  $\text{Cu}_2\text{O}$  undoped films annealed at 450°C show different shape and larger size of the CuO formed grains, consistent with a higher degree of phase transformation, previously visible in the GI-XRD results.

STEM was used to analyse the grains on the surface of  $\text{Cu}_2\text{O}:\text{Mg}$  film annealed at  $350^\circ\text{C}$ . However, the identification of  $\text{CuO}$  phase by the diffraction pattern on the formed grains was not obtained. Moreover, EDS was performed punctually using spot analysis in STEM to identify the local distribution of Mg. Mappings for each element obtained from the  $\text{Cu}_2\text{O}:\text{Mg}$  film annealed at  $350^\circ\text{C}$  are presented in Figure IV-70. This analysis confirms the presence of Mg through all film without significant segregation in the grain boundaries, not easily distinguished. However, the dopant (Figure IV-70c)) appears to present a gradient with the thickness, being preferably located at the interface with the substrate, in the first 100 nm of the film.

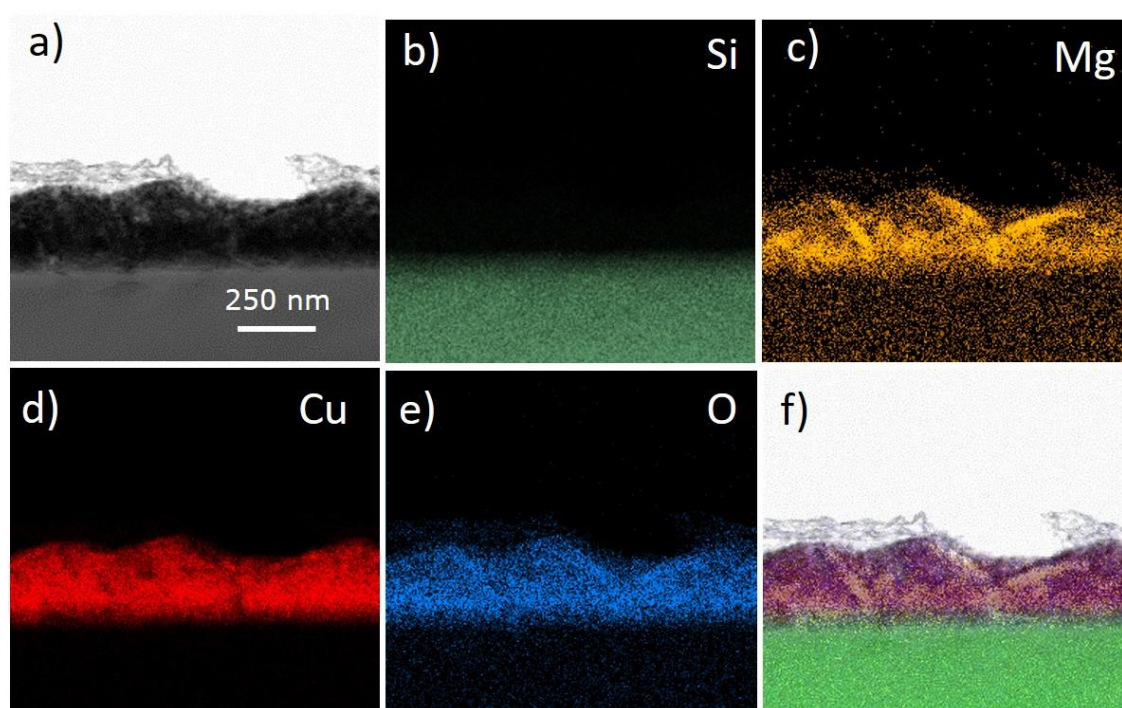


Figure IV-70 a) Bright-field STEM image of  $\text{Cu}_2\text{O}:\text{Mg}$  thin film annealed at  $350^\circ\text{C}$  b-e) Corresponding EDS-STEM elemental mapping of the b) Si, c) Mg, d) Cu, and e) O elements, respectively. f) Superimposition of the corresponding EDS-STEM maps of the Si, Mg, Cu and O elements. The 250 nm scale bar is valid for all images.

Raman spectroscopy was used to clarify the early stage of phase transformation in these sets of samples. This technique is complementary to XRD analysis, but allows for a more local analysis. Raman spectra of as-deposited and annealed  $\text{Cu}_2\text{O}$  thin films are represented in Figure IV-71 a) and b), for the undoped and doped samples respectively. The comparison of the two oxides is based on the appearance of a peak at  $348\text{ cm}^{-1}$ , which is attributed to the  $B_g^1$  mode of  $\text{CuO}$  without correlation to  $\text{Cu}_2\text{O}$ . This is the only peak independent of  $\text{Cu}_2\text{O}$ , since the others at  $298\text{ cm}^{-1}$  ( $A_g$ ) and  $628\text{ cm}^{-1}$  ( $B_g^2$ ) are also visible

in the  $\text{Cu}_2\text{O}$ . For the intrinsic  $\text{Cu}_2\text{O}$ , the  $B_g^1$  mode is barely detected in the film annealed at  $350^\circ\text{C}$ , but the most intense are that attributed to  $\text{Cu}_2\text{O}$  phase. When annealing at  $450^\circ\text{C}$ , the Raman spectrum changes drastically and only peaks of  $\text{CuO}$  are visible, since all the distinctive modes of  $\text{Cu}_2\text{O}$  disappear. On the Mg doped  $\text{Cu}_2\text{O}$  set of samples, the detection of  $\text{CuO}$  is only visible at  $450^\circ\text{C}$ , and even at this temperature, the majority of  $\text{Cu}_2\text{O}$  peaks are still observed.

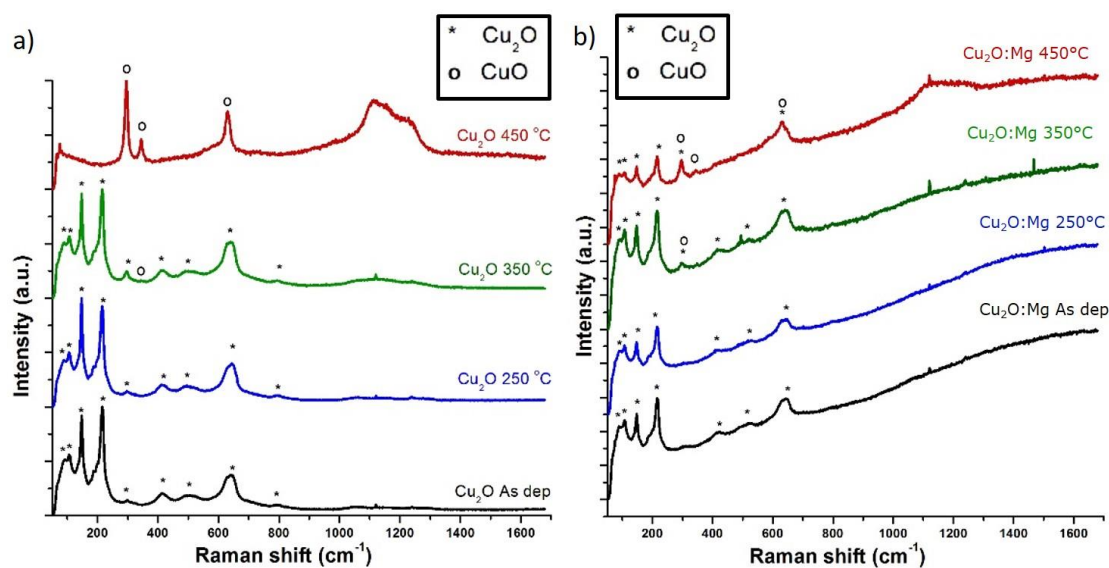


Figure IV-71 Raman spectra of the  $\text{Cu}_2\text{O}$  thin films on glass: a) intrinsic  $\text{Cu}_2\text{O}$ ; b) Mg doped  $\text{Cu}_2\text{O}$ .

The FTIR measurements were performed on films deposited on Si substrate to guarantee a transparency to infrared. In this case, only the as-deposited and the annealed ( $350^\circ\text{C}$ ) films were probed. Figure IV-72 shows the different spectra, with the bonds related to  $\text{Cu}_2\text{O}$ ,  $\text{CuO}$  and  $\text{MgO}$  phases indicated. As already described in the previous section, Mg-O are detected in the Mg doped films. The main difference in this group of samples is the detection of a bond ( $478\text{ cm}^{-1}$ ) related to  $\text{CuO}$  phase on the films annealed at  $350^\circ\text{C}$  which confirm the trend visible previously in GIXRD and Raman.

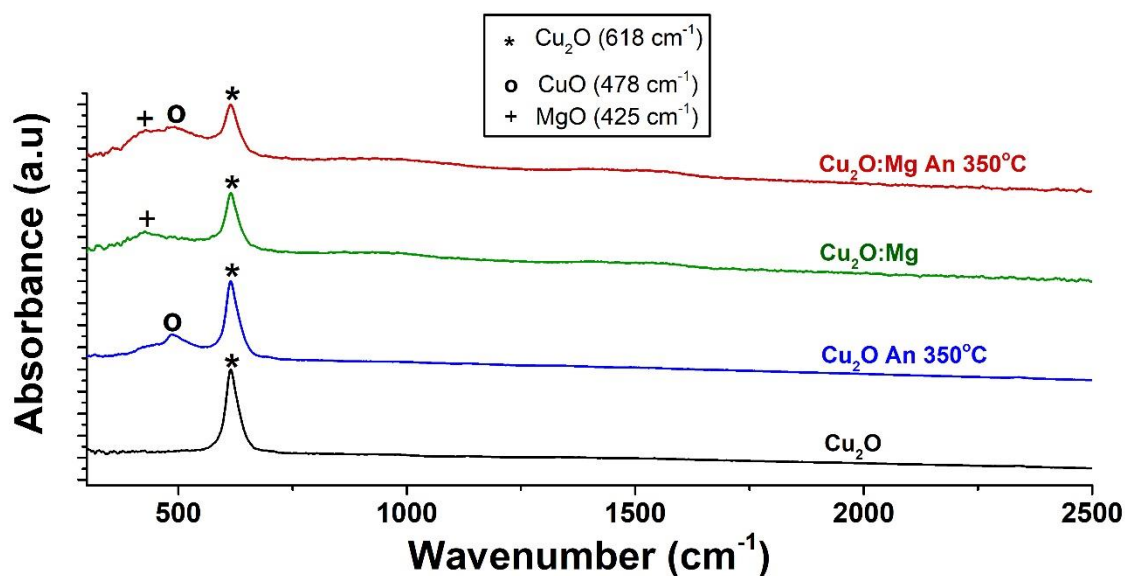


Figure IV-72 FTIR spectra of the  $\text{Cu}_2\text{O}$  thin films deposited on Si. Set of samples attributed to intrinsic and Mg doped  $\text{Cu}_2\text{O}$ , both as deposited and annealed at  $350^\circ\text{C}$ .

XPS provides the means of analysing the composition and the oxidation state of elements at the surfaces, probing the top 10 nm of a film. The surface of the as-deposited samples and those annealed at  $250^\circ\text{C}$  were probed by XPS in order to determine the Cu oxidation state ( $\text{Cu}^+$  in  $\text{Cu}_2\text{O}$  or  $\text{Cu}^{2+}$  in  $\text{CuO}$ ). The Cu oxidation state was analysed by the Cu  $2p_{1/2}$  spectra. The XPS results of the as-deposited and  $250^\circ\text{C}$  annealed samples are presented in Figure IV-73. The presence of  $\text{Cu}^{+2}$  is clearly identified when the doublet is accompanied by satellites at 940-945 eV<sup>23</sup>. The  $\text{Cu}^{+1}$  state or  $\text{Cu}^0$  presents a doublet at 932 eV with a low FWHM<sup>23</sup>. For the  $\text{Cu}_2\text{O}$  as-deposited sample, the satellites at 940-945 eV indicate the presence of  $\text{Cu}^{+2}$ . After the thermal treatment at  $250^\circ\text{C}$ , the intensity of  $\text{Cu}^{+2}$  satellite increases and the Cu  $2p_{3/2}$  peaks are additionally deformed, indicating an increase of  $\text{CuO}$  at the surface of the material. For the samples containing Mg, both as deposited and annealed at  $250^\circ\text{C}$ , satellites are not visible confirming that the films at the surface are formed only of deposited and annealed at  $250^\circ\text{C}$ , the peaks observed are only attributed to the presence of  $\text{Cu}_2\text{O}$ .

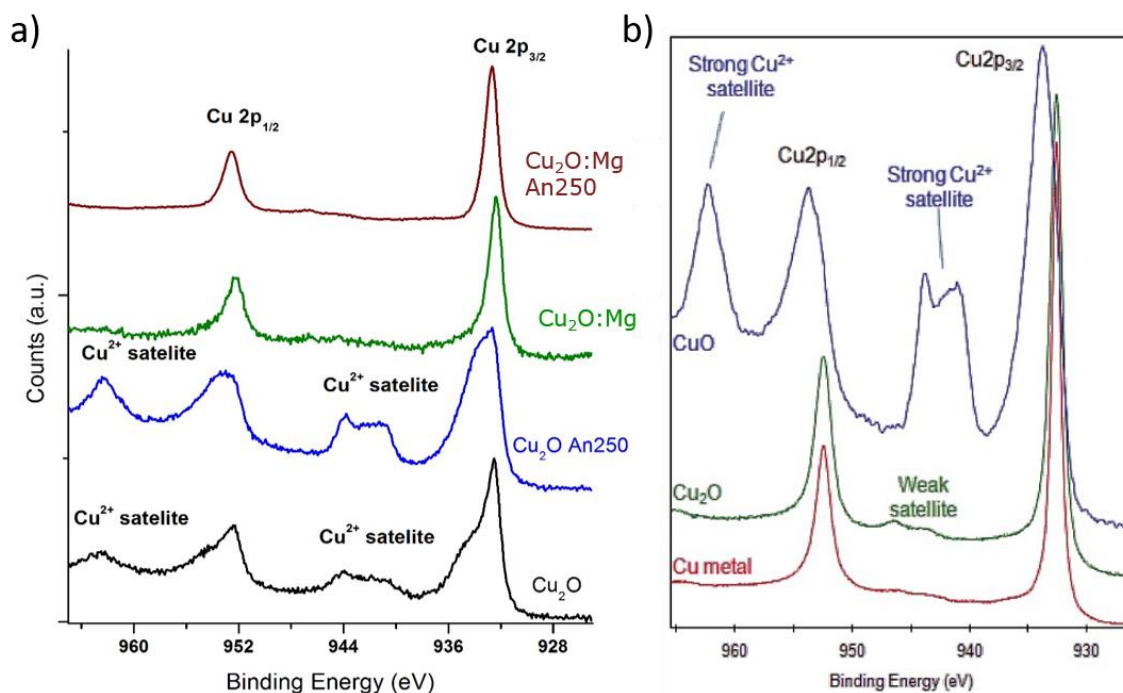


Figure IV-73 a) Cu 2p XPS spectra obtained for the  $\text{Cu}_2\text{O}$  thin films deposited on glass corresponding to intrinsic and Mg doped  $\text{Cu}_2\text{O}$ , both as deposited and annealed at  $250^\circ\text{C}$ . b) Reference spectra of metallic Cu,  $\text{Cu}_2\text{O}$  and CuO adapted from “[www.xpsfitting.com](http://www.xpsfitting.com)”

A complementary technique to XPS that allows to probe the full thickness of the sample and gives information about the chemical environment is EXAFS. This technique is available thanks to Synchrotron facilities in ESRF Grenoble. The two sets of  $\text{Cu}_2\text{O}$  samples were analysed and the Cu-K edge was registered. Two extra samples of  $\text{Cu}_2\text{O}$  and  $\text{Cu}_2\text{O}:\text{Mg}$  were annealed at  $500^\circ\text{C}$  for 30 minutes and analysed exclusively by this method, in order to have a complete CuO film. Athena software enables the treatment of the X-ray absorption near edge structure (XANES) raw data into EXAFS<sup>24</sup>. After applying a background removing, the representation of the Fourier transformations in  $k^2$  from 2 to  $14 \text{ \AA}^{-1}$  are presented in Figure IV-74. Each of the visible peaks can be attributed to a direct neighbour of Cu atom and the respective distance. Figure IV-74 a) shows the spectra related to  $\text{Cu}_2\text{O}$  undoped samples, annealed up to  $500^\circ\text{C}$ . Several changes are visible between the as-deposited and the annealed sample at  $500^\circ\text{C}$  in the neighbour distance comprised between 1 and  $4 \text{ \AA}$ . We will present here the hypothesis of the change induced by the oxidation of  $\text{Cu}_2\text{O}$  into CuO from the changes in the EXAFS spectra. In the first peak corresponding to a neighbour distance between 1 and  $2 \text{ \AA}$  and identified as the oxygen first neighbour (Cu-O 1<sup>st</sup>) for  $\text{Cu}_2\text{O}$  and CuO, we observe a change of intensity of the peak

combined with a small shift to the right with the high temperature annealing, above 450°C. These modifications are connected with the increasing number of O neighbouring atoms between the Cu<sub>2</sub>O and CuO, changing from 2 to 4, as well as a small increase of Cu-O distance, from 1.85 Å in Cu<sub>2</sub>O to 1.95 Å in CuO. In the second peak corresponding to a neighbour distance between 2 - 4 Å and attributed to copper neighbouring atoms (Cu-Cu 1<sup>st</sup>), small changes start to appear as a decrease of intensity of the peak with the lower temperature annealing. At temperatures higher than 450°C, with the transformation into CuO, this peak splits into two parts, possibly attributed to copper neighbours of higher order (1<sup>st</sup>, 2<sup>nd</sup> and 3<sup>rd</sup>), as well as 3<sup>rd</sup> order oxygen neighbours.

In the case of Cu<sub>2</sub>O:Mg, presented in Figure IV-74 b), similar considerations can be inferred for this system, since the first peak also increases in height, and the second peak splits into two. However, it is important to refer the differences in spectrum related to Cu<sub>2</sub>O:Mg annealed at 450°C. In this case, there is an intermediate state for both peaks, Cu-O 1<sup>st</sup> and Cu-Cu 1<sup>st</sup>, not detected before for the intrinsic Cu<sub>2</sub>O system.

In Figure IV-75, the spectra of the Cu<sub>2</sub>O and Cu<sub>2</sub>O:Mg group of samples were fitted using the combination of Cu<sub>2</sub>O and CuO pure EXAFS spectra provided by the boundaries samples of undoped Cu<sub>2</sub>O films and using the *Athena* software. This allowed to quantify the amount of each oxide depending on the annealing temperature. Until the annealing treatment at 350°C, both films present similar quantities of Cu<sub>2</sub>O, more than 85%; however the annealing stage at 450°C, shows drastic differences between the intrinsic and doped Cu<sub>2</sub>O. While in the Cu<sub>2</sub>O film, more than 95% of the film is already CuO, in the Mg -doped Cu<sub>2</sub>O a majority of 60% of the film is still Cu<sub>2</sub>O. This indicates a delayed or partially inhibited transition from Cu<sub>2</sub>O to CuO in the presence of the dopant. In the case of annealing at 500°C both films are mostly CuO, however with some residue of Cu<sub>2</sub>O in the Cu<sub>2</sub>O:Mg case.

The preliminary fitting of the Cu<sub>2</sub>O and CuO pure EXAFS spectra using *Artemis* software is presented in Appendix B.

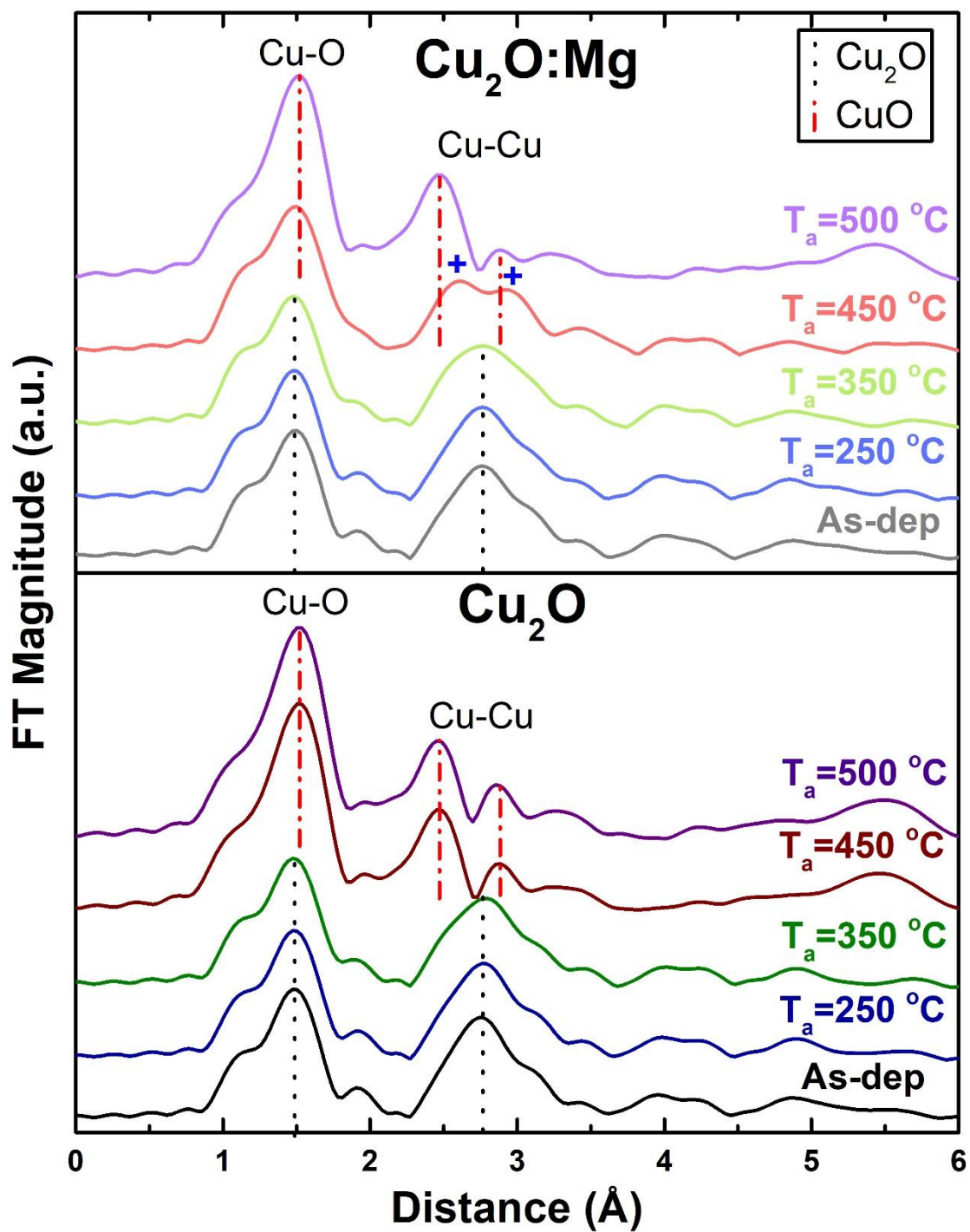


Figure IV-74 EXAFS raw data from Athena – a)  $\text{Cu}_2\text{O}$  and b)  $\text{Cu}_2\text{O}:\text{Mg}$

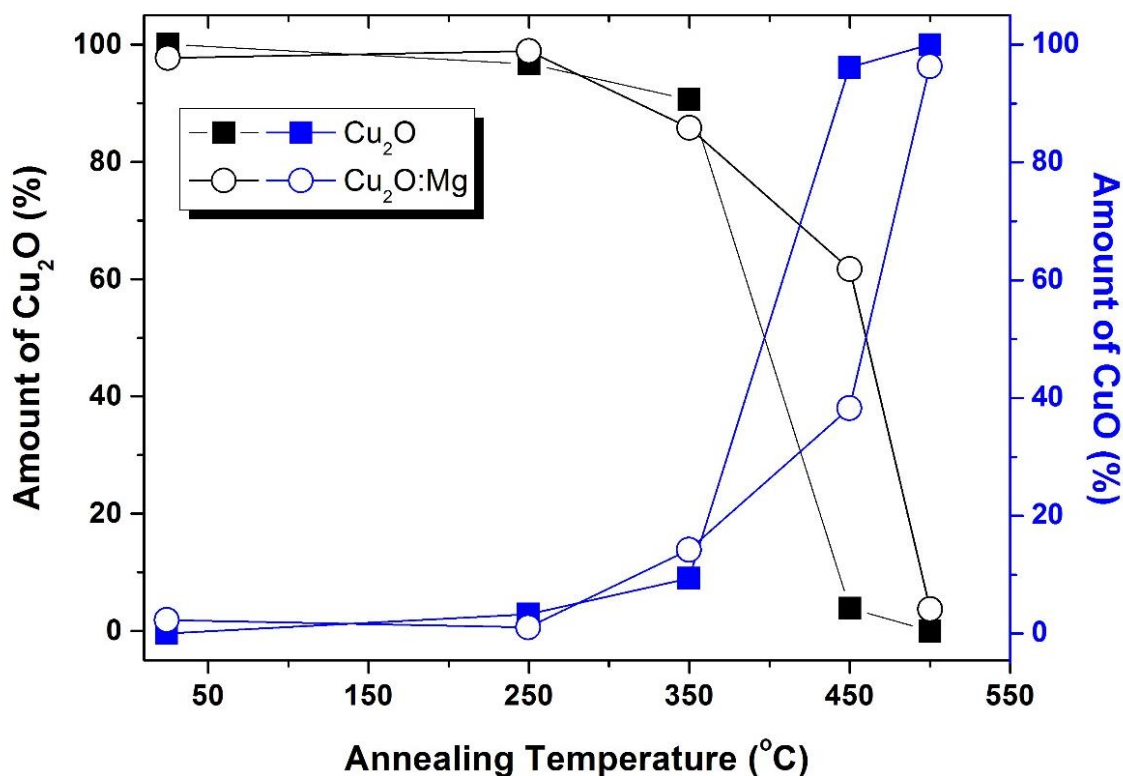


Figure IV-75 Fitting of EXAFS spectra from both  $\text{Cu}_2\text{O}$  group of thin films using pure  $\text{Cu}_2\text{O}$  and  $\text{CuO}$  EXAFS spectra

#### 4.2.3 Electric characterization under temperature

We use the monitoring of the electrical properties as an additional way to follow the transformation of  $\text{Cu}_2\text{O}$  into  $\text{CuO}$  *in situ* during the annealing step. As a matter of fact, the annealing at  $250^\circ\text{C}$  has been used previously to decrease the sheet resistance of our materials, but a complete evaluation of the effect during the annealing was still then lacking. We specifically devote this section to the task. For this study, the same as-deposited sample was cut in several pieces for the different annealing temperatures and the experiments were conducted with in-situ sheet resistance measurements using a 2-probe system. This setup allows us to observe the sheet resistance variation during the heating and cooling process, as well as the effect during the annealing step at a given temperature. The following graphs, presented in Figure IV-76 a) and b), show this variation for the three annealing temperatures, in the case of undoped and doped films, respectively. To compare the results we use the resistance at any time normalized by the initial value, given for each set of samples at the initial point of the curve. The sheet resistance values given for each curve correspond to the values obtained after annealing.

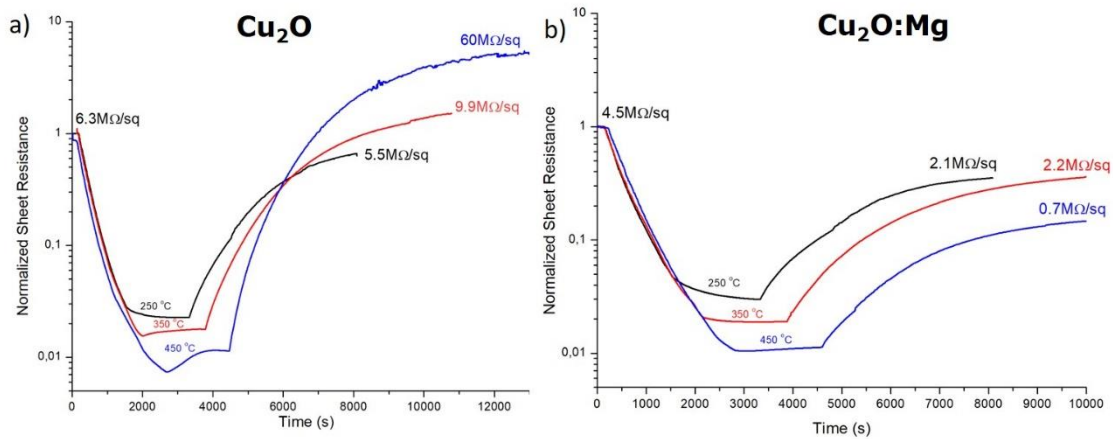


Figure IV-76 Normalized sheet resistance of the  $\text{Cu}_2\text{O}$  thin films during the 3 different annealing steps: 250°C, 350°C and 450°C. a) Intrinsic  $\text{Cu}_2\text{O}$  films; b) Mg doped  $\text{Cu}_2\text{O}$

In the  $\text{Cu}_2\text{O}$  samples and considering only the final sheet resistance, the most efficient annealing approach is the one performed at 250°C, since we obtain a lowering of the resistance during the annealing step, as well as a lower resistance value after the treatments are finished. The total reduction of the resistance with the annealing is 13%, leading to final sheet resistance of 5.5  $\text{M}\Omega/\text{sq}$ . These results corroborates the selection of the temperature for the optimization of temperature. Annealing at 350°C provokes an increase of resistance during the thermal stage, leading to a final resistance higher than the original film (57%). Finally, the annealing at 450°C leads to an even larger increase of resistance during the treatment, potentially attributed to the formation of  $\text{CuO}$ . The sample annealed at 450°C presents the worst electrical response.

We describe now the behaviour during the annealing step at constant temperatures, where the sheet resistance changes in different ways, picture in Figure IV-76 a). On the one hand, at 250°C we observe a constant decrease of resistance, while on the other hand, at 350°C and 450°C, the resistance initially decreases during the heating ramp, but immediately increases from the beginning of the thermal step. The decreases in resistance can be explained by a mechanism associated to the formation of copper vacancies at lower temperature, increasing the density free carriers and reducing the resistivity of the film. The increase of the resistance is related to the phase transformation from  $\text{Cu}_2\text{O}$  to  $\text{CuO}$  at higher temperature, which leads to a general increase of resistivity of the film.

Concerning the Mg doped films, presented in Figure IV-76b), we observe a different overall trend that contrasts with the intrinsic  $\text{Cu}_2\text{O}$  samples. The most efficient annealing treatment concerning the decrease of sheet resistance is the one performed at 450°C, with a reduction of 84% on sheet resistance, resulting in a film with 0.7  $\text{M}\Omega/\text{sq}$ . For

the three selected temperatures, we obtain a more conducting film than the original one after the thermal treatment. Additionally, if we analyse now the resistance behaviour during each step, it is observed that there is a decrease of resistivity for both 250°C and 350°C. This phenomenon can be attributed to copper vacancies generation, as previously stated for the intrinsic Cu<sub>2</sub>O. In the 450°C annealing curve, we have a slight increase of resistance during the thermal stage at the fixed temperature, probably related to the phase transformation from Cu<sub>2</sub>O to CuO, but nonetheless, this film present the lowest resistivity value after the annealing.

Using the variation of the resistivity during the heating and cooling down stages of the annealing treatment is possible to extract the activation energy in the two Cu<sub>2</sub>O types of film. The Arrhenius plots of resistivity in logarithmic scale for the intrinsic and doped Cu<sub>2</sub>O films are shown in Figure IV-77 a), b) and c) for the three annealing temperatures. The values of sheet resistance were converted into resistivity to correlate this results to Sr-doped Cu<sub>2</sub>O previously studied<sup>3</sup>. In a general analysis of all the annealing treatments, the slopes of the intrinsic Cu<sub>2</sub>O films are larger than the Cu<sub>2</sub>O:Mg films, during both heating and cooling stages, represented by the guided triangles in Figure IV-77 b). In the case of intrinsic Cu<sub>2</sub>O samples and for the films annealed at 250°C and 350°C the slopes during heating and cooling are similar; however, for the annealing at 450°C, the slope increases in the cooling process, especially at high temperatures (Figure IV-77c)). This phenomenon can be attributed to the higher quantity of CuO, formed at high temperature, which changes the resistivity behaviour under temperature variation. The samples containing magnesium present a different characteristic than that of undoped ones, in particular on the heating part. There is clearly a change of slope at around 170°C - in the graph at 2.25 (1000/K) - for all 3 annealing curves. By taking this into consideration, we separate the heating ramp of the annealing into different sections, one from room temperature to 170°C, and other from 170°C until the designated annealing temperature.

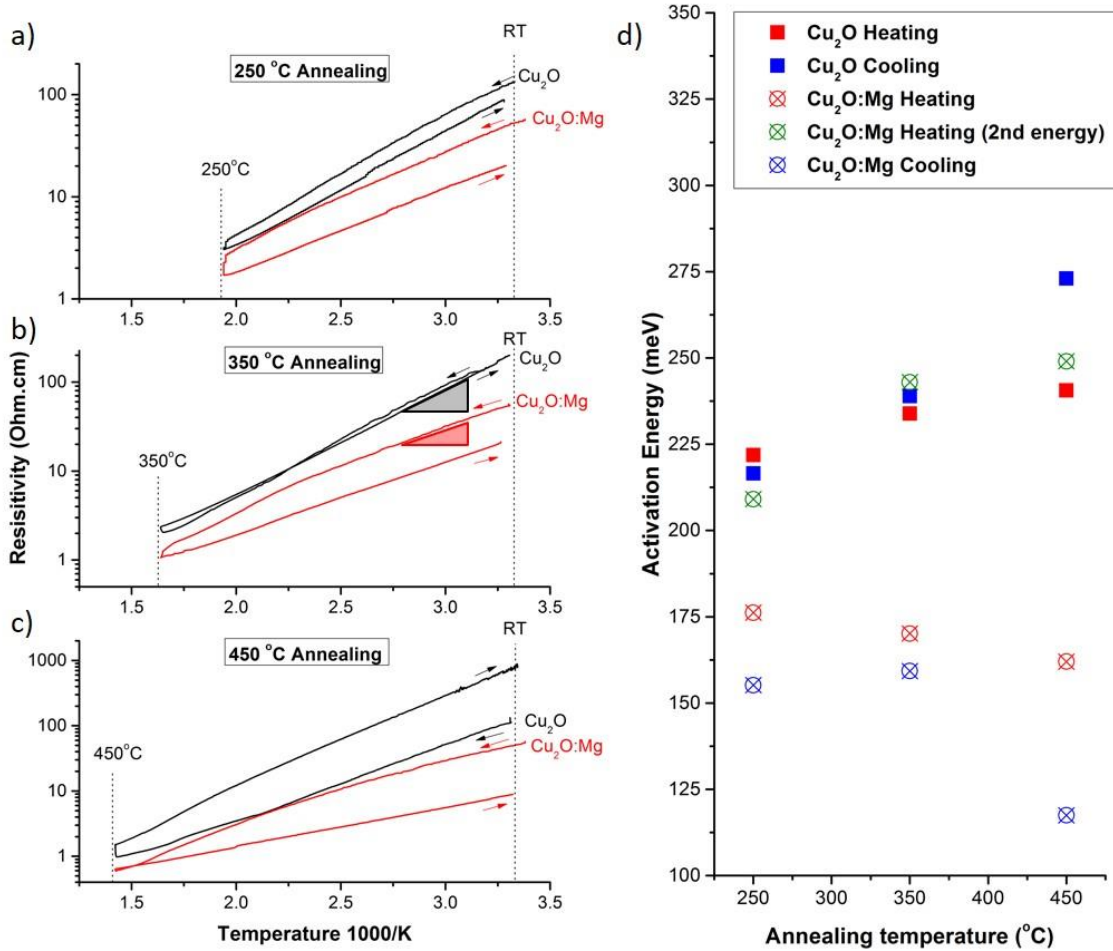


Figure IV-77 Dependence of the resistivity of the Cu<sub>2</sub>O thin films with temperature during the 3 different annealing treatments: a) 250°C, b) 350°C and c) 450°C. Grey and red triangles visible in b) to help the visualization of different slopes; d) activation energies for each sample during heating and cooling.

Similar to previous studies on Cu<sub>2</sub>O resistivity variation with temperature<sup>25</sup>, the linearization of these curves allow us to analyse through the use of an Arrhenius equation, needed to extract the activation energies.

$$\rho = \rho_0 e^{\frac{E}{k_b T}} \quad (IV.1)$$

where  $\rho$  is the resistivity,  $\rho_0$  a constant,  $E$  is the activation energy and  $k_b$  is the Boltzmann constant. In order to obtain this linearization, we depreciate the impact of the mobility dependence with temperature, which allows us to attribute the activation energy to the defects present in the film. The energies obtained from this fittings are plotted in the Figure IV-77d). We have calculated the energy obtained from curves under heating and cooling, but also taking into account the second slope visible in the Cu<sub>2</sub>O:Mg samples for temperatures higher than 170°C. For the variation of resistivity of undoped Cu<sub>2</sub>O films

under heating, the increase of slope with the temperature of annealing leads to values varying from 220 and 240 mV, which are normally attributed to the formation energy of simple copper vacancies,  $V_{Cu^-}$ , in theoretical <sup>1</sup> and experimental <sup>26</sup> studies. This effect is more evident in the activation energy obtained from the cooling step, reaching a value of 273 mV for the film annealed at 450°C.

As described before, in the Mg-doped Cu<sub>2</sub>O system, two different regimes are visible, with a temperature transition around 170°C. In the low temperature regime, the activation energy varies between 162mV and 176mV, while at higher temperature, the activation energy increases with the temperature, from 209mV to 250mV. This value is represented in Figure 27d) as Cu<sub>2</sub>O:Mg heating curve. The variation for temperatures higher than 170°C and labelled as Cu<sub>2</sub>O:Mg heating (2<sup>nd</sup> energy) leads to energies comparable with the heating activation energy for the intrinsic case (~170 mV). For the energy obtained from the cooling curves, we observe lower activation energies, below 160mV, which decrease down to 117mV, after the annealing treatment at 450 °C. This value is lower than that of the simple copper vacancy and it is comparable with the secondary defect observed in Cu<sub>2</sub>O:Sr <sup>3</sup> with an ionization energy of 133mV, as well as acceptor levels detected in Nitrogen doped Cu<sub>2</sub>O at an energy of 121 meV<sup>27</sup>.

To complete the characterization of the electrical properties of the samples and to evaluate the effect of the annealing on the mobility and free charge carrier concentrations, the samples were analysed by *ex situ* Hall Effect. All samples showed p-type behaviour. Figure IV-78 shows the resistivity of the two group of films, measured at room temperature.

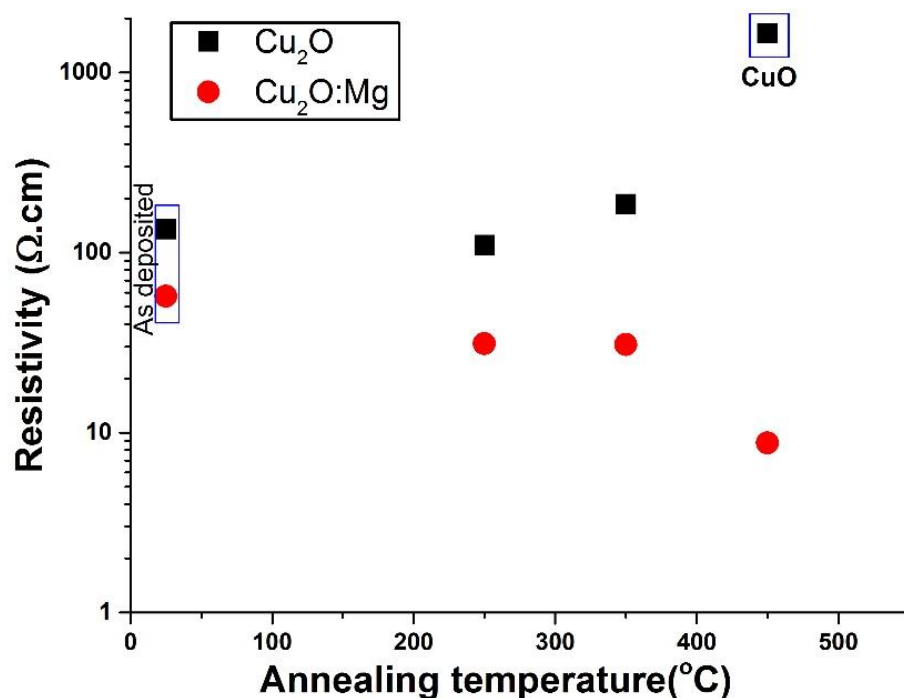


Figure IV-78 Resistivity dependence on the temperature of the annealing treatments for Cu<sub>2</sub>O and Cu<sub>2</sub>O:Mg thin films.

As previously observed in the resistance measurements, the resistivity of the intrinsic Cu<sub>2</sub>O shows a minimum in the film annealed at 250°C, followed by a drastic increase up to 1000 Ω.cm. Concerning the 18% Mg doped film, the lowest point is visible at 450°C, with a value in the 10 Ω.cm range.

Figure IV-79 a) and b) shows the effect of the annealing temperature on mobility and charge carrier density, respectively, of the intrinsic and Mg-doped Cu<sub>2</sub>O films. It was not possible to perform the Hall Effect characterization on the Cu<sub>2</sub>O film annealed at 450°C due to high resistivity values. Concerning the mobility of Mg-doped Cu<sub>2</sub>O films an increase from 1 to 4 cm<sup>2</sup>.V<sup>-1</sup>.s<sup>-1</sup> with annealing temperature is observed; while in the undoped case, the mobility is maintained roughly constant around 9 cm<sup>2</sup>.V<sup>-1</sup>.s<sup>-1</sup>. The free charge carrier density, associated mainly to holes, varied with the two group of samples. On the one hand, the Cu<sub>2</sub>O showed a maximum of charge-carriers density of 6x10<sup>16</sup> cm<sup>-3</sup> at 250°C, followed by a decrease when annealed at higher temperature. While on the other hand, the Mg-doped Cu<sub>2</sub>O films show a general increase of charge carries, presenting the higher value for the film annealed at 450°C, close to 2x10<sup>17</sup> cm<sup>-3</sup>.

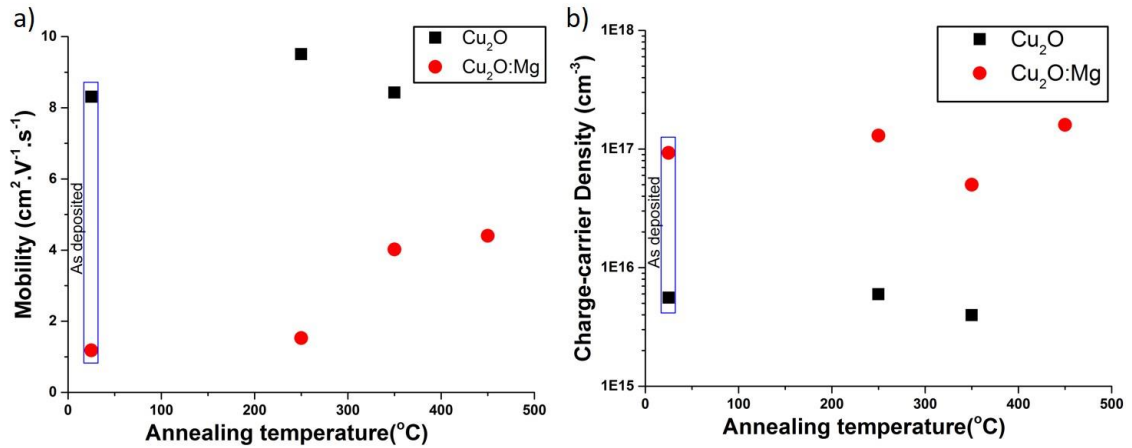


Figure IV-79 a) Mobility and b) charge carriers density dependence on the temperature of the annealing treatments for  $\text{Cu}_2\text{O}$  and  $\text{Cu}_2\text{O}:\text{Mg}$  thin films.

#### 1.4.4 Discussion

The effect of magnesium incorporation on the stability of the  $\text{Cu}_2\text{O}$  phase under different annealing treatments was studied in order to clarify the mechanism of  $\text{CuO}$  formation. Apart from the surface oxidation detected by XPS on samples as-deposited or annealed at  $250^\circ\text{C}$ , the temperature of the formation of  $\text{CuO}$  is similar, starting below  $350^\circ\text{C}$ , in both intrinsic and Mg doped films. This was confirmed by XRD, Raman, EXAFS and indirectly by resistance measurements. However, the formation of  $\text{CuO}$  occurs in a different way between the two sets of films. In intrinsic  $\text{Cu}_2\text{O}$  films at high temperature, the formation of grains attributed to  $\text{CuO}$  is generalized at the surface of the film, while in the Mg-doped films the grains are only formed on a fraction of the surface. This leads to a difference of resistivity behaviour at  $350^\circ\text{C}$ ; a significant reduction of resistivity is caused in the doped samples, while the intrinsic films become more resistive when the  $\text{CuO}$  phase is present. When the annealing temperature increases to  $450^\circ\text{C}$ , the undoped  $\text{Cu}_2\text{O}$  films show a dominant content of  $\text{CuO}$ , increasing drastically its resistivity. In the opposite way, the magnesium-doped  $\text{Cu}_2\text{O}$  films maintained a higher fraction of  $\text{Cu}_2\text{O}$  combined with low resistivity values in the  $10 \Omega.\text{cm}$  range.

The different behaviours between the two sets of samples led us to deduce two distinct mechanisms for the  $\text{CuO}$  formation. On the one hand, the intrinsic  $\text{Cu}_2\text{O}$  starts to form  $\text{CuO}$  by oxidation at the surface and interior of the film. At the surface the  $\text{Cu}^+$  cations are easily oxidized into  $\text{Cu}^{2+}$  in contact with oxygen forming new grains of  $\text{CuO}$  phase. Though in the film, the formation of split copper vacancies induces the formation of  $\text{Cu}^{2+}$  centres, which creates  $\text{CuO}$  nucleation centres inside the grains. In a first stage, the split

copper vacancies leads to an inefficient generation of free holes due to the highly localized character of this defect, which later contributes for a large increase of resistivity by the formation of the parasitic phase throughout the film. The electric transport measurements confirm this hypothesis, due to the increase of resistivity during the annealing stage at 350°C.

On the other hand, in the presence of Mg, the transformation seems to start at the surface of the film, while in the interior of the film, simple copper vacancies are the major defects to be created, facilitated by the presence of the dopant. The large creation of simple copper vacancies increases the number of free charge carriers and consequently reduces the resistivity. As suggested by Isseroff and Carter, doping with Mg can prevent the formation of split vacancies for a single cation vacancy, since the divalent cation would assume a position similar to a split copper vacancy in the crystallographic structure<sup>13</sup>. This fact seems to be confirmed by the low resistivity of the films, even when the surface is covered by the CuO phase. Additionally, the XRD shift detected after the annealing at 450°C can suggest an activation of this mechanism by the changes in crystallographic structure. The inhibition to create split vacancies would reduce the parasitic centres inside the film, being the main mechanism for conduction loss during the annealing stages.

Furthermore, the first activation energy associated to Cu<sub>2</sub>O:Mg of 165mV can be compared to the energy value of a large size impurity–vacancy complex found previously in the Sr-doped system 133mV<sup>3</sup>. One type of defect that can explain this energy is a clustering of a second simple vacancy with the dopant,  $[\text{Mg}_{\text{Cu}} - 2 \cdot \text{V}_{\text{Cu}}]^-$ , which has been suggested by Isseroff and Carter<sup>13</sup>.

The use of EXAFS by synchrotron radiation at ESRF in Grenoble was additionally fundamental to clarify the crystallographic changes with the presence of the dopant as well as the mechanism for phase transformation between Cu<sub>2</sub>O and CuO. Nevertheless the creation of a crystallographic model to fit the data is still ongoing. The combination of these stability results with the changes in conductivity previously discuss can provide a way to better apply this material both in solar cells and electronics, or even new copper oxide-based devices.

## 4.3 Cu<sub>2</sub>O:Mg/ZnO heterojunctions

### 4.3.1 Introduction

The lack of a stable n-type semiconductor Cu<sub>2</sub>O thin film, diminished drastically the possibility of solar cells production based on copper oxide homojunctions. This fact can be overcome by the use of a different n-type semiconductor that present a band alignment compatible with Cu<sub>2</sub>O to form a heterojunction. ZnO, as an n-type semiconductor oxide, can be combined with Cu<sub>2</sub>O, which in this case work as p-type absorber material, due to the lower band-gap. The maximum theoretical efficiency of a ZnO/Cu<sub>2</sub>O solar cells is as high as 20%<sup>28</sup>, however the maximum value achieved by functional devices is only 4.12%<sup>29</sup> for an intrinsic ZnO/Cu<sub>2</sub>O junction [2], which was recently increase to 8.1% in a MgF<sub>2</sub>/ZnO:Al/Zn<sub>0.38</sub>Ge<sub>0.62</sub>O/Cu<sub>2</sub>O:Na heterojunction<sup>30</sup>. Besides, this record of efficiency was achieved by thermal oxidized Cu<sub>2</sub>O, a process that creates large grains in the tens of microns range, reducing the fraction of grain boundaries and increasing the mobility. However, this technique is not suitable for large scale production, since it requires very high temperatures, around 1000 °C<sup>31</sup>. Therefore, the use of chemical deposition techniques for the deposition of Cu<sub>2</sub>O combined with the possibility of depositing ZnO at low temperature pave the way for future implementation of a cost-efficient oxide based solar cells.

The Mg-doped Cu<sub>2</sub>O study, previously discussed, provided two essential results that can have a significant impact in the electrical behaviour of *pn* junctions. On the one hand, the presence of the cation contributed to a higher stability of the Cu<sub>2</sub>O phase, reducing the appearance of CuO parasitic phase. This phase is reported to reduce the performance of an oxide-based solar cell, due to the creation of highly conductive paths in the grains boundaries that short-circuit the device<sup>32</sup>.

On the other hand, the Cu<sub>2</sub>O:Mg thin films showed a high charge-carrier density, up to  $8 \times 10^{17} \text{ cm}^{-3}$ , due to a doping mechanism based on copper vacancy assisted cation incorporation. The larger density of charge carriers (holes) can have an important contribution to an increase of efficiency on a Cu<sub>2</sub>O based solar cell, by reducing the size of the depletion region<sup>33</sup>. This enables a higher electric field and charge collection throughout the cell, by reducing the number of charges lost due to recombination and higher reflection in the back electrode<sup>33</sup>.

As proof of concept, we first simulated a *pn* junction of intrinsic and Mg-doped Cu<sub>2</sub>O on n-type ZnO in a semi-classical approach using numerical simulations based on a finite-difference scheme. For the experimental part, we fabricated these structures by combining the Mg-doped Cu<sub>2</sub>O thin films with ZnO, deposited by pulsed injection metal organic chemical vapour deposition (PI-MOCVD) and by spatial atomic layer deposition (SALD), in order to study the rectifying response of these structures. More specifically, two different structures were studied, *pn* and *np*, in order to understand the electric and optical impact on the device. The study is completed by photovoltaic tests to evaluate the possible application of these structures into solar cells.

### 4.3.2 Simulation of a *pn* junction formed by Cu<sub>2</sub>O/ZnO

Formerly to the fabrication of *pn* junctions experimentally, we decided to simulate the band structure and consequent diode response of these two materials. The simulations of this semiconductor device were based on a mathematical model, using the so-called basic semiconductor equations. The semiconductors must be non-degenerated, with a general behaviour, without any particular assumptions, derived from Maxwell-Boltzmann statistical relations and Maxwell's equations. A numerical solution of the system of basic semiconductor equations is then obtained through a finite-differences method. The simulation was a semi-classical approach to the problem, where we took into account the conservation of charge and mass<sup>34</sup>. The equations are solved in the steady-state regime where the applied voltage is constant, which additionally allows to solve the system in reverse and forwards bias situations.

The group of parameters selected for the two semiconductors were based other works<sup>35,36</sup>, properties of samples fabricated and measured in our labs and general assumptions for *pn* junctions. We assumed a thickness between 200 nm and 1 μm for each film, with values for band-gap energy, mobility, permittivity and effective mass referred in the literature<sup>35,36</sup>. The concentration of defects, both in the interface and trap states was assumed as minimum at a level of 10<sup>10</sup> cm<sup>-3</sup>, to avoid significant contributions to the simulation, while the capture cross section and radiative recombination coefficient were based on *pn* junctions formed by group IV semiconductors<sup>37</sup>. Therefore, in Table IV-10, all the different fixed parameters for the simulation are represented.

## Chapter IV: Magnesium-doped cuprous oxide thin films

Table IV-10 List of constant unvaried during the simulations

<b>Material</b>	<b>Cu<sub>2</sub>O</b>	<b>ZnO</b>
Band Gap (eV)	2,17	3,4
Defects interface (cm <sup>-3</sup> )	1x10 <sup>10</sup>	1x10 <sup>10</sup>
Defects traps (cm <sup>-3</sup> )	1x10 <sup>10</sup>	1x10 <sup>10</sup>
Mobility electrons (cm <sup>2</sup> .V <sup>-1</sup> .s <sup>-1</sup> )	1	10
Mobility holes (cm <sup>2</sup> .V <sup>-1</sup> .s <sup>-1</sup> )	1	10
Relative permittivity	18,1	10,8
Electrons effective mass	0,99	0,3
Holes effective mass	0,58	0,5
Capture cross section (cm <sup>2</sup> )	1x10 <sup>-12</sup>	1x10 <sup>12</sup>
Radiative recombination coefficient (cm <sup>3</sup> .s <sup>-1</sup> )	1x10 <sup>-11</sup>	1x10 <sup>-11</sup>

Here, we discuss two main simulations where the varied parameters are the acceptors concentrations in the p-type semiconductors to simulate intrinsic and doped conditions for Cu<sub>2</sub>O. Considering the previous deposited Cu<sub>2</sub>O:Mg films, we defined the density of acceptors to be from 5x10<sup>15</sup>cm<sup>-3</sup> to 8x10<sup>18</sup>cm<sup>-3</sup> in intrinsic and doped cases, respectively. For ZnO, we used well establishing values from materials previously obtained in Grenoble LMGP<sup>38</sup>, around 10<sup>19</sup>cm<sup>-3</sup><sup>38</sup>. Additionally, the size of the simulated device was adapted to the width of the depletion region between the two cases. These parameters are represented in Table IV-11 and Table IV-12.

Table IV-11 Simulation A - parameters simulating the intrinsic case: Cu<sub>2</sub>O and ZnO films

	<b>Cu<sub>2</sub>O</b>	<b>ZnO</b>
Thickness (μm)	2	2
Acceptors density (cm <sup>-3</sup> )	5x10 <sup>15</sup>	1x10 <sup>10</sup>
Donors density (cm <sup>-3</sup> )	1x10 <sup>10</sup>	1x10 <sup>19</sup>

Table IV-12 Simulation B - parameters simulating the doped case: Cu<sub>2</sub>O:Mg and ZnO films

	<b>Cu<sub>2</sub>O:Mg</b>	<b>ZnO</b>
Thickness (μm)	0.2	0.2
Acceptors density (cm <sup>-3</sup> )	8x10 <sup>17</sup>	1x10 <sup>10</sup>
Donors density (cm <sup>-3</sup> )	1x10 <sup>10</sup>	1x10 <sup>19</sup>

The band diagram and charge concentrations for simulation A are plotted in Figure IV-80. In the  $\text{Cu}_2\text{O}$  case, the band diagram shows the formation of a depletion region mostly on the  $\text{Cu}_2\text{O}$  side, as the concentration of acceptors is lower, compared to the donors on  $\text{ZnO}$ . Consistently to what was suggested in the literature<sup>33</sup>, this region is larger than  $1\ \mu\text{m}$  in intrinsic  $\text{Cu}_2\text{O}$  reaching up to  $3\ \mu\text{m}$  in weakly, non-intentionally, doped  $\text{Cu}_2\text{O}$ ,  $10^{14}\ \text{cm}^{-3}$ .<sup>3</sup> The concentration of electrons and holes in Figure IV-80b) represents the expected profile of majority carriers in both semiconductors, holes in  $\text{Cu}_2\text{O}$  and electrons in  $\text{ZnO}$ , with an abrupt variation especially in the n-type side case.

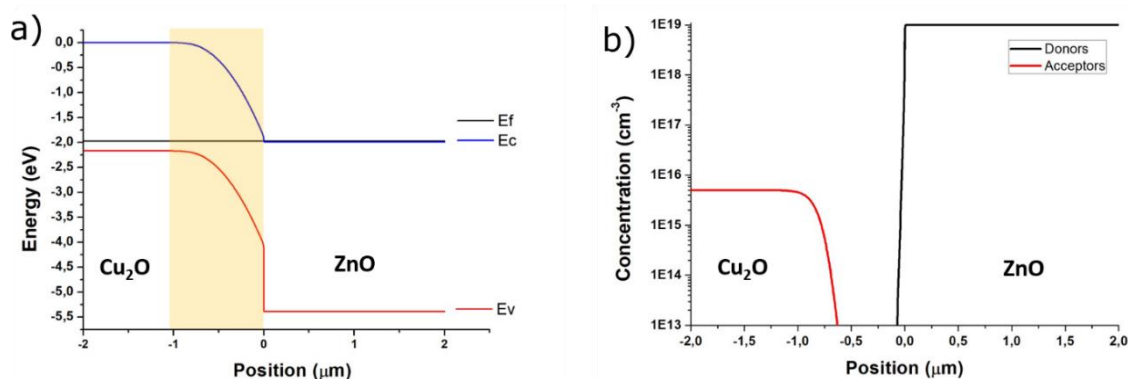


Figure IV-80 a) Band diagram and b) defects concentration of simulation A  $\text{Cu}_2\text{O}$  thin film with low density of acceptors. Depletion region is represented at yellow in figure a)

When we increase the density of acceptors in the  $\text{Cu}_2\text{O}$  side, in order to produce a highly doped film, the size of the depletion region is drastically reduced. As represented in Figure IV-81a), when the acceptors concentration reaches about  $10^{18}\ \text{cm}^{-3}$ , the region depleted in the device shrinks to a width below  $100\text{nm}$ , with a visible small fraction on the  $\text{ZnO}$  side. This confirms the predictions that a highly-doped  $\text{Cu}_2\text{O}$  would reduce the depletion region for several hundreds of nanometres. Also, as expected, the position of the Fermi level is closer to the valence band of  $\text{Cu}_2\text{O}$ .

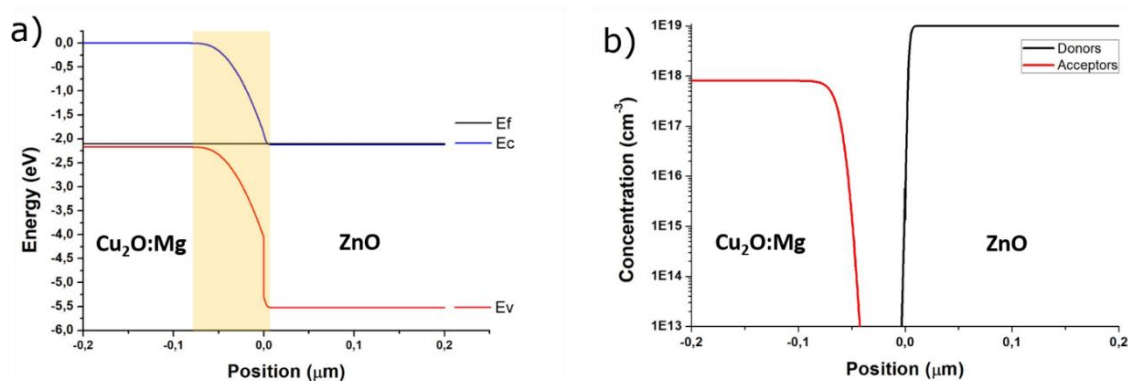


Figure IV-81 a) Band diagram and b) defects concentration of simulation B -  $\text{Cu}_2\text{O}:\text{Mg}$  thin film with high density of acceptors on  $\text{ZnO}$

By applying a bias voltage to the model, we can predict the diode behaviour of the system, as well as the deformation in the band diagram. In Figure IV-82a), the band diagram of Cu<sub>2</sub>O:Mg/ZnO structure is shown under an applied bias of +2.0V. In this case, the depletion region is reduced severely, which results in a total current density passing through the junction of 90 A.cm<sup>-2</sup>, as shown in Figure IV-82b).

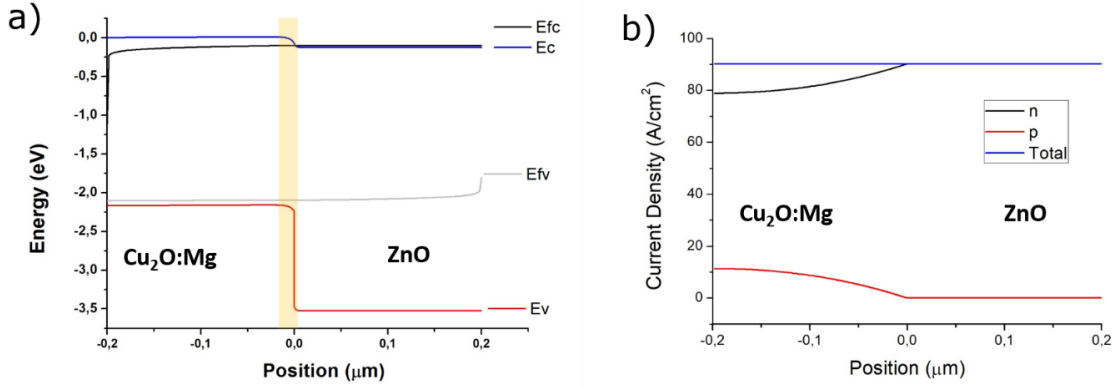


Figure IV-82 a) Band diagram and b) Current Density throughout the device of simulation B Cu<sub>2</sub>O:Mg thin film with high density of acceptors on ZnO thin film under an applied bias of +2.0V

The J-V curve of the two simulated diodes are shown in Figure IV-83. For weak applied voltages, 0 to 1.2V, the low value of the current is caused by the limitation of the numerical simulation. In the rectifying part, above 1.2V, we observe an exponential curve that follows the expected diode equation:

$$J = J_0 \left( e^{\frac{q(V-JA R_s)}{nk_b T}} - 1 \right) \quad (IV.2)$$

where  $J$  is the current density,  $J_0$  the reverse current density,  $q$  the electron charge,  $V$  the applied voltage,  $A$  the contact area,  $R_s$  the series resistance,  $n$  the non-ideality factor,  $k_b$  the Boltzmann's constant and  $T$  the absolute temperature.

Even if the slope are the same and represent a non-ideality factor of 1, it is important to refer the differences in series resistance. In the Cu<sub>2</sub>O case, we observe a change in slope at higher applied voltages, caused by the higher series resistance of the Cu<sub>2</sub>O layer. This fact is originated by the lower density of charge carriers in the oxide and the large width of this junction, which results in an increase of the total resistance.

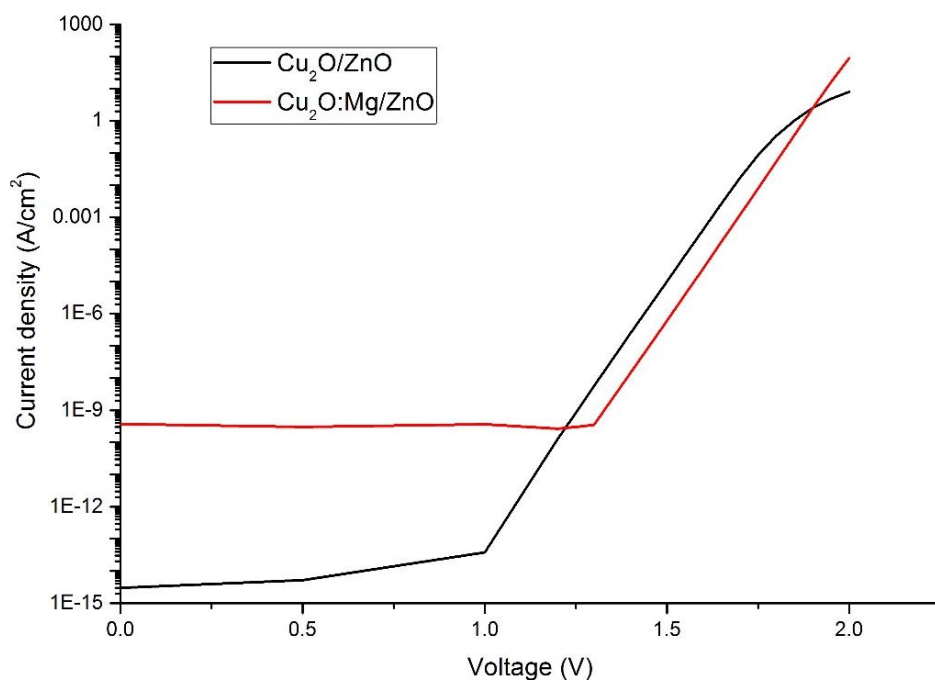


Figure IV-83 JV curve of both simulated diodes  $\text{Cu}_2\text{O}/\text{ZnO}$  and  $\text{Cu}_2\text{O}:\text{Mg}/\text{ZnO}$  between 0 and 2V

### 4.3.3 Deposition of *pn* junction formed by $\text{Cu}_2\text{O}/\text{ZnO}$

The fabrication of all oxide *pn* junctions were performed in two different architectures using a different technique for the deposition of n-type ZnO. In both cases, the oxide films were deposited on an ITO covered glass ( $15 \Omega/\text{sq}$ ) used as bottom electrode and finished by two gold contacts thermally evaporated with a diameter of 3 mm. In some specific cases, silver paste was also used to form metallic electrode, due to short-circuit in the evaporated contacts.

In the first structure, visible in Figure IV-84a), the initial layer consisted in a ZnO film deposited by Pulsed Liquid Injection Metal Organic Chemical vapour deposition (PI-MOCVD) at  $400^\circ\text{C}$  into an Annealsys MC-200 reactor. The optimization of PI-MOCVD for the deposition of ZnO films have been previously by Thomas Cossuet. These films of intrinsic ZnO films present a resistivity of  $10^{-1} \Omega\cdot\text{cm}$ . Afterwards, intrinsic and Mg-doped (18%)  $\text{Cu}_2\text{O}$  films were deposited by AA-MOCVD at  $350^\circ\text{C}$ , as described previously for the stability study, for 3 hours in order to achieve thickness values close to 300nm. In order to increase the free carrier's density in 18%  $\text{Cu}_2\text{O}:\text{Mg}$ , an annealing at  $250^\circ\text{C}$  for 2 hours was performed in the complete device.

The second structure used to test the *pn* junction response was inversed due to the deposition temperatures of the processes, visible in Figure IV-84b). The  $\text{Cu}_2\text{O}$  was first

deposited, followed by a layer of ZnO, in this case by Spatial Atomic Layer Deposition (SALD), visible in Figure IV-84b). The n-type semiconductor was deposited at 200°C with diethylzinc ((C<sub>2</sub>H<sub>5</sub>)<sub>2</sub>Zn; DEZ) and water vapour (H<sub>2</sub>O) as precursors for zinc and oxygen, respectively. N<sub>2</sub> was used as carrier gas for both precursors. The distance between injector and substrate was set to 100 μm, while the sample oscillates under the injector at 8-12 cm/s. The SALD ZnO thin films present resistivity values of 5 x 10<sup>-2</sup> Ω.cm, with a mobility close to 2 cm<sup>2</sup>.v<sup>-1</sup>.s<sup>-1</sup>. More details of ZnO deposition by SALD are available in Nguyen et al. (2017) <sup>38</sup>.

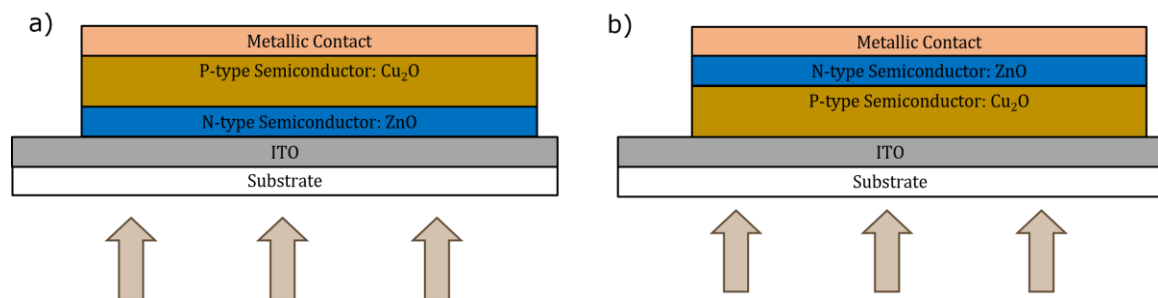


Figure IV-84 pn structures created for Cu<sub>2</sub>O based pn junction study: a) 1<sup>st</sup> – glass/ ITO / ZnO (MOCVD) / Cu<sub>2</sub>O / metal/; b) 2<sup>nd</sup> – glass/ ITO / Cu<sub>2</sub>O / ZnO (SALD) metal. Direction of illuminated light represented by brown arrows

The use of different thin films stacking order was constructed to understand the impact of ZnO as absorbing layer. Since the n-type film presents a higher band gap of 3.4 eV in the UV range, the change of order under solar illumination could increase the light absorption, 1<sup>st</sup> structure, which can result in higher efficiency of the cell.

The use of two separate technique is then justified by the temperatures required to deposit each film. As ZnO by MOCVD was to be deposited at 400°C, it is not possible to process it after Cu<sub>2</sub>O due to formation of CuO, previously discussed. Additionally, ZnO is stable at 350°C, temperature used for Cu<sub>2</sub>O deposition, so we would preserve the general properties of the film. Nevertheless, it is important to report the possible slight changes in charges carries concentrations or mobility of ZnO during heating before the Cu<sub>2</sub>O deposition. The ZnO deposited by SALD allow the use of lower temperatures, 200°C, where Cu<sub>2</sub>O is still stable, therefore the inverse structure could be fabricated.

#### 4.3.3.1 1<sup>st</sup> Structure: ZnO (PI-MOCVD) and Cu<sub>2</sub>O:Mg (AA-MOCVD)

A photograph of the first structure is shown in Figure IV-85, where the ITO uncoated layer is visible in the edge, used for bottom contact. The ZnO film covers the rest

of the transparent part of the device, while the central square of  $\text{Cu}_2\text{O}$  was masked during deposition. Finally, the structure is completed by a circular Au contact of with 3mm diameter, thermally evaporated.

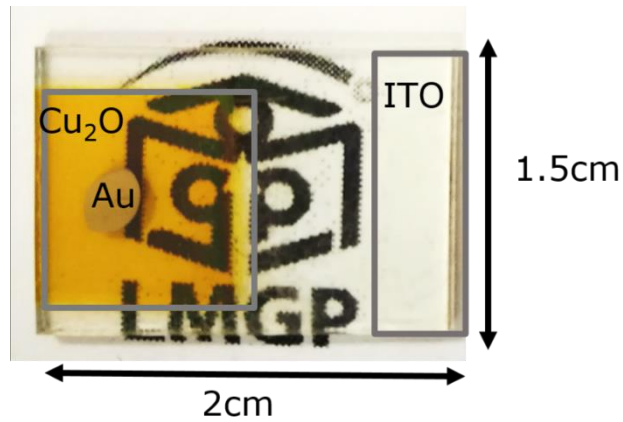


Figure IV-85 Photograph of the first structure: glass / ITO / ZnO (MOCVD) /  $\text{Cu}_2\text{O}$  / Au.

The general morphology of the layer stack before device fabrication is visible by SEM micrograph, presented in Figure IV-86. The two top-view images of  $\text{Cu}_2\text{O}$  and  $\text{Cu}_2\text{O}:\text{Mg}$  heterostructures, Figure IV-86 a) and c) respectively, show a granular structure, however the grains are more visible in the Mg-doped case. Regarding the cross-section images, Figure IV-86 b) and d), the ZnO film has a thickness of 360nm in both doped and intrinsic case. In the p-type semiconductor a slight difference in thickness is detected, with the  $\text{Cu}_2\text{O}$  presenting 260 nm while the  $\text{Cu}_2\text{O}:\text{Mg}$  shows a thicker layer of 330 nm.

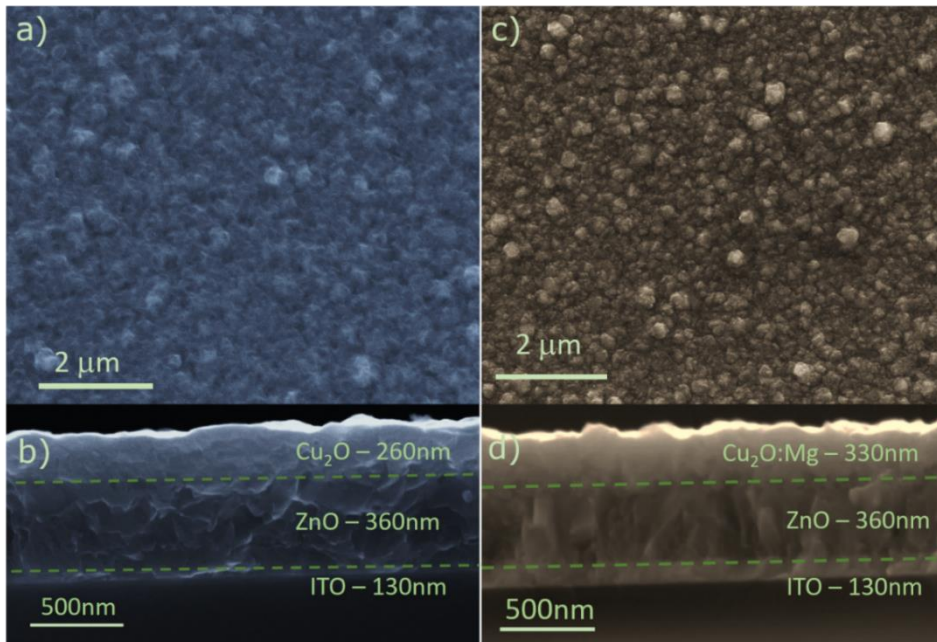


Figure IV-86 SEM micrograph of the top and cross section of a heterostructure of ZnO and  $\text{Cu}_2\text{O}$  (a) and b)) and  $\text{Cu}_2\text{O}:\text{Mg}$  (c) and d))

Complementary analysis was done in parallel by WDS, where the presence of Mg in  $\text{Cu}_2\text{O}$  film was quantified as 18% in total number of cations,  $(\text{Mg}/\text{Cu}+\text{Mg})$ . The EDS elemental mappings of  $\text{ZnO}/\text{Cu}_2\text{O}:\text{Mg}$  junction are presented in Figure IV-87, showing the interface between Zn and Cu in this architecture.

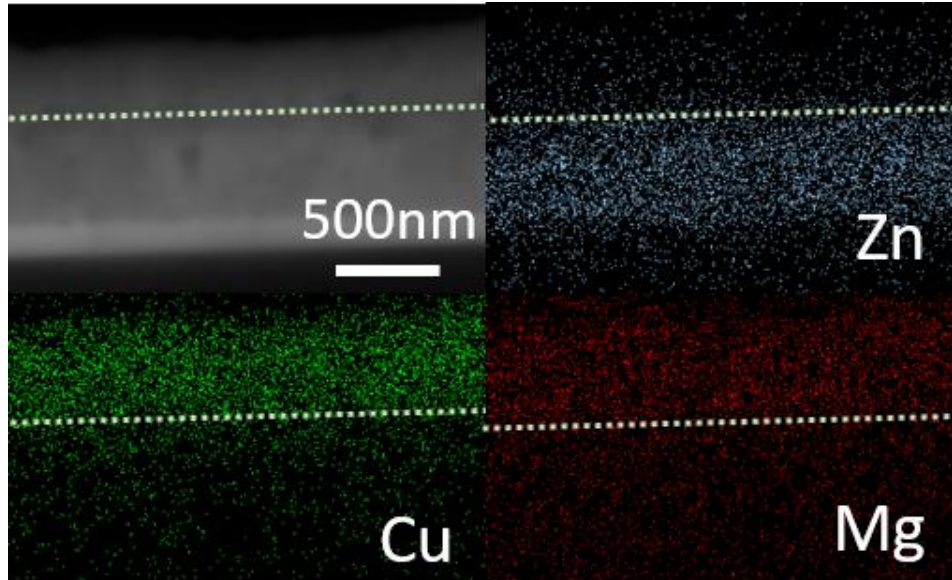


Figure IV-87 SEM micrograph of the cross section and mappings obtained by EDS of the  $\text{Cu}_2\text{O}:\text{Mg}/\text{ZnO}$  junction

The XRD of the *pn* junction is visible in Figure IV-88 a). The peaks of  $\text{Cu}_2\text{O}$  and  $\text{ZnO}$  are detected, confirming the presence of the two oxides in the device. The transmittance spectrum of the  $\text{Cu}_2\text{O}:\text{Mg}/\text{ZnO}$  junction is represented in Figure IV-88 b) with additional spectra of the glass, ITO and  $\text{ZnO}$  film. The graph shows a decrease of transmittance with each added layer as expected. Up to the deposition of the  $\text{ZnO}$  film, the structure is still highly transparent in the visible range of the spectrum, with a total transmittance of 76%. This is due to the wide band gap energies of both ITO and  $\text{ZnO}$  films, which are higher than 3.3 eV. The deposition of a 330nm layer of  $\text{Cu}_2\text{O}$  reduces drastically the transmittance to 35%, especially in the blue range. The fringes visible are due to refractive phenomena of each film's thickness and between the different films. The absorption of each curve is directed associated to the material present in the structure, therefore, the ITO has a band-gap to 4.2,  $\text{ZnO}$  of 3.4eV and  $\text{Cu}_2\text{O}$  of 2.2eV.

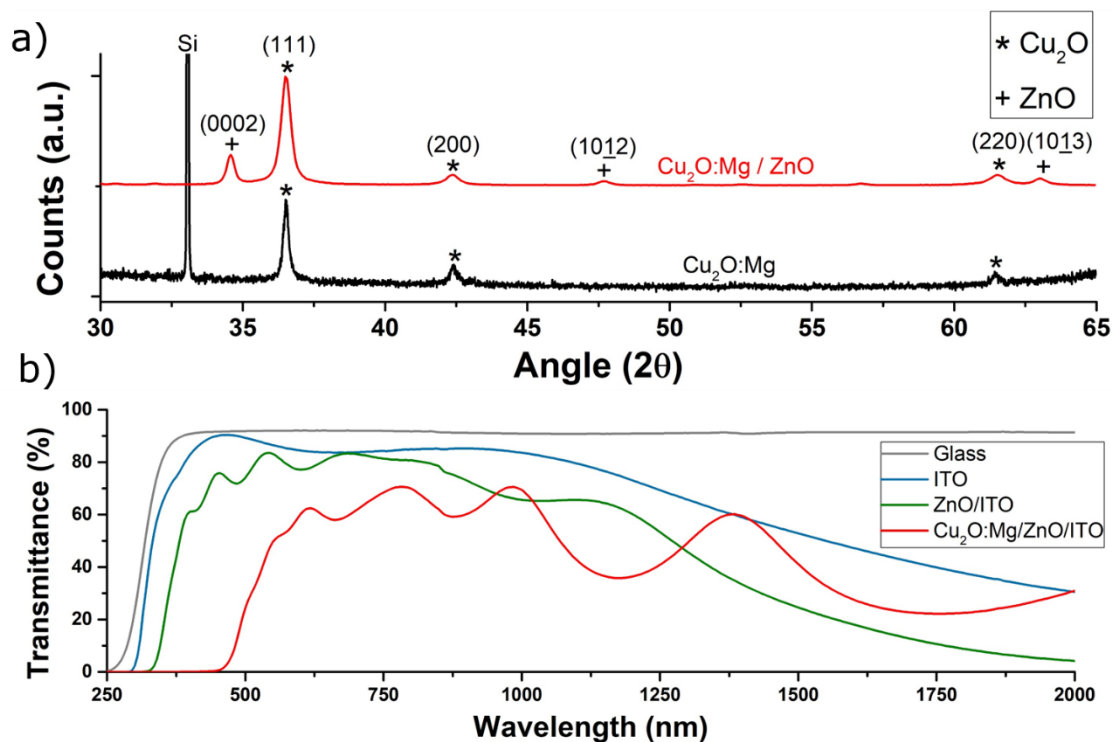


Figure IV-88 a) XRD spectra of  $\text{Cu}_2\text{O:Mg}$  and  $\text{Cu}_2\text{O:Mg/ZnO}$  structure b) Transmittance spectra of Corning glass, ITO covered glass, ZnO/ITO film and the whole structure:  $\text{Cu}_2\text{O:Mg/ZnO/ITO}$

The rectifying behaviour of the  $pn$  junction is presented in the Figure IV-89 and the results are summarized in Table IV-13. The  $\text{Cu}_2\text{O:Mg/ZnO}$  diode showed an improved non-ideality factor of 1.6 when compared with that of the undoped  $\text{Cu}_2\text{O/ZnO}$  diode, 16.2. This is mainly due to the lower leakage current in the  $\text{Cu}_2\text{O:Mg/ZnO}$  case, while the values of the current density at 1V are more similar in both diodes.

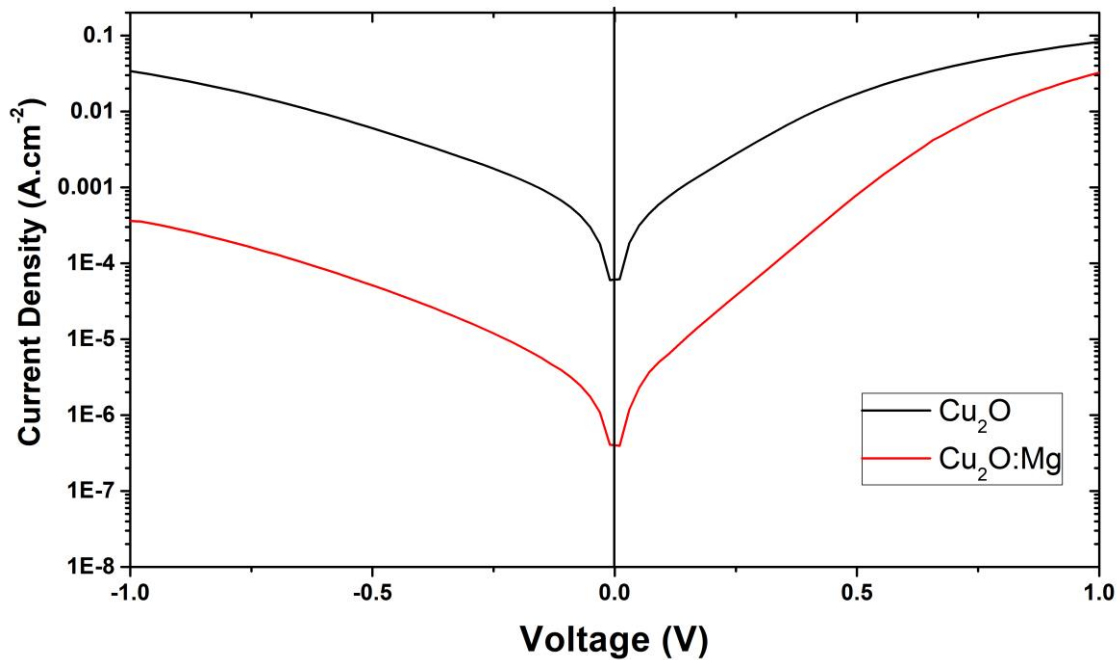


Figure IV-89 JV characteristic of pn junction ZnO/Cu<sub>2</sub>O (intrinsic and Mg doped). Current density presented in absolute value

A post annealing treatment was performed in order to increase the carrier concentration in the Cu<sub>2</sub>O films and therefore, increase the diode response of the devices. The annealing was performed at 250°C for 2 hours, in order to avoid any CuO formation. In Figure IV-90, the diode response between -1V and 1V is clearly visible. In terms of non-ideality factor, there were no significant variations in any diodes. Nevertheless after annealing there was an increase of current in forward and reverse sense. This fact may be attributed to the high concentration of holes in Cu<sub>2</sub>O, which leads to a lower sheet resistance.

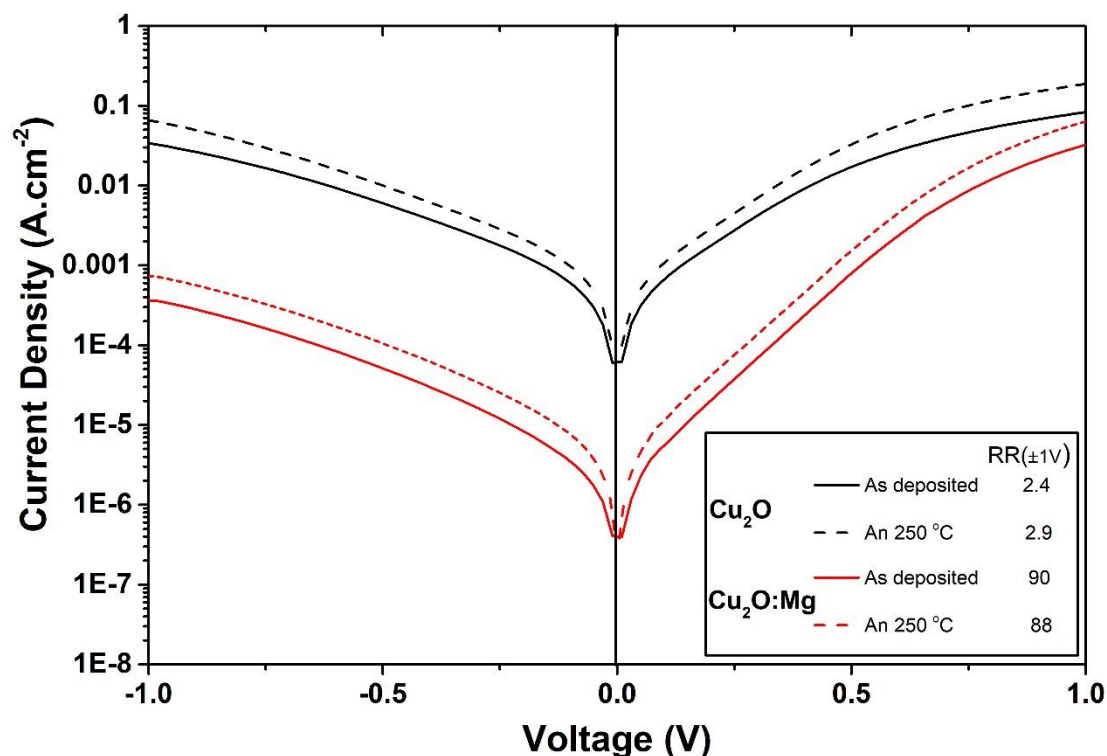


Figure IV-90 JV characteristic of  $pn$  junction between ZnO and Cu<sub>2</sub>O (intrinsic and Mg doped) with and without the anneal step at 260°C. ). Current density presented in absolute value

The comparison of the results obtained for the two kinds of Cu<sub>2</sub>O films, intrinsic and Mg doped, confirm the electrical improvement of the Cu<sub>2</sub>O/ZnO  $pn$  junction using magnesium as a dopant, especially in terms of reverse current.

#### 4.3.3.2 2<sup>nd</sup> Structure: Cu<sub>2</sub>O:Mg (AA-MOCVD) and ZnO (SALD)

In Figure IV-91, the second structure is represented, where in this case, the Cu<sub>2</sub>O film covers the majority of the device part of the device, with a small edge for ITO contact. The Cu<sub>2</sub>O was masked, leaving a central circle of during deposition of ZnO by SALD. As in the previous structure, the metallic contact was ensured by a circular gold film of 3mm diameter.

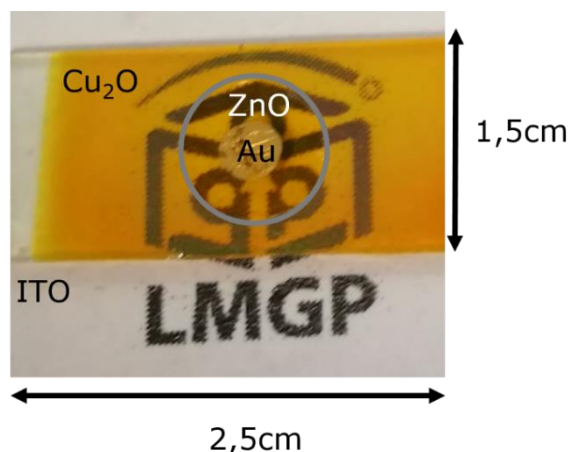


Figure IV-91 Photograph of the second structure: glass / ITO /  $\text{Cu}_2\text{O}$  / ZnO (SALD) / Au. Size of 2.5cm by 1.5cm

The quality of the films and interface was evaluated by SEM cross section, presented in Figure IV-92. In the Figure IV-92a) are visible the 3 different oxide films, where the thickness are 130 nm for the ITO electrode film, 240 nm for the  $\text{Cu}_2\text{O}$  film and 170 nm for the ZnO film. In the Mg-doped  $\text{Cu}_2\text{O}$  case, Figure IV-92b), the p-type layer is larger, with 375nm, similar to what was reported before in the 1<sup>st</sup> structure. The films show a good quality adhesion between the different layers, with highly dense layers.

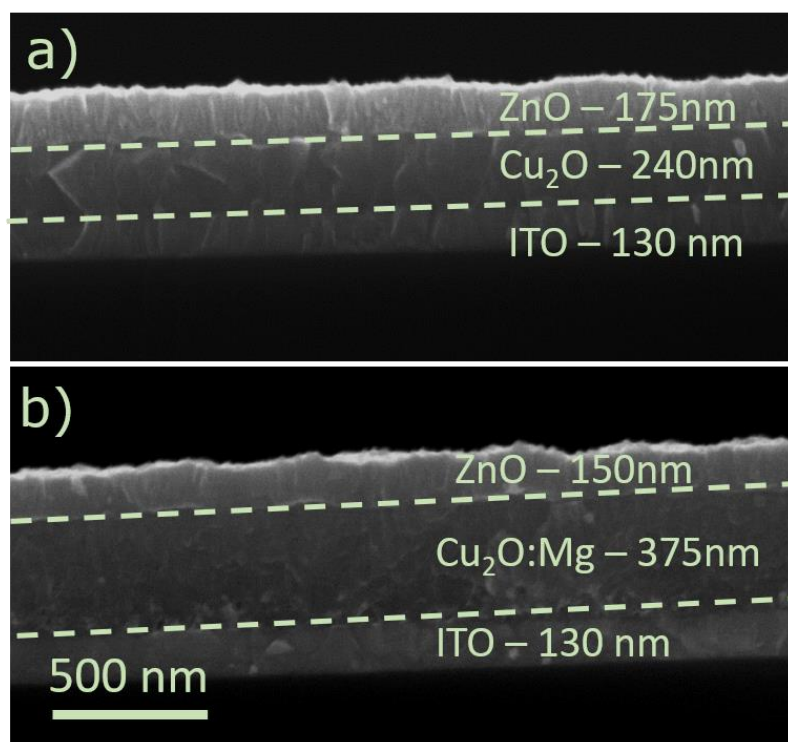


Figure IV-92SEM micrograph of the ZnO/ $\text{Cu}_2\text{O}$  junction; a) intrinsic  $\text{Cu}_2\text{O}$  and b)  $\text{Cu}_2\text{O}:\text{Mg}$

The rectifying behaviour of the *pn* junctions is presented in Figure IV-93, the  $\text{ZnO}_{\text{MOCVD}}$  JV curves were also included for comparison. As the structures are inverted,

the JV curves are also symmetric. The JV curve shows a typical rectifying shape with a leakage current density of  $1 \times 10^{-3} \text{ A.cm}^{-2}$  at +1 V. The ratio between the current at +1V and -1V ( $RR_{\pm 1V}$ ) is 177, for the intrinsic  $\text{Cu}_2\text{O}$  case, while the doped film shows a lower value of 109. In this structure, both diodes are similar, presenting comparable parameters to the  $\text{Cu}_2\text{O:Mg/ZnO}$  junction by MOCVD, reported in Table IV-13. Nevertheless, higher current density values are reported for the SALD case in the forward bias regime.

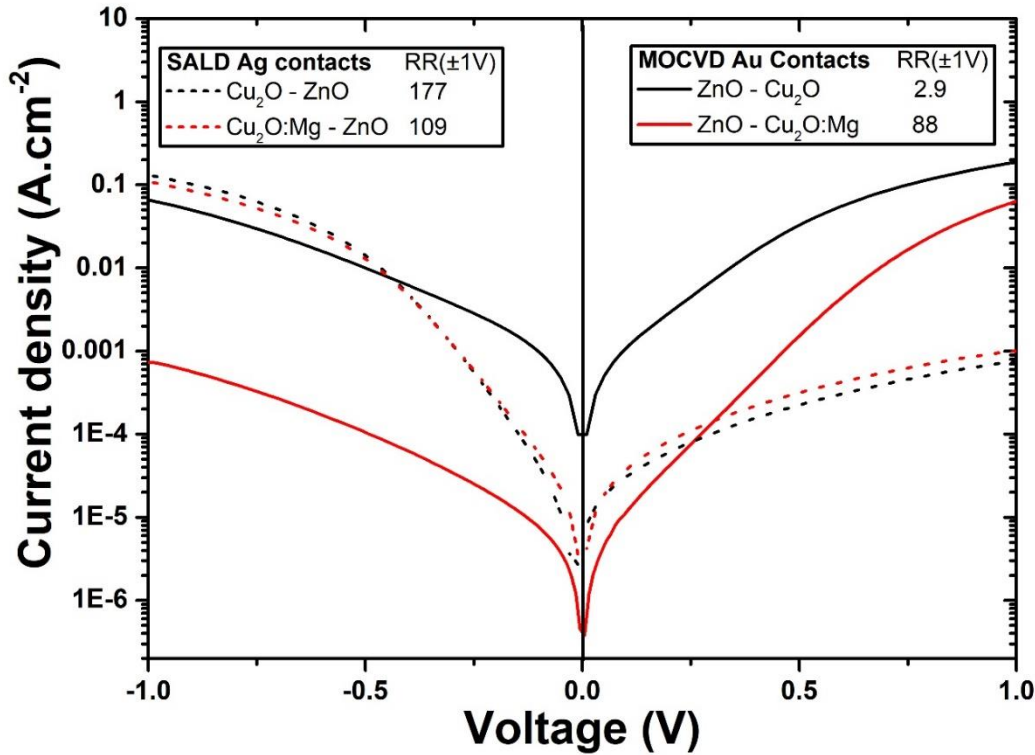


Figure IV-93 JV characteristic of pn junction ZnO/Cu<sub>2</sub>O (intrinsic and Mg doped) with ZnO obtained by SALD (dot curves) and MOCVD (lines). Current density presented in absolute value

The diode parameters were extracted by fitting the experimental curve with the typical diode equation, considering the series and shunt resistances as follows:

$$J = J_0 \left( e^{\frac{q(V-JR_S)}{nk_B T}} - 1 \right) + \frac{V - JR_S}{R_{Sh}} \quad (IV.3)$$

where  $J$  is the current density,  $J_0$  is the reverse current density,  $q$  is the electron charge,  $V$  is the applied voltage,  $R_S$  is the series resistance,  $n$  is the non-ideality factor,  $k_B$  is the Boltzmann's constant,  $T$  is the absolute temperature, and  $R_{Sh}$  is the shunt resistance. In the case of the first structure ZnO/Cu<sub>2</sub>O,  $R_S$ ,  $R_{Sh}$ , and  $J_0$  could not be extracted by the fitting to the implicit equation. Only  $n$  was determined by the ideal diode equation. The fitted

parameters of the different experimental diodes are shown in Table IV-13. The comparison of all diodes led us to conclude that the ones where SALD ZnO is deposited on top of Cu<sub>2</sub>O, show better parameters in general. The non-ideality factor obtained is as low as 2.0, with a rectifying ratio (RR $\pm$ 1V) above 100 for both intrinsic and Mg-doped Cu<sub>2</sub>O. Nevertheless, even if the series resistance is low compared to the ZnO MOCVD cases, being favourable for a diode, the shunt resistance is also lower, which increases the possibility of short-circuit and reduces the global performance of the device.

Table IV-13 Parameters obtain from fittings of pn junctions using equation 1

Structure	Conditions	J (1V) mA.cm <sup>-2</sup>	RR $\pm$ 1V	<i>n</i>	R <sub>s</sub> Ω.cm <sup>2</sup>	R <sub>Sh</sub> kΩ.cm <sup>2</sup>	J (0V) μA.cm <sup>-2</sup>
1 <sup>st</sup> ZnO <sub>MOCVD</sub> /Cu <sub>2</sub> O	As deposited	80	2.43	16.	-	-	-
	Annealed 250°C	190	2.86	15	-	-	-
1 <sup>st</sup> ZnO <sub>MOCVD</sub> /Cu <sub>2</sub> O:Mg	As deposited	33	90.0	2.6	8.0	8.0	0.4
	Annealed 250°C	64	88.4	2.7	4.0	7.4	1.2
2 <sup>st</sup> Cu <sub>2</sub> O/ZnO <sub>SALD</sub>	As deposited	130	170	2.0	3.5	1.9	2.7
2 <sup>st</sup> Cu <sub>2</sub> O:Mg/ZnO <sub>SALD</sub>	As deposited	110	109	2.0	4.3	1.4	2.7

These experimental results are difficultly comparable to the simulated junctions, especially due to diverse rectifying behaviour, and the current density values obtained. Nevertheless, the effect of a more conductive Cu<sub>2</sub>O is the similar in both cases, leading to a reduction of the sheet resistance. This fact is particularly visible in the ZnO<sub>MOCVD</sub>/Cu<sub>2</sub>O:Mg heterojunctions, since a reduction of sheet resistance is clear after the annealing treatment at 250°C.

Cu<sub>2</sub>O/ZnO diodes from other studies show similar results in terms of non-ideality factor and rectifying ration. Heterojunction of Cu<sub>2</sub>O and ZnO deposited by RF sputtering showed in dark IV curves with an non-ideality factor larger than 2.0, reaching up to 3.8 with annealing treatments <sup>39</sup>. These results are similar to the ones here reported, mainly the 1<sup>st</sup> structure. In other work between these two oxides deposited by RF magnetron sputtering <sup>40</sup>, the ratio between the current at -1V and +1V is marginally higher than 100, comparable to the best diodes reported in our work.

#### 4.3.3.3 Photovoltaic performance of the pn junctions

The goal of these structures is the implementation into solar cells. Therefore photovoltaic performances were analysed under AM 1.5G illumination conditions. In

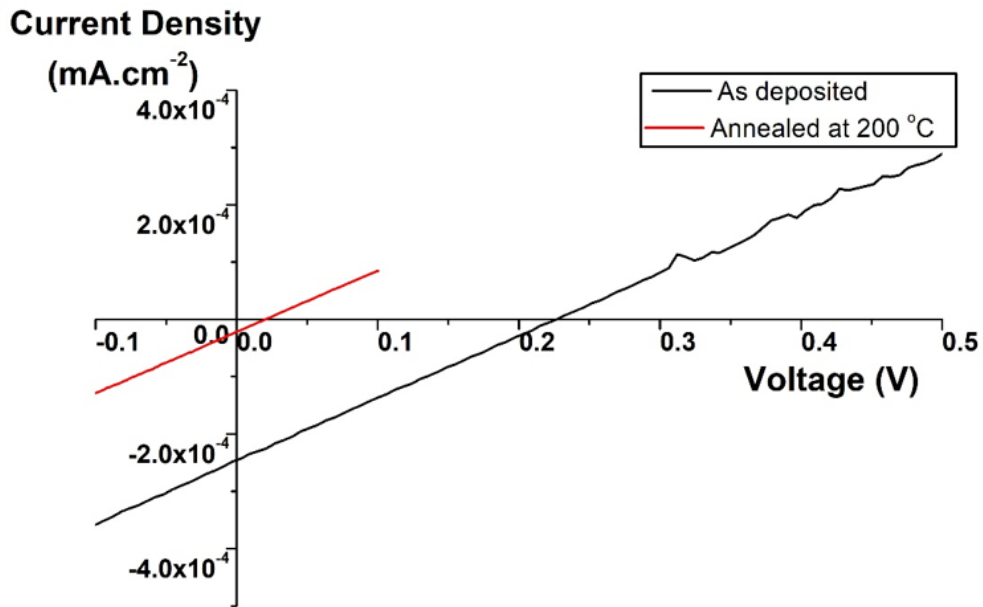
Figure IV-94 are plotted the JV curves under illumination. There were six different *pn* junctions tested:  $\text{Cu}_2\text{O}_{\text{as-dep}}/\text{ZnO}_{\text{MOCVD}}$ ,  $\text{Cu}_2\text{O}_{250^\circ\text{C}}/\text{ZnO}_{\text{MOCVD}}$ ,  $\text{Cu}_2\text{O}:\text{Mg}_{\text{as-dep}}/\text{ZnO}_{\text{MOCVD}}$ ,  $\text{Cu}_2\text{O}:\text{Mg}_{250^\circ\text{C}}/\text{ZnO}_{\text{MOCVD}}$ ,  $\text{CuO}_2/\text{ZnO}_{\text{SALD}}$  and  $\text{Cu}_2\text{O}:\text{Mg}/\text{ZnO}_{\text{SALD}}$ . All of them showed measurable photovoltaic responses except the  $\text{Cu}_2\text{O}/\text{ZnO}_{\text{MOCVD}}$  *pn* junctions, neither as-deposited nor annealed. The relevant photovoltaic parameters of the four working solar cells as open-circuit voltage ( $V_{\text{OC}}$ ) and short-circuit current density ( $J_{\text{SC}}$ ), fill-factor (FF) and efficiency ( $\eta$ ) are represented in Table IV-14. In the MOCVD-grown case, the structure with the as-deposited film showed a  $V_{\text{OC}}$  of 221mV that was drastically decreased after annealing, down to 21.4mV. Even if the annealing temperature used was below the formation of CuO, the thermal treatment seem to short-circuit part of the cell, reducing the overall  $V_{\text{OC}}$ . Additionally, the current density values are quite low, below  $1 \mu\text{A}/\text{cm}^2$ , resulting in efficiency values far below 0.01%.

In the SALD cases, the current density values increased around 3 orders of magnitude for both p-type layers, when compared to the previous case. The  $\text{Cu}_2\text{O}$  cell shows a current density of  $0.79 \text{ mA}\cdot\text{cm}^{-2}$ , the highest measured in these experimental results. In the case of Mg doped  $\text{Cu}_2\text{O}$ , the  $V_{\text{OC}}$  is the highest found, 379 mV, with a reduced  $J_{\text{SC}}$  of  $0.16 \text{ mA}\cdot\text{cm}^{-2}$ . Overall, even with the presence of photovoltaic effect, the efficiency of the cells produced are unable to pass the 0.1% mark.

Table IV-14 Parameters of the different solar cells created. Open-circuit voltage ( $V_{\text{OC}}$ ), short-circuit current density ( $J_{\text{SC}}$ ), fill factor (FF) and efficiency ( $\eta$ )

Sample		$V_{\text{OC}}$ V	$J_{\text{sc}}$ $\text{mA}\cdot\text{Cm}^{-2}$	FF %	$\eta$ %
<b>1<sup>st</sup></b> <b>MOCVD</b> <b><math>\text{Cu}_2\text{O}:\text{Mg}</math></b>	As-deposited	0,221	$-2,5 \times 10^{-4}$	25,3	<0,01
	Annealed 250°C	0,021	$-2,3 \times 10^{-5}$	23	<0,0001
<b>2<sup>nd</sup> –</b>	$\text{Cu}_2\text{O}$	0,194	-0,79	25,8	0,04
<b>SALD</b>	$\text{Cu}_2\text{O}:\text{Mg}$	0,380	-0,16	24	0,02

a) **Cu<sub>2</sub>O:Mg / ZnO by MOCVD: Au contacts**



b) **Cu<sub>2</sub>O / ZnO by SALD: Ag contacts**

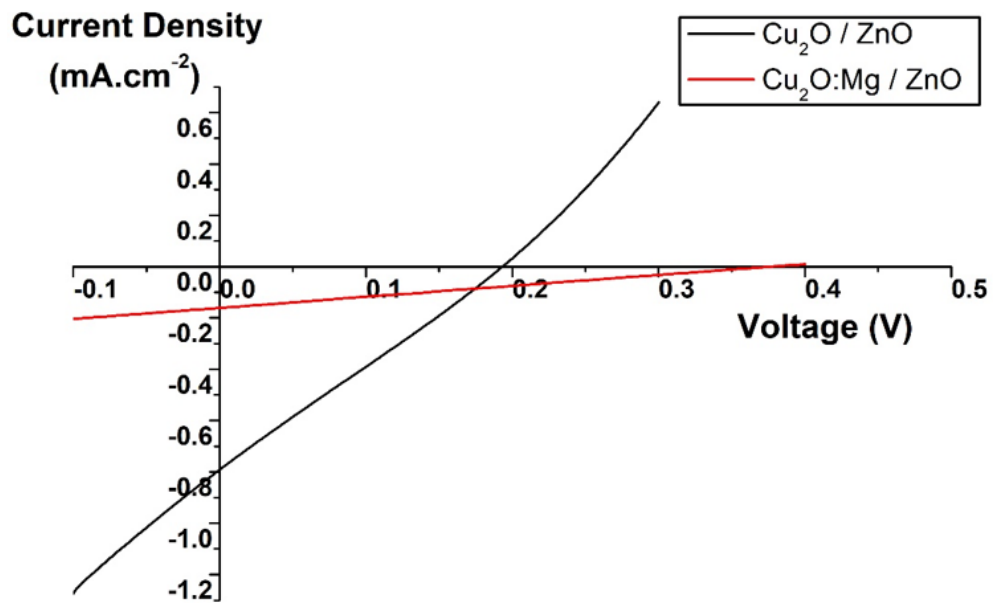


Figure IV-94 JV curves under AM 1.5G illumination of different pn junctions a) Cu<sub>2</sub>O:Mg/ZnO (MOCVD) as deposited and annealed at 250°C; b) Cu<sub>2</sub>O/ZnO (SALD) with Cu<sub>2</sub>O and Cu<sub>2</sub>O:Mg as-deposited.

In the two cells prepared by SALD, we can extract the highest values of J<sub>sc</sub> and V<sub>oc</sub> for us obtained, 0.8 mA.cm<sup>-2</sup> and 380mV, respectively. Considering the physical and chemical deposition techniques of thin films, the values of photovoltaic performance are in the range of other studies on Cu<sub>2</sub>O. In a study by H Akinaga *et al.*<sup>39</sup>, the deposition by magnetron sputtering of Cu<sub>2</sub>O and ZnO thin films led to the formation of a solar cell with

0.4 mA.cm<sup>-2</sup> and 300 mV of J<sub>sc</sub> and V<sub>oc</sub>, respectively. The thickness of the oxide layers is also in the hundreds of nanometres, as in our study, however, the metals used for contacts are different, based on different layers of Pt, Al and Au. Other study by S. Jeong *et al.*<sup>41</sup>, Cu<sub>2</sub>O thin films (280nm) were deposited by MOCVD on ZnO thin films (130nm) in this case deposited by RF sputtering, presenting a comprehensive analysis on the temperature dependence of the PV parameters. The direct comparison of the PV response at room temperature shows V<sub>oc</sub> and J<sub>sc</sub> values of 300mV and 1 mA.cm<sup>-2</sup>. They attributed these meagre PV results to an interface recombination mechanism that is the dominant carrier transport mechanism in these solar cells.<sup>41</sup>

The use of spray-pyrolysis to deposit Cu<sub>2</sub>O was also found in the literature, however in this case combined with TiO<sub>2</sub>, as n-type oxide layer<sup>42</sup>. The open circuit voltage was reported to be up to 350 mV, while the short circuit current density reached a maximum of 0.4 mA.cm<sup>-2</sup>. From the same group was also reported in 2016 a study with the incorporation of Mg in Cu<sub>2</sub>O, deposited also by spray-pyrolysis<sup>43</sup>. In this case, the current density value reached up to 0.9 mA.cm<sup>-2</sup>, with a V<sub>oc</sub> in the same 350 mV range<sup>43</sup>. The J<sub>sc</sub> improvement on the solar cells was attributed to a higher photo-conductivity of cuprous oxide with the Mg incorporation.

In a recent work (2017), developed in the SPIN lab at the University de Liege by Y. Malier under a Master Thesis internship, undoped and Mg-doped Cu<sub>2</sub>O thin films were prepared by radio-frequency magnetron sputtering. *Pn* junctions were then arranged in combination with ZnO:Al. Similar results were reported in terms of diode behaviour, nevertheless, the current-voltage characteristics of *pn* junctions created together with ZnO:Al presented a high leakage current. Moreover, the junctions could only be used as photodiodes as no electrical power could be harnessed upon solar illumination.

These previous reports using sputtering or chemical vapour techniques are drastically supplanted by two other techniques for the growth of Cu<sub>2</sub>O: electrodeposition and thermal oxidation. Both techniques enable the growth of Cu<sub>2</sub>O with mobility values higher than 10 cm<sup>2</sup>.V<sup>-1</sup>.s<sup>-1</sup>. In the case of electrodeposition of Cu<sub>2</sub>O in combination with ZnO, several studies report short-current density values higher than 1 mA cm<sup>-2</sup><sup>44, 45, 46</sup>. A study by T. Buonassisi and R.G. Gordon<sup>47</sup> reports efficiency values as high as 2.85%, with V<sub>oc</sub> and J<sub>sc</sub> of 622 mV and 7.25 mA cm<sup>-2</sup>, respectively. Finally, the use of thermal oxidation of copper sheets is at this moment the best technique to obtain Cu<sub>2</sub>O base solar cells. Various studies by T. Minami<sup>30,31,48-52</sup> show the highest values in terms of

photovoltaic parameters, with short-current density of  $10 \text{ mA}\cdot\text{cm}^{-2}$ <sup>49</sup>, open-circuit voltage of  $1.1 \text{ V}$ <sup>30</sup> and efficiency of  $8.1\%$ <sup>30</sup>, using sodium-doped  $\text{Cu}_2\text{O}$ .

Future studies on these *pn* junction could also be performed to access the applicability of  $\text{Cu}_2\text{O}/\text{ZnO}$  structures for photocatalysis in water splitting processes.

### 4.3.4 Summary

The integration of  $\text{Cu}_2\text{O}$ , intrinsic and Mg-doped, into *pn* junctions was successfully achieved using only chemical vapour deposition approaches. Rectifying behaviour was observed in the junctions created, even with significantly more modest performance when compared to numerically-simulated devices. The Mg doping effect was especially visible in films deposited on MOCVD-grown  $\text{ZnO}$ , reducing the leakage current on the device. When  $\text{ZnO}$  was the last oxide to be deposited by SALD, both intrinsic and doped films showed similar electrical responses.

The idea of this approach was to enable fast, scalable and low-cost technology aiming for full oxide-based solar cells. Nevertheless, photovoltaic performances presented here are obviously far for the best literature devices. The use of AA-MOCVD to produce  $\text{Cu}_2\text{O}$  limits strongly the mobility of these thin films, more than one order of magnitude below the thermally-oxidized  $\text{Cu}_2\text{O}$  films. The impact of this low mobility is strongly visible on the current density values and as consequence the fill factor and efficiency. Additionally, an increase of current density in the diodes annealed at  $250 \text{ }^\circ\text{C}$ , did not lead to improvements in PV performance, as proposed.

## 4.4 Conclusions

A comprehensive study on the impact of magnesium incorporation in cuprous oxide thin films was developed in this chapter. The presence of the dopant was confirmed up to 17% concentration using aerosol-assisted metal-organic chemical vapour deposition under atmospheric pressure condition at  $350^\circ\text{C}$ . As main influences, the films showed a higher roughness, a lower electrical resistivity ( $6.6 \text{ }\Omega\cdot\text{cm}$ ), concentration of holes up to  $8.1 \times 10^{17} \text{ cm}^{-3}$  and a higher stability of the  $\text{Cu}_2\text{O}$  phase under oxidizing environment. The magnesium presence seems to change the mechanism of copper vacancies generation, blocking the formation of split copper vacancies. This leads to a reduce transformation of  $\text{Cu}_2\text{O}$  into  $\text{CuO}$ .

The creation heterojunctions between Cu<sub>2</sub>O and ZnO showed a diode-like behaviour of the devices using both intrinsic and Mg-doped Cu<sub>2</sub>O. Additionally, photovoltaic response was also detected under AM 1.5G illumination. The PV performance is similar to other structures deposited by conventional physical and chemical techniques, however far from the state-of-the art Cu<sub>2</sub>O solar cells, grown by thermal oxidation of copper metallic sheets.

## 4.5 References

- (1) Nolan, M.; Elliott, S. D. Tuning the Transparency of Cu<sub>2</sub>O with Substitutional Cation Doping. *Chem. Mater.* **2008**, *20* (17), 5522–5531.
- (2) Bergerot, L.; Jiménez, C.; Chaix-Pluchery, O.; Rapenne, L.; Deschanvres, J.-L. Growth and Characterization of Sr-Doped Cu<sub>2</sub>O Thin Films Deposited by Metalorganic Chemical Vapor Deposition. *Phys. Status Solidi* **2015**, *212* (8), 1735–1741.
- (3) Brochen, S.; Bergerot, L.; Favre, W.; Resende, J.; Jiménez, C.; Deschanvres, J.-L.; Consonni, V. Effect of Strontium Incorporation on the P-Type Conductivity of Cu<sub>2</sub>O Thin Films Deposited by Metal–Organic Chemical Vapor Deposition. *J. Phys. Chem. C* **2016**, *120* (31), 17261–17267.
- (4) Manin, M.; Thollon, S.; Emieux, F.; Berthome, G.; Pons, M.; Guillon, H. Deposition of MgO Thin Film by Liquid Pulsed Injection MOCVD. *Surf. Coatings Technol.* **2005**, *200* (5–6), 1424–1429.
- (5) Serin, N.; Serin, T.; Horzum, Ş.; Celik, Y. Annealing Effects on the Properties of Copper Oxide Thin Films Prepared by Chemical Deposition. *Semicond. Sci. Technol.* **2005**, *6*, 6094–6104.
- (6) Scherrer, P. Göttinger Nachrichten Math. *Phys* **1918**, *2*, 98–100.
- (7) McCreery, R. L. *Raman Spectroscopy for Chemical Analysis*; John Wiley & Sons, 2005; Vol. 225.
- (8) Meyer, B. K.; Polity, A.; Reppin, D.; Becker, M.; Hering, P.; Kramm, B.; Klar, P. J.; Sander, T.; Reindl, C.; Heiliger, C.; Heinemann, M.; Muller, C.; Ronning, C. The Physics of Copper Oxide (Cu<sub>2</sub>O). *Semicond. Semimetals* **2013**, *88*, 201–226.
- (9) Li, L.-X.; Xu, D.; Li, X.-Q.; Liu, W.-C.; Jia, Y. Excellent Fluoride Removal Properties of Porous Hollow MgO Microspheres. *New J. Chem.* **2014**, *38* (11), 5445–5452.

- (10) Lee, Y. S.; Heo, J.; Winkler, M. T.; Siah, S. C.; Kim, S. B.; Gordon, R. G.; Buonassisi, T. Nitrogen-Doped Cuprous Oxide as a P-Type Hole-Transporting Layer in Thin-Film Solar Cells. *J. Mater. Chem. A* **2013**, *1* (48), 15416.
- (11) Marin, A. T.; Munoz-Rojas, D.; Iza, D. C.; Gershon, T.; Musselman, K. P.; MacManus-Driscoll, J. L. Novel Atmospheric Growth Technique to Improve Both Light Absorption and Charge Collection in ZnO/Cu<sub>2</sub>O Thin Film Solar Cells. *Adv. Funct. Mater.* **2013**, *23* (27), 3413–3419.
- (12) Scanlon, D. O.; Morgan, B. J.; Watson, G. W.; Walsh, A. Acceptor Levels in P-Type Cu<sub>2</sub>O: Rationalizing Theory and Experiment. *Phys. Rev. Lett.* **2009**, *103* (9), 1–4.
- (13) Isseroff, L. Y.; Carter, E. A. Electronic Structure of Pure and Doped Cuprous Oxide with Copper Vacancies: Suppression of Trap States. *Chem. Mater.* **2013**, *25* (3), 253–265.
- (14) Wang, Y.; Miska, P.; Pilloud, D.; Horwat, D.; Mücklich, F.; Pierson, J. F. Transmittance Enhancement and Optical Band Gap Widening of Cu<sub>2</sub>O Thin Films after Air Annealing. *J. Appl. Phys.* **2014**, *115* (7), 2–7.
- (15) Meyer, B. K.; Polity, A.; Reppin, D.; Becker, M.; Hering, P.; Klar, P. J.; Sander, T.; Reindl, C.; Benz, J.; Eickhoff, M.; Heiliger, C.; Heinemann, M.; Bläsing, J.; Krost, A.; Shokovets, S.; Muller, C.; Ronning, C. Binary Copper Oxide Semiconductors: From Materials towards Devices. *Phys. Status Solidi* **2012**, *249* (8), 1487–1509.
- (16) Trivich, D.; Wang, E. Y.; Richard, J. K. Cuprous Oxide Photovoltaic Cells. In *Conference: IEEE photovoltaic specialists conference*,; 1978.
- (17) Resende, J.; Jiménez, C.; Nguyen, N. D.; Deschanvres, J.-L. Magnesium-Doped Cuprous Oxide (Mg:Cu<sub>2</sub>O) Thin Films as a Transparent P-Type Semiconductor. *Phys. Status Solidi* **2016**, *7*, 1–7.
- (18) Figueiredo, V.; Elangovan, E.; Gonçalves, G.; Barquinha, P.; Pereira, L.; Franco, N.; Alves, E.; Martins, R.; Fortunato, E. Effect of Post-Annealing on the Properties of Copper Oxide Thin Films Obtained from the Oxidation of Evaporated Metallic Copper. *Appl. Surf. Sci.* **2008**, *254* (13), 3949–3954.
- (19) Johan, M. R.; Suan, M. S. M.; Hawari, N. L.; Ching, H. A. Annealing Effects on the Properties of Copper Oxide Thin Films Prepared by Chemical Deposition. *Int. J. Electrochem. Sci.* **2011**, *6* (12), 6094–6104.
- (20) Biccari, F.; Malerba, C.; Mittiga, A. Defects and Doping in Cu<sub>2</sub>O: General Properties and Applications. **2009**, No. 688774, 1–28.

- (21) Zhu, Y.; Mimura, K.; Isshiki, M. Oxidation Mechanism of Cu<sub>2</sub>O to CuO at 600 - 1050°C. *Oxid. Met.* **2004**, *62* (October), 207–222.
- (22) Murali, D. S.; Kumar, S.; Choudhary, R. J.; Wadikar, A. D.; Jain, M. K.; Subrahmanyam, A. Synthesis of Cu<sub>2</sub>O from CuO Thin Films: Optical and Electrical Properties. *AIP Adv.* **2015**, *5* (4), 47143.
- (23) Morales, J.; Barranco, A.; Caballero, A.; Holgado, J. P.; Gonza, a R. Interface Effects for Cu , CuO , and Cu<sub>2</sub>O Deposited on SiO<sub>2</sub> and ZrO<sub>2</sub> . XPS Determination of the Valence State of Copper in Cu / SiO<sub>2</sub> and Cu / ZrO<sub>2</sub> Catalysts. *J. Phys. Chem. B* **2002**, *106*, 6921–6929.
- (24) Xpsfitting.com. Cu(0): Cu(II) or Cu(I):Cu(II) Calculations <http://www.xpsfitting.com/2012/01/cu0cuii-or-cuicuii-calculations.html> (accessed Aug 21, 2017).
- (25) Tapiero, M.; Zielinger, J. P.; Noguét, C. Electrical Conductivity and Thermal Activation Energies in Cu<sub>2</sub>O Single Crystals. *Phys. Status Solidi* **1972**, *12* (2), 517–520.
- (26) Figueiredo, V.; Pinto, J. V; Deuermeier, J.; Barros, R.; Alves, E.; Martins, R.; Fortunato, E. P-Type CuO Thin-Film Transistors Produced by Thermal Oxidation. *J. Disp. Technol.* **2013**, *9* (9), 735–740.
- (27) Li, J.; Mei, Z.; Liu, L.; Liang, H.; Azarov, A.; Kuznetsov, A.; Liu, Y.; Ji, A.; Meng, Q.; Du, X. Probing Defects in Nitrogen-Doped Cu<sub>2</sub>O. *Sci. Rep.* **2014**, *4* (111), 7240.
- (28) Olsen, L. C.; Addis, F. W.; Miller, W. Experimental and Theoretical Studies of Cu<sub>2</sub>O Solar Cells. *Sol. Cells* **1982**, *7* (3), 247–279.
- (29) Nishi, Y.; Miyata, T.; Minami, T. The Impact of Heterojunction Formation Temperature on Obtainable Conversion Efficiency in N-ZnO/p-Cu<sub>2</sub>O Solar Cells. *Thin Solid Films* **2013**, *528*, 72–76.
- (30) Tadatsugu, M.; Yuki, N.; Toshihiro, M. Efficiency Enhancement Using a Zn<sub>1-x</sub>Ge<sub>x</sub>O Thin Film as an N-Type Window Layer in Cu<sub>2</sub>O-Based Heterojunction Solar Cells. *Appl. Phys. Express* **2016**, *9* (5), 52301.
- (31) Minami, T.; Nishi, Y.; Miyata, T. High-Efficiency Cu<sub>2</sub>O-Based Heterojunction Solar Cells Fabricated Using a Ga<sub>2</sub>O<sub>3</sub> Thin Film as N-Type Layer. *Appl. Phys. Express* **2013**, *6* (4), 44101.

- (32) Deuermeier, J.; Wardenga, H. F.; Morasch, J.; Siol, S.; Nandy, S.; Calmeiro, T.; Martins, R.; Klein, A.; Fortunato, E. Highly Conductive Grain Boundaries in Copper Oxide Thin Films. *J. Appl. Phys.* **2016**, *119* (23).
- (33) Marin, A. T.; Muñoz-Rojas, D.; Iza, D. C.; Gershon, T.; Musselman, K. P.; MacManus-Driscoll, J. L. Novel Atmospheric Growth Technique to Improve Both Light Absorption and Charge Collection in ZnO/Cu<sub>2</sub>O Thin Film Solar Cells. *Adv. Funct. Mater.* **2013**, *23*, 3413–3419.
- (34) Nguyen, N. D. Electrical Characterization of III-Nitride Heterostructures by Thermal Admittance Spectroscopy. Université de Liège, Belgium 2004.
- (35) Morkoc, H.; Ozgur, U. *General Properties of ZnO*; 2009.
- (36) Nandy, S.; Banerjee, A.; Fortunato, E.; Martins, R. A Review on Cu<sub>2</sub>O and Cu-Based P-Type Semiconducting Transparent Oxide Materials: Promising Candidates for New Generation Oxide Based Electronics. *Rev. Adv. Sci. Eng.* **2013**, *2* (4), 273–304.
- (37) Baert, B. Impact of Electron Trap States on the Transport Properties of GeSn Semiconducting Heterostructures Assessed by Electrical Characterizations. **2016**.
- (38) Nguyen, V. H.; Resende, J.; Jiménez, C.; Deschanvres, J.-L.; Carroy, P.; Muñoz, D.; Bellet, D.; Muñoz-Rojas, D. Deposition of ZnO Based Thin Films by Atmospheric Pressure Spatial Atomic Layer Deposition for Application in Solar Cells. *J. Renew. Sustain. Energy* **2017**, *9* (2), 21203.
- (39) Noda, S.; Shima, H.; Akinaga, H. Cu<sub>2</sub>O/ZnO Heterojunction Solar Cells Fabricated by Magnetron-Sputter Deposition Method Films Using Sintered Ceramics Targets. *J. Phys. Conf. Ser.* **2013**, *433*, 12027.
- (40) El-amin, A. H. Investigation of Semitransparent Cu<sub>2</sub>O / ZnO Based Heterostructure Diodes for Memory and Related Applications. **2014**.
- (41) Jeong, S.; Song, S. H.; Nagaich, K.; Campbell, S. A.; Aydil, E. S. An Analysis of Temperature Dependent Current-Voltage Characteristics of Cu<sub>2</sub>O-ZnO Heterojunction Solar Cells. *Thin Solid Films* **2011**, *519* (19), 6613–6619.
- (42) Pavan, M.; Rühle, S.; Ginsburg, A.; Keller, D. A.; Barad, H. N.; Sberna, P. M.; Nunes, D.; Martins, R.; Anderson, A. Y.; Zaban, A.; Fortunato, E. TiO<sub>2</sub>/Cu<sub>2</sub>O All-Oxide Heterojunction Solar Cells Produced by Spray Pyrolysis. *Sol. Energy Mater. Sol. Cells* **2015**, *132*, 549–556.
- (43) Kardarian, K.; Nunes, D.; Maria Sberna, P.; Ginsburg, A.; Keller, D. A.; Vaz Pinto, J.; Deuermeier, J.; Anderson, A. Y.; Zaban, A.; Martins, R.; Fortunato, E. Effect

of Mg Doping on Cu<sub>2</sub>O Thin Films and Their Behavior on the TiO<sub>2</sub>/Cu<sub>2</sub>O Heterojunction Solar Cells. *Sol. Energy Mater. Sol. Cells* **2016**, *147*, 27–36.

(44) Oku, T.; Yamada, T.; Fujimoto, K.; Akiyama, T. Microstructures and Photovoltaic Properties of Zn(Al)O/Cu<sub>2</sub>O-Based Solar Cells Prepared by Spin-Coating and Electrodeposition. *Coatings* **2014**, *4* (2), 203–213.

(45) Izaki, M.; Shinagawa, T.; Mizuno, K.-T.; Ida, Y.; Inaba, M.; Tasaka, A. Electrochemically Constructed P-Cu<sub>2</sub>O/n-ZnO Heterojunction Diode for Photovoltaic Device. *J. Phys. D. Appl. Phys.* **2007**, *40* (11), 3326–3329.

(46) Ichimura, M.; Song, Y. Band Alignment at the Cu<sub>2</sub>O/ZnO Heterojunction. *Jpn. J. Appl. Phys.* **2011**, *50* (5 PART 1).

(47) Lee, S. W.; Lee, Y. S.; Heo, J.; Siah, S. C.; Chua, D.; Brandt, R. E.; Kim, S. B.; Mailoa, J. P.; Buonassisi, T.; Gordon, R. G. Improved Cu<sub>2</sub>O-Based Solar Cells Using Atomic Layer Deposition to Control the Cu Oxidation State at the P-N Junction. *Adv. Energy Mater.* **2014**, *4* (11), 1–7.

(48) Minami, T.; Nishi, Y.; Miyata, T. High-Efficiency Cu<sub>2</sub>O-Based Heterojunction Solar Cells Fabricated Using a Ga<sub>2</sub>O<sub>3</sub> Thin Film as N-Type Layer. *Appl. Phys. Express* **2013**, *6* (4), 44101.

(49) Minami, T.; Nishi, Y.; Miyata, T. Cu<sub>2</sub>O-Based Solar Cells Using Oxide Semiconductors. *J. Semicond.* **2016**, *37* (1), 14002.

(50) Minami, T.; Nishi, Y.; Miyata, T.; Nomoto, J. I. High-Efficiency Oxide Solar Cells with ZnO/Cu<sub>2</sub>O Heterojunction Fabricated on Thermally Oxidized Cu<sub>2</sub>O Sheets. *Appl. Phys. Express* **2011**, *4* (6), 10–13.

(51) Minami, T.; Nishi, Y.; Miyata, T. Impact of Incorporating Sodium into Polycrystalline P-Type Cu<sub>2</sub>O for Heterojunction Solar Cell Applications. *Appl. Phys. Lett.* **2014**, *105* (21), 1–6.

(52) Minami, T.; Nishi, Y.; Miyata, T. Heterojunction Solar Cell with 6% Efficiency Based on an N-Type Aluminum-Gallium-Oxide Thin Film and P-Type Sodium-Doped Cu<sub>2</sub>O Sheet. *Appl. Phys. Express* **2015**, *8* (2), 22301.

## Chapter V: CuCrO<sub>2</sub> delafossite thin films

5.1	Deposition and characterization of CuCrO <sub>2</sub> films	164
5.1.1	Introduction	164
5.1.2	Experimental	164
5.1.3	Characterization of CuCrO <sub>2</sub> films	165
5.1.4	Conclusion on CuCrO <sub>2</sub> thin films	171
5.2	ZnO/CuCrO <sub>2</sub> Core-Shell Nanowire Heterostructure for Self-Powered UV Photodetectors	172
5.2.1	Introduction	172
5.2.2	Experimental	172
5.2.3	Structural characterization of core-shell structures	173
5.2.4	Electrical characterization of core-shell heterostructures	180
5.2.5	Conclusions on the core-shell heterostructures	185
5.3	Conclusions	186
5.4	References	186

In this chapter we describe the deposition of CuCrO<sub>2</sub> thin films by aerosol-assisted MOCVD, with optimization regarding the cations' concentration ratio. This work has been developed in collaboration with Aissatou Ndong during her master internship at LMGP. In a second part, we investigated the application of this p-type material into a UV photodetector on ZnO nanowire array. This study has been developed in collaboration with Thomas Cossuet, PhD student of LMGP, specialized in ZnO nanowires growth. The device work has been recently submitted as a peer-review article to ACS Applied materials and Interfaces with the name: "*ZnO / CuCrO<sub>2</sub> Core-Shell Nanowire Heterostructure for Self-Powered UV Photodetectors*".

## 5.1 Deposition and characterization of CuCrO<sub>2</sub> films

### 5.1.1 Introduction

The lack of improvements in transparency of Mg-doped Cu<sub>2</sub>O thin films lead us to test an alternative approach, the p-type delafossite phase CuCrO<sub>2</sub>. The intrinsic higher band-gap of 2.8eV<sup>1</sup> and the lower resistivity of 0.1 Ω.cm<sup>2</sup>, when compared to Cu<sub>2</sub>O, can enable the application of this material into transparent semiconductor devices. A detailed presentation of the state of art of this material can be found in section I.1.4. In the study here presented, we optimize the deposition of CuCrO<sub>2</sub> thin films by AA-MOCVCVD. The deposition conditions were based on a particular study by Farrell *et al.*<sup>3</sup>, which reports the growth of undoped CuCrO<sub>2</sub> thin films by spray pyrolysis. This work showed the nanocrystallization of the delafossite phase at temperatures below 400 °C, without any post-annealing treatments. Interestingly, the metal organic precursors and solvent used by Farrell *et al.*<sup>3</sup> are compatible with aerosol system in LMGP, based on a piezoelectric transducer.

### 5.1.2 Experimental

Using the AA-CVD reactor in configuration 2 previously described in Chapter II, the experimental parameters of the solution and deposition are presented in Table V-15. The precursors used were copper acetylacetonate, Cu(acac)<sub>2</sub>, and chromium acetylacetonate, Cr(acac)<sub>3</sub>, with ratio between Cu and the total concentration of cations (Cu/Cu+Cr) varied from 40% to 60% for a total concentration of precursors of 0.02 mol.l<sup>-1</sup> in ethanol. For this study, the time was increased to 90 minutes and the temperature to 400 °C in order to reproduce literature study<sup>4</sup>. Argon with a flow rate of 6 l.min<sup>-1</sup> was used as carrier gas, while O<sub>2</sub> with a flow rate of 1.5 l.min<sup>-1</sup> was used as reaction gas as in Cu<sub>2</sub>O case. These flow-rate values allowed us to maintain a solution consumption rate of 2 ml.min<sup>-1</sup>, resulting in a total solution consumption of 180 ml.

Table V-15 Parameters fixed for the deposition of CuCrO<sub>2</sub>

Parameter	Variation
Solvent	Ethanol
Solution Concentration	0.02 mol.l <sup>-1</sup>
Frequency of vibration	800 kHz
Temperature	400 °C
Gas Flux	7.5 l.min <sup>-1</sup>
O <sub>2</sub> ratio	20%
Extraction pressure	4,5 mmH <sub>2</sub> O
Time	90 minutes

### 5.1.3 Characterization of CuCrO<sub>2</sub> films

The CuCrO<sub>2</sub> films present an optical appearance completely different to Cu<sub>2</sub>O films, as presented in the Figure IV-52. The visual inspection of the film shows clearly the difference of phase, compared to Cu<sub>2</sub>O (Figure IV.1), since the gap energy is higher, so the film is more transparent in the visible range. Nevertheless, due to the absorption in the far-end of the visible range, a light grey color is observed when deposited on glass. As seen before, a good homogeneity throughout the whole sample (area of 4 cm<sup>2</sup> in each substrate) is obtained by this AA-MOCVD method. The film deposited on Silicon shows a thickness dependent color, in this case is close to 100 nm, creating a light blue color film.

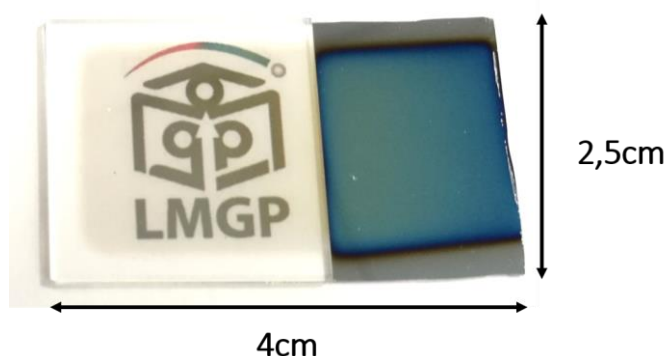


Figure V-95 Photographs of the CuCrO<sub>2</sub> thin film on glass (left) and silicon (right) with a thickness of 95nm

The atomic concentration of cations in the as-deposited sample was quantified by Wavelength dispersive X-ray spectroscopy (WDS) allowing to establish the efficiency of both cations deposition during the CVD process at 400 °C. The copper to total cations ratio (Cu/Cu+Cr) is obtained in the film as a function of the cationic concentration in the solution

is plotted in Figure V-96, together with the film thickness obtained by WDS. The films are Cr-rich, suggesting a more efficient deposition of chromium than copper under the selected deposition conditions. Additionally, a similar trend was observed by J. Crepelliere *et al.*<sup>5</sup> using a pulsed-injection MOCVD system; where it was found a deficit in Cu content into films deposited from solution with atomic concentration of Cu/(Cu+Cr) from 40% to 60%. In terms of films thickness, the values vary from 73 to 170 nm with a large increase for a cationic concentration in solution of 60%. For practical reasons in the readability of the text, from this point of this chapter, we will use the Cu/(Cu+Cr) ratio values obtained by WDS to name the different films deposited, shown in Table V-16.

Table V-16 Cu/(Cu+Cr) ratio in solution and detected by WDS together with the measured thickness

Cu/(Cu+Cr) solution (%)	Cu/(Cu+Cr) WDS (%)	Thickness (nm)
40	24 ± 1	73
50	46 ± 1	95
60	56 ± 1	170

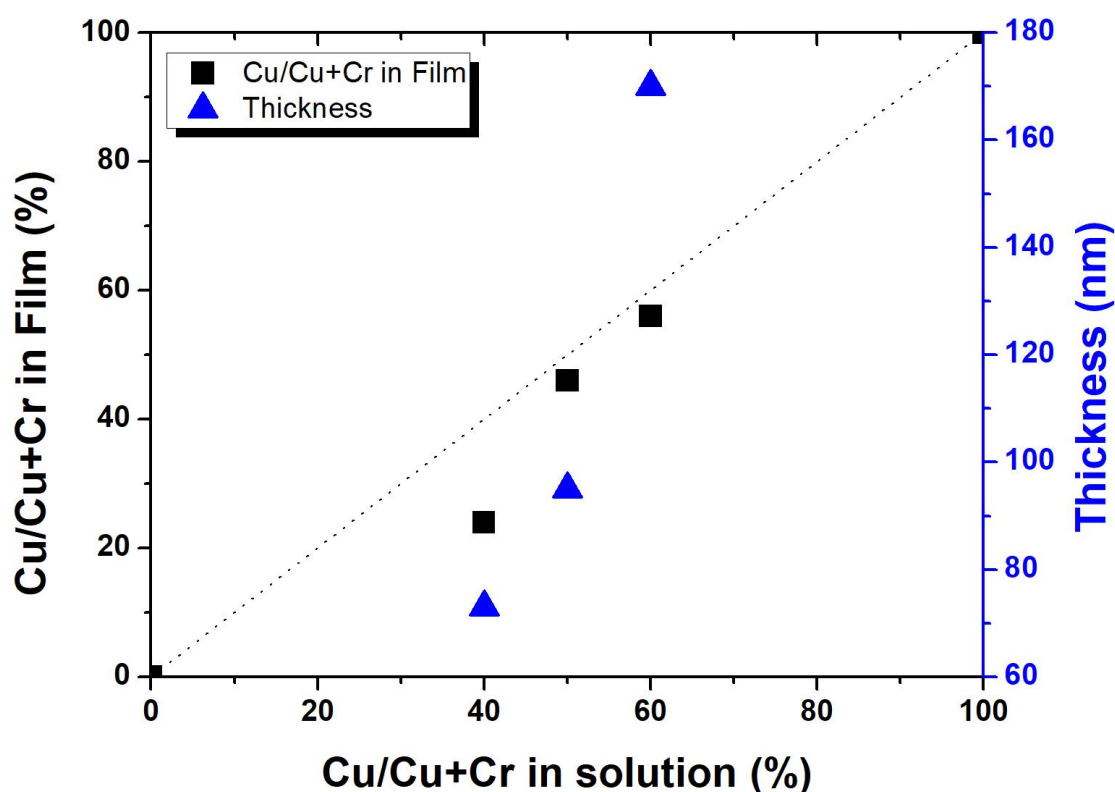


Figure V-96 Relative Cu/(Cu+Cr) content as obtained from EDS quantification analysis compared to the amount in solution. Black dotted line represents the 1:1 relation. Variation of thickness with the Cu/(Cu+Cr) ration in solution is represented too.

The thin film surface was analyzed by SEM to observe the microstructural effects due to copper content variation. The surface morphology of these three samples are represented in Figure V-97. In the sample with the lowest Cu content, 24%, elongated grains with a rough surface are visible. Similar results are reported in the literature for previous MOCVD<sup>2</sup> or spray pyrolysis studies<sup>6</sup>, in which a lower content of Cu origins needle-shaped structures. With the increase of Cu content, the grains become rounded shaped and densely packed, as already reported<sup>2</sup>. For illustration, the 46% atom Cu film cross section is displayed in the

Figure IV-55, with an average thickness of 95 nm.

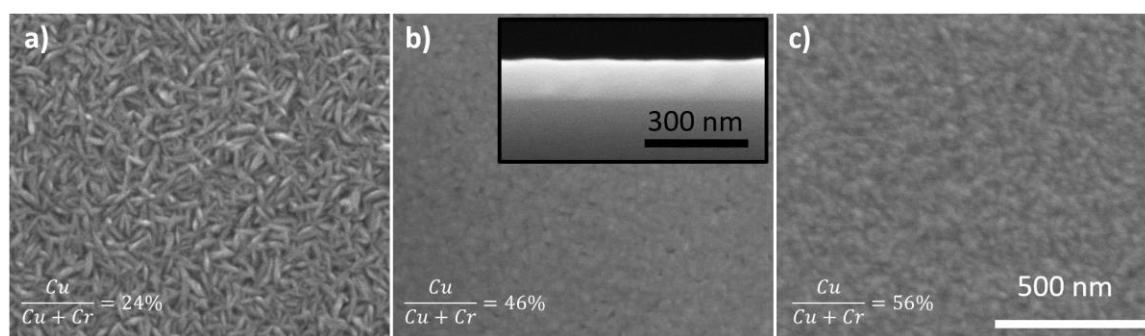


Figure V-97 SEM images of CuCrO<sub>2</sub> thin films deposited on glass at 400°C. Same magnification was used for all the top-view pictures (50000x) with the same scale for all the images. Cu/Cu+Cr ratio: a) 24%, b) 46% with the respective cross-section and c) 56%

XRD characterization, shown in Figure IV-58, was performed in Bragg-Brentano configuration on films deposited on glass. For the lowest Cu content, i.e. 24% of Cu content, no XRD peaks are detected, which lead us to conclude the presence of an amorphous or nano-crystalline phase. For the films with a higher Cu content, 46% and 56%, the XRD spectra is marked by the presence of the (012) and (110), diffraction peaks with various intensity at 36.4° and 62.4°, respectively. These diffraction peaks are attributed to the rhombohedral delafossite phase according to the 04-010-3330 file of the International Center for Diffraction Data (ICDD). The relatively small intensity and broad width of these peaks may reveal a low degree of crystallinity of the CuCrO<sub>2</sub> thin film. This can be attributed to the deposition temperature of 400 °C, which is typically close to the lowest crystallization temperature of the delafossite phase<sup>7</sup>. The crystallite size is estimated to be between 18 and 20nm in the two samples, as deduced from the (012) peak at 36.4° using the Scherrer's equation<sup>8</sup>.

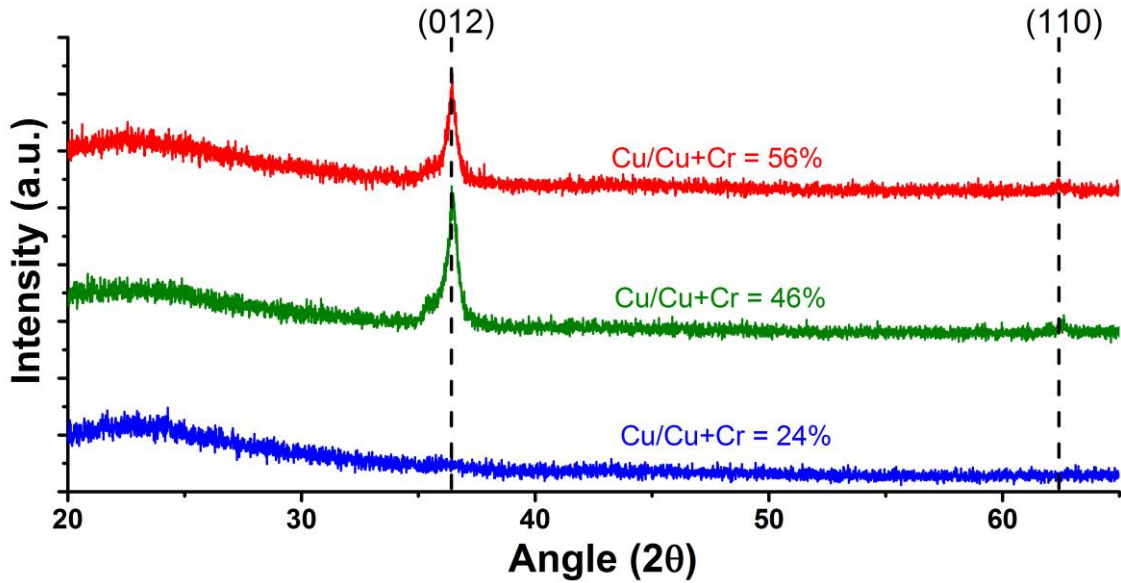


Figure V-98 XRD spectra in the Bragg-Berentano configuration of the CuCrO<sub>2</sub> thin films on glass. Reference spectrum of CuCrO<sub>2</sub>: ICDD n° 04-010-3330

The phase identification study was completed with Raman spectroscopy measurements. Concerning the analysis of Raman experiment let us recall that the delafossite ABO<sub>2</sub> compounds crystallize in a rhombohedral structure (space group R-3m or D<sub>3d</sub><sup>9</sup>). The 4 atoms of the primitive cell give rise to 12 zone center vibrational modes, 9 of them being optical modes and 3 being acoustic modes. The distribution of the different atoms in special Wyckoff positions is as follows: A and B atoms are in special positions 3a and 3b, respectively, the oxygen atoms in special position 6c. According to the method of nuclear site group analysis<sup>10</sup> and after subtraction of the three acoustic modes ( $A_{2u} + E_u$ ) of the total representation of the crystal, the irreducible representations associated to the optical modes can be expressed as:

$$\Gamma_{opt} = A_{1g} + E_g + 2 A_{2u} + 2 E_u \quad (V. 1)$$

where  $A_{1g}$  and  $E_g$  are Raman-active modes and  $A_{2u}$  and  $E_u$  modes are infrared (IR)-active modes. It should be noted that vibrational modes coming from A and B atoms are IR-active only and have no contribution to the Raman spectrum, which means that only oxygen atoms move in the Raman modes. The Raman spectra obtained with a wavelength of 488 nm are presented in Figure V-99. In coherence with the XRD results, the spectrum obtained from the film with the lowest Cu content does not present well-defined Raman peaks. In the two spectra registered from the films with higher Cu content, two Raman modes at 457 and 707

$\text{cm}^{-1}$  are detected that can be assigned to the modes  $E_g$  and  $A_{1g}$ <sup>11</sup> of the CuCrO<sub>2</sub> phase, respectively. The first mode, weakly observed on the decreasing tail of the Rayleigh line at  $107 \text{ cm}^{-1}$ , corresponds to an infrared-active mode  $E_u$  of the CuCrO<sub>2</sub> phase<sup>12</sup>. Other additional modes of weak intensity particularly a in the  $520\text{-}650 \text{ cm}^{-1}$ , also occur in the CuCrO<sub>2</sub> thin film spectrum. Such additional modes, can be assigned to defect-induced modes, have already been reported at  $536$  and  $586 \text{ cm}^{-1}$ <sup>11</sup>, and  $538$ ,  $557$ ,  $623$  and  $668 \text{ cm}^{-1}$ <sup>13</sup>. The comparison of our spectrum with IR spectra of the CuGaO<sub>2</sub> and CuAlO<sub>2</sub> delafossite compounds from Pellicer-Porres *et al.*<sup>14,15</sup> indicates that the CuCrO<sub>2</sub> additional modes in the  $520\text{-}650 \text{ cm}^{-1}$  range very close to those of the three  $E_u$  and  $A_{2u}$  CuGaO<sub>2</sub> and CuAlO<sub>2</sub> modes, as it is already the case for the first  $E_u$  mode at  $107 \text{ cm}^{-1}$  ( $122$  and  $144/149 \text{ cm}^{-1}$  in CuGaO<sub>2</sub> and CuAlO<sub>2</sub>, respectively). Owing to the very weak Raman signal of the additional modes, we cannot accurately symmetry assign them, but they are very likely IR modes. The presence of these modes, normally Raman-inactive in the CuCrO<sub>2</sub> Raman spectrum, indicates relaxed selection rules generated by a local symmetry breaking probably due to the presence of defects in the structure, such as Cu vacancies or oxygen interstitials. Moreover, the Raman spectra of both the CuCrO<sub>2</sub> thin films also emphasize the presence of carbon-based residual species, related to the by-products of the organic ligand of the AA-CVD precursors through the observation of the D- and G-bands characteristic of C-C bonds pointed at  $1356$  and  $1600 \text{ cm}^{-1}$ .

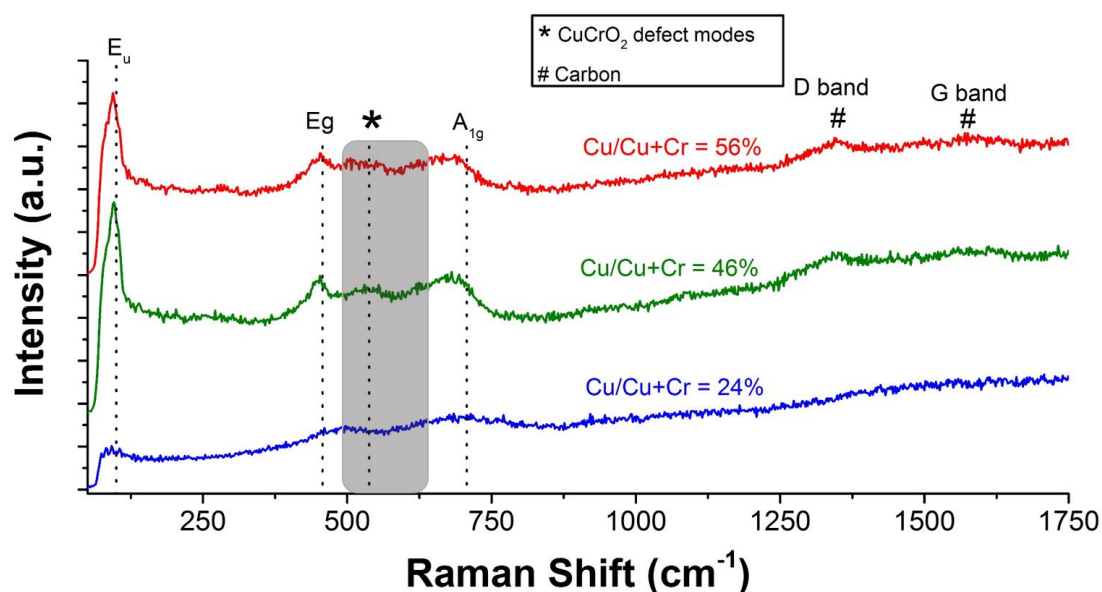


Figure V-99 Raman spectra of the CuCrO<sub>2</sub> thin films on glass

The optical total transmission of the CuCrO<sub>2</sub> films were scanned. The data corresponding to the three films are plotted in Figure V-100 a). The transmittance in the

visible range (390 nm – 700 nm) varies between 60% in the thinner case to 38% in the 56% Cu/(Cu+Cr). The thicker film show a lower transmittance, even in the near infra-red region. This fact is common of CuCrO<sub>2</sub> films, due to high reflectance<sup>16</sup>. Comparing with Cu<sub>2</sub>O films, the transmittance is slightly higher, especially for the 46% Cu content film. In terms of absorption edge, we calculated the direct band-gap for the different films, represented in Figure V-100 b). The two samples with higher Cu shows a value close to 3.2eV, while the 24% film has a value higher, which is attributed to the amorphous phase discussed previously.

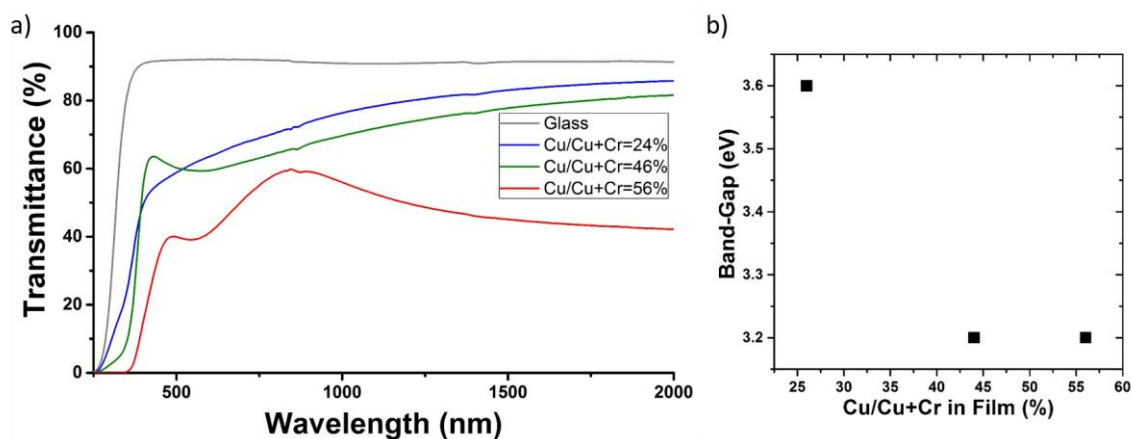


Figure V-100 a) Transmittance spectra from 250 nm to 2000 nm of the CuCrO<sub>2</sub> thin films on glass. The bare glass substrate transmittance is also represented as reference. b) Direct band-gap obtained from the transmittance spectra

Finally, the samples were electrically characterized. The electrical resistivity values obtained by Van der Pauw measurements are plotted in Figure V-99. We have also included the values of undoped Cu<sub>2</sub>O thin films previously presented in this manuscript and that of Cr<sub>2</sub>O<sub>3</sub> deposited in LMGP. The increase of Cu content affects the resistivity drastically, inducing a decrease from 100 Ω.cm, obtained for the film containing 24% of Cu, to the lowest value of 0.1Ω.cm, obtained for a film containing 56% of Cu. This value is lower than that obtained for pure Cu<sub>2</sub>O.

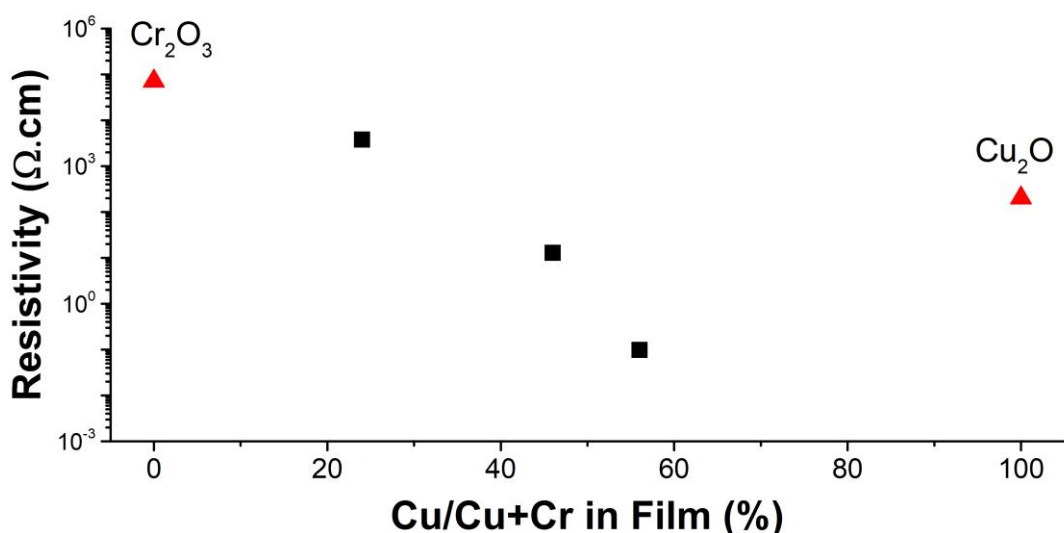


Figure V-101 Resistivity values obtained for the CuCrO<sub>2</sub> thin films as a function of copper content. Resistivity values for Cr<sub>2</sub>O<sub>3</sub> and Cu<sub>2</sub>O films are also represented

The origin of this lower resistivity was then investigated by Hall Effect measurements using a Van der Pauw configuration. Unfortunately, the hall coefficient sign was unable to be determined. As reported by the literature<sup>6</sup>, the mobility values of CuCrO<sub>2</sub> are below 1cm<sup>2</sup>.V<sup>-1</sup>.s<sup>-1</sup>, which are under the limit of the Hall Effect system used. Considering the mobility values in a 0.1cm<sup>2</sup>.V<sup>-1</sup>.s<sup>-1</sup> range, the density of free holes would vary from 10<sup>18</sup> cm<sup>-3</sup> in the 24% Cu film and up to 10<sup>21</sup> cm<sup>-3</sup> in the richest Cu content film.

#### 5.1.4 Conclusion on CuCrO<sub>2</sub> thin films

The growth of CuCrO<sub>2</sub> thin films by AA-MOCVD was achieved with noteworthy results in terms of transparency and resistivity, comparable with the literature<sup>4,5</sup>. The films prepared with an equimolar solution of both precursor showed a stoichiometry of 46% of Cu content, close to the ideal ratio for CuCrO<sub>2</sub>. They present a good compromise of optical and electrical properties, with a transmittance of 60% and resistivity values close to 10 Ω.cm. This film ratio was then selected to be tested for devices application.

## 5.2 ZnO/CuCrO<sub>2</sub> Core-Shell Nanowire Heterostructure for Self-Powered UV Photodetectors

### 5.2.1 Introduction

CuCrO<sub>2</sub> presents a high interest as p-type semiconductor because of its high conductivity, and its wide direct band gap energy. A state of art of this material has been resumed in section I.1.4. Besides, it presents a suitable type-II band alignment with ZnO. The combination of CuCrO<sub>2</sub> with ZnO has allowed to develop UV-sensor also discussed in section I.2.7. Nevertheless, nanostructured heterojunctions consisting in core-shell heterostructure based on ZnO nanowires (NW) have been ever reported so far. The use of nanowire arrays can improve the performance of a photo-electrical device, due to an increase of surface-to-volume ratio<sup>17</sup>, enhanced light trapping processes<sup>18-20</sup>, efficient charge carrier separation and collection over the nanowire, caused by the high mobility electron pathways in the monocrystalline NW<sup>18,21</sup>. In this work, we present the first fabrication of a ZnO/CuCrO<sub>2</sub> core-shell NW heterojunction using surface scalable chemical deposition techniques, and its integration into a self-powered UV photodetector.

### 5.2.2 Experimental

The growth of ZnO NW with controlled length and diameter has been developed and studied at LMGP in previous works<sup>22</sup>. ZnO NW arrays were grown by chemical bath deposition (CBD) on commercial 130 nm-thick ITO /glass substrates (Delta Technologies). The ITO/glass substrates were initially cleaned in an ultrasonic bath of acetone and then in a beaker containing isopropanol for 15 min each to remove any contaminants. Then, a ZnO seed layer was deposited onto the ITO thin layer by dip coating based on sol-gel reactions. This ZnO layer is required to control the nucleation, growth and structural morphology of ZnO NWs<sup>23</sup>. A 0.375 mol.l<sup>-1</sup> equimolar solution of zinc acetate (Zn(CH<sub>3</sub>COO)<sub>2</sub>·2H<sub>2</sub>O) and monoethanolamine (MEA) dissolved in absolute ethanol was used. More details can be found in Cossuet *et al.*<sup>24</sup>. A two-step heat treatment was subsequently performed at 300 °C for 10 minutes and at 500 °C for 1 h to remove residual organic compounds and to crystallize the ZnO seed layer, respectively. The Chemical Bath Deposition (CBD) of ZnO NWs was achieved on the ZnO seed layer/ITO/glass substrate by using a 0.03 mol.l<sup>-1</sup>

equimolar solution of zinc nitrate hexahydrate [Zn(NO<sub>3</sub>)<sub>2</sub>·6H<sub>2</sub>O] and hexamethylenetetramine [C<sub>6</sub>H<sub>12</sub>N<sub>4</sub>] dissolved in deionized water. The substrates were placed face down into a sealed beaker filled with the equimolar solution and heated at 90 °C for 3 hours in a regular oven. After the growth, the substrates were rinsed with deionized water, and dried with nitrogen <sup>25</sup>.

The deposition of the CuCrO<sub>2</sub> thin films in the form of a semiconducting shell covering the ZnO NW arrays was achieved by AA-MOCVD. The solution-based process was identical to the one explain in Section 1.2 in this chapter. The main parameters are resumed in Table V-15. Corning glass and ZnO/ITO covered glass were also used as substrates in order to obtain details on the film properties and compare the thin film with the nanowire configuration. The ZnO film used were deposited by Pulsed Liquid Injection Metal Organic Chemical vapor deposition (PI-MOCVD) at 400 °C into an Annealsys MC-200 reactor similar to the case presented in the Chapter IV.3. Both copper and chromium precursors were equimolar in concentration. The deposition was performed for 1 h at 400 °C. The solution consumption rate of 2 ml.min<sup>-1</sup>, resulting in a total solution consumption of 120 ml. Circular silver contacts with a diameter of 0.5 mm defining the size of the self-powered UV photodetector were deposited by thermal evaporation on top of the ZnO / CuCrO<sub>2</sub> core-shell NW heterostructures.

### 5.2.3 Structural characterization of core-shell structures

The morphologies of the ZnO/CuCrO<sub>2</sub> core-shell NW heterostructures at different elaboration step are shown in Figure V-102 by top-view and cross-sectional FESEM images. At left, SEM images show the ZnO NWs with a mean length around 800 nm and a mean diameter in the range of 35 to 65 nm. They grow vertically on the 40 nm-thick polycrystalline ZnO seed layer to form a dense array of about 53 NW/μm<sup>2</sup>. They typically nucleate on the *c*-axis oriented grains of the seed layer, and subsequently elongate along the polar *c*-axis <sup>23</sup>. Following the deposition of the CuCrO<sub>2</sub> shell, the smooth surface and hexagonal shape of ZnO NW is transformed into a rougher surface and rounded morphology over the whole NW array, as seen in Figure V-102 c). Consequently, the ZnO/CuCrO<sub>2</sub> core-shell NW heterostructures have a broader apparent diameter in the range of 50 to 200 nm and are separated each other by a decreased mean distance. The CuCrO<sub>2</sub> shell follows the elongated shape of the ZnO NWs with high uniformity and conformity, from their bottom to their top, as shown in Figure V-102 d). Top-view and cross-sectional

FESEM images of the final whole self-powered UV photodetectors made of ZnO/CuCrO<sub>2</sub> core-shell NW heterostructures, including the thermo-evaporated Ag contact, are presented in Figure V-102 e) and f). The Ag contact forms a rough thin film and appears to cap the ZnO/CuCrO<sub>2</sub> core-shell NW heterostructures, by mostly covering their top and slightly their vertical sidewalls to an approximate depth of about 300 nm.

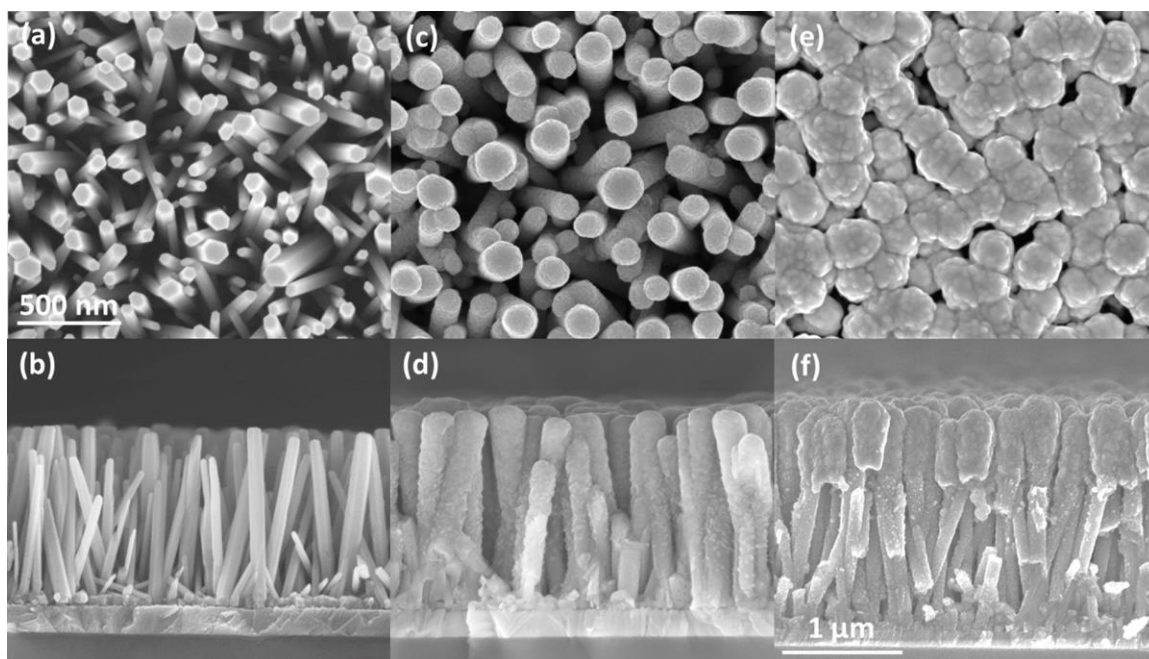


Figure V-102 FESEM images at different steps during the fabrication of the core-shell heterostructure: a) Top-view and b) cross-sectional of ZnO NW arrays grown on ITO/glass substrate, c) Top-view and d) cross-sectional of CuCrO<sub>2</sub>/ZnO NW heterostructures, and e) Top-view and f) cross-sectional of CuCrO<sub>2</sub>/ZnO NW heterostructures covered with the Ag contact. The 500 nm scale bar is valid for images (a-d) and 1 μm for f) only.

The Grazing incidence X-Ray diffraction (GIXRD) patterns spectra of the CuCrO<sub>2</sub> thin film on glass substrate, of the ZnO NW arrays on ITO/glass substrate, and of the ZnO / CuCrO<sub>2</sub> core-shell NW heterostructures on ITO/glass substrate, are presented in Figure V-103. The GIXRD pattern of the CuCrO<sub>2</sub> thin film is marked by the presence of the (012), (104), (110), and (116) diffraction peaks with various intensity at 36.4°, 40.9°, 62.4° and 71.5°, respectively. Due to the Grazing Incidence technique, more peaks are visible than in the previous study of section (V.1), however low degree of crystallinity of the CuCrO<sub>2</sub> thin film is similar. The GIXRD pattern of the ZnO NW arrays is dominated by the intense (0002) diffraction peak at 34.4°, revealing that ZnO NWs are crystallized in the wurtzite phase. Additionally, (10 $\bar{1}$ 0), (10 $\bar{1}$ 1), (10 $\bar{1}$ 2), (11 $\bar{2}$ 0), and (10 $\bar{1}$ 3) diffraction peaks occurring at 31.8, 36.3, 47.6, 56.7, 62.9° are attributed to the polycrystalline ZnO seed layer according to the 00-036-1451 ICDD file. The GIXRD pattern of the ZnO/CuCrO<sub>2</sub> core-

shell NW heterostructures on ITO/glass substrates show the presence of many diffraction peaks, which combine the features of each semiconductor in the stacking as discussed above, i.e. the ITO thin layer, ZnO seed layer and NWs, as well as the CuCrO<sub>2</sub> shell. The two main (012) and (110) diffraction peaks of the CuCrO<sub>2</sub> shell at 36.4° and 62.4° overlap with the diffraction peaks of the ZnO seed layer and very likely exhibit a relatively small intensity. Nevertheless, it should be noted that the long tail of the (012) diffraction peak at 36.4° is very likely related to the CuCrO<sub>2</sub> shell.

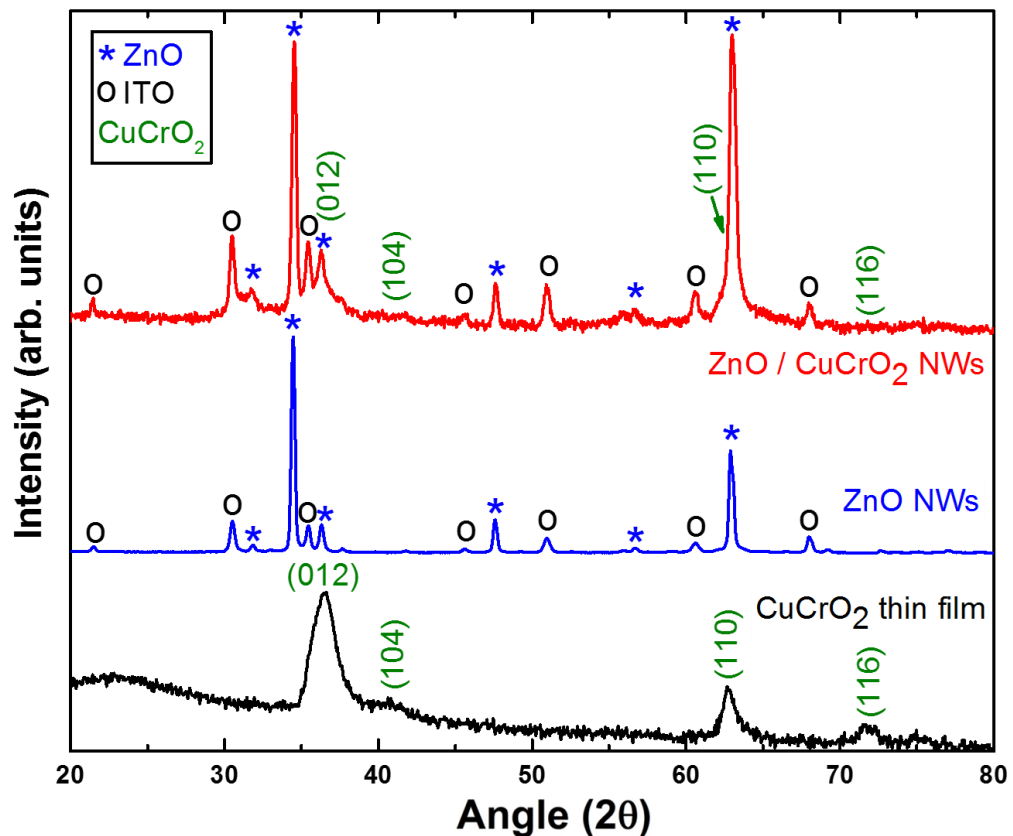


Figure V-103 a) GIXRD patterns of the CuCrO<sub>2</sub> thin film deposited on glass substrate, of ZnO NW arrays grown on ITO/glass substrate, and of ZnO/CuCrO<sub>2</sub> core-shell NW heterostructures grown on ITO/glass substrate.

Raman scattering spectra of the CuCrO<sub>2</sub> thin film, ZnO NW arrays and of the core-shell NW heterostructures are presented in Figure V-104. In the CuCrO<sub>2</sub> thin film case, we observe a similar spectrum to the previous section (V.1), with Raman, IR-active and defect induced modes visible in the spectrum. In the ZnO NW case, the correlated ZnO Raman lines occur at 99 cm<sup>-1</sup> (E<sub>2</sub><sup>low</sup>), 334 cm<sup>-1</sup> (E<sub>2</sub><sup>high</sup>-E<sub>2</sub><sup>low</sup>), 439 cm<sup>-1</sup> (E<sub>2</sub><sup>high</sup>), 587 cm<sup>-1</sup> (E<sub>1</sub>(LO)<sup>low</sup>), 1106 cm<sup>-1</sup> (2LO), and 1160 cm<sup>-1</sup> (2A<sub>1</sub>(LO), E<sub>1</sub>(LO); 2LO)<sup>26</sup>. The remaining Raman

peaks as identified by the dark open circles are attributed to the ITO thin layer and its correlated phonon modes at 591 and 1102  $\text{cm}^{-1}$  also occur in the corresponding Raman spectrum. On the core-shell NW structure, the Raman lines at 458  $\text{cm}^{-1}$  ( $E_g$ ), 709  $\text{cm}^{-1}$  ( $A_{1g}$ ), and the additional defect-induced modes, particularly those at  $\sim 106$ , 207 and 754  $\text{cm}^{-1}$ , are direct evidence of the CuCrO<sub>2</sub> shell crystallized in the delafossite phase<sup>3,12,11</sup>. Moreover, the Raman spectra of both the CuCrO<sub>2</sub> thin film and the ZnO/CuCrO<sub>2</sub> core-shell NW heterostructures also emphasize the presence of carbon-based residual species, related to the by-products of the organic ligand of the deposition technique, through the observation of the D- and G-bands characteristic of C-C bonds pointed at 1356 and 1600  $\text{cm}^{-1}$ .

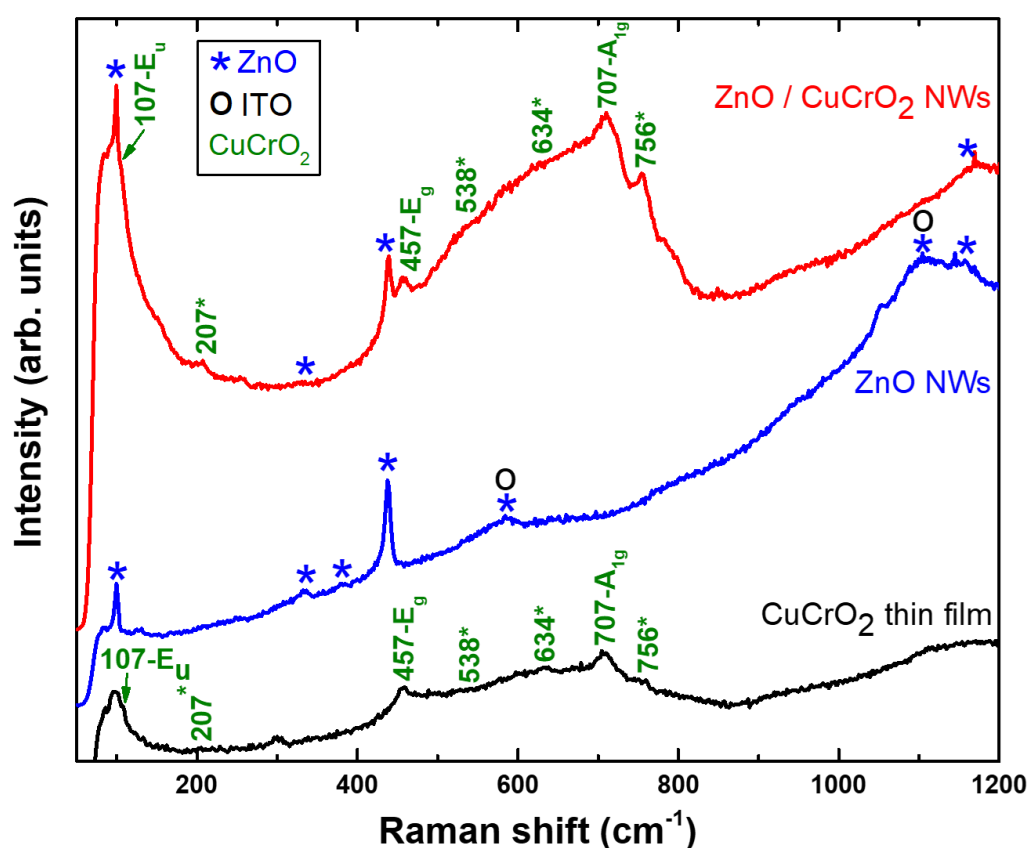


Figure V-104 Raman scattering spectra of the CuCrO<sub>2</sub> thin film deposited on glass substrate, of ZnO NW arrays grown on ITO/glass substrate, and of ZnO/CuCrO<sub>2</sub> core-shell NW heterostructures grown on ITO/glass substrate. The CuCrO<sub>2</sub> defect-induced modes are indicated by a green star.

A detailed local investigation of the structural morphology and of the chemical composition of the ZnO/CuCrO<sub>2</sub> core-shell NW heterostructures is presented from Figure V-105 to Figure V-107, by TEM and HRTEM imaging, EDS-STEM mapping, and Automated crystal phase and orientation mapping with precession (ASTAR) mapping, respectively. The TEM image in Figure V-105 a) confirms that the polycrystalline CuCrO<sub>2</sub>

shell uniformly covers the ZnO NW with a high degree of uniformity and conformity. The CuCrO<sub>2</sub> shell is found to be about 35 nm-thick. The selected area electron diffraction (SAED) pattern in Figure V-105 b) is assigned to the delafossite phase of the CuCrO<sub>2</sub> shell, which is in agreement with the GIXRD patterns and Raman spectra. The HRTEM image of the ZnO/CuCrO<sub>2</sub> interface recorded at the top of the ZnO NW in Figure V-105 c) shows no epitaxial relationship between the ZnO NW and the CuCrO<sub>2</sub> shell. The absence of heteroepitaxy is likely due to the large lattice mismatch between ZnO and CuCrO<sub>2</sub>.

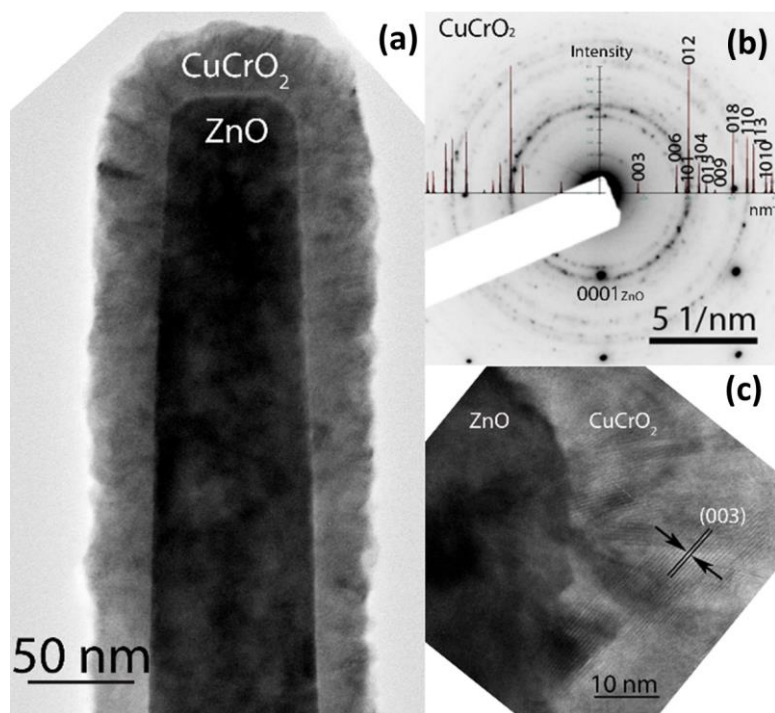


Figure V-105 a) TEM image of a ZnO/CuCrO<sub>2</sub> core-shell NW heterostructure. b) Corresponding SAED pattern identifying the CuCrO<sub>2</sub> rhombohedral delafossite phase along with a theoretical diffraction pattern of the present phase as computed with the software JEMS. c) Corresponding HRTEM image of the ZnO / CuCrO<sub>2</sub> interface recorded close to the top face of the ZnO NW.

EDS-STEM elemental maps showing the spatial distribution of the Zn, Cu, Cr and O elements within the ZnO/CuCrO<sub>2</sub> core-shell NW heterostructure are presented in Figure V-106.

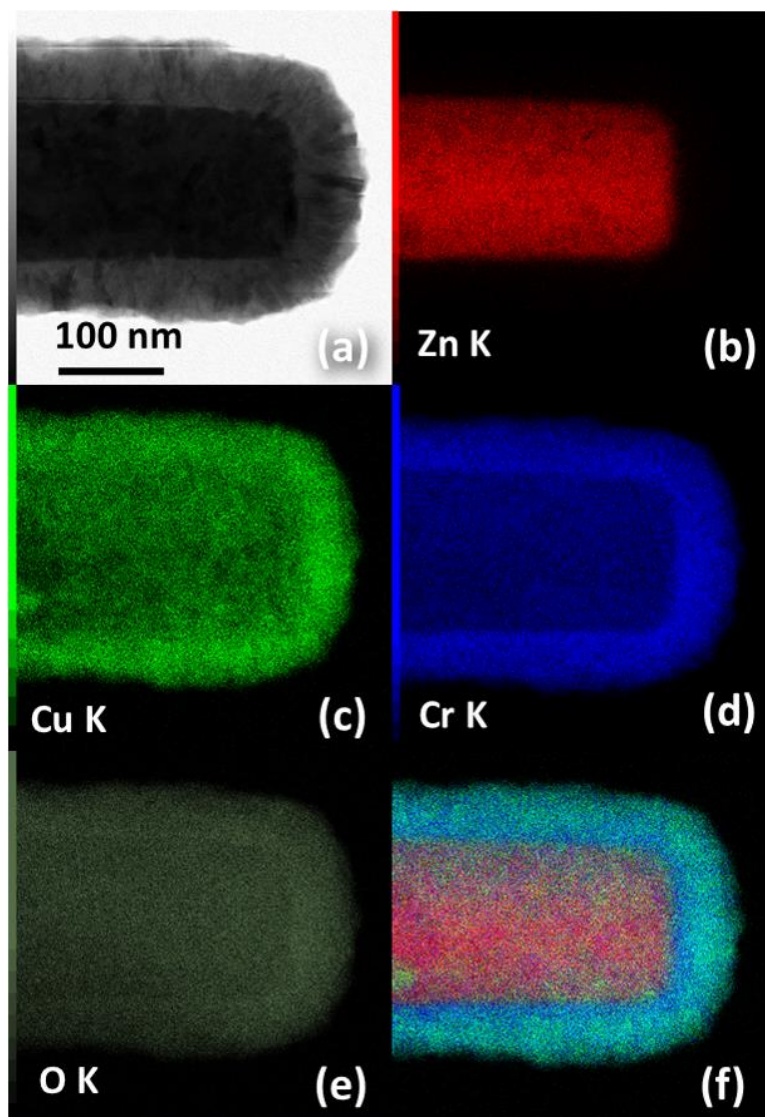


Figure V-106 a) Bright-field STEM image of a ZnO/CuCrO<sub>2</sub> core-shell NW heterostructure. b-e) Corresponding EDS-STEM elemental maps of the b) Zn, c) Cu, d) Cr, and e) O elements, respectively. f) Superimposition of the corresponding EDS-STEM maps of the Zn, Cr, and Cu elements. The 100 nm scale bar is valid for all images.

The Zn element signal is clearly of significance only in the core of the heterostructure, corresponding to the ZnO NW. In contrast, the presence of Cu and Cr elements is confirmed in all the heterostructure, as expected from a conformal coating. The related signals are more intense in the part surrounding the Zn elements, according to geometrical effect related to the core-shell configuration of the heterostructure. The O element signal is detected in all the ZnO/CuCrO<sub>2</sub> core-shell NW heterostructure. All in all, the superimposed EDS-STEM elemental map in Figure V-106 f) together with Figure V-102 d) and Figure V-105 a) provide strong evidence that AA-CVD is a highly relevant

technique for the conformal deposition of thin films on high aspect ratio nanoscale structures.

ASTAR maps representing the crystalline phase and orientation of the ZnO/CuCrO<sub>2</sub> core-shell NW heterostructures are shown in Figure V-107 a) and Figure V-107 b), respectively, to overcome the inherent spatial localization on the nanometer scale of the HRTEM imaging. Basically, the few nanometer-sized incident electron beam was precessed and scanned over the ZnO/CuCrO<sub>2</sub> core-shell NW heterostructure<sup>27,28</sup>. At each location, the recorded experimental electron diffraction pattern was compared with a complete set of theoretical diffraction patterns, namely the so-called templates computed for all possible crystalline phases and orientations, and fitted to identify the involved crystalline phase and orientation. From the present approach, the CuCrO<sub>2</sub> shell in Figure V-107 a) is found to be composed of small nano-grains, in the 5 to 10 nm range, with the exclusive delafossite phase grown on both the top face and along the vertical sidewalls of the ZnO NWs. This correlates very well with the identified phases, and it shows a lower size of the grains when compared to thin films deposited on glass, with a crystallite size around 20nm.

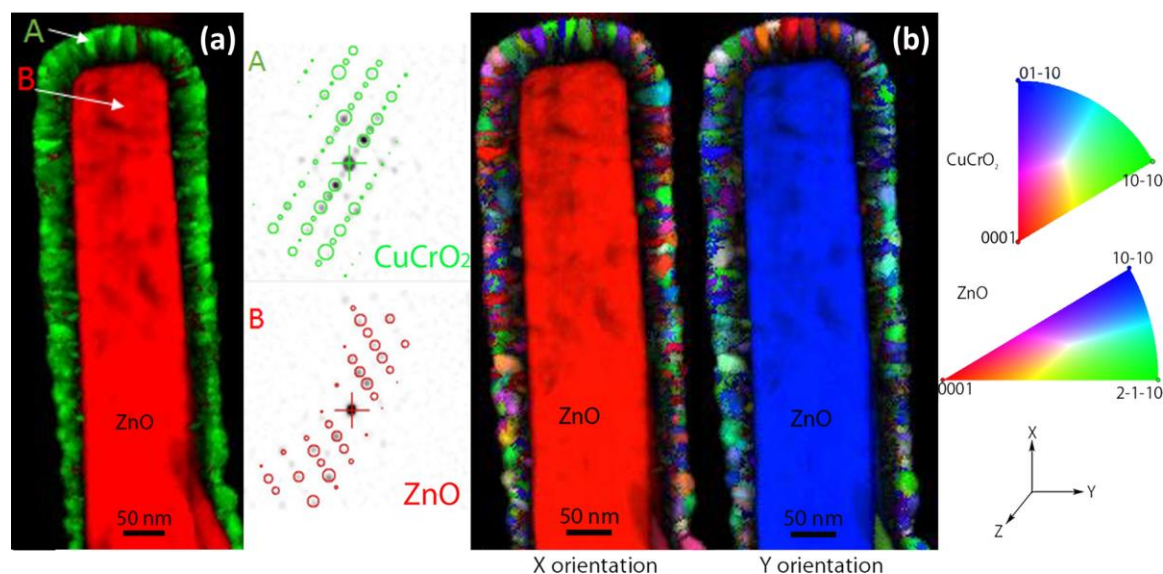


Figure V-107 a) ASTAR map representing the crystalline phases of a ZnO/CuCrO<sub>2</sub> core-shell NW heterostructure, the ZnO and CuCrO<sub>2</sub> crystal phases being represented in red and green, respectively. The insets are the electron diffraction patterns collected at the points designated by A and B on the corresponding map, in which the open circles represent the theoretical electron diffraction patterns of wurtzite ZnO and rhombohedral CuCrO<sub>2</sub>. b) Corresponding ASTAR map representing the crystalline orientations of the ZnO/CuCrO<sub>2</sub> core-shell NW heterostructure, along the X- and Y-axes as indicated in the inset. The color scales for wurtzite ZnO and rhombohedral CuCrO<sub>2</sub> are given in the insets.

No other crystalline phase is identified in the local analysis. On the one hand, the orientation maps on the ZnO NW, as presented in Figure V-107 b), confirm the oriented growth along the  $c$ -axis. In contrast, the nano-grains composing the CuCrO<sub>2</sub> shell present a broad orientation distribution, where neither epitaxial relationship with the ZnO NW nor strong preferential orientations (*i.e.*, texture) are revealed. However, when the growth axis is considered, it is revealed that the grains on the top face of the ZnO NWs (see X-orientation map) and on their vertical sidewalls (see Y-axis orientation map) are both close to the  $[01\bar{1}0]$  to  $[10\bar{1}0]$  orientations. Additionally, the CuCrO<sub>2</sub> nano-grains on the top face of the ZnO NW indicate that a columnar growth regime has proceeded. Their elongated-grain shape strongly contrasts with the grain morphology on the vertical sidewalls of the ZnO NW, which is formed by much smaller grains, further indicating that a distinct growth regime may have taken place.

#### 5.2.4 Electrical characterization of core-shell heterostructures

A schematic representation of the self-powered UV photodetector made of ZnO/CuCrO<sub>2</sub> core-shell NW heterostructures covered with the Ag contact is presented in Figure V-108 a) together with the corresponding energy band diagram in Figure V-108 b).

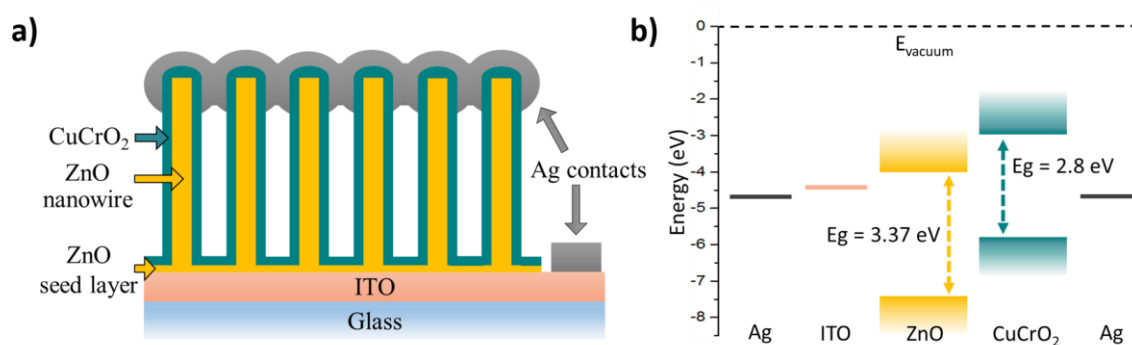


Figure V-108 a) Schematic of the self-powered UV photodetector based on ZnO/CuCrO<sub>2</sub> core-shell NW heterostructures. b) Corresponding energy band diagram.

Basically, the working principle of the photodiode is based on the UV illumination from the glass substrate side, where the incident photons pass through the ITO thin layer with the band gap energy higher than 4.2 eV<sup>29</sup>. These photons are first absorbed in the ZnO NWs and afterward in the CuCrO<sub>2</sub> shell, leading to the photo-generation of electron-hole pairs possibly in both layers and at the interface. By taking into account the positions of the conduction band minimum and of the valence band maximum, the  $pn$  heterojunction

between ZnO and CuCrO<sub>2</sub> generates a depletion layer with staggered gaps. The electron affinities of ZnO and CuCrO<sub>2</sub> have typically been reported as 4.0 eV and 3.0 eV<sup>1</sup>, respectively, while their band gap energy are about 3.37 and 2.8 eV<sup>9</sup>, respectively. The successive type II band alignments efficiently favours charge carrier separation and collection and thus prevents the recombination of photo-generated electron-hole pairs, thus resulting in the creation of the photocurrent.

The dark J-V characteristic of the self-powered UV photodetector made of Zn/CuCrO<sub>2</sub> core-shell NW heterostructures is shown in Figure V-109 and reveals a high rectifying behaviour with a reverse current density below  $2 \times 10^{-4}$  A/cm<sup>2</sup> at -1 V, and a forward current density of 0.9 A/cm<sup>2</sup> at +1 V.

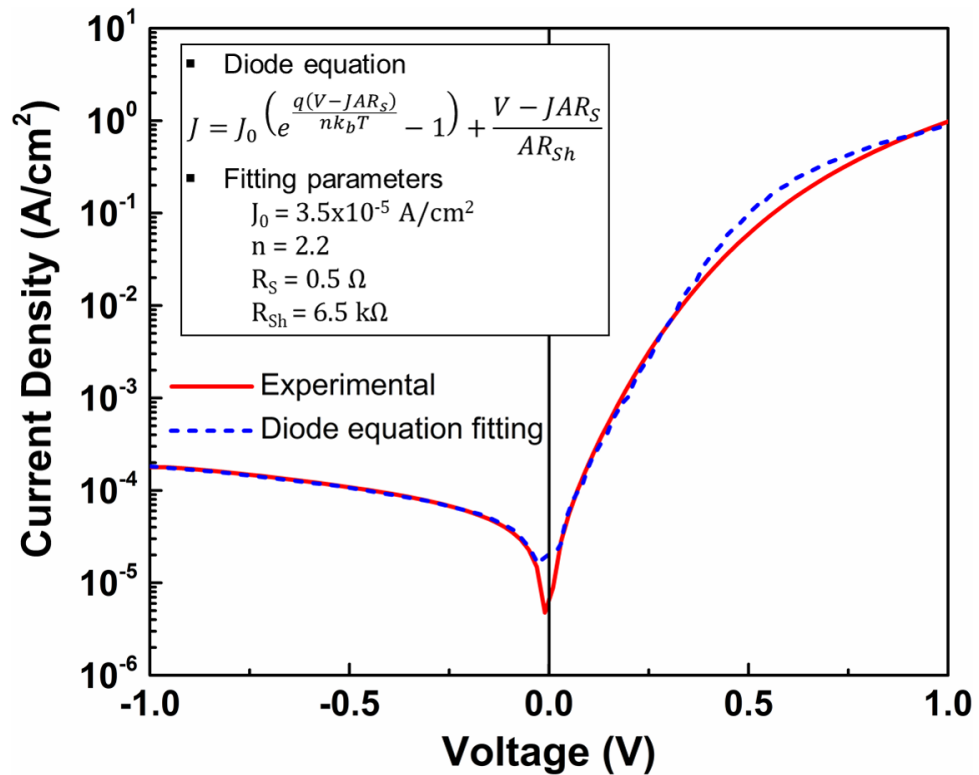


Figure V-109 J-V measurements under darkness conditions of the self-powered UV photodetector made of ZnO/CuCrO<sub>2</sub> core-shell NW heterostructures. The value of the rectification ratio at  $\pm 1$  V is 5500.

The rectifying ratio between the forward current density to the reverse current density at  $\pm 1$  V is as high as 5500, which is considerably larger than the ratio of 70 at  $\pm 1.5$  V for the diode made of ZnO/CuCrO<sub>2</sub> thin films as reported by Tonooka *et al.*<sup>30</sup>. The JV tests also performed on planar films showed a lower diode response, pictured in Figure V-110. In this case, the diode behavior was detected for higher applied voltages, larger than 2V, with significantly lower rectifying ratio, around 20 at  $\pm 5$  V.

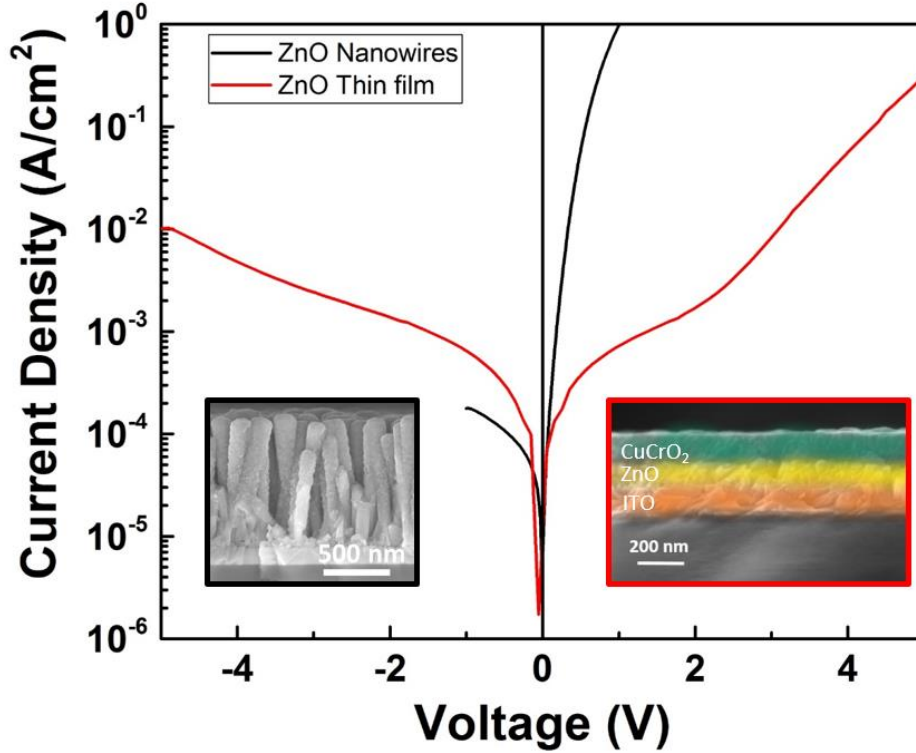


Figure V-110 J-V measurements under darkness conditions of ZnO/CuCrO<sub>2</sub> core-shell NW and planar heterostructure. SEM cross section of both devices are also represented.

As already stated before for other materials <sup>31</sup>, employing nanostructured heterojunction configuration strongly enhance their performances as compared to thin film configuration. The device response drastically increases due to a higher surface-to-volume ratio, resulting in a large interface between the two semiconductors. The total area of the heterojunction was estimated to increase by a factor of at least five considering the NW density, average diameter and covered sidewalls by the CuCrO<sub>2</sub> shell. The single crystalline nature of ZnO NWs can also improve the electrical conduction as a result of their high mobility and of the absence of grain boundaries. The diode parameters for the ZnO/CuCrO<sub>2</sub> core-shell NW array were extracted by fitting the experimental curve with the typical diode equation, considering the series and shunt resistances as follows:

$$J = J_0 \left( e^{\frac{q(V-JAR_S)}{nk_B T}} - 1 \right) + \frac{V - JAR_S}{AR_{Sh}} \quad (V.2)$$

where  $J$  is the current density,  $J_0$  is the reverse current density,  $q$  is the electron charge,  $V$  is the applied voltage,  $A$  is the contact area,  $R_S$  is the series resistance,  $n$  is the non-ideality factor,  $k_B$  is the Boltzmann's constant,  $T$  is the absolute temperature, and  $R_{Sh}$  is the shunt resistance. The non-ideality factor  $n$  of the diode is found to be 2.2, indicating a good diode behaviour. The relatively large shunt resistance of 6.5 k $\Omega$  is correlated with

the small reverse current density at -1 V, which can be attributed to the conformal CuCrO<sub>2</sub> shell and to the high mobility in the ZnO NW. Moreover, the series resistance of 0.5  $\Omega$  originates from the quality of the metallic contact and from the high conductivity of the CuCrO<sub>2</sub> shell<sup>32</sup>. Overall, the fitted values of  $J_0$ ,  $n$ ,  $R_S$  and  $R_{Sh}$  as well as the rectification ratio of the ZnO/CuCrO<sub>2</sub> core-shell NW heterostructures reveal the high quality of the  $pn$  heterojunction.

The absorption spectrum of the ZnO/CuCrO<sub>2</sub> core-shell NW heterostructures as deduced from total transmittance and direct reflectance measurements together with the responsivity of the corresponding self-powered UV photodetector are shown in Figure V-111.

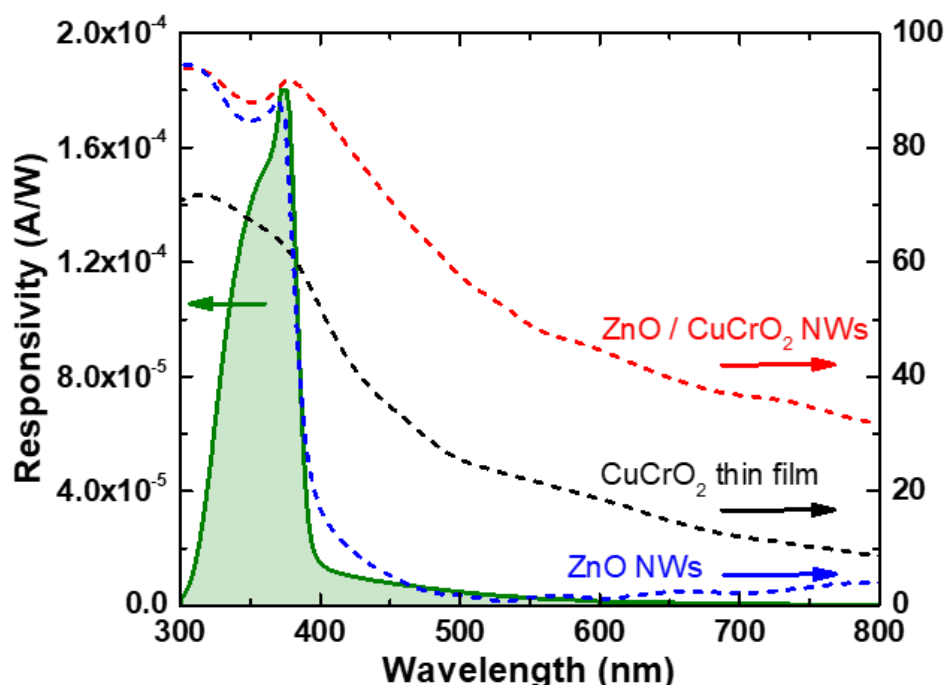


Figure V-111 Responsivity and absorption measurements of the self-powered UV photodetector made of ZnO/CuCrO<sub>2</sub> core-shell NW heterostructures, as well as absorption measurements of the ZnO NW array deposited by CBD on ITO/glass and of the CuCrO<sub>2</sub> thin film deposited on glass.

An absorption higher than 85 % below 400 nm is obtained in the UV region. This is due to the wide band gap energies of both oxides, which are higher than 2.8 eV, and to the antireflective character of the nanostructured NW array<sup>33</sup>. The responsivity of the self-powered UV photodetector (*i.e.*, the photo-generated current per unit incident light power) shows only one peak centred around 374 nm, which very well correlates with the 3.37 eV band gap energy of ZnO and confirms that the photo-generation of charge carriers

predominantly occurs in the ZnO NWs. The maximum responsivity of  $1.87 \times 10^{-4}$  A/W at 374 nm is achieved, followed by a sharp drop to  $1.49 \times 10^{-5}$  A/W at 400 nm. Subsequently, it gradually decreases to reach values lower than  $10^{-6}$  A/W above 650 nm. Furthermore, the responsivity drop correlates well with the absorption drop observed for ZnO NWs on ITO/glass substrates without the CuCrO<sub>2</sub> shell, as shown in Figure V-111. In other words, the CuCrO<sub>2</sub> shell very likely acts mainly as a hole transporting materials and does not significantly contribute to the responsivity signal. The UV-to-visible rejection ratio (374-550 nm) of 68, highlights that the device acts as a suitable selective UV photodetector. The rejection ratio is comparable to other ZnO core-shell NW heterostructure based-UV photodetectors, such as ZnO / CuSCN devices<sup>34,35</sup>.

Moreover, JV measurements of the UV photodetector made of ZnO/CuCrO<sub>2</sub> core-shell NW heterostructures under darkness and AM 1.5G illumination conditions are shown in Figure V-112.

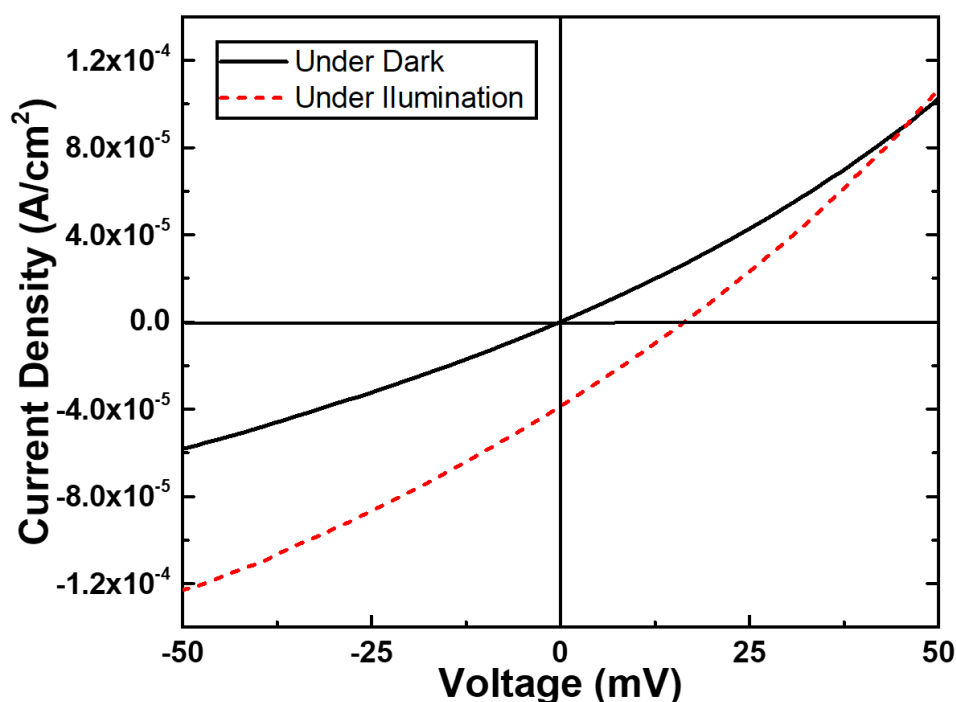


Figure V-112 JV measurements under darkness and under AM 1.5G illumination conditions of the self-powered UV photodetector made of ZnO/CuCrO<sub>2</sub> core-shell NW heterostructures.

The suitable photovoltaic effect with an open-circuit voltage ( $V_{oc}$ ) and short-circuit current density ( $J_{sc}$ ) of 16 mV and  $37 \mu\text{A}/\text{cm}^2$ , respectively, reveal that the ZnO/CuCrO<sub>2</sub> heterojunction is able to properly separate and collect the photo-generated charge carriers,

which demonstrate that this UV photodetector offers self-powering capabilities. The higher specific surface area of the heterojunction is expected to enhance light trapping processes in the ZnO NW arrays, as well as to exhibit a larger total volume of depletion region and longer carrier lifetime<sup>36</sup>. However, the  $V_{OC}$  of 16 mV is fairly low, especially when compared to other delafossite phase material like CuAlO<sub>2</sub>, which presents a  $V_{OC}$  of 250 mV when combined with ZnO NWs<sup>37</sup>. The use of a CuAlO<sub>2</sub> layer filling the ZnO NW arrays and thus planarizing the electrical contact may account for the improvement of the PV performances. The reduced PV performances of our device may also be explained by the CuCrO<sub>2</sub> properties themselves, especially the anisotropy of its electronic properties<sup>38</sup>, and its typical low hole mobility. The present findings reveal that an all-oxide core-shell NW heterostructure grown by chemical deposition techniques appear as a promising candidate as self-powered UV photodetectors.

### 5.2.5 *Conclusions on the core-shell heterostructures*

An original core-shell heterostructure made of ZnO NWs covered with a conformal CuCrO<sub>2</sub> shell was successfully achieved through a low-cost surface scalable chemical fabrication route. The structural morphology of the CuCrO<sub>2</sub> grains shows a columnar grain growth at the top of the ZnO NWs, while it consists of smaller nano-grains on their vertical sidewalls. Although no epitaxial relationships occur as revealed by ASTAR maps, the different grain morphology obtained on the different ZnO faces implies distinct growth mechanisms taking place in each case. This heterostructure successfully works as a diode, with a rectification ratio as high as 5500 at  $\pm 1$  V, which is much better than similar planar diodes. It further exhibits a high absorption above 85% in the UV region. Moreover, the device presents a maximum responsivity of 187  $\mu\text{A/W}$  under zero bias at 374 nm and a high UV-to-visible rejection ratio (374-550 nm) of 68 together with a PV effect under standard AM1.5G illumination. The combination of the high rectification ratio, of the high absorption in the UV region, and of the significant responsivity offers promising possibilities for the use of this heterostructure as a self-powered UV photodetector. Eventually, the use of CBD and AA-CVD at temperatures below 500 °C is favorable for the implementation of all oxide-based self-powered UV photodetectors with reduced costs and large scale production.

### 5.3 Conclusions

The growth of CuCrO<sub>2</sub> thin films and consequent implementation into a nanostructured photodetector was successfully achieved in this work. The delafossite phase was obtained at temperature compatible with glass substrate and different n-type semiconductor oxides, enable by the chemical deposition using organic precursors. The focus on a different copper-based oxide with a large band-gap than Cu<sub>2</sub>O was fundamental to show the possible application of this delafossite material in transparent or UV-light oriented devices, other than transparent electronics.

### 5.4 References

- (1) Robertson, J.; Clark, S. J. Limits to Doping in Oxides. *Phys. Rev. B - Condens. Matter Mater. Phys.* **2011**, *83* (7), 1–7.
- (2) Crépellière, J.; Lunca Popa, P.; Bahlawane, N.; Leturcq, R.; Werner, F.; Siebentritt, S.; D., L. Transparent Conductive CuCrO<sub>2</sub> Thin Films Deposited by Pulsed Injection Metal Organic Chemical Vapor Deposition: Up-Scalable Process Technology for an Improved Transparency/conductivity Trade-Off. *J. Mater. Chem.* **2016**, 31–37.
- (3) Farrell, L.; Norton, E.; Smith, C. M.; Caffrey, D.; Shvets, I. V.; Fleischer, K. Synthesis of Nanocrystalline Cu Deficient CuCrO<sub>2</sub> a High Figure of Merit P-Type Transparent Semiconductor. *J. Mater. Chem. C* **2016**, *4* (1), 126–134.
- (4) Farrell, L.; Norton, E.; Dowd, B. J. O.; Caffrey, D.; Shvets, I. V.; Fleischer, K.; Farrell, L.; Norton, E.; Dowd, B. J. O.; Caffrey, D.; Shvets, I. V.; Fleischer, K. Spray Pyrolysis Growth of a High Figure of Merit , Nano-Crystalline , P-Type Transparent Conducting Material at Low Temperature Spray Pyrolysis Growth of a High Figure of Merit , Nano-Crystalline , P -Type Transparent Conducting Material at Low Temperatur. **2015**, *31901*, 2–7.
- (5) Crépellière, J.; Popa, P. L.; Bahlawane, N.; Leturcq, R.; Werner, F.; Siebentritt, S.; Lenoble, D. Transparent Conductive CuCrO<sub>2</sub> Thin Films Deposited by Pulsed Injection Metal Organic Chemical Vapor Deposition: Up-Scalable Process Technology for an Improved Transparency/conductivity Trade-Off. *J. Mater. Chem. C* **2016**, *4* (19), 4278–4287.

- (6) Sánchez-Alarcón, R. I.; Oropeza-Rosario, G.; Gutierrez-Villalobos, A.; Muro-López, M. A.; Martínez-Martínez, R.; Zaleta-Alejandre, E.; Falcony, C.; Alarcón-Flores, G.; Fragoso, R.; Hernández-Silva, O.; Perez-Cappe, E.; Laffita, Y. M.; Aguilar-Frutis, M. Ultrasonic Spray-Pyrolyzed CuCrO<sub>2</sub> Thin Films. *J. Phys. D. Appl. Phys.* **2016**, *49* (17).
- (7) Farrell, L.; Norton, E.; Smith, C. M.; Caffrey, D.; Shvets, I. V.; Fleischer, K. Synthesis of Nanocrystalline Cu Deficient CuCrO<sub>2</sub> - a High Figure of Merit P-Type Transparent Semiconductor. *J. Mater. Chem. C* **2016**, *126* (4), 126–134.
- (8) Scherrer, P. Göttinger Nachrichten Math. *Phys* **1918**, *2*, 98–100.
- (9) Scanlon, D. O.; Watson, G. W. Understanding the P-Type Defect Chemistry of CuCrO<sub>2</sub>. *J. Mater. Chem.* **2011**, *21* (11), 3655.
- (10) Rousseau, D. L.; Bauman, R. P.; Porto, S. P. S. Normal Mode Determination in Crystals. *J. Raman Spectrosc.* **1981**, *10* (1), 253–290.
- (11) Garg, A. B.; Mishra, A. K.; Pandey, K. K.; Sharma, S. M. Multiferroic CuCrO<sub>2</sub> under High Pressure: In Situ X-Ray Diffraction and Raman Spectroscopic Studies. *J. Appl. Phys.* **2014**, *116* (13).
- (12) Han, M.; Wang, J.; Deng, Q.; Wang, J.; Li, W.; Zhang, P.; Li, C.; Hu, Z. Effect of Annealing Temperature on Structural, Optoelectronic Properties and Interband Transitions of CuCrO<sub>2</sub> Nanocrystalline Films Prepared by the Sol–gel Method. *J. Alloys Compd.* **2015**, *647*, 1028–1034.
- (13) Aktas, O.; Truong, K. D.; Otani, T.; Balakrishnan, G.; Clouter, M. J.; Kimura, T.; Quirion, G. Raman Scattering Study of Delafossite Magnetoelectric Multiferroic Compounds: CuFeO<sub>2</sub> and CuCrO<sub>2</sub>. *J. Phys. Condens. Matter* **2012**, *24* (3), 36003.
- (14) Pellicer-Porres, J.; Segura, A.; Martínez, E.; Saitta, A. M.; Polian, A.; Chervin, J. C.; Canny, B. Vibrational Properties of Delafossite CuGaO<sub>2</sub> at Ambient and High Pressures. *Phys. Rev. B* **2005**, *72* (6), 64301.
- (15) Pellicer-Porres, J.; Martínez-García, D.; Segura, A.; Rodríguez-Hernández, P.; Muñoz, A.; Chervin, J. C.; Garro, N.; Kim, D. Pressure and Temperature Dependence of the Lattice Dynamics of CuAlO<sub>2</sub> Investigated by Raman Scattering Experiments and Ab Initio Calculations. *Phys. Rev. B* **2006**, *74* (18), 184301.
- (16) Barnabe, A.; Thimont, Y.; Lalanne, M.; Presmanes, L.; Tailhades, P. P-Type Conducting Transparent Characteristics of Delafossite Mg-Doped CuCrO<sub>2</sub> Thin Films Prepared by RF-Sputtering. *J. Mater. Chem. C* **2015**, *3* (23), 6012–6024.

- (17) Lieber, C. M.; Wang, Z. L. Functional Nanowires. *MRS Bull.* **2007**, *32* (2), 99–108.
- (18) Garnett, E. C.; Brongersma, M. L.; Cui, Y.; McGehee, M. D. Nanowire Solar Cells. *Annu. Rev. Mater. Res.* **2011**, *41* (1), 269–295.
- (19) Michallon, J.; Bucci, D.; Morand, A.; Zanucoli, M.; Consonni, V.; Kaminski-Cachopo, A. Light Trapping in ZnO Nanowire Arrays Covered with an Absorbing Shell for Solar Cells. *Opt. Express* **2014**, *22* (S4), A1174.
- (20) Michallon, J.; Bucci, D.; Morand, A.; Zanucoli, M.; Consonni, V.; Kaminski-Cachopo, A. Light Absorption Processes and Optimization of ZnO/CdTe Core-shell Nanowire Arrays for Nanostructured Solar Cells. *Nanotechnology* **2015**, *26* (7), 75401.
- (21) Zhang, Y.; Wang; Mascarenhas, A. “Quantum Coaxial Cables” for Solar Energy Harvesting. *Nano Lett.* **2007**, *7* (5), 1264–1269.
- (22) Guillemin, S. Mécanismes de Croissance de Nanostructures de ZnO Par Voie Chimie Liquide et Caractérisation Avancée. INSA de Lyon 2014.
- (23) Guillemin, S.; Rapenne, L.; Roussel, H.; Sarigiannidou, E.; Brémond, G.; Consonni, V. Formation Mechanisms of ZnO Nanowires: The Crucial Role of Crystal Orientation and Polarity. *J. Phys. Chem. C* **2013**, *117* (40), 20738–20745.
- (24) Cossuet, T.; Appert, E.; Thomassin, J.-L.; Consonni, V. Polarity-Dependent Growth Rates of Selective Area Grown ZnO Nanorods by Chemical Bath Deposition. *Langmuir* **2017**, acs.langmuir.7b00935.
- (25) Guillemin, S.; Appert, E.; Roussel, H.; Doisneau, B.; Parize, R.; Boudou, T.; Bremond, G.; Consonni, V. Controlling the Structural Properties of Single Step, Dip Coated ZnO Seed Layers for Growing Perfectly Aligned Nanowire Arrays. *J. Phys. Chem. C* **2015**, *119* (37), 21694–21703.
- (26) Šćepanović, M.; Grujić-Brojčin, M.; Vojisavljević, K.; Bernik, S.; Srećković, T. Raman Study of Structural Disorder in ZnO Nanopowders. *J. Raman Spectrosc.* **2010**, *41* (9), 914–921.
- (27) Rauch, E. F.; Portillo, J.; Nicolopoulos, S.; Bultreys, D.; Rouvimov, S.; Moeck, P. Automated Nanocrystal Orientation and Phase Mapping in the Transmission Electron Microscope on the Basis of Precession Electron Diffraction. *Zeitschrift für Krist.* **2010**, *225* (2–3), 103–109.
- (28) Consonni, V.; Rapenne, L.; Renou, G.; Roussel, H.; Gérard, L.; Cuscó, R.; Artús, L.; André, R.; Rauch, E. F. Identifying and Mapping the Polytypes and Orientation

Relationships in ZnO/CdSe Core-shell Nanowire Arrays. *Nanotechnology* **2016**, 27 (44), 445712.

(29) Farhan, M. S.; Zalnezhad, E.; Bushroa, A. R.; Sarhan, A. A. D. Electrical and Optical Properties of Indium-Tin Oxide (ITO) Films by Ion-Assisted Deposition (IAD) at Room Temperature. *Int. J. Precis. Eng. Manuf.* **2013**, 14 (8), 1465–1469.

(30) Tonooka, K.; Kikuchi, N. Preparation of Transparent CuCrO<sub>2</sub>:Mg/ZnO P-N Junctions by Pulsed Laser Deposition. *Thin Solid Films* **2006**, 515 (4), 2415–2418.

(31) Ding, J.; Sui, Y.; Fu, W.; Yang, H.; Zhao, B.; Li, M. ZnO Nanorod array/CuAlO<sub>2</sub> Nanofiber Heterojunction on Ni Substrate: Synthesis and Photoelectrochemical Properties. *Nanotechnology* **2011**, 22 (29), 295706.

(32) Tripathi, T. S.; Niemelä, J.-P.; Karppinen, M. Atomic Layer Deposition of Transparent Semiconducting Oxide CuCrO<sub>2</sub> Thin Films. *J. Mater. Chem. C* **2015**, 8364–8371.

(33) Lee, Y. J.; Ruby, D. S.; Peters, D. W.; McKenzie, B. B.; Hsu, J. W. P. ZnO Nanostructures as Efficient Antireflection Layers in Solar Cells. *Nano Lett.* **2008**, 8 (5), 1501–1505.

(34) Hatch, S. M.; Briscoe, J.; Dunn, S. A Self-Powered ZnO-Nanorod/CuSCN UV Photodetector Exhibiting Rapid Response. *Adv. Mater.* **2013**, 25 (6), 867–871.

(35) Garnier, J.; Parize, R.; Appert, E.; Chaix-Pluchery, O.; Kaminski-Cachopo, A.; Consonni, V. Physical Properties of Annealed ZnO Nanowire/CuSCN Heterojunctions for Self-Powered UV Photodetectors. *ACS Appl. Mater. Interfaces* **2015**, 7 (10), 5820–5829.

(36) Park, S.; Kim, S.; Sun, G. J.; Byeon, D. B.; Hyun, S. K.; Lee, W. I.; Lee, C. ZnO-core/ZnSe-Shell Nanowire UV Photodetector. *J. Alloys Compd.* **2016**, 658, 459–464.

(37) Bu, I. Y. Y. Optoelectronic Properties of Novel Amorphous CuAlO<sub>2</sub>/ZnO NWs Based Heterojunction. *Superlattices Microstruct.* **2013**, 60, 160–168.

(38) Poienar, M.; Hardy, V.; Kundys, B.; Singh, K.; Maignan, A.; Damay, F.; Martin, C. Revisiting the Properties of Delafossite CuCrO<sub>2</sub>: A Single Crystal Study. *J. Solid State Chem.* **2012**, 185 (November 2011), 56–61.



## Chapter VI - Conclusions and future perspectives

In the work here presented, we successfully prepared two different copper-based oxides thin films, aiming on the electrical and optical enhancements, and we integrated them into *pn* junctions for energy and light sensing devices.

After a preliminary screening of different cations as possible p-type dopants for Cu<sub>2</sub>O, the incorporation of **magnesium in cuprous oxide** thin films was successfully achieved by aerosol-assisted metal-organic chemical vapour deposition under atmospheric pressure condition at 350 °C. The magnesium content could be increased up to 17% concentration in cubic Cu<sub>2</sub>O phase without the appearance of any magnesium-related phase. The incorporation had a strong effect on the electrical properties, reducing the **resistivity to 6.6 Ω.cm**, by increasing the **charge carrier density up to 8.1x10<sup>17</sup> cm<sup>-3</sup>**. This result was attributed to the increase of simple copper vacancies, induced by the presence of magnesium in a tetrahedral position, leading to an increase of the hole concentration, as calculated by Nolan *et al.*

Post-deposition annealing treatments in oxidizing conditions are commonly performed on Cu<sub>2</sub>O thin films to enhance electrical and optical properties; nevertheless, parasitic CuO phase usually starts to be formed in the films at 300 °C. **The dopant presence in the films had a substantial impact on the stability of the Cu<sub>2</sub>O phase under these oxidizing conditions.** The Mg-doped Cu<sub>2</sub>O thin films exhibit a reduced amount of CuO phase than the intrinsic Cu<sub>2</sub>O films when compared on the same thermal treatments conditions. This fact is due to a different CuO formation mechanism between intrinsic and doped thin films. As suggested by Isseroff and Carter, doping with Mg can prevent the formation of split vacancies for a single cation vacancy, since the divalent cation would assume a position similar to a split copper vacancy in the crystallographic structure. Consequently, the reduction of split copper vacancies leads to lower concentration of CuO nucleation centres, which inhibits the formation of the parasitic phase in the bulk of the film. Moreover, the reduce presence of CuO phase in the Mg-doped Cu<sub>2</sub>O has

## Chapter VI - Conclusions and future perspectives

advantageous consequences for thin films properties, showing a lower resistivity and higher transparency than the intrinsic Cu<sub>2</sub>O.

Concerning the doped Cu<sub>2</sub>O material, a comprehensive analysis of other dopants, especially Sn, Ni and Co, could be required to understand the impact of these divalent cations in a broader way. The use of other deposition techniques, using chemical or physical routes, would possibly provide a more efficient way to incorporate these elements, which posed substantial challenges for the constraints of the AA-MOCVD technique. A comprehensive study on the temperature-dependent Hall Effect on the Cu<sub>2</sub>O:Mg thin films could also clarify the energy level of different acceptors. Moreover, other strategies can be explored to improve the conduction properties of Cu<sub>2</sub>O thin films, combining it with other conductive materials.

The combined finding about the material stability and the higher conductivity of Cu<sub>2</sub>O:Mg led to the **application of these thin films to *pn* junctions** formed with ZnO, an n-type transparent conducting oxide. The structures showed diode-like behaviour with rectification ratios in the 100 range and photovoltaic response with an open-circuit voltage values up to 300mV. Nevertheless, the solar cells showed low current density values, below 1mA.cm<sup>-2</sup> due to intrinsic characteristics of the CVD-prepared films. Low carrier mobility and presence of carbon species hinder the path to junction improvement. These observations stress that the need of using supplementary techniques, as thermal oxidation of metallic copper or electrodeposition in the perspective of Cu<sub>2</sub>O:Mg-based solar cell design.

As the increase of transparency of Cu<sub>2</sub>O could not be reached in the previously described work, other copper-based oxide systems with a larger band-gap were considered. Therefore, the p-type semiconductor alloy **CuCrO<sub>2</sub>** was developed and thin films were successfully deposited by aerosol-assisted metal-organic chemical vapour deposition. These materials exhibit optical and electrical properties similar to state-of-the-art reports, with a direct band-gap of 3.2eV and resistivity values of 0.1 Ω.cm.

As a consequence, this delafossite material was implemented into an original **core-shell heterostructure in combination with ZnO** towards application as a **UV photodetector**. This heterostructure functionally operates as a diode, with a rectification ratio as high as 5500 at ±1 V, denoting larger improvements compared to diodes with similar junctions under planar architecture, which present rectification ratio below 100. It further exhibits optical absorption above 85% in the UV region.

## Chapter VI - Conclusions and future perspectives

Moreover, the device presents a maximum responsivity of  $187 \mu\text{A/W}$  under zero bias at 374 nm and a high UV-to-visible rejection ratio (374-550 nm) of 68 together with a PV response under standard AM1.5G illumination. The combination of the high rectification ratio, high absorption coefficient in the UV region, and of the remarkable responsivity offers promising possibilities for the application of such a heterostructure as a self-powered UV photodetector. Further optimization of this core-shell device can be achieved with the variation of nanowires size and diameter,  $\text{CuCrO}_2$  shell thickness or even the use of another delafossite material. Moreover, different applications as gas sensor or water splitting device would deserve some attention in the near future.

In conclusion, this research work was dedicated to the synthesis and characterization of copper-based oxides with the constant aim of ultimately incorporating them into opto-electric systems, fulfilling the initial intention, "*from material to devices*".

## **Chapter VI - Conclusions and future perspectives**

Appendix

Appendix

## 7.1 A – EXAFS Data Fittings

In order to identify the EXAFS spectra with the crystallographic structure of the material, a theoretical EXAFS spectra is created by *Arthemis* software, using the crystallographic parameters of the oxide and the variation of EXAFS parameters and then fitted by comparison to optimize the simulation. The list of variable parameters, presented in Table A-17, are related to the number of neighboring atoms (N), distance to the neighboring atom (R), change in half-path length ( $\Delta R$ ), energy shifts depending on the atom type ( $\Delta E$ ), mean squared displacement ( $\sigma^2$ ) and passive electron reduction factor ( $S_0^2$ ).

In our case, we will fixed the N and  $S_0^2$  to theoretical values. Only the two first interaction paths will be used for  $\text{Cu}_2\text{O}$ , corresponding to Cu-O 1<sup>st</sup> and Cu-Cu 1<sup>st</sup> first neighbors. N will be 2 for Cu-O and 12 for Cu-Cu. We will use three first interaction paths will be used for CuO, corresponding to Cu-O 1<sup>st</sup>, Cu-Cu 1<sup>st</sup> and Cu-Cu 2<sup>nd</sup> first neighbors. N will be 4 for all of them. The passive electron reduction factor ( $S_0^2$ ) was fixed to 0.813 that allows to fit the Cu-O 1<sup>st</sup> peak for both phases and it is in agreement with the literature<sup>3</sup>. For this study we select the as-deposited  $\text{Cu}_2\text{O}$  film and the film annealed at 450°C which is similar to that annealed at 500°C, showing that the transformation of  $\text{Cu}_2\text{O}$  into CuO is finished for this sample. The preliminary fittings of the EXAFS characterization with the theoretical EXAFS model is visible in Figure A-113.

Table A-17 Fitting parameters of EXAFS data by *Arthemis*

Oxide	Neighbouring atom to Cu	Order	N	$S_0^2$	$\sigma^2$	$\Delta E$	R	$\Delta R$
<b><math>\text{Cu}_2\text{O}</math></b>	O	1st	2	0.813	0.0055	7.9	1.84880	0.018
	Cu	1st	12	0.813	0.01450	7.9	3.01910	0.04500
<b>CuO</b>	O	1st	4	0.813	0.00225	0	1.94750	0.00000
	Cu	1st	4	0.813	0.00400	0	2.88440	0.01921
	Cu	2nd	4	0.813	0.00500	0	3.07080	0.01744

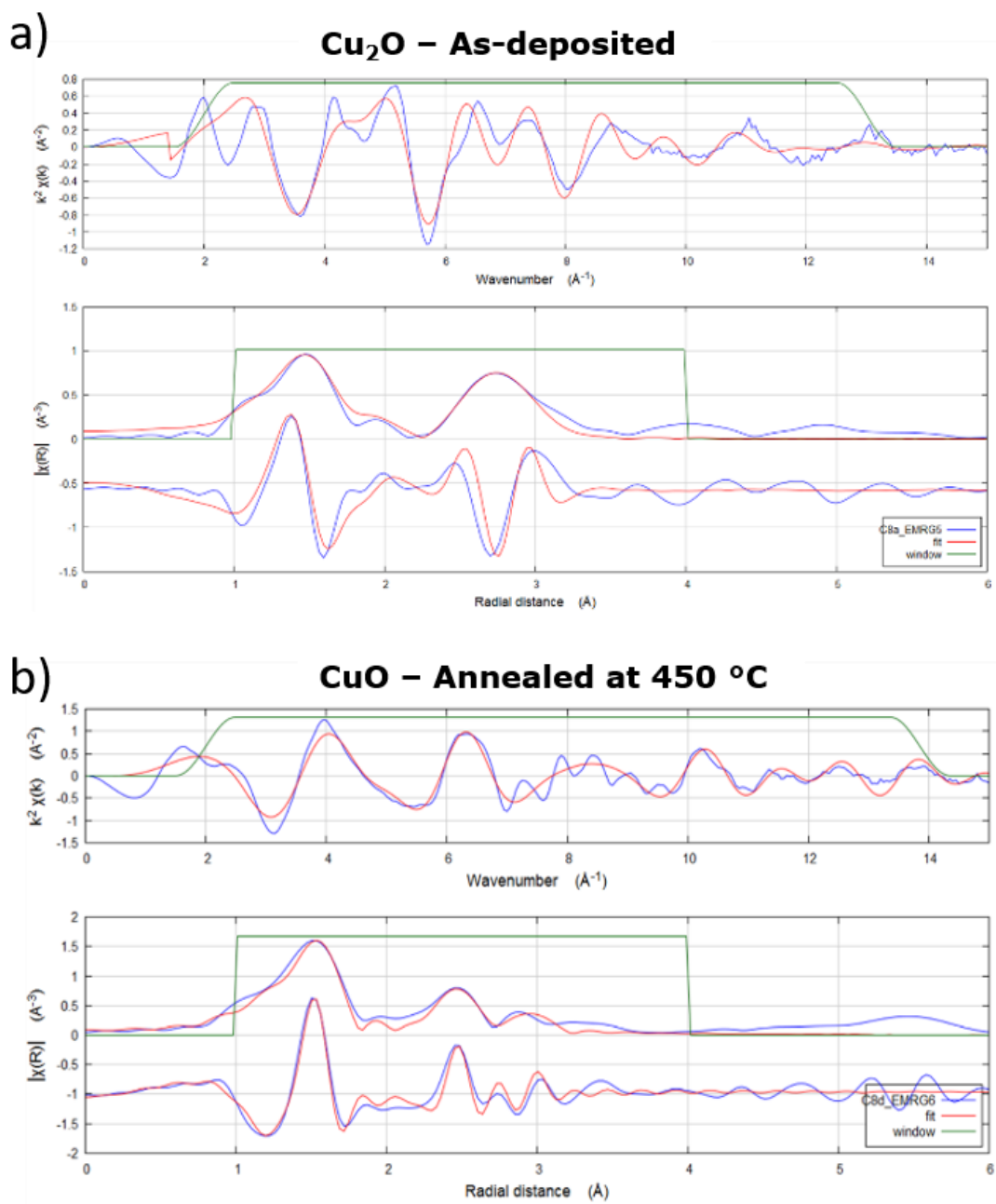


Figure A-113 Preliminary fitting of the Cu  $k$ -edge represented in  $k^2$  and the used parameter for a) as deposited Cu<sub>2</sub>O film and b) CuO reference obtained by oxidation of Cu<sub>2</sub>O at 450°C during 30 minutes. Experimental spectra in blue lines and fitted data in red lines. Green line represents the  $k$  window used (1-4)

The fitting of these two extreme spectra in the EXAFS study seem to correspond well with the crystallographic order of both copper oxides. The  $k^2$  fitted curve show a good agreement with the experimental one, which led to a correct Fourier transform fitting in the distance to the neighboring atom plots.

## 7.2 B – PDF X-Ray Files

Copper (I) oxide – Cuprous Oxide - Cuprite -  $\text{Cu}_2\text{O}$ 

<i>Pattern</i> : 04-007-9767		<i>Radiation</i> = 1.540598		<i>Quality</i> : High		
Cu <sub>2</sub> O		<b>2th</b>	<b>i</b>	<b>h</b>	<b>k</b>	<b>l</b>
Copper Oxide		29.572	51	1	1	0
<i>Also called</i> : copper(I) oxide, Cuprite		36.428	999	1	1	1
		42.314	343	2	0	0
		52.468	11	2	1	1
		61.384	254	2	2	0
		65.556	1	2	2	1
		69.594	3	3	1	0
		73.528	184	3	1	1
		77.384	39	2	2	2
		84.944	2	3	2	1
		92.415	21	4	0	0
		96.157	1	3	2	2
		99.926	1	4	1	1
		103.740	45	3	3	1
		107.617	32	4	2	0
		111.579	1	4	2	1
		115.653	1	3	3	2
		124.276	34	4	2	2
		133.903	1	5	1	0
		139.339	31	5	1	1
<b>Lattice</b> : Cubic		<b>Mol. weight</b> = 143.09				
<b>S.G.</b> : Pn-3m (224)		<b>Volume [CD]</b> = 77.77				
<b>a</b> = 4.26850		<b>Dx</b> = 6.110				
<b>Z</b> = 2		<b>I/lor</b> = 7.94				
ANX: A2X. LPF Collection Code: 1503192. Polymorphism: Room temperature phase. Sample Source or Locality: Canada. Temperature of Data Collection: 295 K. Unit Cell Data Source: Single Crystal. Data collection flag: Ambient.						

Appendix

**Copper(II) oxide – Tenorite - CuO**

Pattern : 00-048-1548

Radiation = 1.540600

Quality : High

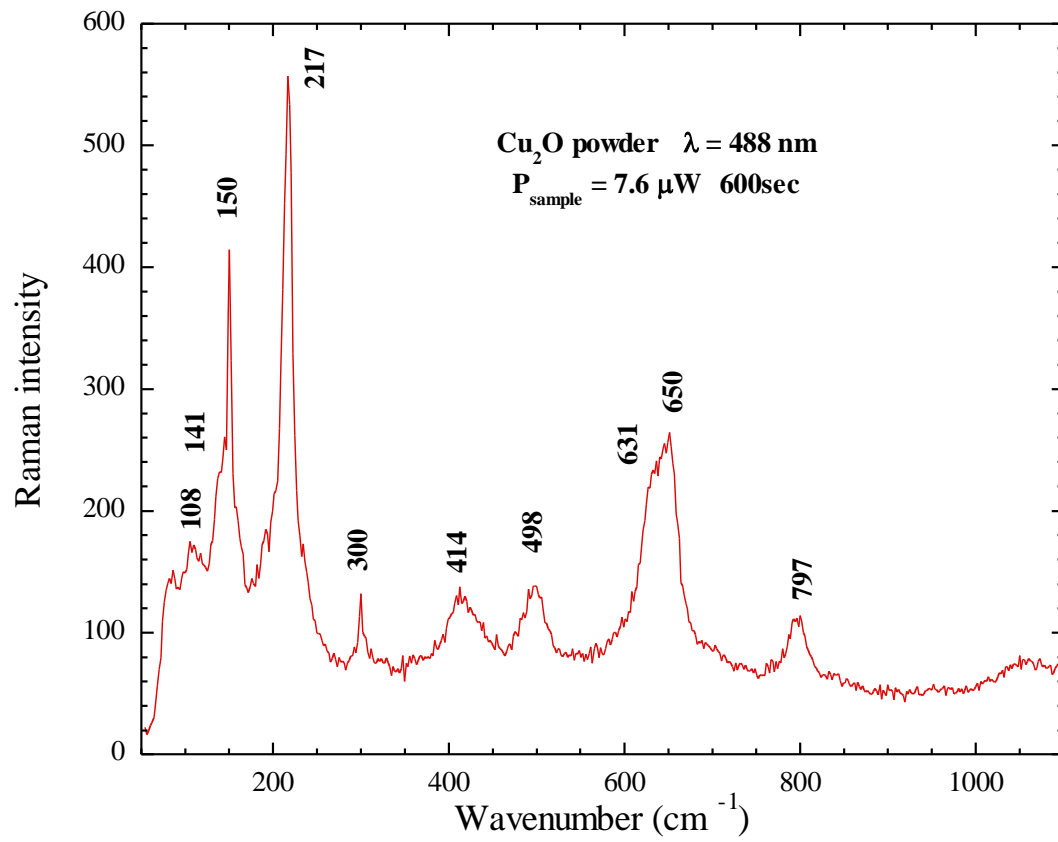
CuO		2th	i	h	k	l
		32.509	13	1	1	0
		35.418	37	0	0	2
		35.544	100	1	1	-1
		38.709	99	1	1	1
	Copper Oxide	38.903	21	2	0	0
	Tenorite, syn	46.260	3	1	1	-2
		48.717	30	2	0	-2
		51.344	1	1	1	2
		53.487	7	0	2	0
		56.743	1	0	2	1
		58.265	10	2	0	2
		61.526	20	1	1	-3
		65.813	10	0	2	2
		66.222	15	3	1	-1
		66.449	1	3	1	0
		67.905	6	1	1	3
		68.125	14	2	2	0
		68.907	1	2	2	-1
		71.683	1	3	1	-2
		72.373	5	3	1	1
		72.944	1	2	2	1
		74.978	6	0	0	4
		75.245	5	2	2	-2
		79.733	1	0	2	3
		80.157	2	2	0	-4
		80.241	1	1	1	-4
		82.362	4	3	1	-3
		83.065	2	2	2	2
		83.568	2	4	0	0
		*83.568	2	3	1	2
		86.533	1	4	0	-2
		86.775	1	2	2	-3
		87.968	1	1	1	4
		88.054	1	1	3	0
		89.790	3	1	3	-1
		91.729	1	1	3	1
		95.565	1	2	0	4
		98.392	1	0	2	4
		*98.392	1	2	2	3
		99.684	2	3	1	3
		101.935	1	4	0	2
		103.357	2	1	1	-5
		103.565	2	2	2	-4
		107.049	2	4	2	0
		109.519	1	1	3	-3
		110.170	3	4	2	-2
		111.191	1	4	0	-4
		113.489	2	1	1	5
		114.060	1	4	2	1
		*114.060	1	3	3	-1
		115.744	1	1	3	3
		116.838	1	5	1	-1
		120.221	1	2	2	4
		120.509	3	3	3	1
		*120.509	3	3	1	-5
<b>Lattice</b> : Base-centered monoclinic		<b>Mol. weight</b> = 79.55				
<b>S.G.</b> : C2/c (15)		<b>Volume [CD]</b> = 81.22				
<b>a</b> = 4.68830	<b>beta</b> = 99.51	<b>Dx</b> = 6.505				
<b>b</b> = 3.42290						
<b>c</b> = 5.13190						
<b>a/b</b> = 1.36969		<b>Z</b> = 4				
<b>c/b</b> = 1.49928						
Additional Patterns: To replace 00-005-0661. Sample Preparation: "Cu <sub>2</sub> (OH) <sub>3</sub> NO <sub>3</sub> " was thermally decomposed to form "CuO". This was annealed at 1000 C in air for 5 hours. Unit Cell Data Source: Powder Diffraction. Data collection flag: Ambient.						
Langford, J., Louer, D., J. Appl. Crystallogr., volume 24, page 149 (1991)						

# Appendix

## Copper Chromium oxide – CuCrO<sub>2</sub>

Pattern : 04-010-3330		Radiation = 1.540600			Quality : High	
CuCrO <sub>2</sub>		2th	I	h	k	l
Copper Chromium Oxide Mcconnellite, syn		15 533	18	0	0	3
		31 369	391	0	0	2
		35 217	60	1	0	1
		36 410	998	0	1	2
		40 870	344	1	0	4
		43 081	18	0	1	5
		47 835	15	0	1	9
		51 898	3	1	0	7
		55 855	267	0	1	8
		62 413	199	1	1	0
		64 761	9	1	1	3
		65 460	170	1	0	10
		65 460	170	0	0	19
		70 733	3	0	1	11
		71 520	105	1	0	2
		73 738	4	0	2	9
		74 461	66	2	0	4
		77 330	39	0	2	4
		79 475	9	2	0	15
		82 979	7	1	0	10
		*82 979	7	1	1	0
		85 110	1	0	2	7
		*85 110	1	0	0	15
		88 804	40	0	1	14
		*88 804	40	0	1	18
		96 968	73	0	2	10
		*96 968	73	1	1	19
		101 044	1	2	0	11
		102 587	1	0	1	1
		104 883	9	2	0	2
		105 807	30	1	2	1
		108 357	11	0	1	4
		108 596	29	2	1	5
		110 748	9	1	2	13
		113 588	1	0	2	15
		116 747	1	1	1	7
		*116 747	1	2	0	14
		120 833	49	2	1	8
		*120 833	49	1	2	0
		127 643	20	3	0	3
		130 895	1	0	3	10
		130 895	1	0	1	11
		131 106	38	2	1	6
		138 869	1	1	2	1
		139 011	24	3	2	1
		*139 011	21	0	2	1
		142 163	1	0	1	1
		143 364	17	0	1	1
		148.413	39	1	1	1
<b>Lattice</b> : Rhombohedral <b>S.G.</b> : R-3m (166) <b>a</b> = 2.97340 <b>c</b> = 17.10000 <b>Z</b> = 3		<b>Mol. weight</b> = 147.54 <b>Volume [CDJ]</b> = 130.93 <b>Dx</b> = 5.614 <b>I/Cor</b> = 5.23				
ANX: ABX <sub>2</sub> . Habit: plate-like. LPF Collection Code: 1002490. Sample Preparation: STARTING MATERIALS: K <sub>2</sub> Cr <sub>2</sub> O <sub>7</sub> :CuO CRUCIBLE: platinum crucible. Unit Cell Data Source: Single Crystal. Data collection flag: Ambient.						
Calculated from LPF using POWD-12++ Crottaz, O., Kubel, F., Z. Kristallogr., volume 211, page 482 (1996)						
<b>Radiation</b> : CuKα1 <b>Lambda</b> : 1.54060 <b>SSFOM</b> : F30=112(0.0073,36)		<b>Filter</b> : <b>d-sp</b> : Calculated spacings				

### 7.3 C – Raman spectrum of Cu<sub>2</sub>O powder



## List of communications

### Journal Articles:

1. **J. Resende**, C. Jiménez, N D Nguyen, J.L. Deschanvres “*Magnesium-doped cuprous oxide (Mg:Cu<sub>2</sub>O) thin films as a transparent p-type semiconductor*” Phys. Status Solidi A, 213: 2296–2302 (2016) Impact factor: 1.85 - N° of citations: 4
2. S. Brochen, L. Bergerot, W. Favre, **J. Resende**, C. Jiménez, J.L. Deschanvres, V. Consonni “Effect of Strontium Incorporation on the p-Type Conductivity of Cu<sub>2</sub>O Thin Films Deposited by Metal-Organic Chemical Vapor Deposition”, J. Phys. Chem. C, 120 (31), pp 17261–17267 (2016) Impact factor: 4.509 - N° of citations: 1
3. VH Nguyen, **J Resende**, C Jiménez, ..., D. Bellet, D. Muñoz-Rojas “*Deposition of ZnO based thin films by atmospheric pressure spatial atomic layer deposition for application in solar cells*” J. Renewable Sustainable Energy 9, 021203 (2017) Impact factor: 1.276 - N° of citations: 2

### Book Chapter:

D Muñoz-Rojas, H Liu, **J Resende**, D Bellet... Chapter: *Materials for Photovoltaic Solar Cells* in the book - Materials for Sustainable Energy Applications: Conversion, Storage, Transmission, and Consumption (2016)

### Oral presentations:

1. 2017 E-MRS Spring Meeting and Exhibit “A novel ZnO / CuCrO<sub>2</sub> core shell nanowire heterostructure for UV photodetectors” in Strasbourg, France
2. TCM 16 “Cation-doped Cu<sub>2</sub>O as a transparent p-type semiconducting oxide with enhanced performances: A comparison between Strontium and Magnesium incorporation” in Crete, Greece
3. Colloque National du GDR 2016 “Magnesium-doped Cuprous Oxide: An improved transparent p-type semiconductor oxide” in Autrans, France

### Poster presentation:

2015 E-MRS Fall Meeting and Exhibit “*Magnesium-doped Cuprous Oxide (Mg:Cu<sub>2</sub>O) thin films as a transparent p-type semiconductor oxide*” in Warsaw, Poland